Investigation on Surface Integrity in Ultra-precision Cutting of Single Crystalline Optical Materials for Microcavity

February 2018

Yuta Mizumoto

A Thesis for the Degree of Ph.D. in Engineering

Investigation on Surface Integrity in Ultra-precision Cutting of Single Crystalline Optical Materials for Microcavity

February 2018

Graduate School of Science and Technology
Keio University

Yuta Mizumoto

List of Contents

Nomenclature

Roman symbols

A	Area where applied force acts
A_c	Intersectional area between rake face of tool and workpiece
A'	Projected area onto slip plane
b	Burgers vector
B	Correlation length
c	Semimajor axis
C	Cleavage fracture parameter
d	Semiminor axis
d_c	Critical uncut chip thickness
d_{max}	Maximal uncut chip thickness
D	Diameter of cavity
e	Base of natural logarithm
E	Young's modulus
E_{in}	Energy stored in a cavity
E_s	Specific cutting energy
$E(x, y, z)$	Electric field in a cavity
f	Feed per revolution
f_0	Off-set frequency
f_n	Mode frequency for n-th order
$f_{chatter}$	Chatter frequency
f_{rep}	Repetitive frequency
f_{res}	Resonant frequency
F	Applied force on a crystal
F'	Projected force onto slip plane
F_c	Cutting force
F_t	Thrust force
G	Rigidity modulus
H	Hardness
k	Mode interval between the resonances
K_c	Fracture toughness
l	Contact length
L	Cavity length
$L_{chatter}$	Measurement length for chatter marks
m	Mode number (integer) (except for chapter 3)
m	Schmid factor for i-th slip or twinning system (chapter 3)
n	Refractive index

$n_{chatter}$	Wavenumber of chatter mark
n_{eff}	Effective refractive index
p	Number of coalesced a{100} dislocation
P	Plastic deformation parameter
P_{out}	Energy dissipated from a cavity per cycle
P_{th}	Threshold value of the optical input power
Q	Quality factor
Q_i	Intrinsic Q factor
Q_r	Q factor related to loss due to radiation and affected by the bending loss
$Q_{b,abs}$	Q factor affected by the absorption loss of the bulk material
$Q_{s,abs}$	Q factor affected by surface absorption due to the lattice transformation
Q_{scat}	Q factor affected by the Rayleigh scattering due to the surface roughness
Q_{TPA}	Q factor affected by the loss due to two-photon absorption (TPA)
$Q_{TPA,FC}$	Q factor affected by the loss due to TPA-induced free carrier absorption
R	Nose radius
R_a	Arithmetic surface roughness per line (one dimension)
R_q	Root-mean-square surface roughness
R_y	Theoretical surface roughness
S_a	Arithmetic surface roughness per area (two dimension) to
T	Rotational speed of turning spindle
$T_i(\mu)$	Parameter estimating the probability of slip activation
U	Total energy for crack initiation
U_E	Elastic energy
U_S	Surface energy
V	Cavity volume
V_f	Cutting speed
v_l	Frequency of the l-th longitudinal mode
V_m	Mode volume
w	Width of dislocation
W_L	Mechanical energy of the body (amount of work done by the applied loads)
w_p	Plastic work required to spread the crack

Greek symbols

α	Rake angle
α_{abs}	Absorption coefficient
β	Force angle
γ	Specific surface energy
δ	Cutting direction
ε	Dielectric constant of the cavity
θ	Angle between the applied stress and slip plane normal vector

Λ	Correction factor
λ	Angle between the applied stress and slip direction
λ_m	Resonant wavelength for m-th order
λ_{eff}	Effective resonant wavelength
λ_i	Input wavelength
λ_r	Resonant wavelength
λ_{FWHM}	Full width at half maximum of the resonant wavelength
ν	Poison's ratio
ρ	Radius of curvature
σ	Tensile stress
σ_a	Applied tensile stress
σ_c	Resolved tensile stress
σ_F	Breaking stress for fracture
σ_L	Constant load for crack initiation
τ_{phot}	Photon lifetime
τ_{pn}	Peierls-Nabarro stress
τ_s	Resolved shear stress
τ^{crit}	Critical resolved shear stress
τ_i^{crit}	Critical resolved shear stress for i-th slip system
φ	Angle between the applied stress and cleavage plane normal vector
χ	Fitting coefficient
ω	Resonant angular frequency
$\omega_{natural}$	Natural vibration frequency

Matrix and vector

$\boldsymbol{b}$	Burgers vector
$\boldsymbol{C_p}$	Cleavage plane normal vector
$\boldsymbol{F}$	Applied force
$\boldsymbol{l}$	Dislocation line
$\boldsymbol{S_d}$	Slip direction vector
$\boldsymbol{S_p}$	Slip plane normal vector

Superscript

i	i-th slip or twinning system
j	j-th cleavage

Abbreviations

AFM	Atomic Force Microscope
ATT	Attenuator

BC	Basal Cleavage
BDT	Brittle-Ductile Transition
BCC	Body-Centered Cubic
B-NPD	Boron-Doped Nano-Polycrystalline Diamond
BS	Basal Slip
BT	Basal Twinning
CaF_2	Calcium Fluoride
CCD	Charge Coupled Device
CRSS	Critical Resolved Shear Stress
DOC	Depth Of Cut
EBSD	Electron BackScatter Diffraction
EDFA	Erbium Doped Fiber Amplifier
EEM	Elastic Emission Machining
FCC	Face-Centered Cubic
FEM	Finite Element Method
FSR	Free Spectral Range
FFT	Fast Fourier Transfer
FWM	Four-Wave Mixing
HCP	Hexagonal Closest Packed
IFFT	Inverse Fast Fourier Transfer
$LiNbO_3$	Lithium Niobate
LED	Light Emitting Diode
MgF_2	Magnesium Fluoride
NC	Numerical Control
NPD	Nano-Polycrystalline Diamond
PC	Prismatic Cleavage (except for chapter 6)
PC	Polarization Controller (in chapter 6)
PCD	Poly Crystalline Diamond
PDMS	Polydimethylsiloxane
PhC	Photonic Crystal
PRS	Prismatic Slip
PWM	Power Meter
PYS	Pyramidal Slip
RC	Rhombohedral Cleavage
RT	Rhombohedral Twinning
SCD	Single Crystalline Diamond
SEM	Scanning Electron Microscope
SiO_2	Silicon Dioxide
TE	Thermal Expansion
TO	Thermo-Optic

TOM	Thermo-Opto-Mechanical
UPCT	Ultra-Precision Cylindrical Turning
XRD	X-Ray Diffraction
WGM	Whispering Gallery Mode
WLI	White Light Interferometer

1. Introduction

Development of optical technology has drastically changed and enriched people's lives. The technology has contributed to electrical devices such as cell phones, personal computers, digital cameras, or optical fibers, light sources of LED or laser, photodiode, CCD. Even now, its application is expanding and the technology becomes essential more and more. As a recent advanced technique, an optical microcavity is attracting interests as a next-generation optical device. The microcavity is capable of confining light at a certain spot for a certain amount of time, hence, it is a candidate for high sensitive bio-sensors, source of low-power laser and optical frequency comb, or all-optical signal processing.

These devices have been supported by micro and nanomanufacturing processes. Although etching or electron beam lithography are considered to be suitable for fabricating materials in nanoscale, recent advancement of ultra-precision machine tool enabled us to obtain a nanometric surface in a machining process. Supported by improvement of motion and positioning accuracy of machine tools and enhancement of cutting edge accuracy, ultra-precision technique lead us to machine brittle materials. It has been natural that ceramics materials, for instance, glasses or optical materials are machined by brittle mode and finished by polishing, however, ultra-precision machining process opened a new avenue towards developing a ductile-regime machining of the brittle materials i.e. machining of those without brittle fracture. In 1990, Blake and Scattergood presented the existence of critical depth of cut in the brittle-ductile transitional area in diamond turning of single crystalline silicon and germanium [1]. When the depth of cut, which corresponds to relative magnitude of the displacement between a cutting tool and workpiece, is shallower than some critical value, crack-free surface can be achieved. Their works spurred many researchers to focus on analyzing the mechanism of brittle materials machining all over the world. Then, ultra-precision machining process is one of the strong options to fabricate ceramics, in addition to lithography or etching process. In particular, it has been used for manufacturing of complicated shapes, such as freeform optics. However, a lot of challenges still remain in cutting of brittle materials. Especially, machining of crystalline materials is still difficult because its crystallographic effect has to be considered due to the size effect caused by depth of cut in nanometric level. Additionally, there are not many studies which comprehensively discuss the surface integrity, including the subsurface region.

The objective of this dissertation aims to investigate the cutting mechanisms of single crystalline materials and establish the manufacturing process of high-Q WGM (Whispering Gallery Mode) crystalline microcavities using only an ultra-precision cutting process. The cavity performance strongly depends on the cavity shape, surface

quality, and material properties. For the material properties, single crystalline CaF_2 (Calcium Fluoride) and sapphire show the potential for the high-Q WGM microcavity. To make a crystalline microcavity, a cutting process is required because the process enables to make a microcavity with high form accuracy. However, the cutting process induces brittle fracture on the surface and distortion of crystalline lattice in subsurface region, due to the brittleness and crystal anisotropy. Therefore, their machinability is still an issue. In terms of crystallography, the surface and subsurface integrity of CaF_2 and sapphire in ultra-precision cutting were scrutinized on the basis of the resolved stress model. Based on the obtained results, CaF_2 WGM microcavities were manufactured by only the ultra-precision cutting, and the influence of the ultra-precision cutting on the cavity performance was clarified.

2.   State of the art

This chapter provides fundamentals of optical microcavity and its application. Further, it will give some general background information about machining of brittle materials. For both optics and manufacturing fields, short literature reviews are described. Finally, the objective of the research will be presented.

2.1   Optical microcavity

2.1.1   Characteristics

Recent advancement of nanofabrication technique enabled us to downsize the cavity size and manufacture a various cavity shape [2]. However, regardless of the cavity size or shape, the basic theory of the cavity system does not greatly change compared to the classical model. In this section, the characteristics of the cavity, principle of optical microcavity, quality factor, and mode volume are described.

Principle of optical microcavity

Optical microcavity is an optical device that can confine light in a certain space, and generally the size is less than millimeter scale. The confinement can be realized by the "resonance". Fabry-Perot cavity is chosen as an example of explaining the cavity system. In the Fabry-Perot cavity, two complete reflection mirrors are deployed opposite, and the light is repetitively reflected (Fig. 2-1(a)). When the phase shifting does not occur during the light path, the light can be amplified by the interaction between light and matter. This is so-called "resonance", and Eq.(2-1) holds [3].

$$m\lambda_m = 2nL \qquad\qquad (2\text{-}1)$$

In other words, an optical path in the cavity $2nL$ corresponds to the integral multiple of the input light wavelength $m\lambda_m$, and the light can be confined (Fig. 2-1(b)). At the same time, the different resonance modes exist according to the mode numbers m.
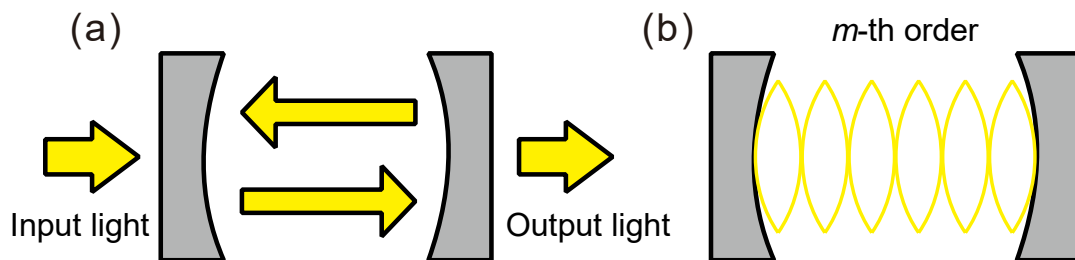

Fig. 2-1 Schematic illustration of (a) Fabry-Perot cavity system and (b) mth-order modes excited in a Fabry-Perot cavity [3].

Quality factor

Once after light is confined in the cavity, the light attenuates by being absorbed in the cavity. Quality factor (Q factor) is one of the most important values to evaluate the duration time of confining light. Q factor is defined as "How long a cavity can confine light.", and expressed by Eq.(2-2) [3].

$$Q = \omega \frac{E_{in}}{P_{out}} \qquad (2\text{-}2)$$

This equation indicates that the larger the stored energy E is and the smaller the dissipated energy per cycle P_{out} is, the longer the light can be confined in the cavity. Eq.(2-2) can be re-written by Eq.(2-3).

$$Q = \omega \tau_{phot} \qquad (2\text{-}3)$$

The photon lifetime τ_{phot} expresses the time until when intensity of the confined light attenuates to one-e times. The longer the photon lifetime is, the longer the interaction time between light and matter. Given that there is no loss in the cavity, the Q factor can be infinitely high and the cavity can eternally confine light, however, some causes are limiting the Q factor in reality. The overall Q factor [4] is given by Eq.(2-4).

$$Q_i^{-1} = \left(Q_r^{-1} + Q_{b,abs}^{-1} + Q_{s,abs}^{-1} + Q_{scat}^{-1}\right) + \left(Q_{TPA}^{-1} + Q_{TPA,FC}^{-1}\right) \qquad (2\text{-}4)$$

Intrinsic Q factor Q_i consists of two main parts, linear (left brackets) and nonlinear (right brackets). At a low power regime, the nonlinear part can be neglected. Thus, focusing on the linear part, the cavity demands for an extremely smooth surface, low absorption coefficient, and high coupling rate, which lead to the theoretically ultra-high Q cavity. In other words, if even one of the Q factors show a low value, the cause can be a bottleneck and deteriorates the intrinsic Q factor.

Mode volume

Mode volume is also an important factor for the cavity. The mode volume is defined as "How small the light-confined space can be", and expressed by Eq.(2-5) [5].

$$V_m = \frac{\iiint \varepsilon |E(x,y,z)|^2 dxdydz}{max[\varepsilon |E(x,y,z)|^2]} \qquad (2\text{-}5)$$

The distribution of light in the cavity is expressed by Eq. (2-5), and the smaller the mode volume is, the energy of light per volume is larger, thus, the more easily the light and matter interact. Mode volume is actually related to the cavity size, therefore downsizing of the cavity may has a great advantage for the integration. On the basis of Q factor and mode volume V_m, various kinds of the cavities are summarized by Vahala [2] as shown in Fig. 2-2.

2.1.2　Types of microcavity

Owing to the micro and nano manufacturing process, several sorts of microcavities have been developed. Most of the cavities are simply classified into three types; (1) Fabry-Perot, (2) Whispering gallery mode (WGM), and (3) photonic crystal (PhC). In this section, on the basis of the classification, several kinds of microcavities are briefly introduced.

Fabry-Perot cavity

Fabry-Perot cavity is one of the well-known cavities, and mainly utilized for the oscillator of the semiconductor laser [6]. Two planar mirrors which show high reflection rate are arranged opposite in parallel, and the input light is repetitively reflected in-between. 1.8×10^{10} (at 852 nm wavelength) Q factor can be obtained [7]. However, its cavity length reaches to 4 mm, therefore, it is not easy to be integrated on a chip. Recently, the cavity system is used to research the interaction between single atom and single photon. In spite of a simple structure, it can achieve Q factor of 3.5×10^7 at 852 nm wavelength which could be calculated by a finesse value of 4.8×10^5 with a mode volume of $1.690 \ \mu m^3$ [8]. In order to overcome the challenge regarding the size of Fabry-Perot cavity, micropillar cavities were developed.

The cavity consists of a circular cross section and a core of which $0.7 - 40 \ \mu m$ diameter, and fabricated using the reactive ion etching of an aluminum gallium arsenide planar microcavity grown by molecular beam epitaxy [9, 10]. Its cavity size of 0.5 μm is significantly smaller than other cavities, however, the Q factor is relatively lower (e.g. 2.0×10^3 Q factor at 1 μm diameter). For conjunction or manipulation of emitting photons,
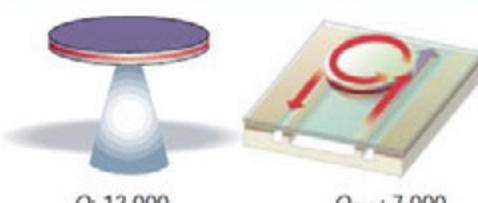

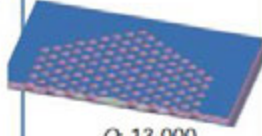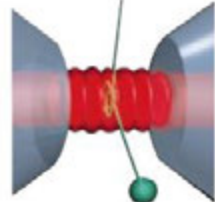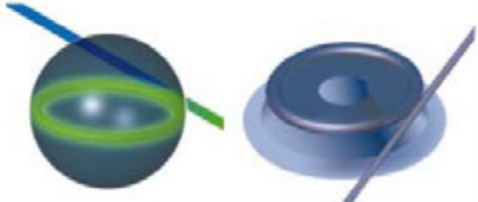Fig. 2-2 Micro-cavities are organized by column according to the confinement method used and by row according to high Q and ultrahigh Q [2]. (Vahala KJ. Optical microcavities. Nature 2003;424(6950):839-46. Reprinted with permission from Nature Publishing Group.)

the micropillar cavity is appropriate. In addition, quasiatom or quantum dot can be integrated in the cavity as an emitter.

Photonic crystal

Highly advanced chemical manufacturing technique e.g. etching has enabled us to uniformly form extremely small air holes of approximately 100 nm radius on a silicon slab (see the part of photonic crystal in Fig. 2-2) [2]. With the feature, PhC cavity exhibits epic phenomena. Because of the periodically deployed holes, periodical distribution of refractive indexes generates on the chip. Due to the periodical crystal structure, Bragg's reflection of photons occurs same as the one of electrons i.e. the photonic band gap can be formed. Some specific wavelength light which corresponds to the band gap is prohibited to propagate, thus, can be confined. The cavity size is extremely small, and it is easy to integrate on a chip (Q factor of 1.2×10^6, mode volume of 1.7 μm^3) [11]. For more practical application, deep-ultraviolet photolithography was recently hired to manufacture the PhC cavity that recorded the Q factor of 2.2×10^5 [12]. There is an advantage of productivity and circuit-integrity in the case of PhC cavity, however, it is difficult to fabricate PhC cavity made of single crystalline materials because the aforementioned fabrication process is not applicable to fabricate single crystalline materials. Hence, it is a challenge to obtain the high Q PhC cavity with crystalline materials.

Whispering gallery mode cavity

WGM microcavities are circular or spherical cavities. The word WGM is originated from Whispering Gallery under the dome of St. Paul's Cathedral in London [13]. Because of the smooth sidewall and circularity, when one whispers, the voice wave propagates along the sidewall by continuous reflection along the wall, and he finally can hear his whisper from his back side. Analogous to the principle, an optical WGM can be explained as follows. When light is inputted into the WGM cavity, the light propagates along the cavity surface based on the total internal reflection, and it comes back to the inputted position. If the phase of the returned light fits the one of the inputted light, a resonance occurs as shown in Fig. 2-3. Based on the principle, several types of the WGM cavity was developed. For the coupling, a taper optical fiber can be used. The input light, indeed, originates from the evanescent light which was formed by the total internal reflection of the light in an optical fiber.

For the first example, microsphere cavity is chosen (see the cavity in the lower row and left side of WGM column in Fig. 2-2). Microsphere cavity can be formed by melting the tip of an optical fiber using high-power CO_2 laser [14]. Owing to the surface tension during the cooling process, a microsphere cavity can be naturally formed. In the cavity,

WGM resonance generates, and high Q value of 2.0×10^7 with 250 μm diameter can be achieved. Recently, the WGM resonance in the microsphere is used to attempt to precisely measure the diameter of the sphere [15]. Although this type of cavity features high Q, it is difficult to assemble and integrate in the circuits.

Toroid cavity is a cavity proposed by Armani [16] and regarded as a high-Q microcavity with 100 μm diameter that features the Q factor of 10^8 order (see the cavity in the lower row and right side of WGM column in Fig. 2-2). The toroid cavity can be manufactured by taking four steps:

1) Thermal film growth of SiO_2 (Silicon Dioxide) is conducted on silicon substrate.
2) Disk-shaped photoresist pad is formed on the substrate by photolithography.
3) The substrate is processed by sacrifice layer etching using Xenon difluoride gas
4) The cavity rim is formed by melting the outside of SiO_2 by CO_2 laser reflow.

Especially, the melting process by CO_2 laser is important, and the surface can be smooth due to the surface tension when cooling, which leads to suppression of surface scattering [17].

Although the above-mentioned cavities are very useful for the application, its manufacturing process limits the utilization of single crystalline materials. Savchenkov simulated the theoretical Q factors of single crystalline materials based on the bulk loss, and showed the potential for ultra-high Q microcavities [18]. Compared to silica which had been conventionally used for the base material, sapphire or $LiNbO_3$ (Lithium Niobate) [19] show almost the same Q factors in a wide range of wavelength, and the Q factor of CaF_2 was much higher [18]. One of the difficulty to manufacture the single crystalline microcavities is that the conventional chemical manufacturing process, for instance, etching is prohibited. Because of the crystal anisotropy, it is difficult to make a form such a bulge-shape WGM cavity [20]. Laser melting can transform the phase of
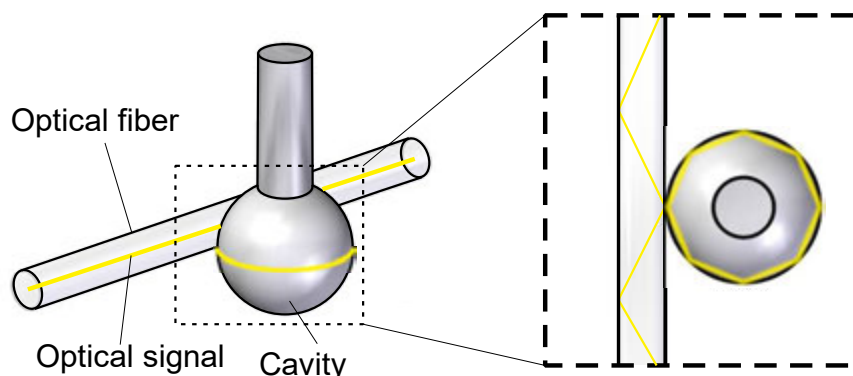
Fig. 2-3 Principle of WGM resonance. When light enters the cavity from an optical fiber, the light propagates along the spherical internal wall in the cavity based on a total internal reflection, and the comes back to the inputted position. If the phase of the returned light fits the one of the inputted light, a resonance occurs.

material, namely, the surface can be transformed from single crystalline layer to polycrystalline one, thus the process is also not applicable. To manufacture the WGM crystalline microcavities, machining process such as diamond polishing is demanded [18]. Grudinin used the diamond turning process to directly fabricate the crystalline materials [21]. Normally, single crystalline materials such as CaF_2 are characterized by hardness, brittleness, and crystal anisotropy, therefore, it is difficult to obtain a smooth and homogeneous surface which is suitable for the microcavity because brittle fracture generate. However, by carefully choosing the cutting parameters, for example, critical uncut chip thickness, it is possible to machine the optical materials same as metal materials, and manufacture the optical devices which satisfy the demanded surface integrity [22]. Combination of cutting and polishing, Grudinin obtained the crystalline microcavity which exceeds the Q factor of 4.0×10^8 [21]. Except for the work, several researchers worked on manufacturing the single crystalline WGM microcavities by using machining process, and evaluated the cavity performance until today [23-28]. In contrast, Kudo [29] employed crystal growth method that is based on a laser heated pedestal growth to the fabricate sapphire microcavity. Although the Q factor was not high (Q factor of 1.6×10^4), the work suggested that single crystalline WGM microcavities could be manufactured without machining process.

2.1.3   Comparison among microcavities

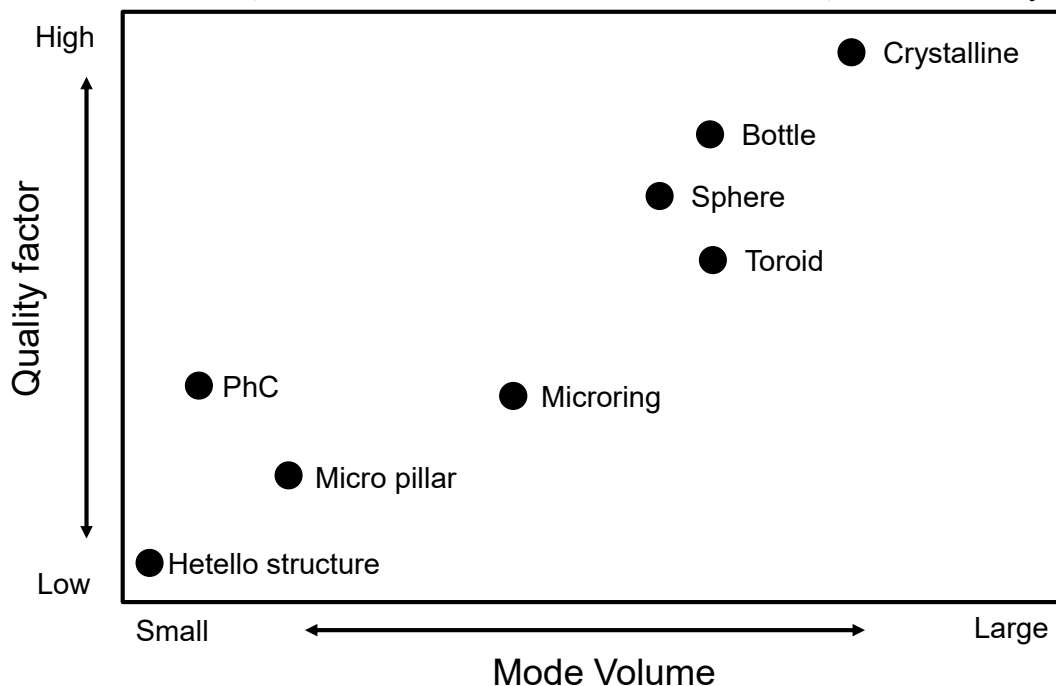As above-mentioned, there are several kinds of the microcavities, and each cavity has

Fig. 2-4 Q factor and mode volume among different sort of cavity types [4, 10, 11, 16, 18, 30-32]. In terms of Q factor, crystalline cavity is the highest.

its specific characteristics. On the basis of Q factor and mode volume V_m, the microcavities are summarized in Fig. 2-4. The following cavities were chosen as representatives for the comparison; PhC cavity [11], micropillar cavity [10], toroid cavity [16], bottle cavity [30], sphere cavity [31], crystalline cavity [18], ring cavity [4], and hetello structure cavity [32].

Crystalline cavity is the most superior in terms of Q factor, and bottle, sphere, and toroid cavities made of SiO_2 are following. Since those cavities are finished by CO_2 laser or polishing processes, the scattering loss can be lower. It should be noted that the high Q factors are also supported by the low absorption coefficients [18]. The other cavities are fabricated by chemical or bottom-up processes, and thus, the surface integrity or form accuracy can be worse than the former ones. In contrast, although Q factors are low, those mode volumes are also smaller, which means light-matter interaction can be more enhanced. Since the fabrication technique can process the nanometric surface and shape, the cavity size itself can be easily downsized, which can be useful for integrated circuits.

The Q factor and mode volume V_m share the trade-off relation, therefore, it is difficult to conclude which cavity is the best. The decision of the usage of cavity also depends on the application. However, if the Q factor is too low, the opportunity that one uses the cavity in a practical way will be lost even if the mode volume V_m is small. Moreover, recent advancement of ultra-precision machining process began to shows the potential to manufacture the high-Q and low-V_m cavity. Thus, this study focuses on the development of WGM crystalline microcavities. Fig. 2-5 shows the limitation of the Q factor made of crystalline materials [18]. Notably, CaF_2 and sapphire theoretically feature the high Q factors in a wide range of wavelength regime. Therefore, if one can fabricate those crystalline materials without serious damage on the surface, the more
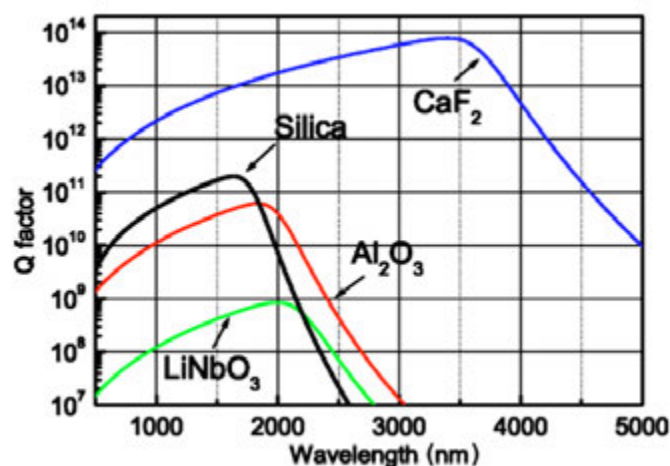

Fig. 2-5 Projected limitation of the Q factor for crystalline WGM resonators by bulk material attenuation. Overall, CaF_2 shows the highest Q factor [18]. (Savchenkov AA, Ilchenko VS, Matsko AB, Maleki L. Kilohertz optical resonances in dielectric crystal cavities. Phys Rev A 2004;70(5):051804(R). Reprinted with permission from American Physical Society.)

downsized WGM crystalline cavity which satisfies the high-Q and low-V_m will be likely manufactured.

2.1.4 Application

From the past time, the cavities have been mainly used for laser diode, however, emergence of various kinds of microcavities expanded their practical application. In this section, bio sensor [33], all-optical signal processing circuit [11], and optical frequency comb [34] are introduced as the expected application.

Bio sensor

Bio sensing technique, such as detection of virus, ideally demands for ultra-high sensitivity, miniaturization and label-free. Especially, labels can structurally and functionally interfere with an assay, thus, it is difficult to exactly examine the molecular behavior on site and in real time [33]. For label-free sensing, various kinds of methods [33, 35-37] are utilized. In these methods, bio-sensing using WGM cavity shows excellent sensitivity because light can interact with targets efficiently. When the molecule binds the cavity, the resonance shifts because of the increased cavity radius. One could detect the size and the density of the molecule by measuring the shifts [33].

All optical processing circuit

Network traffic has been increased day by day for the past decades due to the development of various network systems [38]. With recent emergence of Internet of Things (IoT) concepts, it is easy to guess that the network traffic can be explosively increasing and necessary to efficiently carry and process tremendous amount of data. Although optical signal data is carried through an optical fiber, its signal processing is conducted by electrical signal that is converted from the optical signal. As light is too fast to store in a small space, the signal processing is not performed by the optical signal. A microcavity can be one of the breakthrough devices for all optical signal processing circuits. For example, Tanabe used the PhC cavity to trap and delay photons and showed the possibility of dynamic control of light and optical memory [11]. Although it is more difficult to assembly into the integrated circuits, the high-Q WGM cavity can be a candidate as shown by Pollinger [30]. He made an add/drop filter by changing the coupling position of the bottle cavity and optical fibers for the aim of signal processing.
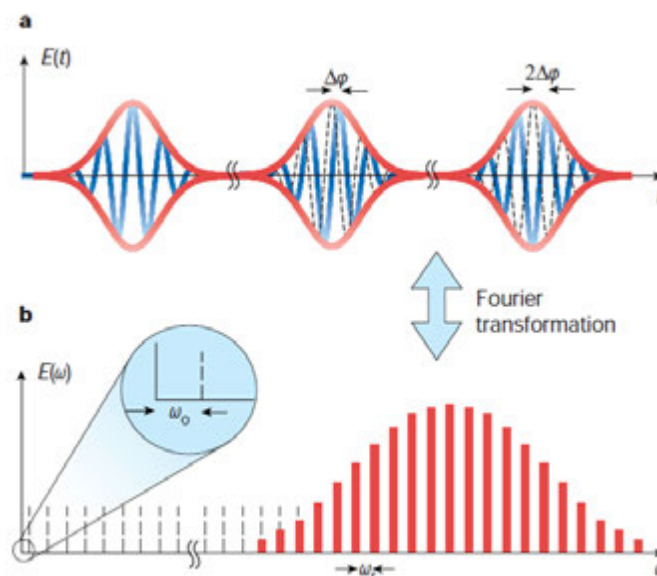
Optical frequency comb

Optical frequency comb was developed to precisely measure the light frequency [39]. As shown in Fig. 2-6, the optical frequency comb indicates the frequency spectra which are ultra-precisely aligned at regular intervals on the frequency axis [34]. The optical

frequency comb has been well studied, and particularly Haensch and Hall contributed their efforts to develop the technology. Haensch et al found that they could measure optical frequencies by optical frequency comb [40], and Hall et al demonstrated to measure absolute frequency chains by using optical combs [41]. The great achievements lead Haensch and Hall to share the Nobel prizes in 2005. Nowadays, the national standard for length is determined by optical frequency comb, and expected to be also applied in astronomy or medical science [39]. For optical frequency comb source, Ti:Sapphire laser or fiber laser are used, which are made of large optical solid-state laser cavity systems and expensive, and miniaturization of the comb source is still a challenge. A microcavity is expected to solve the problems as a novel optical frequency comb source. When some frequency light is inputted into the optical microcavity, FWM (Four-Wave Mixing) which is an effect of third-order non-linear optics generates, and another light which differs from the input frequency light generates at regular intervals [25].

Named after this phenomena, the comb generator using an optical microcavity is called a Kerr frequency comb. To use the Kerr frequency comb, same as the optical frequency comb, it is necessary to broaden the range of frequencies and make the cavity performance stable. However, it is a challenge to obtain a stable Kerr frequency comb because it is difficult to satisfy the demanded properties of ultra-high Q factor, thermal and mechanical stability, and anomalous dispersion (The nature that refractive index at shorter wavelength is smaller than the one at longer wavelength in a specific wavelength regime [42]).

Fig. 2-6 Principle of Optical frequency comb: Consecutive pulses of the pulse train emitted by a mode-locked laser and the corresponding spectrum. (a) Variation of electric field in the time domain (b) FFT spectrum in the frequency domain [34]. (Udem T, Holzwarth R, Hansch TW. Optical frequency metrology. Nature 2002;416(6877):233-7. Reprinted with permission from Nature Publishing Group.)

It is already noted that high Q factor is demanded for the optical microcavity. Except that, characteristics of dispersion and thermal stability are very important for the Kerr frequency comb.

As shown in Fig. 2-6 (a), considering light pulse propagates in the cavity, the pulse (envelope curve) includes approximately 100 carrier waves. Due to the dispersion in the cavity, the propagation speed of envelop wave and carrier wave is different, which causes the phase shift $\Delta\emptyset$. This shifts makes a frequency offset ω_0 (indicated in Fig. 2-6 (b)). Based on the relation $f_0 = \Delta\emptyset f_{rep}/2\pi$, n-th mode frequency f_n is described as follows:

$$f_n = nf_{rep} + f_0 \qquad (2\text{-}6)$$

To determine the absolute frequency of the specific spectrum of the optical frequency comb or Kerr frequency comb, it is necessary to achieve an octave-spanning bandwidth of spectra. This is caused by the fact that an off-set frequency (i.e. zero-order mode frequency) which generates from Kerr frequency comb can be determined by Eq.(2-7):

$$2f_n - f_{2n} = f_0 \qquad (2\text{-}7)$$

This is called f- $2f$ referencing [34]. Until today, there is no work which succeeded to generate an octave-spanning bandwidth Kerr frequency comb by the microcavity which shows anomalous dispersion over octave-spanning. There is a trade-off between the bandwidth of the anomalous dispersion and threshold of the input optical power for generation of Kerr frequency comb. Thus, when one tries to generate a Kerr frequency comb by enhancing the light-matter interaction, the bandwidth of anomalous dispersion can be narrow. The threshold value of input optical power P_{th} to generate a Kerr frequency comb is described by Eq.(2.8) [43].

$$P_{th} \propto \frac{V}{Q^2} \qquad (2\text{-}8)$$

The equation shows that the input optical power P_{th} can be smaller by enhancing the light-matter interaction Q^2/V. On the other hand, it is reported that the bandwidth of Kerr frequency comb becomes narrow by downsizing the cavity volume [44]. Therefore, recently some researchers began to control the cavity shape to change the effective refractive indexes, and design the dispersion, maintaining the enhancement of light-matter interaction [26, 45].

Due to the high input optical power, another problem arises, which is thermal stability. Since a high optical power is inputted into the cavity, even if the absorption coefficient of the cavity material is low, a little heat can generate in the cavity, and a temperature changes in the cavity, which leads to the change of resonant frequency. Here, Eq.(2-1) is re-written by Eq.(2-9).

$$2\pi r n_{eff} = m\lambda_r \qquad (2\text{-}9)$$

If a temperature changes in the cavity, a resonant wavelength λ_r changes by the TO (Thermo-Optic) and TE (Thermal Expansion) effects as follows;

1) TO effect: an effective refractive index n_{eff} changes, therefore, λ_r also changes.

2) TE effect: a cavity radius r changes, therefore, λ_r also changes.

Regarding a coefficient of thermal expansion, the coefficient is always a positive value, therefore, r become larger and λ_r shifts towards a longer wavelength side. However, TO effects can make n_{eff} smaller or bigger depending on the materials, thus, λ_r can shift towards either shorter wavelength or longer one. For example, on one hand, SiO_2, sapphire, and MgF_2 (Magnesium Fluoride) show positive thermos-optical coefficients, on the other hand, CaF_2, BaF_2, PDMS (Polydimethylsiloxane) show the negative ones [45, 46]. In the case of a negative thermos-optical coefficient, TOM (Thermo-Opto-Mechanical) oscillation occurs, and the cavity performance become unstable. The detail is explained in Chapter 6. Although the optical properties of each material against TOM oscillation was investigated, there is no report to suppress the TOM oscillation because utilization of SiO_2 or MgF_2 in which TOM oscillation does not occur becomes a mainstream. However, CaF_2 or BaF_2 show near-zero material dispersion in telecom or mid-infrared bandwidth, whose feature is favorable for generation of Kerr frequency comb. Therefore, those materials are worth to use as a Kerr frequency comb source, and especially CaF_2 shows high Q factor. If one could manufacture the CaF_2 microcavity which suppresses TOM oscillation, CaF_2 can be a source of stable Kerr frequency comb.

2.2   Machining of brittle materials

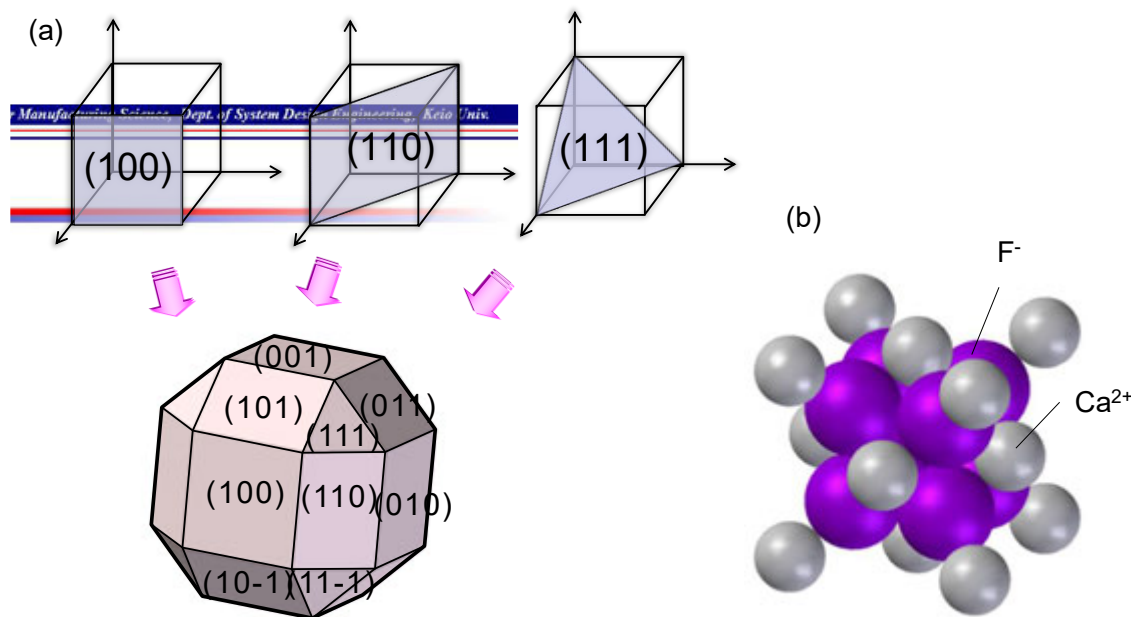For high Q microcavity, single crystalline materials are favorable as above-mentioned.

Fig. 2-7 (a) Crystallographic diagram with the representative crystallographic planes and (b) Schematic illustration of CaF_2 crystal structure formed by the Ca^{2+} ions and F^- ions.

Especially, CaF_2 theoretically shows the highest Q factor. Although theoretical Q factor of sapphire is similar to SiO_2, its thermal stability is also preferable for optical microcavity. To manufacture the CaF_2 or sapphire WGM cavity, ultra-precision machining process is most appropriate, however, those materials are classified into difficult-to-cut materials due to their brittleness. In this section, some general background about ultra-precision machining of brittle materials is given.

2.2.1   Optical materials

In the following, the basic material properties of CaF_2 and sapphire are briefly introduced.

Calcium fluoride

In a wide range of wavelength regime, CaF_2 shows an excellent permeability and anomalous dispersion. Its crystal structure is a cubic fluorite structure, which consists of the Ca^{2+} ions arranged in a face-centered cubic lattice and F^- ions in a cubic lattice (Fig. 2-7). The lattice constant is given as 0.54603 nm, then CaF_2 belongs to the space group Fm3m [50]. Cubic fluorite structure features Mohs hardness of 4, which also can be expressed by Knoop hardness values of 158.3 N/mm^2. While CaF_2 is relatively a soft material in minerals , it is also a brittle material originated from cleavage [51]. CaF_2 has an excellent transparency in the range of 125 nm to 10 μm wavelength i.e. in the deep ultra-violet spectral regime to the infrared light regime, and its reflection rate between two planes is 5.6 % that is extremely lower than other optical crystalline materials. Moreover, it shows anomalous dispersion and cancels out the effect of aberration in optic system. Additionally, CaF_2 is less deliquescent than other crystalline materials [52], therefore, one can use CaF_2 in a physically and chemically stable condition. The material properties of CaF_2 is listed in Table 2-1. Because of its excellent optical property, CaF_2 is

Table 2-1 Material properties of CaF_2

Parameter	Value	Ref
Permeable wavelength [μm]	0.125 − 12	[47]
Reflection loss [%]	5.6 (4 μm wavelength)	[47]
Knoop hardness [kg/mm^2]	158.3	[47]
Young's modulus [GPa]	75 (25 ℃)	[48]
Thermal conductivity [cal/cm Sec℃]	2.32×10^{-2}	[47]
Coefficient of thermal expansion [/℃]	24×10^{-6} (20 − 60 ℃)	[47]
Melting point [℃]	1360	[47]
Specific heat [cal/g℃]	0.204 (0℃)	[47]
Fracture toughness [$MPa\text{-}m^{1/2}$]	0.4 − 0.6	[49]

widely used in the industry e.g. spectroscopic mirror [53], 157 nm lithography system [54], optical windows [55]. However, CaF_2 is characterized by brittleness and crystal anisotropy, and the optical devices prohibit the existence of cracks. For the non-crack surface, the machined surface has to be finished by polishing after cutting or grinding process. The prospective fabrications of the complicated shape (e.g. aspherical lenses, diffraction gratings and microcavities) is the ultra-precision machining process [56].

Sapphire

Next to natural diamond, sapphire is an industrial mineral which shows the extremely high hardness. Single-crystal sapphire (also called corundum or α-Al_2O_3) consists of a lattice formed by Al^{3+} and O^{2-} ions to HCP (Hexagonal Closest Packed) with a ratio c/a = 2.73 for room temperature (c: length along c-axis. a: length along a1-, a2-, a3-axes. In Fig. 2-8 (b)). It belongs to the space group R-3c [57] and consist of a hexagonal crystal cell including a rhombohedral cell in the center of the hexagon. For the further consideration, only the frequently used crystal orientations are named as c-, a-, m- and r-planes (see Fig. 2-8).

Sapphire has very high mechanical durability and scratch resistance. On the Mohs scale, sapphire exhibits a hardness of 9 and expressed in Knoop hardness values of
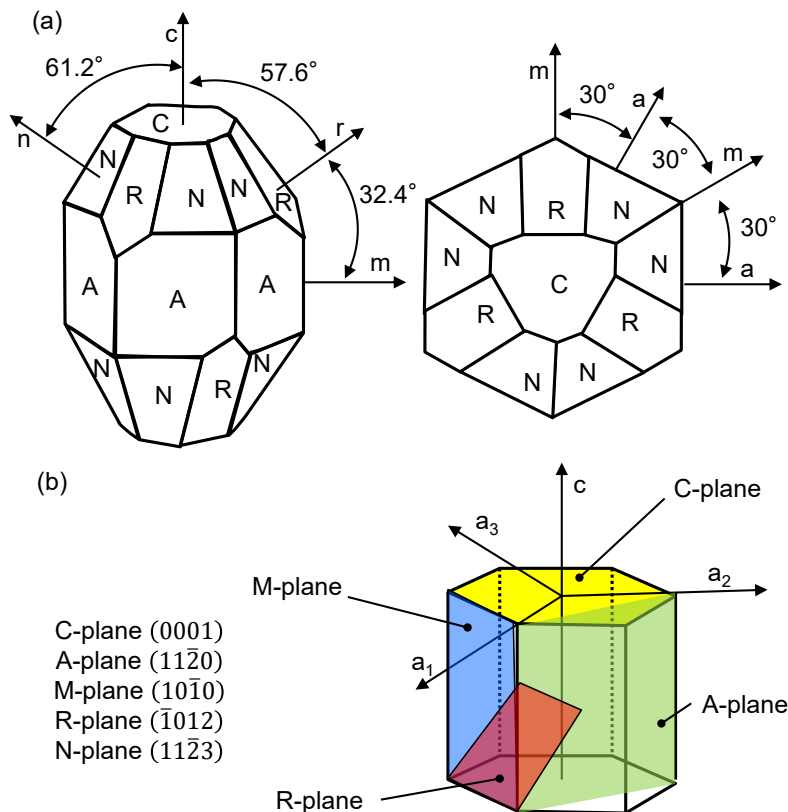

Fig. 2-8 (a) Crystallographic diagram with angular relationships between the common crystallographic planes and (b) hexagonal cell with common planes in structural cell notation [57]

Table 2-2 Material properties of sapphire

Parameter	Value	Ref
Permeable wavelength [μm]	$0.17 - 6.5$	[47]
Reflection loss [%]	12.0 at 4 μm wavelength	[47]
Knoop hardness [kg/mm^2]	$1525 - 2200$	[57]
Young's modulus [GPa]	$322 - 470$	[57]
Thermal conductivity [cal/cm Sec℃]	6.0×10^{-2} (Parallel to c-axis)	[47]
	5.5×10^{-2} (Perpendicular to c-axis)	
Coefficient of thermal expansion [/℃]	6.7×10^{-6} (Parallel to c-axis)	[47]
	5.0×10^{-6} (Perpendicular to c-axis)	
Melting point [℃]	2030	[47]
Specific heat [cal/g℃]	0.18 at 25 ℃ temperature	[47]
Fracture toughness [MPa-m$^{1/2}$]	2.14	[58]

around $1525 - 2200$ N/mm^2. The Young's modulus is stated as $322 - 470$ GPa in the literature [57]. It also has superior optical properties that is highly transparent in the wide range of wavelength regime ($170 - 6500$ nm). The material properties of sapphire is listed in Table 2-2.

Owing to the material property, sapphire shows a shock resistance, thermal and chemical stability and an excellent permeability in the wide range of wavelength. For the application, it is used for LED substrate, cover glass of watches, bearing, jewelry or optical windows and so on [57, 59]. The properties are also favorable for microcavities, and the thermal characteristics are better than those of CaF$_2$, thus, some researchers also worked on development of the high-Q sapphire microcavity [28].

Conventionally, sapphire substrate has been widely used in the industry as a functional material. The substrate is manufactured through dicing by laser or grinding, edge-chamfer, flattening by grinding [60] and finishing process by polishing [61]. However, the material properties and crystal structure makes it difficult to fabricate, and its machinability is still an issue.

2.2.2 Ultra-precision machining

Not only the above-mentioned optical devices, but a lot of products have been supported by the advancement of manufacturing technologies. With the development in the industry, scale of manufacturing technique has been downsized from mili to micro or nano levels. Until today nano-fabrication technologies have been well studied and documented, and those technologies enabled us to make new products.

Taniguchi presented that if the speed of the development of manufacturing technique

was maintained at that time, one would reach to the necessity of nano-fabrication technique [62] as shown in Fig. 2-9 (proposed by Taniguchi [63], updated by McKeown [64] and Goel [65]). Stemmed from that time, various kinds of manufacturing techniques were developed: Ultra-precision machining, laser processing, etching, ion-milling, plasma processing, coating, photolithography. For the last decades, micromachining and its related studies have been reviewed several times [63-69]. A new review paper was published even in 2017, thus, still it is an technology which attracts notice [70]. This section especially focuses on ultra-precision machining.

"Ultra-precision machining" means the achievement of dimensional tolerances in the order of 0.01 μm and surface roughness of 1 nm. The dimensions of parts or elements of the produced parts may be as small as 1 mm and the resolution and repeatability of the machines used must be in the order of 10 nm [63]. To realize the demands for ultra-precision machine tools, a lot of industrial companies developed the manufacturing technique of ultra-precision machine tool and machining process itself. In this dissertation, the focal point particularly goes to the material removal process between tool and workpiece in cutting.
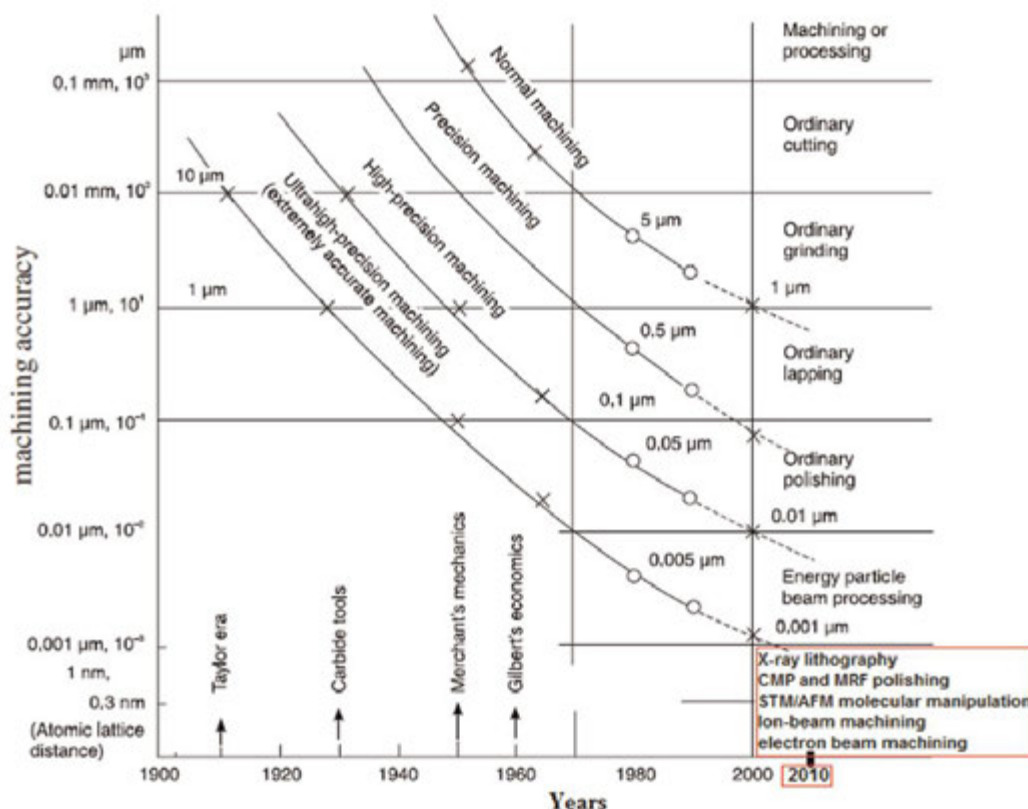

Fig. 2-9 Evolution of machining accuracy-Taniguchi's predictions [63] (updated by McKeown [64]) beyond 2000 to include state-of-the-art manufacturing processes (shown in the red box) [65] (Goel S, Luo XC, Agrawal A, Reuben RL. Diamond machining of silicon: A review of advances in molecular dynamics simulation. Int J Mach Tool Manu 2015;88:131-64. Reprinted with permission from Elsevier B.V.)

The simple cutting model can be expressed by the schematic illustration of interference between cutting tool and workpiece (Fig. 2-10). In cutting process, the cutting edge penetrates into the workpiece, and chip forms on the rake face of the cutting tool based on the plastic flow and sliding-off motion. In cutting of metals, the uncut chip thickness is estimated to a few $10-100$ μm. Therefore, the thickness is much larger than the edge radius, and the size effect of the cutting edge can be ignored. Moreover, a lot of crystal grains exist in the deformed region, and the workpiece material can be regarded as uniform continuous body in the macro viewpoint. However, one cannot apply the idea for ultra-precision cutting because the uncut chip thickness can be nanometric scale, and the edge radius cannot be ignored. In addition, crystallographic effects e.g. crystal orientation, lattice defect, or grain boundary of the workpiece also influences on the cutting performance, therefore, it is prohibited to simply apply the classical cutting model for the ultra-precision cutting [71].

Fig. 2-10 shows the difference of chip formation according to the relationship between edge radius of tools and uncut chip thickness. When the uncut chip thickness is smaller than the edge radius, the effective rake angle becomes negative even if the rake angle is designed as a positive value. In this case, if one try to cut the workpiece with quite small depth of cut, chip cannot generate, in other words, cutting process does not occur, and rather the workpiece is just compressed by the tool (Plowing) [72]. The critical value to determine the cutting mode or plowing mode is called minimum uncut chip thickness. Next, if the uncut chip thickness is equal to the minimum uncut chip thickness, shear deformation starts i.e. chip formation occurs. When the uncut chip thickness is larger than the minimum uncut chip thickness, chip formation and material removal process start. Therefore, one always has to take consideration into the relationship between minimum uncut chip thickness and edge radius.
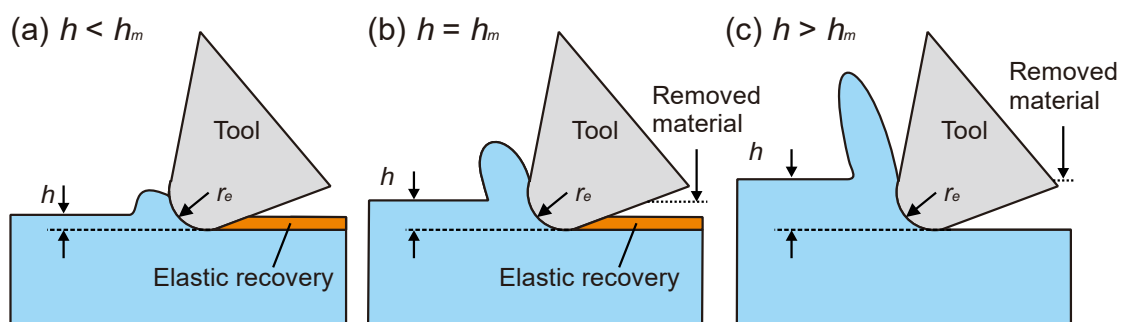
Fig. 2-10 Chip formation in dependency with the minimum chip thickness in micromachining process (a) When the uncut chip thickness h is far smaller than the edge radius r_e, chip does not form i.e. one cannot cut materials (plowing). (b) When h exceeds some critical value (minimum uncut chip thickness), the chip starts forming. (c) When h is much deeper than the critical value, the chip can be easily formed (formatted by the author) [72].

2.2.3 Surface formation

A quality of manufactured products is determined by the surface integrity. Not limited to the visual sense, surface integrity influences on a lot of properties: wear resistance, fatigue strength, thermal conductivity, electrical conductivity, reflectivity, absorption coefficient. In this section, surface roughness, brittle-ductile transition, and subsurface quality are focused on.

Surface roughness

The ideal turning model (Fig. 2-11) is assumed where no vibration and built-up edge exist between tool and workpiece. Based on the shape of the cutting tool, surface irregularity is formed on the workpiece in axial direction of workpiece cylinder, and this is surface roughness. Assuming that the depth of cut is small, and surface is finished by only nose part of the cutting tool, surface roughness R_y and R_a are given by Eqs. (2-10) and (2-11) [71, 73].

$$R_y = R - \frac{1}{2}\sqrt{4R^2 - f^2} \approx \frac{f^2}{8R} \qquad (2\text{-}10)$$

$$R_a \approx \frac{0.032f^2}{8R} \qquad (2\text{-}11)$$

Thus, surface roughness can be decreased by using larger nose radius R and setting a feed per revolution f as small as possible. However, small feed per revolution leads to inefficiency of cutting if the rotational speed is kept constant. Moreover, if nose radius becomes too large, thrust force in the radial direction increases, which might cause the deterioration of surface quality or form accuracy. Therefore, an actual surface roughness strongly depends on the relative vibration between tool and workpiece, built-up edge, tool wear, shape of workpiece, material property. Recently, the surface roughness S_a has started to be used which shows the surface roughness in two dimensions, whereas the surface roughness R_a shows the surface roughness in one dimension.
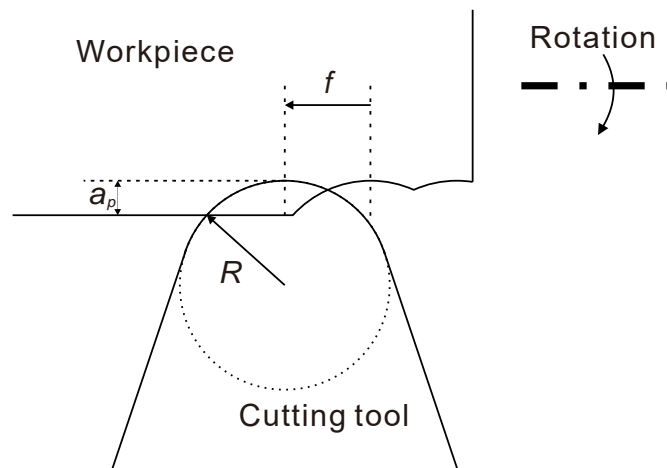

Fig. 2-11 Schematic illustration of cutting model in turning operations.

Brittle ductile transition

Brittleness has been one of the challenges in cutting. Different from metals, the deformation mechanism of brittle materials is not governed by ductility, therefore, it is well known that crack initiates in conventional cutting or grinding of brittle materials. It indicates that brittle materials show the ductility in some region for the past decades, however, Bifano firstly presented that there is a ductile-regime in machining of brittle materials. Bifano [74] noticed that when setting uncut chip thickness as less than critical value, one could grind fused silica in ductile-regime, in analogy with metal cutting i.e. BDT (Brittle-Ductile Transition) existed. Rooted in the term, research interests in ductile-regime machining of brittle material expanded all over the world. A classical cutting model for brittle materials was firstly proposed by Blake and Scattergood in turning of germanium and silicon [1]. As shown in Fig. 2-12, when feeding a cutting tool constantly, its uncut chip thickness differs from the cutting points, and critical uncut chip thickness t_c is defined as the point where the first crack occurs. A side view of the model shows a quasi-orthogonal cutting model, and a crack occurs when depth of cut exceeds a critical uncut chip thickness. It is essential to identify the critical value of each brittle materials in this way.

Blake et al also noticed that a negative rake angle of the cutting tool could enhance the ductility of brittle materials and increase the critical uncut chip thickness. It was assumed that the compression stress which was formed in front of the cutting edge suppressed the formation of brittle fracture. The discussion is supported by various works that hydrostatic pressure stress field are formed by a negative rake angle tool, and the field promoted plastic deformation in cutting of brittle materials [48, 75-81]. Although the critical uncut chip thickness can differ depending on material property, its theoretical value d_c can be calculated by Eq. (2-12) [82, 83].

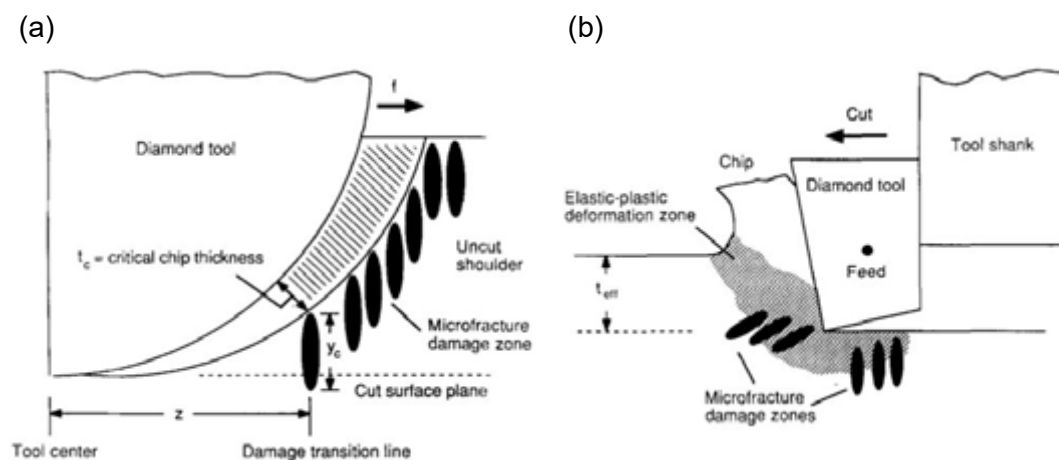(a)   (b)

Fig. 2-12 Model for ductile regime machining with nose round tool (a) Front view of the model (b) Side view of the model [1]. (Blake PN, Scattergood RO. Ductile-Regime Machining of Germanium and Silicon. J Am Ceram Soc 1990;73(4):949-57. Reprinted with permission from John Wiley & Sons)

$$d_c = \chi \left(\frac{E}{H}\right)\left(\frac{K_c}{H}\right)^2 \tag{2-12}$$

The equation shows that critical uncut chip thickness can be determined by elastic modulus E, hardness H, and fracture toughness K_c. Fitting coefficient χ depends on the tool geometry, and in the case of turning process, χ was determined as 0.15 by Bifano [82]. Notably, any vibration or disturbance in the cutting process are ignored in this model, thus, the actual critical value does not necessarily follow the equation. In addition, one exception regarding material property exists, which is crystal orientation [84].

Discussion of slip and cleavage is inevitable in cutting of brittle materials. As shown in Fig. 2-13, on one hand, slip promotes the ductile fracture of materials i.e. plastic deformation, on the other hand, cleavage is a trigger for brittle fracture. The details of the mechanisms are explained in Chapter 3. In ultra-precision cutting, the activated deformation based on dislocation in an atomic level has to be considered because they strongly affect the surface integrity. The phenomenon is known as crystal anisotropy, and the surface quality greatly depends on the cutting crystalline planes or directions. There are a lot of works regarding the investigation of the influence of the crystal anisotropy on surface integrity in machining: silicon [79, 80, 85], CaF_2 [48, 56, 86, 87], MgF_2 [84], $LiNbO_3$ [88, 89], sapphire [90].

Subsurface damage

While surface roughness indicates the geometrical evaluation of the surface quality on the surface, subsurface damage means the change of inner structure in the material, which affects fatigue strength, residual stress, or optical performance. This is caused by the extensive plastic flow under high temperature and high pressure in a cutting process. Then, the subsurface damage indicates the layer which shows a different material
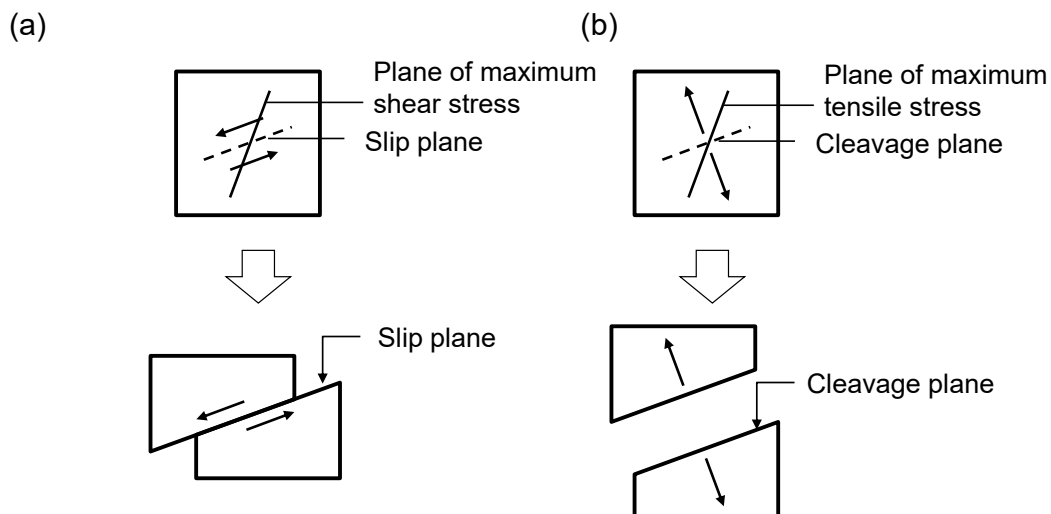

Fig. 2-13 Model for deformation mechanism related to cutting process: (a) Slip (b) Cleavage (formatted by the author) [77]

property from its base material. The layer causes the variation of crystal structure, hardness or residual stress. In general, one can suppress the subsurface layer by increasing the shear angle, setting a cutting condition to decrease the stress concentration region or supplying lubricant. However, the mechanism of the subsurface generation strongly depends on the material property of the workpiece or machining process, therefore, subsurface damage has been discussed in machining field and material science field, including measurement method and repairing (relaxing) method. [71, 91, 92]. Various kinds of measurement or analyses methods of subsurface damage caused by ultra-precision machining were studied e.g. TEM observation [79, 81, 85, 86, 93-98], Raman spectroscopy [99-101], stress releasing by etching [102-104]. TEM observation enables us to directly observe the crystalline lattice arrangement in subsurface layer, therefore, this technique is a strong way for the analysis of crystalline materials.

2.2.4　Cutting tool

As mentioned in section 2.2.2, the edge radius is one of the most important factors in ultra-precision cutting, therefore, it is necessary to choose an appropriate cutting tool that satisfies the demanded edge accuracy. In the case of brittle materials, its critical depth of cut is estimated as a few tens to hundreds nm, and thus, the edge radius has to be extremely sharp. Considering the existing polishing technique and material property, natural or synthesized diamond can be a candidate. For the diamond cutting tools, three types of diamond tools are commonly used; SCD (Single Crystalline Diamond) made of single crystalline bulk diamond, PCD (Poly Crystalline Diamond) made by sintering diamond particles with metal binder materials, and NPD (Nano-Polycrystalline Diamond) made by directly bonding nano-sized diamond grains by high-pressure high-temperature method [105-107]. As shown in Table 2-3, each tool has its own material property. SCD tool is most widely used for machining of optical materials or surface

Table 2-3 Characteristics of SCD, PCD and NPD [105]

Parameter	SCD	PCD	NPD
Structure	Cubic	Diamond grains $(1 - 20\ \mu m)$	Diamond grains $(30 - 50\ nm)$
Hardness [GPa]	$80 - 120$	50	$110 - 125$
Isotropy	×(anisotropy)	○	○
Fracture resistance	× (111) cleavage	○	○
Heat resistance [℃]	1600	600	1600
Edge accuracy [nm]	< 10	< 500	< 50
Transparency	○	×	○

finishing of metals. Advanced polishing technique makes the edge radius extremely sharp (< 10 nm). The edge accuracy depends on crystal orientation because its polishing rates actually changes due to the crystal anisotropy, thus (100) or (110) are often chosen for rake face. However, high polishing rate relates to the ease of tool wear, hence, there is a trade-off between the edge accuracy and tool wear rate [108]. Additionally, its cleavage also causes tool breakage. To overcome the disadvantage, PCD tool was developed. The PCD does not show cleavage, therefore, the fracture toughness was improved compared to SCD tool, but the edge radius becomes poorer (< 500 nm) because of its large grains and binders. To integrate the advantages of SCD and PCD tools, Sumiya developed NPD [107] that is made by synthesis of nano-sized crystalline grains by ultra-high pressure and high-temperature method [106]. The NPD tools feature better mechanical properties since the trans-granular bounadries prohibits crack propagation, and the nano-sized grains without bonding materials contribute to sharp edge radius. In diamond turning of polymer, machined surface can be deteriorated by tribo-microplasma [73], which can be induced by the extensive friction between insulator cutting tool and insulator workpiece [109]. Sumiya developed B-NPD (Boron-Doped Nano-Polycrystalline Diamond) which was synthesized by direct conversion sintering using graphite containing boron. The B-NPD tool that shows electrical conductivity and wear resistance, and successfully suppressed the tribo-microplasma damages in sliding tests of fused silica [110, 111].

2.2.5 Other fabrication process

Fabrication technique is not limited to machining. As summarized in section 2.2, various kinds of microcavities are manufactured by various kinds of fabrication methods. In this section, several fabrication methods are introduced: polishing, etching, laser machining, crystal growth.

Polishing

As a surface finishing process, polishing is one of the most frequently used process in the industry, in particular for optical materials. For instance, it is essential to polish the ground BK7 glass lenses to eliminate brittle fracture or grinding marks [112]. One can flow abrasive particles between workpiece and polishing tool, or the abrasive particles themselves can be embedded onto the polishing tool [71]. Polishing enables us to obtain the uniform surface decreasing the residual strain, however, pro-longed polishing deteriorates the form accuracy. For the large aperture wafer, Namba developed the float-polishing technique to obtain the uniform surface and subsurface in an atomic level. Conventionally, polishing technique has been difficult to apply for the micro order parts, nevertheless, EEM (Elastic Emission Machining) that was developed by Mori made it

possible to enhance the surface integrity of the microcomponents with significantly low load [113, 114]. By applying some energy of motion on microparticles and flowing onto the workpiece, some chemical reaction occurs between the workpiece and the surface of the particles, and the smooth surface can be achieved in an atomic level. Recently, EEM is used for manufacturing of mandrels that is used for ellipsoidal focusing mirrors for soft x-ray microscopy, thus, it can be utilized for polishing the optical materials which have cylinder shape [115].

Etching

Etching is a chemical fabrication process which removes materials by chemical or electrical-chemical method, and the micro or nanotextured surface can be obtained by chemical erosion. Etching process does not generate plastic deformation, therefore, it does not change the subsurface structure compared to cutting or grinding process. Since one can make a small parts by etching, toroid cavity and PhC cavity are manufactured by etching [11, 16]. However, etching process requires a clean room and safety environment for human because the processing media is dangerous. In addition, when applying etching on single crystalline materials, the etching speed differs from crystal orientation [116] (the surface are mainly processed along cleavages) , therefore, it is difficult to obtain the uniform spherical shape such as WGM microcavities made of single crystalline materials.

Laser machining

Laser is light which shows a high density of optical energy amplified by a cavity, which has been used for sensing technique. However, the laser machining with high output power has been considered as a useful method in the industry, which is applied on metals, ceramics, polymer or composite material [117]. For example, drilling holes on sapphire wafer was conducted by pulsed-laser [118]. For manufacturing of cavity rim part of toroid cavity, laser process is used [16]. In order to extend the laser machining in nanoscale, recently, there is a work to accumulate pulsed-laser at a tip of AFM (Atomic Force Microscope) cantilever by using near-field effect, and remove material in nanoscale by local abrasion [119]. Also, laser can be used as an assisting tool for cutting of difficult-to-cut materials [120]. Since tool wear does not have to be considered for laser machining, once the optimal machining condition is determined, one could fabricate workpiece as long as the laser oscillation occurs. However, laser machining requires a lot of energy consumption to oscillate, and the processed surface can melt. Therefore, the surface roughness can be worse than other fabrication process. Also, high temperature at the processing point can cause the variation of crystalline structure, and thus the phase of single crystal can transform, which prohibits the usage for crystalline microcavities.

Table 2-4 Comparison among nano fabrication processes related to manufacturing of microcavities
(○: good, △: medium ×: bad)

Parameter	Cutting	Polishing	Etching	Laser	Crystal growth
Surface roughness Ra [nm]	5−20 [123]	≤ 1 [94]	10−35 [123]	45−140 [123]	≤ 65 [29]
Subsurface damage	△	○	○	×	○
Crack formation	△	○	○	△	○
Geometry-variation	○	×	×	△	×
Form accuracy	○	△	×	×	×

Crystal growth

Crystal growth method is generally used to artificially make a crystal, but it can be applied for manufacturing of microcavities. One manufactured the CaF_2 cavities and sapphire ones using Czochralski method [29, 121, 122]. During melting the base material with high power CO_2 laser, Kudo controlled the velocity of lifting the base crystal to make a form of the microcavity. The scattering loss from the cavity can be suppressed because brittle fracture does not generate in this process. This is a bottom-up method, therefore, it can be useful for miniaturization of the microcavity. For example, Chen used the crystal growth method to manufacture a nanosized microcavity [32]. However, crystal can easily grow towards the specific direction, thus, the final shape can be formed by its original crystal structure, which leads to the deterioration of the form accuracy.

2.2.6 Comparison among fabrication process

Until this section, several fabrication methods were introduced. To clarify the advantages and disadvantages of each fabrication process, it is worth summarizing the fabrication process in terms of surface roughness, subsurface damage, geometry-variation, crack formation, and form accuracy (see Table 2-4).

Machining has an advantage of geometry-variation and form accuracy because the final shape can be formed by the shape of cutting tool and numerically-controlled machine tool. Although crack initiation is a challenge, the machined surface can be attained by ductile-regime cutting. Because of the plastic deformation, SSD cannot be inevitable. The best surface integrity can be obtained by polishing. Owing to the principle, subsurface structure can be organized in an atomic level [94]. However, pro-longed polishing deteriorates the form accuracy. Especially for the microcavity, the high form accuracy is crucial, otherwise, the resonance does not occur. Additionally, considering the form accuracy also influences on the dispersion tailoring of the cavity [26], and thus, current polishing is less likely to use in this dissertation. Etching can avoid the change

of subsurface structure or crack initiation, on the other hand, in the case of crystalline materials etching has a disadvantage of form accuracy because of the anisotropy, and is difficult to form a bulged-shape such as spherical shape. Laser machining also causes SSD because high energy can be absorbed in a material. Surface roughness also can be worse in the case of laser processing. Crystal growth was a good candidate for manufacturing the microcavities. Since the surface can be formed naturally, its subsurface structure is identical with the base material and no crack occurs. Nevertheless, because the microcavities are formed according to its crystal structure, it is assumed to be difficult to enhance the Q factor and dispersion tailoring, crystal growth can be out of option.

As above discussed, each process has its own advantage and disadvantage, thus, an appropriate fabrication process should be hired depending on the required microcavity type. Indeed, researchers use appropriate approaches for their demanding microcavity. Aiming to manufacture WGM crystalline microcavities, ultra-precision machining is one of the most-prone fabrication processes as shown by Grudinin [21], although there are some challenges.

2.3 Short literature review on machining of single crystalline brittle materials

Originated from the Blake, Bifano, Blackly, Scattergood and Nakasuji between 1989 to 1991 [22, 67, 68, 82], a lot of researchers have studied the ultra-precision machining of brittle materials. There is too much literature to review, therefore, in this section, the review in this dissertation especially focuses on single crystalline optical materials and semiconductor materials.

Silicon has been one of the most useful semiconductor materials in the industry, which spurred researchers study the silicon machining as reviewed by Goel [65]. As mentioned in section 2.2.3, the negative rake face angle can enhance the ductility in cutting of brittle materials [1]. In the case of silicon cutting, for example, Yan experimentally examined a mechanism of crack formation, and the large negative rake angle suppressed the brittle fracture [78]. He also analyzed stress and temperature distribution by FEM (Finite Element Method) to analyze the mechanism in silicon cutting, and showed that 15 GPa hydrostatic pressure was formed and the temperature at cutting point was elevated to 300 ℃. At the same time, an effective negative rake angle could be increased by designing larger the edge radius, which resulted in increasing the thrust force and decreasing the uncut chip thickness [124]. The high-temperature and high-pressure phenomena in the vicinity of cutting point was also indicated by Goel's molecular dynamics simulation [125, 126]. When focusing on influence of crystal anisotropy in

silicon cutting, several researchers experimentally investigated the variation of the surface integrity by altering cutting direction [1, 77, 127]. After the works, Shibata used Schmid factor to quantitatively discuss the anisotropic BDT in silicon turning. The Schmid factor shows the ease of activation of slip systems in terms of geometrical relationship between applied force and slip systems. Shibata also investigated the subsurface layer by TEM observation, therefore, comprehensively discussed the surface integrity in silicon cutting. Later, Yan introduced the slip factor which corresponds to Schmid factor, and discussed the material deformation behavior in silicon cutting, and investigated the phase transformation in subsurface layer (e.g. amorphous layer, strained layer, or line defects).

Although the amount of machinability study of CaF_2 does not correspond to the one of silicon, those materials have been very important industrial ceramics, hence, various researchers attempted to theoretically or experimentally analyze the material deformation mechanisms [48, 49, 56, 76, 86, 94, 103, 127-132].

Furukawa examined the machinability of single crystalline materials, poly-crystalline materials, amorphous materials in ultra-precision scale. They chose CaF_2 as one of them, and found the regularity on the machined surface, in which cleavage took a key role [127]. Yan investigated the cutting mechanisms of CaF_2 more in details, and discussed the influence of negative rake angle, lubricant, or crystallographic effects in face turning process [48, 76]. The achievement was used for manufacturing WGM CaF_2 cavities as shown by Grundinin [21]. In the meanwhile, the similar anisotropic behavior on surface integrity was observed in grinding process by Namba [103]. He also conducted ultra-precision float-polishing on the CaF_2 ground surface whose crystalline structure were regularly aligned i.e. strain-free surface was achieved [94]. Recently, Wang noticed that asymmetric crystal anisotropy existed in a single groove in plunge-cut tests (cracks were observed in one-side of the single groove.). He used a crystal plasticity FEM which assimilates slip rate to analyze the mechanism [86]. For quantitative discussion on crystal anisotropy, fracture toughness parameter was recently employed by Chen [49].

Sapphire shows high hardness, therefore, main machining processes have been grinding [133, 134] and polishing [61]. Due to the hardness, compared to conventional grinding, assisted grinding process (e.g. elliptical vibration) are greatly helpful for sapphire machining, which can enhance the surface integrity or wear resistance [135, 136]. For polishing, chemical mechanical polishing method is also used [137-139]. To avoid tool wear, laser machining is also a candidate for sapphire machining, therefore, various fabrication processes have been studied [118]. Recent interests in the usage of sapphire goes to manufacturing parts with microfeatures or microgrooves as seen in optical microcavities [28], and thus, rather cutting process is more suitable for free-form microoptics, therefore, also some researchers conducted the scribing process [140, 141]

or cutting [90]. Regarding crystal anisotropy, Matsumura experimentally investigated the anisotropic machinability of r-plane sapphire [90], however, the discussion in terms of crystallography was not sufficiently conducted.

2.4 Objective of this study

2.4.1 Motivation and objective

As reviewed in section 2.1, various kinds of optical microcavities exist according to its application. This dissertation focuses on high-Q microcavities, and WGM microcavity made of crystalline materials is chosen. In particular, to generate Kerr frequency comb with stability, the following properties are required.

1. Ultra-high Q factor

2. Anomalous dispersion

3. Thermal and mechanical stability

First, combination of ultra-precision cutting and polishing is normally used to manufacture crystalline WGM microcavities as shown by Grudinin [21] or Wang [25]. However, pro-longed polishing deteriorates the form accuracy of the microcavity which is manufactured by cutting. Therefore, the WGM cavities are ideally manufactured by only cutting. Secondly, the refractive index of dielectric materials changes depending on wavelength, which is known as a dispersion. The dispersion can be determined by material dispersion and the microcavity shape, and it is assumed that the desired shape can be obtained by only ultra-precision cutting. Thirdly, the cavity which features a negative thermo-optical coefficient which causes the periodical thermal instability of the cavity performance by TOM oscillation. To overcome the challenges, it is necessary to design and manufacture the cavity structure which quickly diffuses the heat from the cavity part, which can be possible by ultra-precision cutting. To achieve the cavity that satisfies the aforementioned properties, CaF_2 is one of the ideal materials for the microcavities because CaF_2 shows high permeability, its Q factor is theoretically the highest [18]. In addition, CaF_2 shows anomalous dispersion in wide wavelength regime, however, its thermal stability is poor because of its negative thermos-optical coefficient [18]. Until today, there is no CaF_2 microcavity which fulfills the demanded properties i.e. high-Q, anomalous dispersion, and thermal stability on TOM oscillation. Although the theoretical Q factor of sapphire is not as high as CaF_2, its thermal stability makes also sapphire a candidate for WGM crystalline microcavities [28].

As reviewed in section 2.3, CaF_2 and sapphire are difficult-to-cut materials, and characterized by its brittleness and crystal anisotropy. Concerning CaF_2, most researchers focused on face turning or flattening to manufacture an aspherical lens, stepper for lithography. Mostly, (111) cleavage plane is selected, therefore, their

investigation mainly remains in (111) plane [48, 49, 76, 86]. There is no work which investigated the machinability of CaF_2 in cylindrical turning process where cutting crystalline planes and crystalline directions constantly change, and the anisotropic deformation behavior of CaF_2 cutting should be discussed quantitatively. Also, there is few studies which discusses the SSD in CaF_2 cutting [86], therefore, it is necessary to comprehensively discuss the surface and subsurface integrity. Sapphire has been often used as a functional material, therefore, various researchers worked on grinding [133-136] , or polishing [137-139], whereas there is few work regarding cutting [90]. For instance, Matsumura investigated the anisotropic deformation behavior of sapphire by using cubic boron nitride ball-end mill, however, the crystallographic evaluation was not sufficiently conducted [90]. Nevertheless, for manufacturing the microparts such as WGM sapphire microcavities, the cutting mechanism of sapphire should be clarified.

In this dissertation, plunge-cut tests were conducted to investigate the BDT mechanism. In particular, influence of crystal anisotropy on the surface integrity was discussed by changing the cutting crystalline planes and crystalline directions. To discuss the material deformation behavior in terms of slip system and cleavages, the resolved stress model was used. The UPCT (Ultra-Precision Cylindrical Turning) tests of CaF_2 were also performed to discuss the surface integrity and subsurface formation, aiming to manufacture the WGM microcavities.

In the meanwhile, the machinability of (0001)-plane single crystalline sapphire was also investigated by plunge-cut tests. In the deformation process of sapphire, it is reported that twinning contributes to the ductility [142], therefore, the anisotropic deformation behavior was comprehensively discussed in terms of slip systems, twinning and cleavages. For both materials, some weighting factors were also introduced to scrutinize the experimental results including possible secondary slip, twinning, and cleavages.

By using the obtained results, WGM microcavities were manufactured. Influence of crack, SSD, and cavity shape on Q factor was evaluated. Dispersion-tailored microcavity for controlling the dispersion was manufactured and evaluated. A hybrid microcavity was manufactured and evaluated for the thermal stability of the CaF_2 cavity.
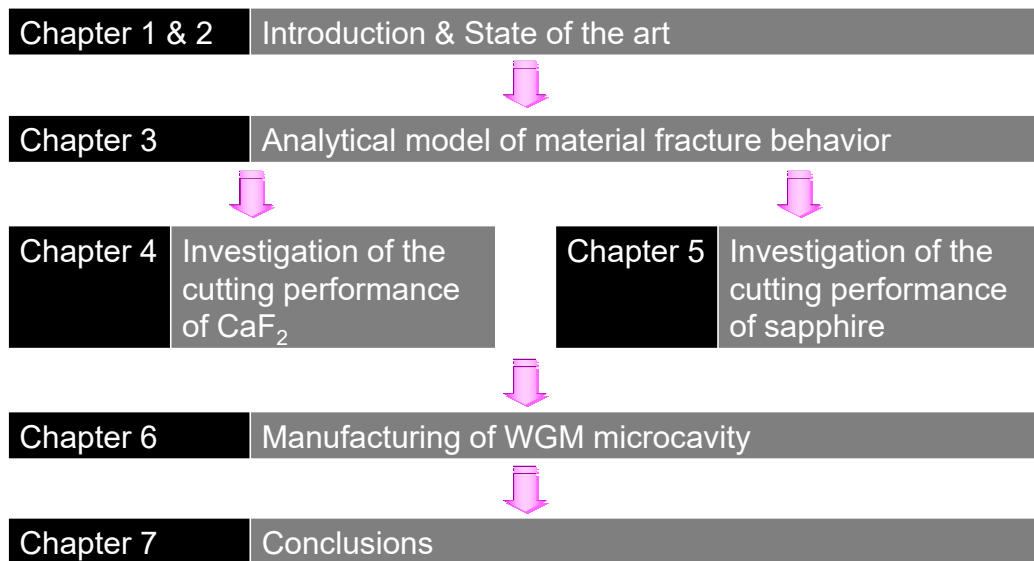
2.4.2　Organization of the dissertation

The summary of organization of the dissertation is shown in Fig. 2-14.

In Chapter 1, the background and purpose of the dissertation is briefly introduced.

In Chapter 2, the principle, types, manufacturing methods, and application of optical microcavities are described. Particularly focusing on WGM crystalline microcavities, some general background and challenges regarding ultra-precision cutting of crystalline materials are presented. Through the review on machining of single crystalline CaF_2 and

Chapter 1 & 2	Introduction & State of the art
Chapter 3	Analytical model of material fracture behavior
Chapter 4	Investigation of the cutting performance of CaF_2
Chapter 5	Investigation of the cutting performance of sapphire
Chapter 6	Manufacturing of WGM microcavity
Chapter 7	Conclusions

Fig. 2-14 Organization of the present dissertation

sapphire, the objective of the dissertation is declared.

In Chapter 3, fundamentals of material fracture behavior and analytical model is provided. To analyze the anisotropic material deformation of the crystalline materials, resolved stress model under the tensile loading condition is adapted for the plunge-cut tests.

In Chapter 4, machinability of the CaF_2 substrates and cylinder are evaluated in the plunge-cut tests and UPCT tests, respectively. With respect to the machined surface and subsurface, the following factors are evaluated: influence of process parameter, type of tool and crystal anisotropy. The plastic deformation parameter and cleavage fracture parameter were computed.

In Chapter 5, machinability of the sapphire substrates is evaluated in the plunge-cut tests. Additionally, indentation tests and TEM observation are conducted. Same as CaF_2, the crystal anisotropy and material fracture behavior are discussed based on the computation of the fracture parameters.

In Chapter 6, WGM microcavity is manufactured, and the performance was evaluated. Especially, influence of brittle fracture and shape dependency on cavity performance is investigated. The cavity is designed based on electro-magnetic field analyses. Also, dispersion tailored cavity is designed and manufactured. Based on the FEM simulation of heat diffusion, the hybrid cavity is designed and manufactured.

In Chapter 7, conclusions of the dissertation are summarized.

3. Analytical model of material fracture behavior

This chapter provides fundamentals of material fracture system in cutting. Further, it will give an analytical model of material fracture behavior in this dissertation.

3.1 Material fracture system

In ultra-precision cutting, the uncut chip thickness reaches to a few tens or hundreds nanometers, therefore, the cutting mechanism has to be analyzed in the viewpoint of nanoscale. In general, slip system and cleavage are essential to discuss the BDT of crystalline materials (Fig. 2-13). Plastic deformation is induced by a lot of slip dislocation, whereas cleavage causes the brittleness, hence, it is necessary to consider the influence of those fracture mechanisms on the surface integrity. For HCP crystal such as sapphire, it is reported that twinning deformation also contributes to the ductility i.e. plastic deformation [142]. In this section, each fracture mechanism and analytical model is introduced.

3.1.1 Slip system

Slip system that consists of slip plane and slip direction portends the ductile-regime cutting. A simple model where some stress is applied on crystal is shown in Fig. 3-1 [144]. When shear stress acting, the atoms move by a distance of one atom through repetition of breaking and forming the bonds between atoms. The plane along which the atom glides is called slip plane. Slip can be explained by a concept of dislocations which is a
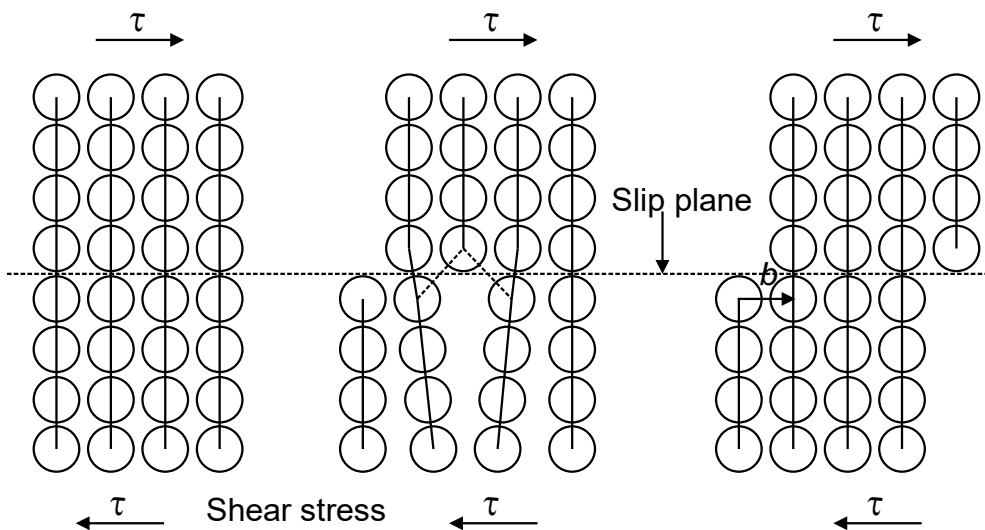
Fig. 3-1 Schematic illustration of slip activation involving breakage and formation of the bonds (formatted by the author) [143]

one-dimensional line defect. For screw dislocations the dislocation line vector l is parallel to the Burgers vector b, whereas the two vectors are perpendicular each other in the case of dislocation. Dislocations can glide over a certain plane (slip planes), which are defined by Burgers vector b and dislocation line vector l. Normally the dislocation glide over the most densely packed planes, which corresponds to slip planes. Then, slip always occurs in the direction of the Burgers vector b (along the most closely packed directions in the slip planes), which is called slip direction for crystalline materials. As the slip planes and directions depend on its crystalline structure and element
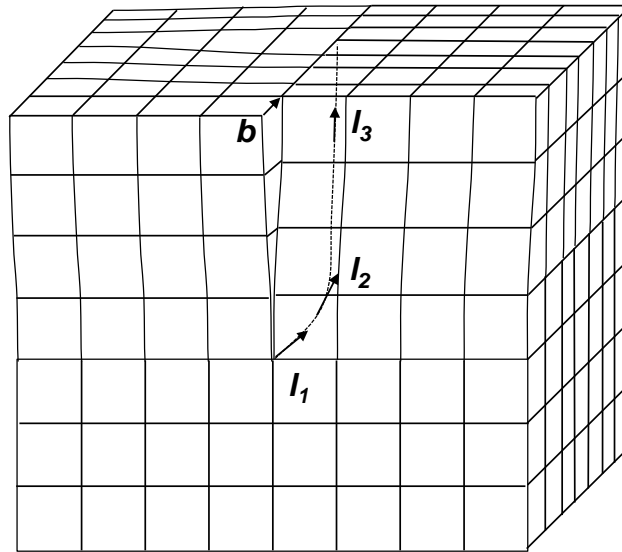
Fig. 3-2 Schematic illustration of dislocation mode; The screw dislocation is defined by the geometrical relation of Burger's vector b and dislocation line vector l_1 (l ∥ b). The edge dislocation is defined by the geometrical relation of Burger's vector b and dislocation line vector l_3 (l ⊥ b). The relation of b and l_2 show mixture characteristics (formatted by the author). [144]
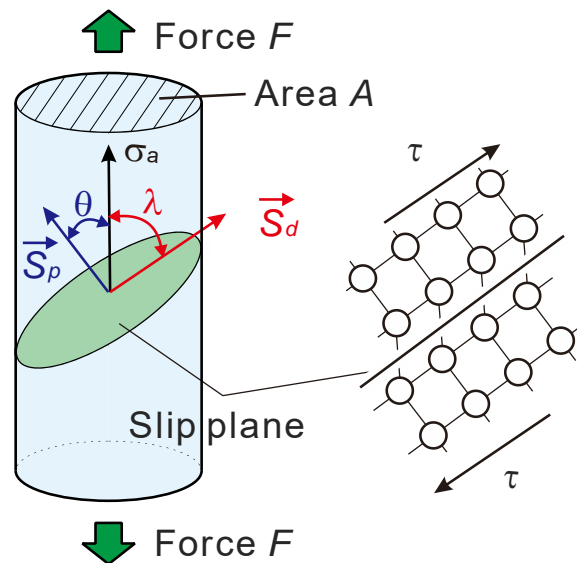
Fig. 3-3 Schematic illustration of resolved shear stress model under tensile loading condition [143]

composition, the slip systems vary depending on the materials.

For movement of the dislocation, the necessary shear stress is given by Peierls-Nabarro model [143]:

$$\tau_{pn} = \frac{2G}{1-v} \exp\left(\frac{-2\pi w}{b}\right) \tag{3-1}$$

If the width of the dislocation w (several atomic spacing) is bigger, and the Burger's vector b is smaller, the Peierls-Nabarro stress is smaller according to Eq. (3-1). Thus, a dislocation takes place on the closed-packed plane in the closest-packed direction. When the dislocation barriers are short, the critical stress which is required to activate a dislocation glide is relatively high. Dislocation easily glides for broad dislocations, where the atomic spacing is great. Therefore, these materials are ductile and only small stresses are required to produce large strains whereas ceramics tend to have narrow lattice spacing, which requires the high stresses for the movement of dislocations. Because of that, the ceramics become hard and brittle.

A large number of dislocations induce plastic deformation, which is necessary for ductile-regime cutting. Plastic deformation occurs when an applied stress exceeds a critical value. This means that slip begins on specific planes along specific directions. The critical value is called critical resolved shear stress (CRSS). The deformation is usually associated with slip mechanism (note that other mechanism may be involved.). As shown in Fig. 3-3, when loading a tensile force F on a crystal cylinder which has a cross-sectional area A, the induced stress σ_a can be described by Eq. (3-2) [144]:

$$\sigma_a = \frac{F}{A} \tag{3-2}$$

In this model, slip plane normal vector S_p (i.e. slip plane) is inclined to the tensile loading axis with the angle θ, and the slip direction S_d is inclined to the same axis with angle λ. Slip occurs on the specific slip plane, and a projected area onto a slip plane A' is given as follows:

$$A' = \frac{A}{\cos\theta} \tag{3-3}$$

Slip direction S_d is also inclined to the tensile loading axis with the angle λ, therefore, the force is resolved to slip direction:

$$F' = F\cos\lambda \tag{3-4}$$

From those equations, the resolved shear stress (RSS) τ_s is obtained:

$$\tau_s = \frac{F}{A}\cos\theta\cos\lambda \tag{3-5}$$

The part of $\cos\theta\cos\lambda$ is known as the 'Schmid factor' m, which determines how easily a slip system is activated. Schmid factor features maxima when $\theta=\lambda=45$ °, and varies in the range of $-0.5 < m < 0.5$. When the RSS value exceeds some critical value, a slip

occurs, and the critical value is named as critical resolved shear stress (CRSS). The value can be determined for each slip system (primary slip or secondary ones), and the slip system that firstly reaches at CRSS is firstly activated. In other words, it is necessary to apply stress which surpasses the CRSS value to deform materials.

3.1.2 Cleavage

Brittle fracture can always deteriorate machined surface, and has been intensively discussed. In the case of crystalline materials, the fracture originates from so-called 'cleavage planes', where the density of the atoms is high. Analogous to slip it occurs on some specific plane where a tensile stress surpasses a critical value. Sohncke formulated the law as Eq.(3-6) [143]:

$$\sigma_c = \frac{F}{A}\cos^2\varphi \tag{3-6}$$

For separation of crystal body along cleavage planes, the tensile stress acting on the cleavage plane should be considered and is given by $F\cos\varphi$. Same as Eq. (3-3), a projected area is $A/\cos\varphi$, and the resolved tensile stress is obtained by Eq. (3-6) (Fig. 3-4).

The primitive model in regards to brittle fracture was proposed by Griffith [143, 145]. He considered that crack initiation relates to the releasing of growing strain energy, and attempted to quantitatively analyze the mechanism in terms of energy equilibrium. Assuming that a perfect glass contains only one small crack, for a static-crack system, the total energy can be described as below:

$$U = (-W_L + U_E) + U_S \tag{3-7}$$
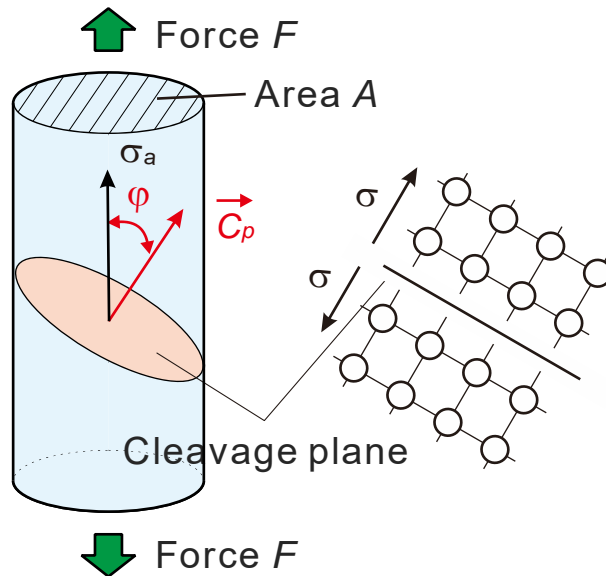
Fig. 3-4 Schematic illustration of resolved tensile stress model under tensile loading condition [143]

The thermodynamic equilibrium is expressed by the mechanical energy of the body W_L, elastic energy U_E, and the surface energy U_S. Each term is expressed as follows:

$$W_L = 2U_E \tag{3-8}$$

$$U_E = \pi c^2 \frac{\sigma_L^2}{E} \tag{3-9}$$

$$U_S = 4c\gamma \tag{3-10}$$

With the equations, Eq. (3-7) is written by Eq. (3-11).

$$U = -\pi c^2 \frac{\sigma_L^2}{E} + 4c\gamma \tag{3-11}$$

The minus sign shows strain energy released by the growth of a crack. The tensile stress acts on the surface of the crack. For constant load and plane strain conditions, the following relation is obtained:

$$\sigma_L = \sqrt{\frac{2\gamma E}{(1-v^2)\pi c}} \tag{3-12}$$

For plane stress condition, $v = 0$. Although Griffith's theory was a breakthrough for understanding of brittle fracture, the theory could be applied to amorphous materials, such as glasses. In the case of metal, one had to consider the different nature of plastic deformation in metals. Orowan extended the Griffith's theory considering the plastic deformation. Orowan showed that the work of plastic deformation which takes place in the region of a thinner material in comparison of the crack length plastic deformation can contribute to the surface energy of the crack, and reflected the relation on the Eq. (3-9) for plane stress condition:
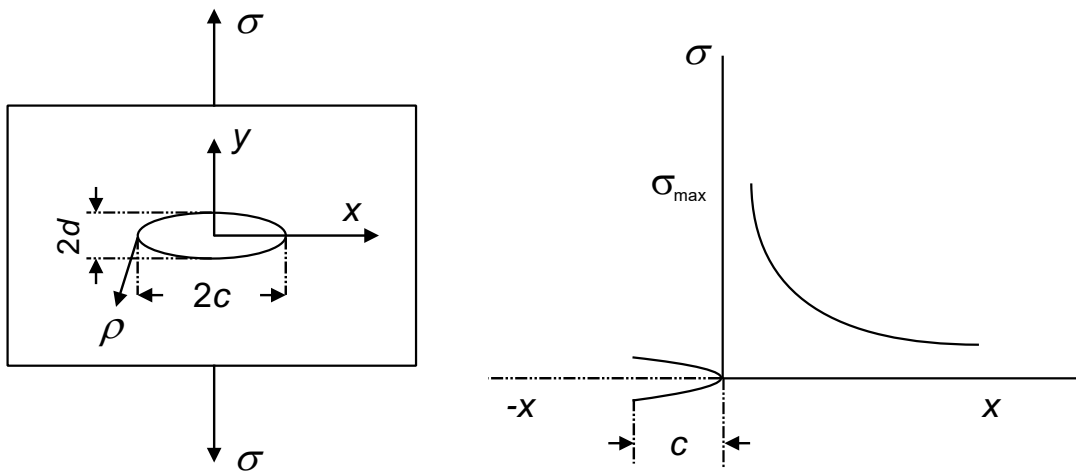
Fig. 3-5 Griffith's crack model. An elliptical microcrack exists in a glass and the tensile stress distributes from the origin of crack (formatted by the author) [143].

$$\sigma_L = \sqrt{\frac{2E(\gamma + w_p)}{\pi c}} \tag{3-13}$$

Therefore, Eq.(3-8) can be re-written.

$$U = -\pi c^2 \frac{\sigma_L^2}{E} + 4c(\gamma + w_p) \tag{3-14}$$

The plastic work is much larger than the surface energy, which is estimated by Orowan. This lead Orowan's relation to incorporate the plastic-deformation energy in the vicinity of fracture surface and neglect the surface energy.

$$\sigma_L \approx \sqrt{\frac{2Ew_p}{\pi c}} \tag{3-15}$$

Considering that plastic deformation is formed by a large number of dislocations, a role of dislocation has to be considered. Zener suggested that crack can be nucleated at pile-ups of dislocations, where sufficient stress for the nucleation of cracks form. The pile-up concept is essential to the explanation of the role of dislocation, and Cottrell considered the model of crack formation by dislocation pile-ups in a BCC (Body-Centered Cubic) metal. He considered the intersection of a/2 <111> dislocation forms a <100> dislocations wedging the crack. The fracture stress is calculated by the specific surface energy, and the Burgers vector of the dislocation and the number of dislocations:

$$\sigma_F = \frac{2\gamma}{pb} \tag{3-16}$$

Here, it can be concluded that brittle fracture can be originated from plastic deformation, and pile-up phenomena caused by slip or twin form cracks [143].

3.1.3 Twinning

Twinning may be also a contributing factor for plastic deformation except slip. When applying force to a crystal body, atoms move a fractional atomic spacing. Then, the crystal lattice structure is re-arranged, which is a major difference between slip and twinning. Whereas a crystal structure does not change due to a slip, twinning greatly changes the atomic arrangement. Twins are categorized into two groups; "mechanical twins" and "annealing twins". Mechanical twins are induced by mechanical deformation process such as indentation, i.e. also known as "deformation twins", and found in HCP crystals. For example, basal twins induced by grinding process are directly observed by TEM observation in sapphire [96]. Annealing twins take place in FCC (Face-Centered Cubic) crystals. The twins occur in crystal growth process, therefore, it is also called growth twins. Similar to Schmid's law for slip, twinning system can be also operated by CRSS. As shown in Fig. 3-6, mirror symmetry can be seen at the boundary of twin planes

where a fractional portion of crystal lattice changes compared to the previous crystal structure. Thus, twin bands are formed. It is still controversial that the mechanism of twinning relates to dislocations, however, it is anticipated that the plastic deformation is sustained by slip and twinning deformation in the case of HCP crystal such as sapphire [143, 144].

3.2 Analytical procedure of material fracture mechanism

Material fracture mechanisms are formulated by various researchers as mentioned in Section 3.1. Especially, a resolved stress model describes a tendency for plastic deformation or brittle fracture, therefore, the model has been often used for analyses of anisotropic fracture mechanisms.

Schmid factor expresses a tendency for activation of slip which are associated with plastic deformation in terms of geometrical relation between applied force and slip system [143]:

$$m = \cos\theta\cos\lambda \qquad (3\text{-}17)$$

Simply, the more an absolute magnitude of Schmid factor m is, the more prone the corresponding slip systems are operated. Therefore, the calculation was used for the explanation of material fracture behavior. In the case of the indentation tests, this relation was extended to consider the indenter geometry (explanation will be given in Eq.(3.15)) [146, 147]. However, simple geometrical calculation of Schmid factor does not explain all of the possible slip activation because the CRSS values differ depending on
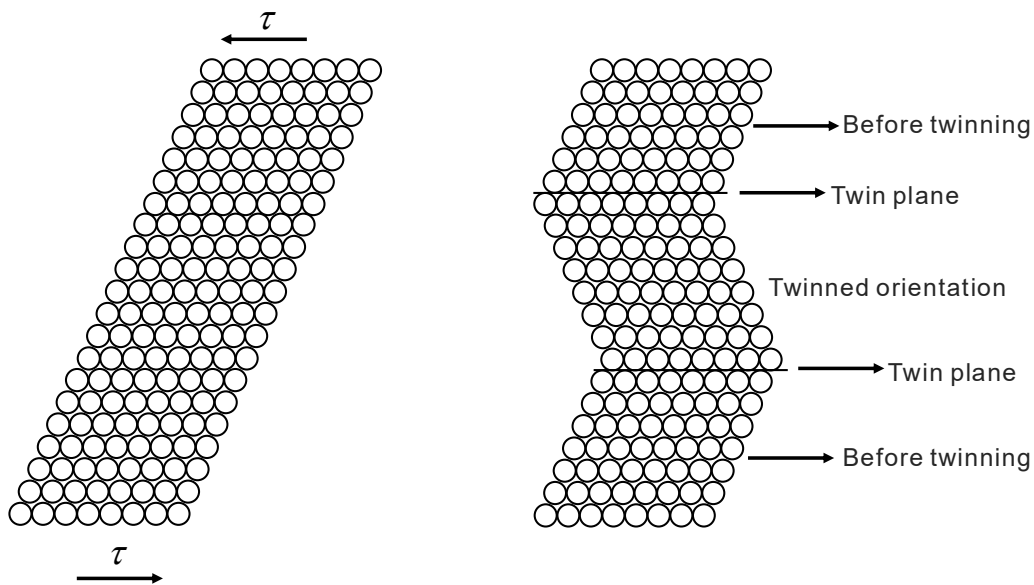
Fig. 3-6 Schematic illustration of twinning deformation (formatted by the author)[143]

slip systems. Especially for low-symmetry crystal sapphire, several slip and twinning systems exist [148].

Nowak's model was a breakthrough for that [147]. He proposed a new resolved shear stress model in nanoindentation tests as follows:

$$T_i(\mu) \propto \frac{\tau_i}{\tau_i^{crit} \Big/ \min_i \tau_i^{crit}} \Lambda \tag{3-18}$$

This equation shows that a parameter estimating the possibility of slip activation is expressed by a correction factor Λ and a ratio of CRSS for i-th slip system to minimum CRSS among all of the slip systems. A correction factor Λ denotes orientation of the indented crystal surface [147]. The factor was introduced to compensate the orientation of indenter facets which causes the different crystal rotation caused by a slip. The CRSS values mean the minimum required stress for slip activation, therefore, the values can be utilized for ranking the ease of each slip activation. By considering the ratio of those, the weighted Schmid factor was calculated for all possible slip systems.

3.2.1 Calculation of deformation and fracture parameters

As described by Eq. (3-14), Schmid factor m can be calculated by the product of cosine values $\cos\theta\cos\lambda$. The values are expressed as below:

$$\cos\theta = \frac{S_p \cdot F}{\|S_p\| \cdot \|F\|} \tag{3-19}$$

$$\cos\lambda = \frac{S_d \cdot F}{\|S_d\| \cdot \|F\|} \tag{3-20}$$

Therefore, cosine θ value shows the relation of the inner product of slip plane normal vector S_p and applied force vector F divided by slip plane normal vector S_d norm and applied force F norm. Cosine λ value is expressed in the same procedure. Applied force F is substituted by resultant force F_r in cutting which can be measured by a dynamometer.

Based on the idea of Nowak and other researchers [147], the obtained i-th Schmid factor m_i is ranked by i-th CRSS values as follows:

$$P_i = \frac{m_i}{\tau_i^{crit} \Big/ \min_i \tau_i^{crit}} \tag{3-21}$$

The i-th Schmid factor m_i is weighted based on the ratio of CRSS values for i-th slip system to minimum CRSS values among all of the possible slip systems. The weighted Schmid factor P_i is named as plastic deformation parameter P_i in this dissertation. CRSS values are estimated from the literature (Munoz's data for CaF₂ [129] and Clayton's data for sapphire [148]). It should be noted that the CRSS values are different

according to the literature due to the difficulty of the measurement or calculation, especially for sapphire [147-149]. In the dissertation, Clayton's results were used because he comprehensively discussed all of the deformation system i.e. slip systems, twinning and cleavages [148]. As mentioned in section 3.1.3, twinning is induced by shear stress and contributes to plastic deformation for HCP crystals. It has been a controversial matter to consider the CRSS value for twinning because its deformation process is different from slip [147], however, it is evident that twinning is also involved in the ductility, therefore, the plastic deformation parameter P was calculated for twinning systems.

The CRSS values depend on the temperature, and the more a temperature increases, the more easily slip is activated, in other words, the CRSS values decrease. In reality, some slip systems are not activated under the room temperature. However, it is reported that the temperature in the vicinity of the cutting edge is elevated to 200 ℃ in ductile-regime cutting of silicon [124]. According to Munoz's report, the primary slip system {100}⟨110⟩ and the secondary one {111}⟨110⟩ could be activated at around 200 ℃. Therefore, the CRSS values are estimated at the temperature of around 200 ℃. Other slip plane {110} also exists, however, the slip system was activated at more than 400 ℃ temperature, therefore, the {110} slip plane is omitted in the dissertation. For sapphire, various deformation systems (rhombohedral twinning, basal twinning, basal slip, prismatic slip, and pyramidal slip) exist as shown in Table 3-2, and RT is the easiest to be activated in terms of CRSS. The twinning process is assumed to be unidirectional and is possible under compressive load in respect to the c-axis, whereas the slip process is bidirectional. In regards to the pyramidal slip, it is activated only by tensile loading along the c-axis [148]. Hence, the absolute values of the plastic deformation parameter P values for slip systems are used, whereas only negative values of the one is used for twinning. Only for pyramidal slip the positive value is used for the calculation.

Similar parameters also can be calculated for cleavage. As noted in section 3.1.2, cleavage can be described by using the relationship of the angle between applied force vector $\boldsymbol{F}$ and the cleavage plane normal $\boldsymbol{C_p}$. Therefore, the tendency for anisotropic cleavage can be postulated as follows:

$$\sigma_c \propto \frac{F}{A} cos^2\varphi \Lambda \tag{3-22}$$

Cosine φ is described, analogous to Eq.(3.17):

$$cos\varphi = \frac{\boldsymbol{C_p} \cdot \boldsymbol{F}}{\|\boldsymbol{C_p}\| \cdot \|\boldsymbol{F}\|} \tag{3-23}$$

For cleavage fracture, the energy of two new surface to form a pair of halved surfaces, 2γ, are required [150]. The necessary tensile stress for separation of materials along cleavage is proportional to surface energy γ as described by Eq.(3-16), therefore, the

Table 3-1 Slip systems of CaF₂ (CRSS values are estimated from the Munoz's data [129] at the temperature of 200℃)

Slip system	Miller index	CRSS τ_i^{crit} [MPa]
Primary slip system	$\{100\}\langle 110\rangle$	3.42
Secondary slip system	$\{111\}\langle 110\rangle$	17.04

Table 3-2 Slip and twinning systems of sapphire (CRSS values are estimated from the Clayton's data [148] at the temperature of 200 ℃)

Slip (Twinning) system	Miller-Bravais index	CRSS τ_i^{crit} [GPa]
Rhombohedral twinning (RT)	$\{1\bar{1}02\}\langle 1\bar{1}0\bar{1}\rangle$	0.41
Basal twinning (BT)	$(0001)\langle \bar{1}010\rangle$	2.23
Basal slip (BS)	$(0001)\langle 11\bar{2}0\rangle$	2.23
Prismatic slip (PRS)	$\{11\bar{2}0\}\langle 10\bar{1}0\rangle$	1.65
Pyramidal slip (PYS)	$\{0\bar{1}11\}\langle 10\bar{1}1\rangle$	4.49

tendency for cleavage can be quantified by surface energy γ for specific planes. In this dissertation, the cleavage fracture parameter C_j for j-th cleavage plane is defined as follows:

$$C_j = \frac{\cos^2\varphi}{\gamma_j \Big/ \min_j \gamma_j}$$
(3-24)

In a similar manner, cleavage is also quantified incorporating surface energy. Cleavages occur at room temperature, therefore, possible cleavages have to be considered. For CaF₂, perfect {111} cleavage is a primary cleavage, and partially {110} cleavage is confirmed as a secondary cleavage [51] (see Table 3-3). For sapphire, basal cleavage, prismatic cleavage and rhombohedral cleavage exist [148, 151]. By merging the existing experimental data, the cleavage fracture parameter C is computed.

3.2.2　Calculation flow

Schematic illustration of the calculation procedure is shown in Fig. 3-7. Crystallographic information (slip system, cleavage, workpiece orientation) and the force inclination angle are inputted at first. If the material is sapphire, some transformation procedure is demanded. Sapphire is expressed by Miller-Bravais indices $(h\ k\ i\ l)[u\ v\ t\ w]$, therefore, the expression has to be transformed into Miller indices $(H\ K\ L)[U\ V\ W]$. After that, the hexagonal coordinate system is converted into Cartesian coordinate system [152-154], namely, the coordinate system is adjusted to the following calculation. By using the crystallographic information of the workpiece and

Table 3-3 Cleavage planes and surface energy of CaF₂ (Surface energy values are taken from Janicki's data [51])

Cleavage plane	Miller index	Surface energy γ [J/m²]
Perfect cleavage	{111}	0.384
Partial cleavage	{110}	0.723

Table 3-4 Cleavage planes and surface energy of sapphire (Surface energy values are taken from Wiederhorn [151] and Clayton's data [148])

Cleavage plane	Miller-Bravais index	Surface energy γ [J/m²]
Basal cleavage (BC)	(0001)	≤ 40
Prismatic cleavage (PC)	{$\bar{1}010$}	7.3
Rhombohedral cleavage (RC)	{$\bar{1}012$}	6

applied force vector, the analysis condition is initialized. Rodrigues' rotation formula is employed to calculate every force vector as an axis of main plane normal vector. Those procedures are complemented in Appendix. For every force direction, the angular relationship between slip (cleavage) system and force vector is calculated e.g. Schmid factor for slip systems. By incorporating the CRSS values and surface energies, the calculated values are weighted, and then the plastic deformation parameter P and cleavage fracture parameter C are obtained.

3.3　Summary

　This chapter describes a fundamental of material fracture mechanism related to the cutting process i.e. slip, cleavage, and twinning. The analysis procedure of anisotropic fracture behavior on the basis of the above-mentioned mechanisms is presented, and adapted to the cutting process. The contents are summarized as follows:

1. General background and fundamental mechanisms of slip, cleavage, and twinning are introduced, which strongly affect the surface integrity in ultra-precision cutting.

2. For analysis of anisotropic fracture behavior, resolved stress model was presented and adapted to the cutting process. CRSS and surface energy are incorporated so that one can comprehensively discuss the anisotropic fracture behavior including all possible slip, twinning system and cleavage planes.
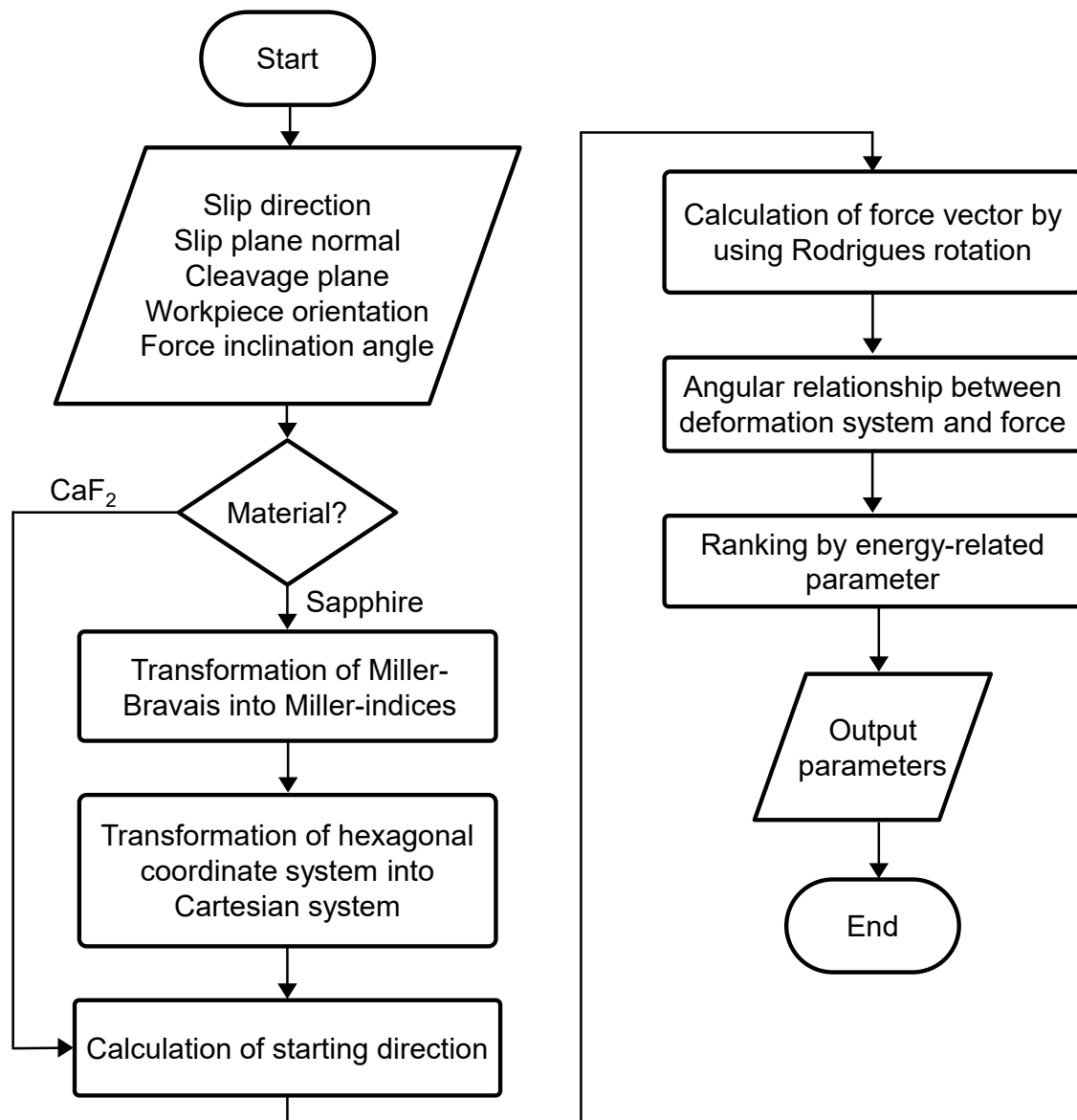
Fig. 3-7 Calculation flow of the plastic deformation parameter and cleavage fracture parameter

4. Investigation of the cutting performance of CaF$_2$

This chapter describes the influence of process parameters and crystal anisotropy on the machinability of CaF$_2$ in cutting tests. In section 4.1, the plunge-cut tests were conducted. The parameters proposed in chapter 3 are calculated to discuss the anisotropic deformation behavior in plunge-cut tests. In section 4.2, UPCT tests were carried out, and the surface integrity was discussed. The SSD induced by UPCT was also investigated by TEM observation.

4.1 Plunge-cut test

A plunge-cut test is one of the fundamental processes to investigate the BDT in cutting of brittle materials [79, 84, 86]. In the tests, the CDC values and surface morphologies were examined.

4.1.1 Experimental setup

On the ultra-precision 4-axis vertical machine tool (UVM-450C, TOSHIBA MACHINE Ltd.), plunge-cut tests were conducted. CaF$_2$ substrate (13 mm × 38 mm × 1 mm) was directly fixed by a vacuum chuck system which consists of a base plate, a dynamometer (9256A1, Kistler), an adapter plate, and a vacuum chuck on the X stage as shown in Fig. 4-1(a). CaF$_2$ was pre-polished to remove existing cracks before the experiments. (100), (110), and (111) planes were selected for cutting crystalline plane (main plane). As a type of tool, SCD was used. The used tools are different depending on the tests, however, only rounded-nose tools were used through the whole tests. One of the used SCD tools (with 0.2 mm rounded-nose radius, −20° rake, 8° clearance) is shown in Fig. 4-1 (b). By
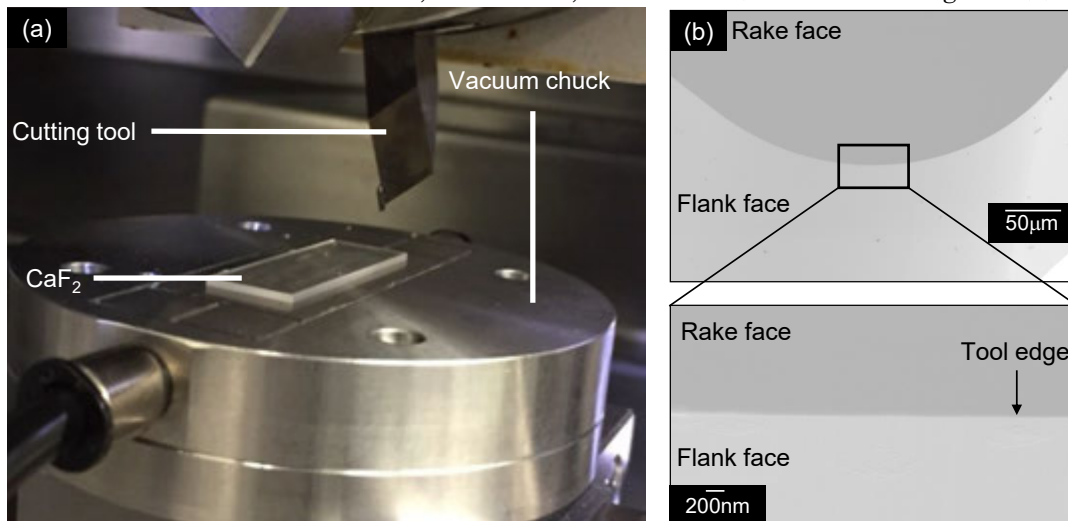
Fig. 4-1 Experimental setup. (a) Image of plunge-cut tests (b) SEM image of the used SCD tool (Tool #1, 0.2 mm nose radius, −20° rake angle, 8° clearance angle)

Table 4-1 Process parameter of the plunge-cut tests of CaF₂

Parameter	Value
Cutting speed V_f [mm/min]	20, 50, 100, 200, 500, 1000, 1500
Depth of cut a_p [nm]	$0-2000$
Cutting slope D/L	1/500
Cutting direction δ [°]	$0-330$ (increments of 30)
Crystal orientation of cutting plane	(100), (110), (111)
Type of cutting tool	SCD
Nose radius R [mm]	0.2, 0.05, 0.01
Rake angle α [°]	$0,\ -10,\ -20,\ -30$
Atmosphere	Dry

SEM (Scanning Electron Microscope) observation, the edge radius is estimated as less than 50 nm. The value is relatively close to the reference value (see Table 2-3), however, it should be noted that the estimation is a more qualitative manner compared to AFM measurement [155]. The DOC (Depth Of Cut) a_p continuously changes with a constant cutting slope D/L (Fig. 4-2 (b)). The cutting slope was set to 1/500, which means that DOC reaches from 0 to 2 µm when length of the groove is 1mm. Continuous motion of x- and z-axes fed by NC (Numerical Control) program enabled us to set the cutting slope. Once the tool reaches to maximal DOC, the tool is fed to the same direction but decrease the DOC with the same D/L. Owing to the procedure, it is possible to avoid the high impact force which acts on the tool edge and causes the tool breakage. The cutting direction δ was increased in increments of 30 ° until 330 ° (Fig. 4-2 (a)). The tests were repeated three times for each cutting condition. The machined grooves were observed by FE-SEM (Merlin Compact VP, Carl Zeiss) for each cutting direction δ. The DOC was measured using a WLI (White Light Interferometer, New View TM6200, Zygo). The CDC
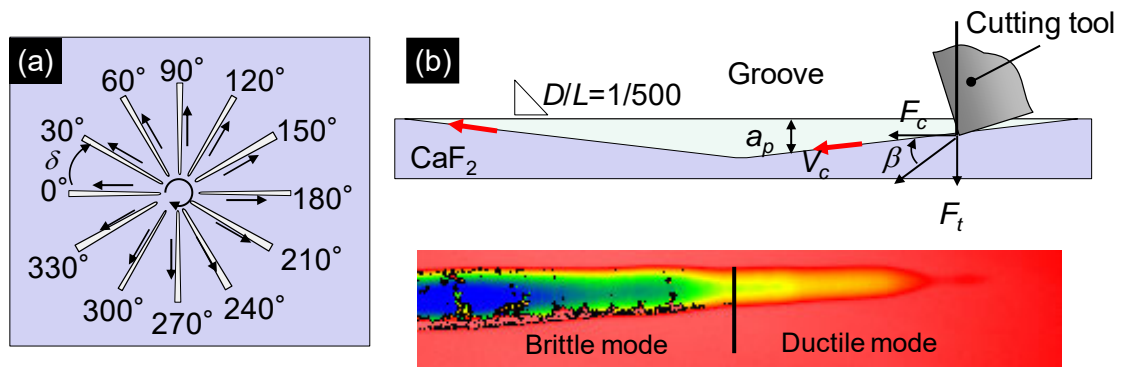
Fig. 4-2 Schematic illustration of the experimental procedure. (a) Cutting direction δ is rotated by 30 ° till a full rotation. (b) Once cutting tool reaches to the maximum depth, then goes up with the same cutting slope D/L. The CDC values are measured by WLI measurement where the black spots firstly appear.

was defined as the depth where a first crack appears. Since WLI methods is based on the light interferometer, the surface is required to be smooth enough for measurement. Therefore, missing data point (indicated as black spots in Fig. 4-2 (c)) is caused by cracks. Ethanol or acetone was used to eliminate dust on the surface before the measurement. The average value of the measured CDC was utilized. The process forces were measured by a dynamometer (9256A1, KISTLER). Experimental condition is listed in Table 4-1, and the rake angle was changed by rotating the a-axis.

4.1.2   Machinability of (100) plane

On (100) plane, influence of the process parameters (cutting speed, rake angle, nose radius) and crystal anisotropy are investigated.

Process parameter

For the investigation of influence of process parameter, the cutting crystalline plane and directions are fixed as (100) plane and [011] direction (cutting direction δ is 0 ° on (100) plane). The cutting tool with -20 ° rake and 0.2 mm nose radius was employed. Fig. 4-3 shows that the CDC values do not change significantly according to the cutting speed, analogous to the other work e.g. CaF$_2$ [49], germanium and silicon [1]. The cutting speed is related to the cutting power for material removal in cutting, and thus critical cutting speed which generates the energy enough to cut materials. In principle, a high cutting speed is sometimes favorable to enhance the surface quality and reduce the machining time and cutting force [156, 157]. For instance, in the scratch of c-plane sapphire, increasing the scratch velocity improved the strain rate and suppressed the
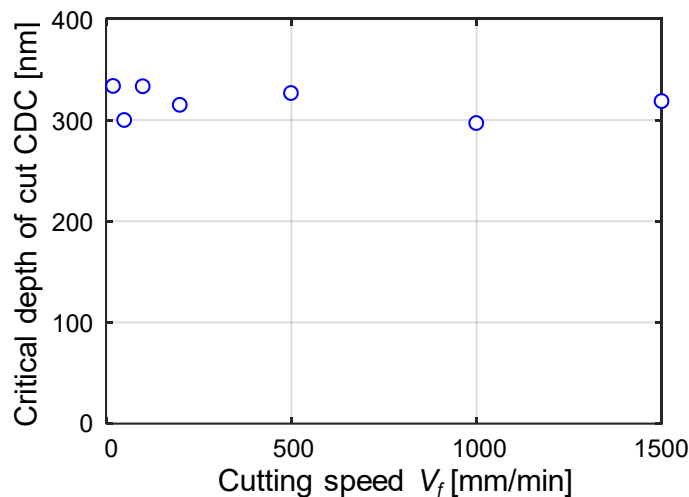
Workpiece:	Cutting tool:	Process parameter:
Material: CaF$_2$	Type: SCD	Cutting speed V_f [mm/min]:Variable
Main plane: (100)	Rake angle α [°]: -20	Depth of cut a_p [nm]:0-2000
Cutting direction: [011]	Nose radius R [mm]: 0.2	Slope D/L:1/500

Fig. 4-3 Relationship between cutting speed V_f and critical depth of cut CDC

growth of cracks [141]. Notably, high cutting speed also causes the crack initiation because an induced residual stress will be released by brittle fracture. Therefore, there should be an optimal cutting velocity in cutting of CaF$_2$. However, the optimal value was not clearly identified in the range of $20 - 1500$ mm/min. In the following tests, the cutting speed was set as 200 mm/min.

It is widely anticipated that rather tool geometry has a great influence on the surface quality in diamond turning process [156]. Indeed, several reports show that the variation of rake angle affects the BDT phenomena [1, 49, 76]. However, as shown in Fig. 4-4 (a), rake angle does not significantly affect the CDC values, and the results are different from the previous works [1, 48, 49, 76, 80]. Normally, utilization of negative rake face angle can restrain the crack formation because a hydrostatic pressure is formed in a compressive stress field underneath the cutting edge. On the other hand, a great negative rake angle rather deteriorates the surface because the chip formation is apt not to occur, rather plowing occurs (see section 2.2.2 and [48]). Interestingly, the smaller the nose radius is, the smaller the CDC value is. Nose radius is one of the essential parameters which affect the cutting performance such as regenerative chatter, or surface integrity. For example, Chen showed that using a smaller nose radius lead to reduce the thrust force and suppress chatter [158]. Such as rake angle, there is also an optimal value depending on material [159]. In general, the contact area between the tool and machined surface increases with the increments of nose radius. Plastic deformation region is strongly affected by the contact area, where the hydrostatic pressure forms. Since the compressive stress region is smaller, it is assumed that the hydrostatic
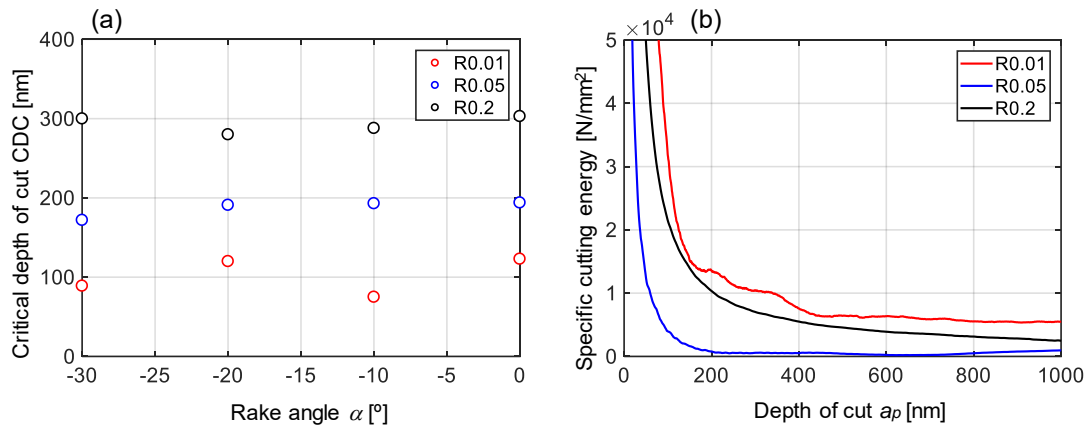
Workpiece:	Cutting tool:	Process parameter:
Material: CaF$_2$	Type: SCD	Cutting speed V_f [mm/min]:200
Main plane: (100)	Rake angle α [°]:Variable	Depth of cut a_p [nm]:0-2000
Cutting direction: [011]	Nose radius R [mm]: Variable	Slope D/L:1/500

Fig. 4-4 Influence of rake angle α and nose radius R on (a) critical depth of cut CDC and specific cutting energy

pressure can be also smaller or stress acting on the material does not distribute and rather the stress is easy to focus on a small zone so that the crack easily initiates.

Since the cutting energy depends on the tool geometry, the cutting energy is normalized according to the inherent area which contributes to cutting volume. This is so-called specific cutting energy, and that enables us to evaluate the cutting energy fairly and independently from the tool geometry. The specific cutting energy represents the energy required for a unit volume of workpiece [140]. In the plunge-cut process, it can be replaced that the acting force per cross-sectional area of the groove. The specific cutting energy E_s is given as:

$$E_s = \frac{F_c}{A_c} \qquad\qquad (4\text{-}1)$$

Fig. 4-4 shows the energy-DOC curve in accordance with nose radius (0 ° rake angle). The specific cutting energy becomes rapidly higher as DOC decreases, which originates from the size effect in a small volume of cutting. Similar results are obtained in other work [140]. Since the DOC becomes larger, the cutting mode transits from ductile-regime to brittle-regime, in other words, the BDT takes place. It is well known that the force curve is normally fluctuated and does not increase in brittle-regime because the cutting energy dissipates from brittle fracture. Therefore, Wang [140] noticed that one could predict the CDC value from the curves, and the real CDC relatively fit the predicted CDC. Based on the results, the curve shifts towards right-top direction when the CDC is higher, however, the obtained results in this tests do not follow the idea. One of the reasons might originate from the uncertainty of the estimated DOC. Although the machining process was conducted by an NC program, the workpiece is not perfectly parallel. Therefore, the actual obtained grooves are sometimes longer or shorter than the expected ones, and the DOC is estimated from the width of actual grooves which can be observed by optical microscope. In addition, the cutting force itself is very small, and thus it is difficult to identify the actual starting point of the groove and force curve.

Compared to previous studies, the used nose radius is quite smaller (usually more than 1 mm), therefore, the tendency of the CDC values can change if extending to more than 1 mm nose radius. There is a limitation of the nose radius in this study considering of manufacturing a microcavity, hence, here it is concluded that a nose radius significantly affects the CDC values compared to other process parameters. The ease of hydrostatic compressive stress generation can be a major reason.
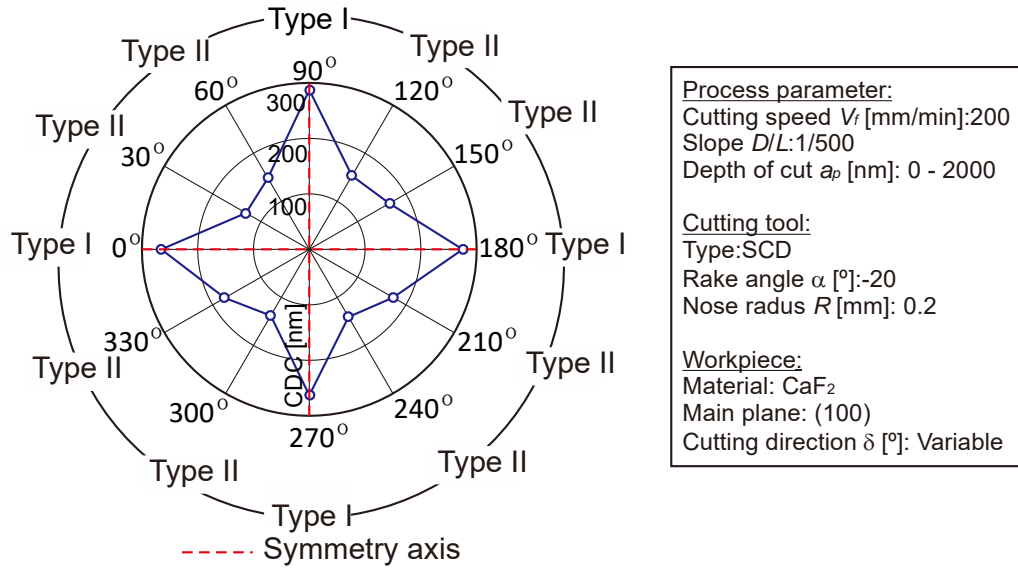
Fig. 4-5 CDC values and classification of surface morphology of (100) plane

Crystal anisotropy

For the following tests, the SCD tool with $-20\,°$ rake and 0.2 mm nose radius was used. Fig. 4-5 shows the CDC values and classification of surface morphology of the machined grooves on (100). The CDC value and surface morphology change depending on the cutting directions. The surface morphologies in the vicinity of BDT are shown in Fig. 4-6: type I—a smooth surface with fine lamellar fracture (Fig. 4-6 (a)); type II— lamellar step and fracture sculpted by the cleavage planes (Fig. 4-6 (b) and (c)). Based on the crystal structure (Fig. 4-7), the CDC values and surface morphologies are characterized by a four-folded symmetry along the [011] and [01$\bar{1}$] axes (in the cutting directions of 0 °, 90 °, 180 °, and 270 °). For analysis of crystal anisotropy, the plastic deformation parameter P and cleavage fracture parameter C are computed. The tendency for activation of each deformation system are shown in the P-δ and C-δ curves in Fig. 4-8. The maximal CDC values coincide with the high P-parameter values of {100}⟨011⟩ slip system in the directions of 0 °, 90 °, 180 °, and 270 °. Thus, it is anticipated that the slip systems contribute to promote the plastic deformation and enhance the ductile-regime cutting in those directions. On the other hand, the C-parameter value is also the highest for the same directions. In the case of plunge-cut tests of sapphire, the high C-parameter corresponds to the minimal CDC, however, those do not fit the CaF₂ case. The detailed discussion will be introduced in Chapter 5. The type I brittle fracture in 0 ° cutting direction is observed in the perpendicular direction to the cutting direction, which corresponds to (1$\bar{1}\bar{1}$) cleavage (Fig. 4-6 (a) and red line of the part of (1$\bar{1}\bar{1}$) in Fig. 4-7) and the high C-parameter of (1$\bar{1}\bar{1}$). The sculpted fracture (Fig. 4-6 (b) and (c), and part of the Type II) in 30 ° and 60 ° cutting directions
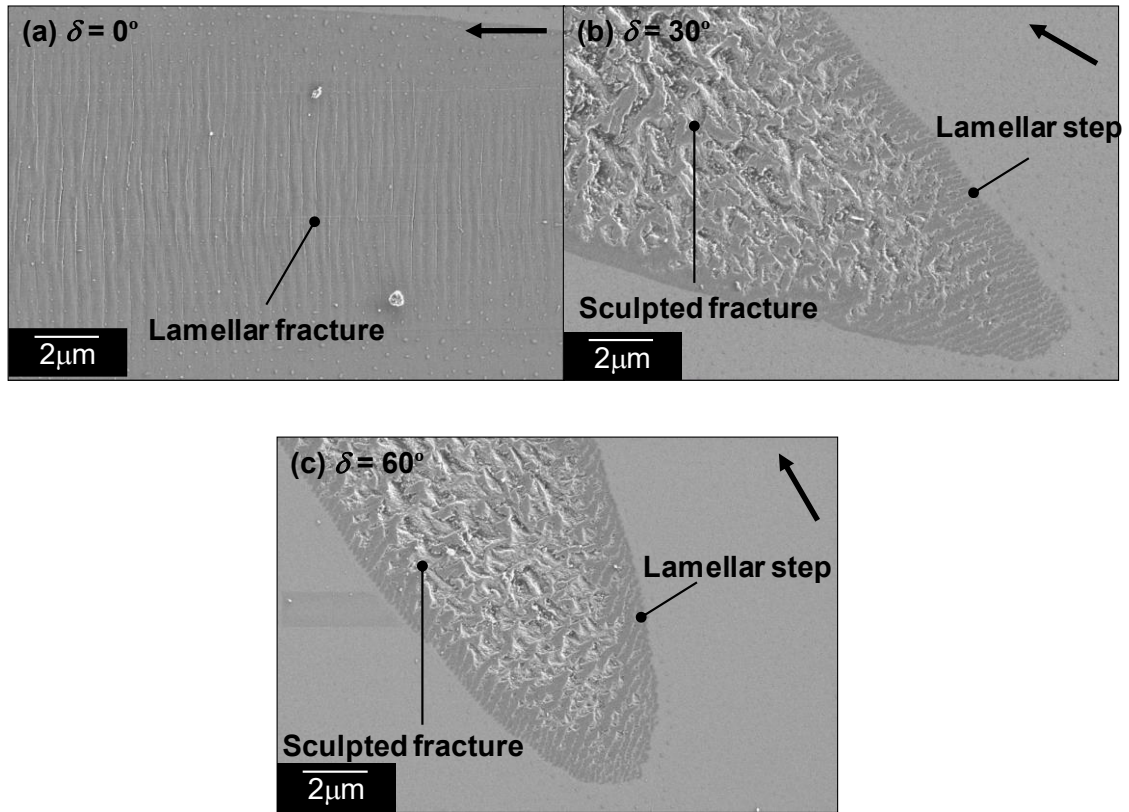
Fig. 4-6 Surface morphologies of (100) plane: (a) type I—a smooth surface with fine lamellar fracture; (b), (c) type II—lamellar step and fracture sculpted by cleavage (a black arrow indicates the cutting direction)
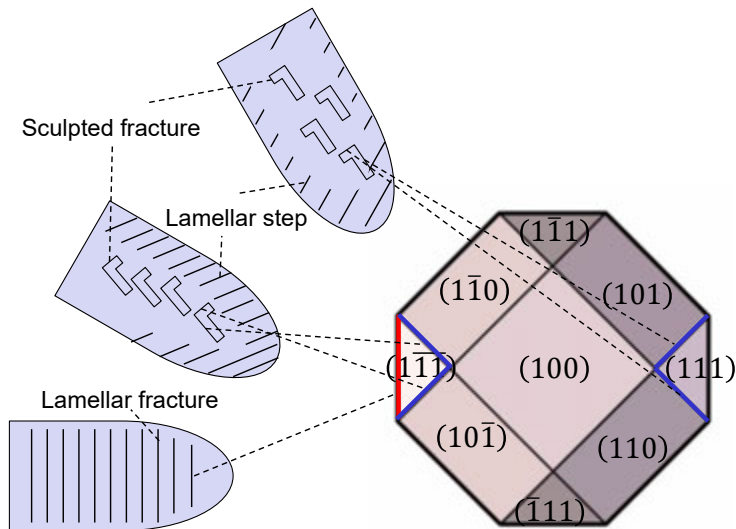
Fig. 4-7 Schematic illustration of the surface morphologies on (100)

are regularly formed by respectively $(1\bar{1}\bar{1})$ and (111) cleavages which are also sustained by the corresponding high C-parameter value of each cleavages. At the beginning of the grooves and along the outside of the grooves, the lamellar steps regularly run along which do not correspond to {111} and {110} cleavages.

From the top view of machined surface, the step can correspond to ⟨012⟩. There is a report that such steps were also observed in the direction of ⟨211⟩, or ⟨3$\overline{12}$⟩ in heating process [130], therefore, the steps can be a part of the directions and related to cleavage or slip.

4.1.3 Machinability of (110) plane

In the following sections, the influence of crystal anisotropy was investigated. In the plunge-cut experiments of (110) plane, two-folded symmetry features the CDC values and various fracture types of the machined grooves (Compare Fig. 4-9, Fig. 4-10, Fig. 4-11, and Fig. 4-12): type I— a cleavage ($\overline{1}1\overline{1}$) fracture running along the vertical
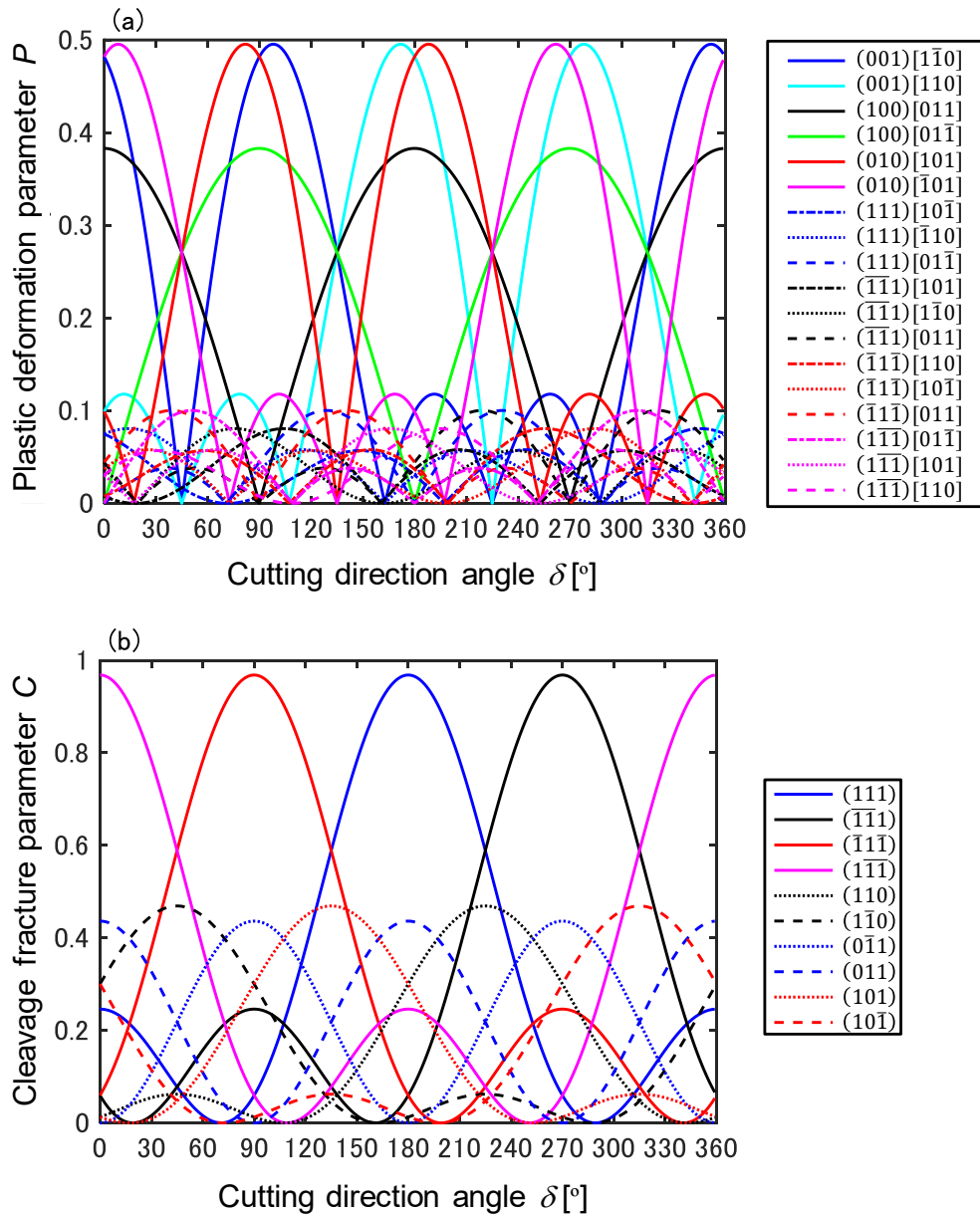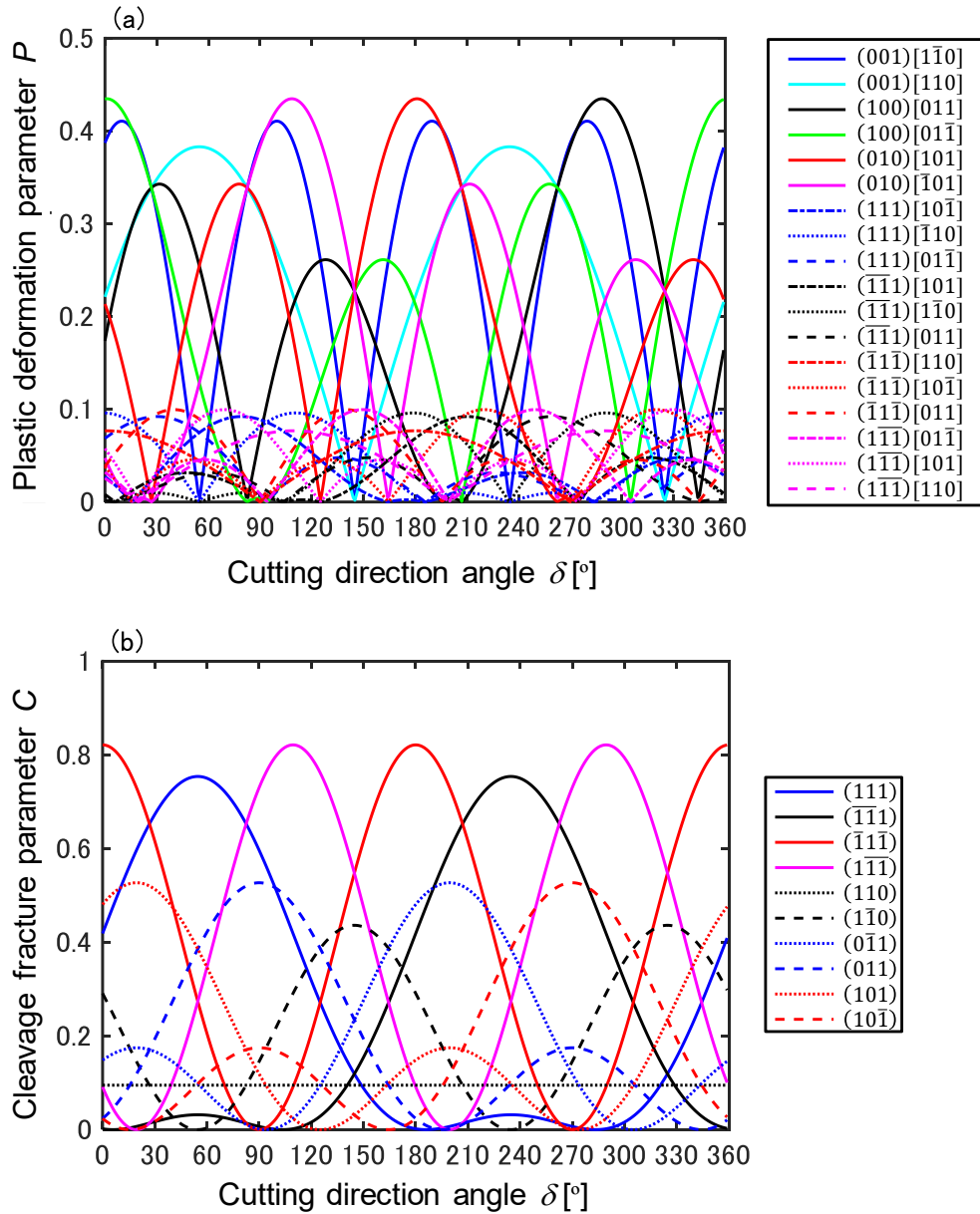

Fig. 4-8 Variation of (a) plastic deformation parameter P and (b) cleavage fracture parameter C of (100) plane

direction to the cutting direction (Fig. 4-11 (a)),and a cleavage $(\bar{1}1\bar{1})$ fracture along the same direction as the Type I fracture (Fig. 4-11 (b)); type II— a line fracture perpendicular to the cutting direction caused by the (111) cleavage (Fig. 4-11 (c)); type III— a smooth surface with coming-off lamellar fracture that could be induced by the $(\bar{1}11)$ cleavage and elastic recovery (Fig. 4-11 (d)); type IV— a $(\bar{1}11)$ fracture (Fig. 4-11 (e)); type V— a line brittle fracture induced by the $(1\bar{1}0)$ cleavage and a large fracture sculpted by the combination of the $(1\bar{1}\bar{1})$, $(\bar{1}1\bar{1})$, and $(1\bar{1}0)$ cleavages (Fig. 4-11 (f)).
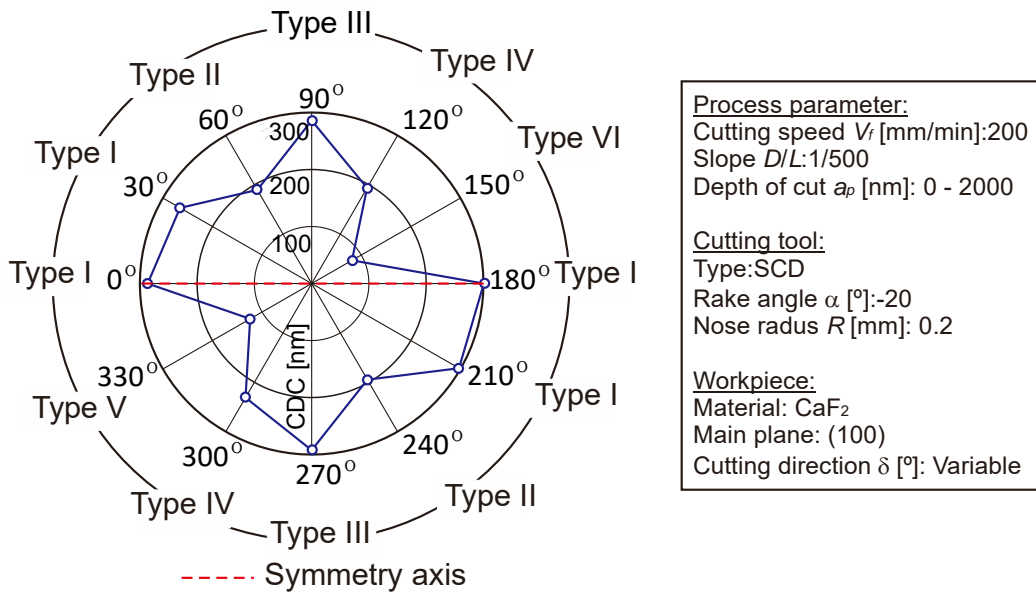
Fig. 4-9 CDC values and classification of surface morphology on (110) plane
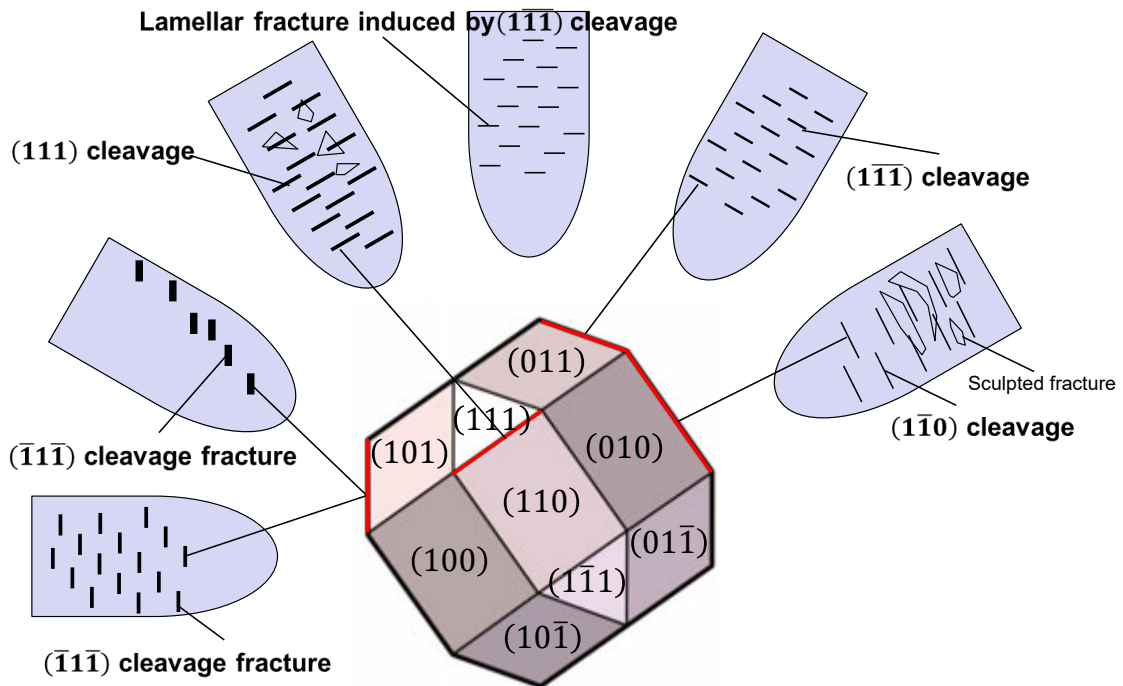
Fig. 4-10 Schematic illustration of the surface morphologies on (110)

Except for 150º cutting direction, the CDC values does not rapidly change. Especially the CDC values are maximal at the cutting directions of 0 º and 90 º, which are associated with the high P parameters (see Fig. 4-12 (a)). Rather, the P parameter values decrease in the direction of 150º and 330º where the corresponding CDC values are minimal compared to other cutting directions, therefore, the low value of P parameter also indicates the low CDC values. Overall, the line fracture which are formed in the perpendicular direction to the cutting direction on each cutting direction firstly, and each fracture type corresponds to the cleavage planes which feature higher C parameters in
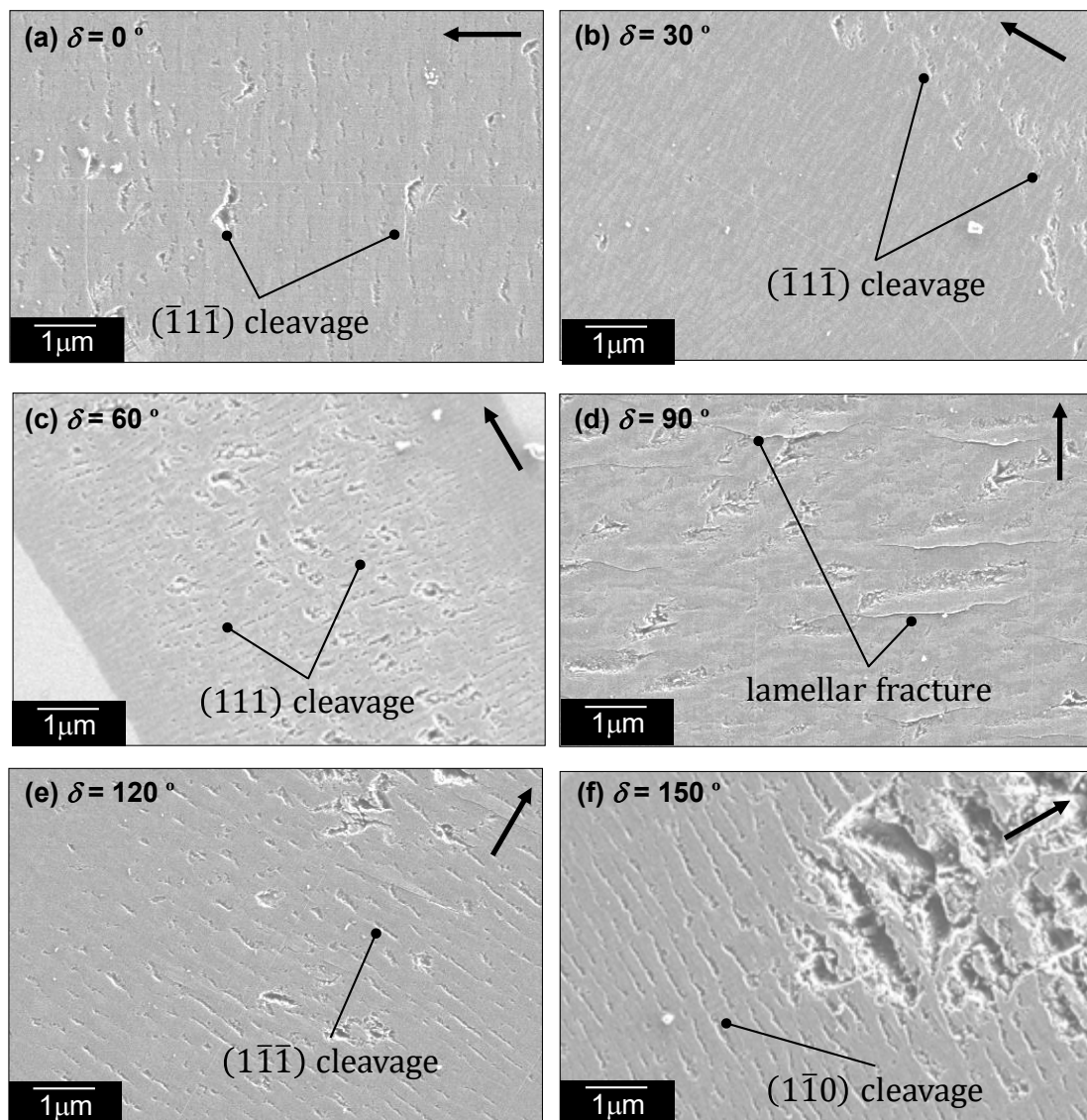
Fig. 4-11 Surface morphologies of (110): (a), (b) type I— a line fracture along cleavage $(\bar{1}1\bar{1})$ (c) type II— a line fracture perpendicular to the cutting direction caused by the (111) cleavage (d) type III— a smooth surface with turned-up lamellar fracture that could be induced by the $(\bar{1}11)$ cleavage and elastic recovery (e) type IV— a $(\bar{1}11)$ fracture (f) type V— a line brittle fracture induced by the $(1\bar{1}0)$ cleavage and a large fracture sculpted by the combination of the $(1\bar{1}\bar{1})$, $(\bar{1}1\bar{1})$, and $(1\bar{1}0)$ cleavages (a black arrow indicates the cutting direction)

(a)

(b)

Fig. 4-12 Variation of (a) plastic deformation parameter P and (b) cleavage fracture parameter C of (110) plane

Fig. 4-12 (b). The tendency was seen in the cutting direction of 0 º in plunge-cut tests of (100) plane which shows higher CDC values. The fracture type will be discussed in the next section, including the results of (111) plane.

4.1.4 Machinability of (111) plane

Similar to other works [76, 86], three-fold symmetry manifests itself in the CDC values and corresponding surface morphologies in the case of (111) plane (Fig. 4-13 and Fig. 4-14): Type I—a microtorn fracture (Fig. 4-14 (a) and (c)), Type II—a trapezoidal fracture (Fig. 4-14 (b)), Type III—a smooth surface with a fine lamellar fracture (Fig. 4-14 (d)).
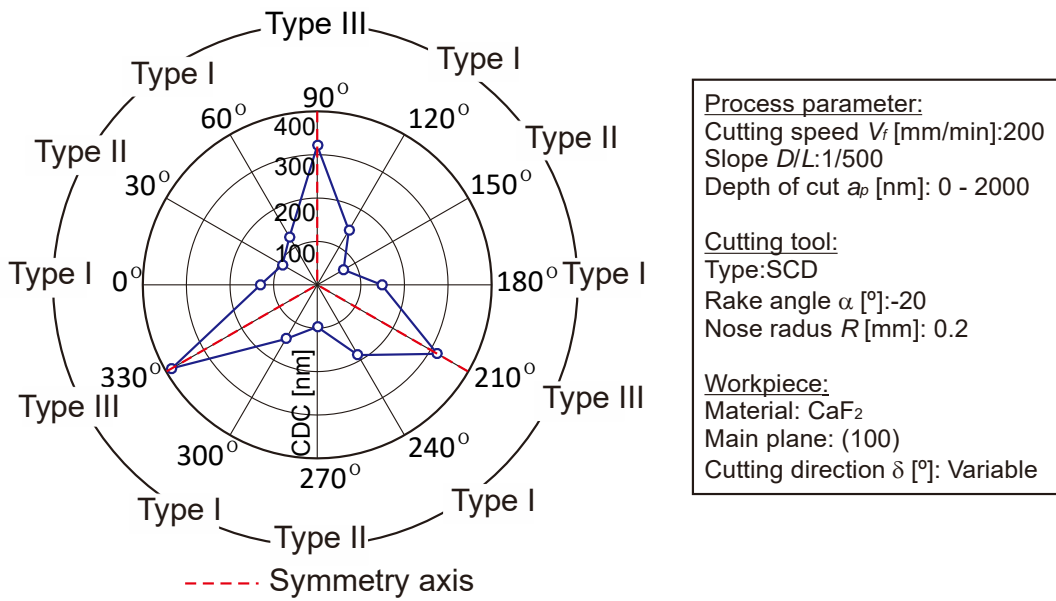
Fig. 4-13 CDC values and classification of surface morphology of (111)
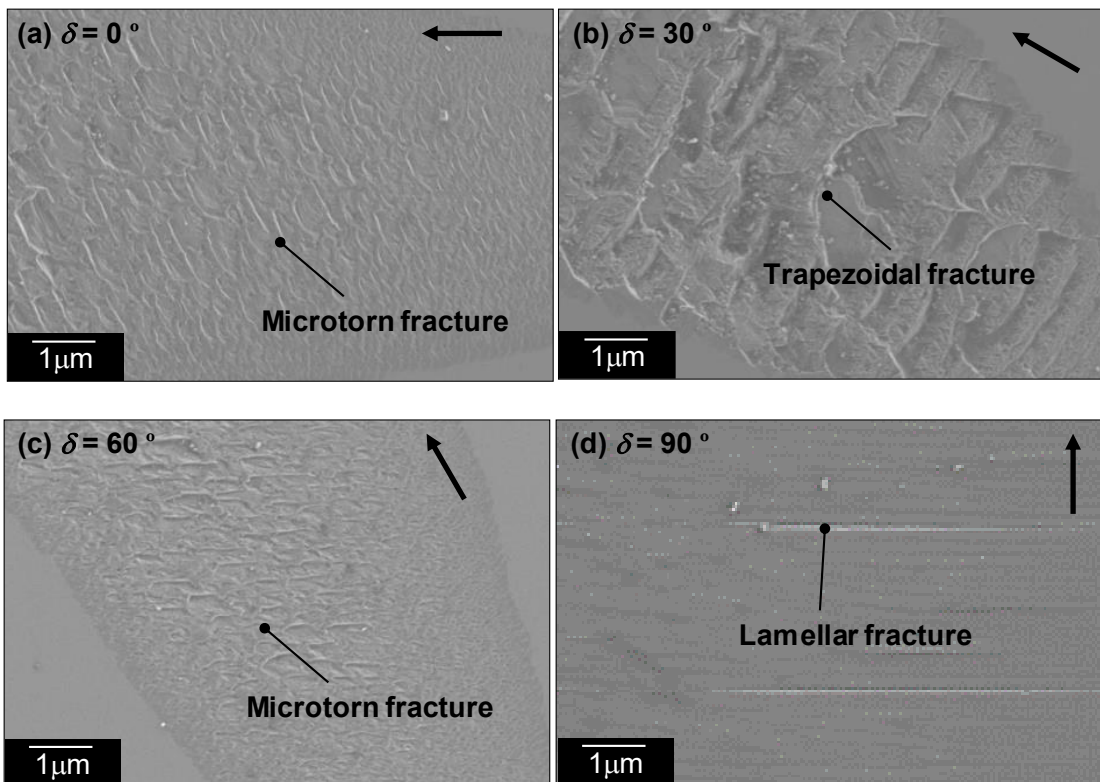
Fig. 4-14 Surface morphologies of (111): (a) and (c) Type I—a microtorn fracture (b) Type II—a trapezoidal fracture (d) Type III—a smooth surface with a fine lamellar fracture

The P-parameters are maxima in the vicinity of 90 º, 210 º, and 330 º cutting directions, and those parameters decrease at the 30 º, 150 º, and 270 º directions where the CDC values are minimal (Fig. 4-16). Type I fracture was observed at the cutting directions of every 60 º from 0 º. Microtorn fractures in the directions of 0 º and 60 º were regularly formed along $(1\bar{1}1)$ and $(\bar{1}11)$ cleavages. Unique brittle fracture of Type II can be

observed in the directions of 30 º, 150 º, and 270 º where most of the C parameters are intersecting near 0.3. It is difficult to identify which cleavage dominates the surface morphologies but rather it is assumed that the fact that those cleavages take place at the same time results in this unique trapezoidal fracture. The lamellar fracture was observed in 90 º, 210 º, and 330 º directions. The same type fracture was also observed in cutting of (100) and (110) planes where the CDC values are high. As shown in Fig. 4-17, cracks are formed by median crack by compressive stress and lateral crack by residual tensile elastic stress [65, 160]. The fact that the CDC values are high shows the higher ductility, therefore, the surface can be more elastic. Right after the tool passes, the combination of the cracking and the residual elastic tensile stress beneath the cutting tool can form a lamellar fracture in a coming-off manner. In the origin of the crack initiation, the machined surface was pulled to elastically recover by the tensile stress, then the surface come off with crack generation. Fig. 4-18 shows the collected continuous chip along the groove of 210 º cutting direction on (111) plane which exhibits the high CDC value. The chip was formed as a saw-tooth type chip [161], which can be seen in metal cutting, and can be an evidence that the ductile-regime cutting was performed.

From the above-mentioned results and discussion, on each main planes (100), (110), and (111), anisotropy of the BDT can be discussed by the computed parameters and CDC values. P parameter, which means the tendency of possible slip activation, agrees well with the CDC values, whereas C parameters misfit the CDC values. Nevertheless, the fracture morphologies can be rather described by C parameters, thus it can be said
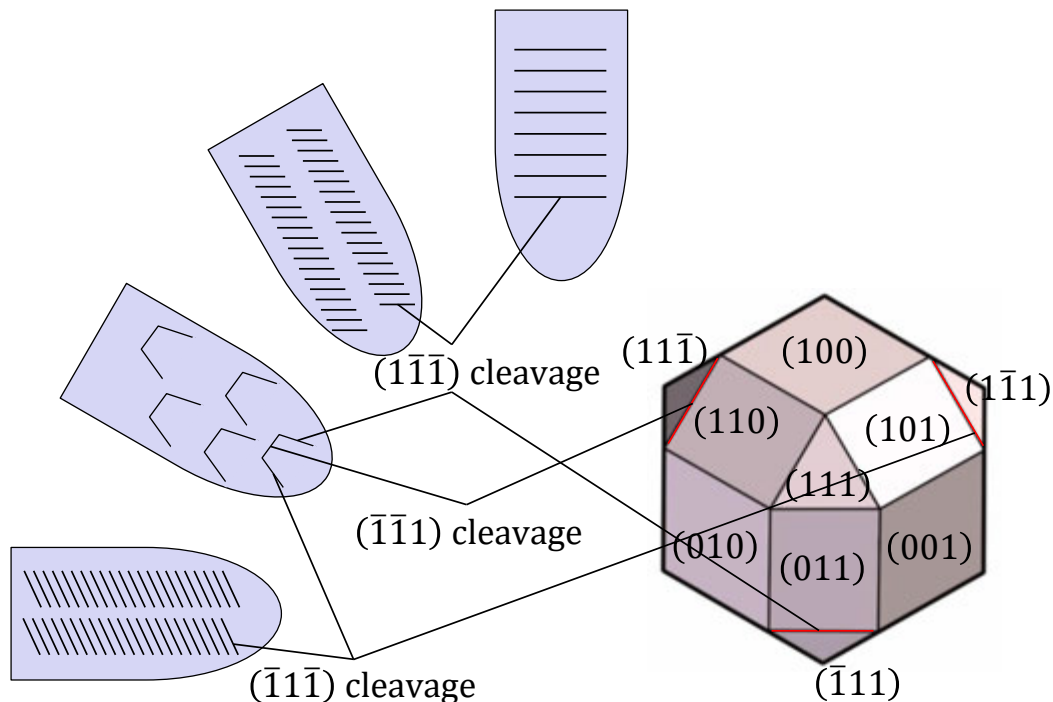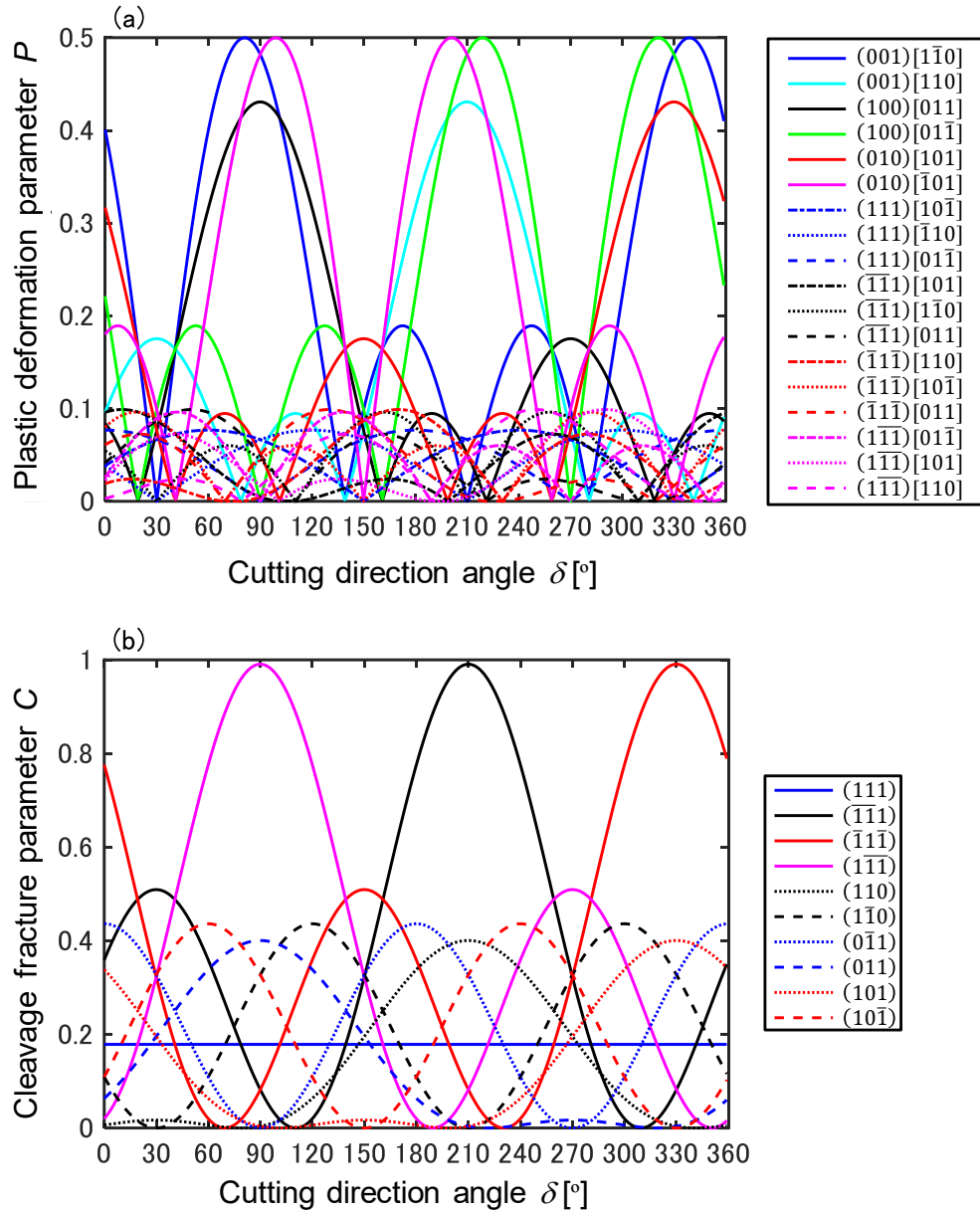

Fig. 4-15 Schematic illustration of surface morphologies on (111)

Fig. 4-16 (a) Plastic deformation parameter P and (b) Cleavage fracture parameter C of (111) plane

that the brittle fracture can be characterized by the corresponding cleavages. The experimental results indicate that the CDC value was over 50 nm on any crystalline plane and crystalline direction, therefore, one could cut the CaF₂ in ductile-mode cutting in arbitrary crystalline direction. Notably, the derived values were based on the experimental results in this dissertation. For example, the minimal values of P parameters on (100) plane exist in cutting directions of 45 °, 135 °, 225 °, and 315 °, where the cutting tests were not performed. Therefore, the actual minimal CDC value can be lower in other crystalline plane or direction.
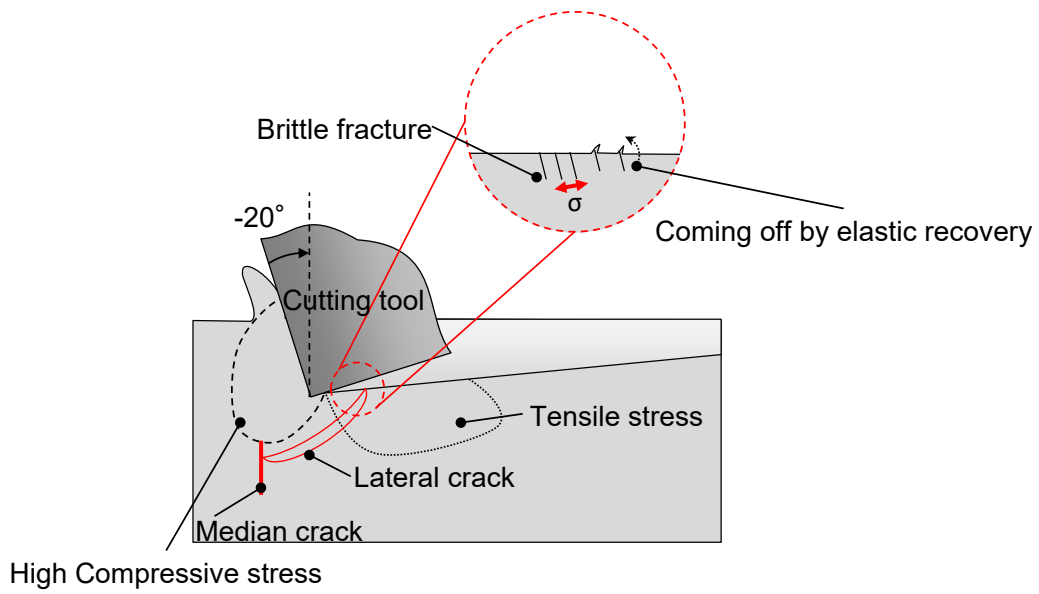
Fig. 4-17 Schematic illustration of a fine lamellar fracture and coming-off brittle fracture [65, 160].
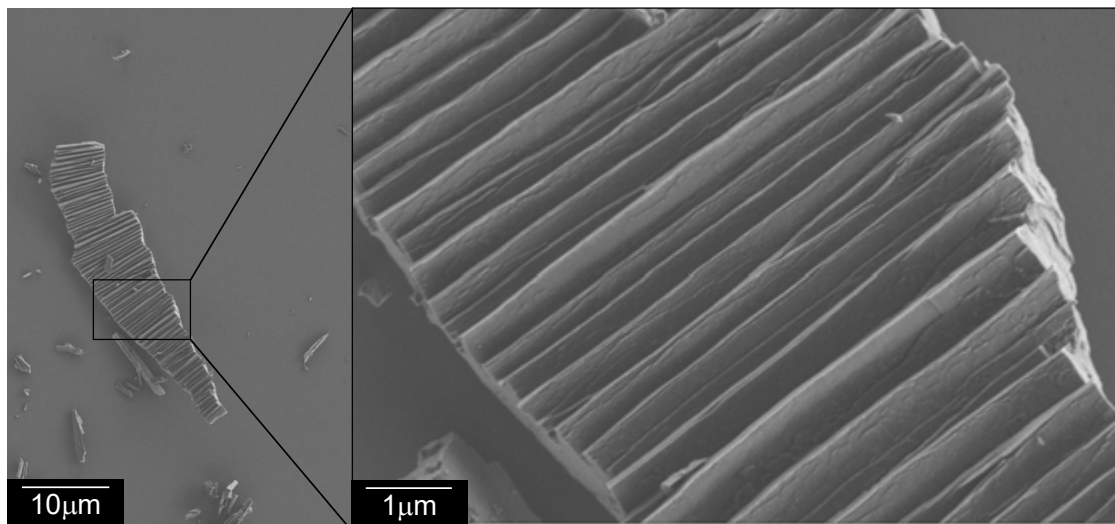
Fig. 4-18 Saw-tooth chip along the 210° cutting direction on the (111) plane.

4.2 Cylindrical turning test

4.2.1 Experimental setup

UPCT (Ultra-Precision Cylindrical Turning) was carried out using an ultra-precision aspheric surface machine tool (ULG-100E, TOSHIBA MACHINE Ltd.). A CaF$_2$ cylinder workpiece with 35 mm length and 6 mm diameter was used. The CaF$_2$ was fixed in a brass jig by adhesive wax, and then clamped by a collet chuck (Fig. 4-19). The collet chuck was mounted onto a vacuum chuck. The crystal orientation of the end face was set as (100), (110), or (111). Firstly, a workpiece was turned in brittle-regime (rough cutting) to form the CaF$_2$ cone with 1 mm diameter under the following cutting condition: 1000 min^{-1} rotational speed, 20 µm/rev feed per revolution, and 2 µm depth of cut. After rough cutting, pre-finish cutting was conducted to eliminate the large cracks under the following cutting conditions: 1000 min^{-1} rotational speed, 3.0 µm/rev feed per revolution, and 100 nm depth of cut, and 5 µm total removal depth. Finally, the surface was finished by ductile-regime cutting with 1 µm total removal depth.

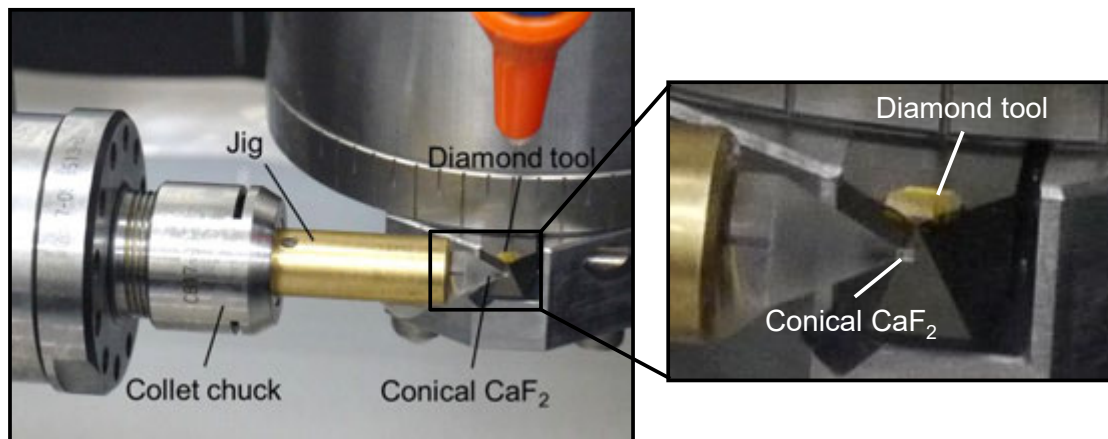Variation of the condition of finish cutting is listed in Table 4-3. It should be noted that

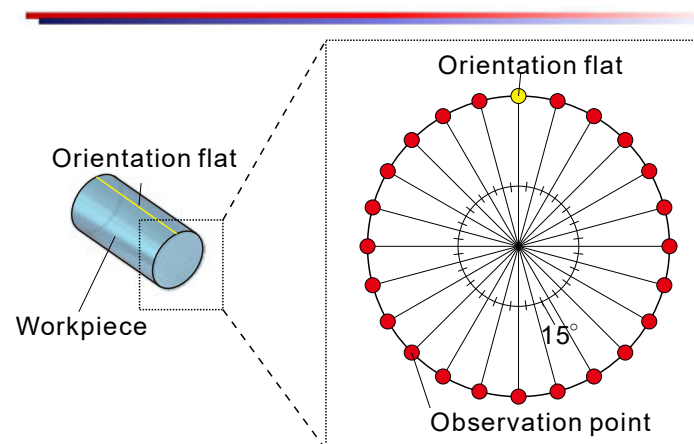Fig. 4-19 Experimental setup of UPCT

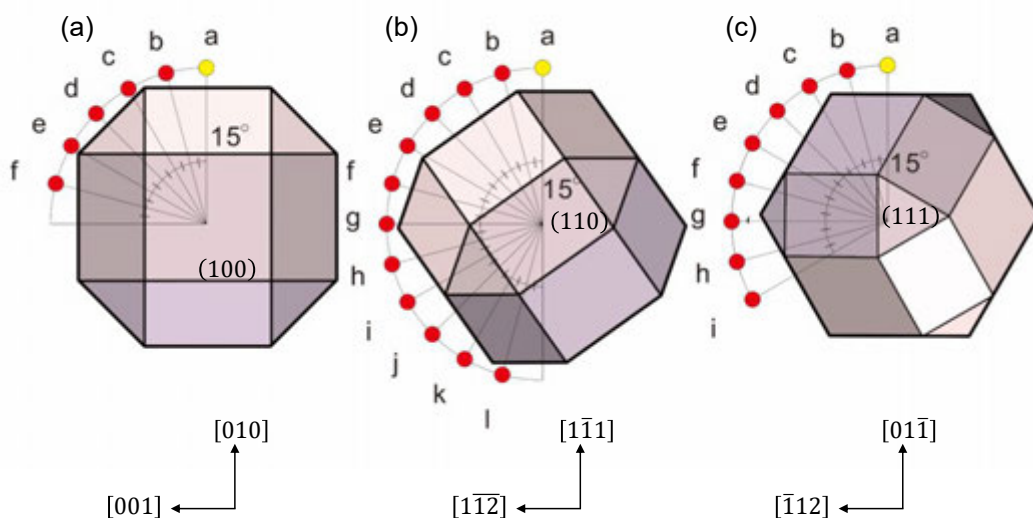

Fig. 4-20 Observation points of UPCT

a cutting speed is proportional to rotational speed. As a cutting tool, SCD tool was mainly used (partially B-NPD tool). The specification of the tools is listed in Table 4-2. The DOC a_p in a radial direction is set to 50 nm. Based on the results of the plunge-cut tests, it was assumed to obtain the surface without cracks around the entire surface according to the quasi-turning model [1] (see Fig. 2-12). As described in section 4.1, the surface integrity of CaF₂ depends on crystalline planes and directions. Since the cutting crystalline planes and directions simultaneously and continuously change, the whole

Table 4-2 Specification of the used tools in UPCT tests

Specification	Tool #1	Tool #2	Tool #3
Nose radius R [mm]	0.2	0.05	0.01
Rake angle α [°]	−20	0	0
Open angle [°]	90	40	40
Orientation of rake face	(100)	(100)	(100)

Table 4-3 Variation of process parameter of the UPCT tests

Parameter	Value
Cutting speed V_f [m/min]	0.94, 2.20, 3.14, 4.71
Rotational speed T [min⁻¹]	300, 700, 1000, 1500
Feed per revolution f [μm/rev]	0.1, 0.3, 0.7, 1, 3, 5, 7
Depth of cut a_p [nm]	50
Orientation of end face of workpiece	(100), (110), (111)
Lubricant	Water-soluble oil (diluted by 1:100 ratio)

Fig. 4-21 Crystallographic diagrams of the observation points which are viewed from the end face (a) (100), (b) (110), and (c) (111) planes.

cylindrical surface is necessary to be investigated. The entire surface is divided into 24 points (Fig. 4-20), and the surface morphologies and surface roughness S_a at each point were observed by optical microscope (VHX-600 and VHX-5000, KEYENCE) and the WLI. Each observation point is named with the order of English alphabet (Fig. 4-21), and the observation point (a) is determined as 0 ° (starting point). For each end face, the observation point (a) is identified by [010] for (100), [1$\bar{1}$1] for (110), and [01$\bar{1}$] for (111) (see Fig. 4-21). Since the machined surface is characterized by some symmetry based on the crystal structure, the representative observation points for evaluation of surface morphologies are limited depending on the crystal orientation of the end face. For example, six observation points are set in the case of (100) plane (Fig. 4-21 (a)).

4.2.2   Evaluation of surface morphology and surface roughness

Process parameter

For each test, crystal orientation of the end face of CaF₂ are set to (100), respectively. The surface roughness S_a values at 24 measured points was averaged. Variation of surface roughness S_a depending on rotational speed T and feed per revolution f is shown in Fig. 4-22 and Fig. 4-23, respectively. Analogous to the results of plunge-cut tests in section 4.1.2, the surface roughness was not affected by rotational speed (cutting speed). The maximal rotational speed of work spindle is 1500 min⁻¹ and rather the diameter of the cavity does not exceed over 1 mm, therefore, it means little to deeply investigate the influence of cutting speed in this study. Determining that 1000 min⁻¹

Workpiece:
Material: CaF₂
Orientation of end face: (100)

Cutting tool:
Type: SCD
Rake angle α [°]: -20
Nose radius R [mm]: 0.2

Process parameter:
Rotational speed T [min⁻¹]: Variable
Feed per revolution f [μm/rev]: 1.0
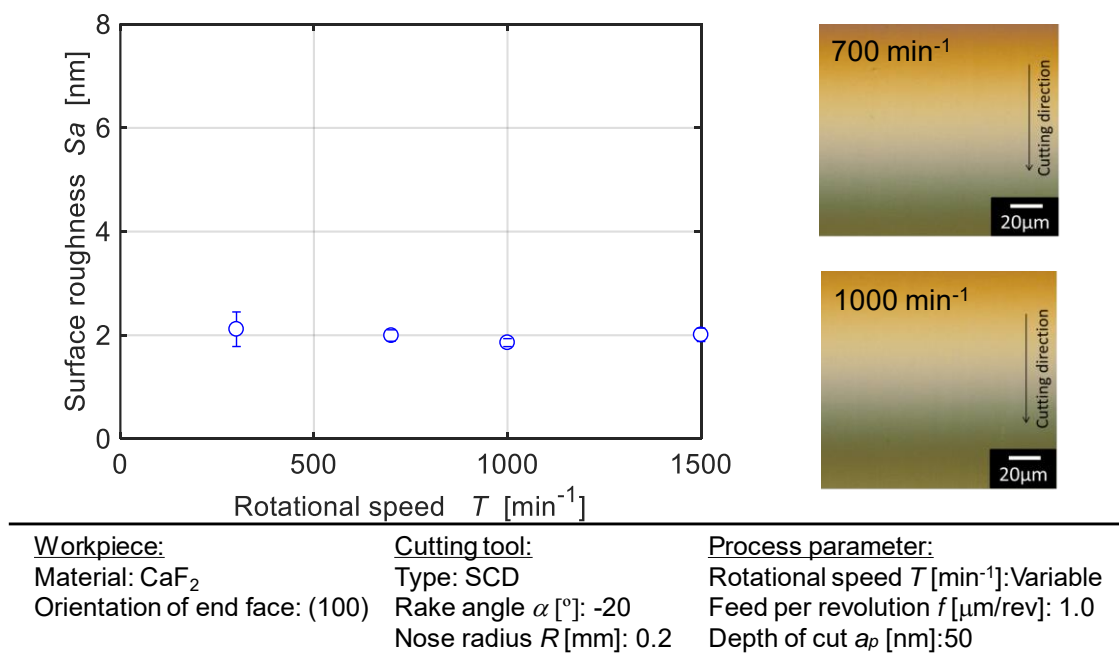Depth of cut a_p [nm]: 50

Fig. 4-22 Variation of surface roughness S_a in accordance with rotational speed T

rotational speed T is optimal in this test, the following tests were performed. Compared to the cutting speed, a feed per revolution affects the surface quality more. Although the surface is smooth in low feed regime (f = 0.1 − 0.7 μm/rev), the brittle fracture begins to exhibit over 1.0 μm/rev feed per revolution (see Fig. 4-23) and the S_a value increases. In turning, the critical uncut chip thickness can be determined by combination of DOC and feed per revolution [1, 162]. Even if the DOC is smaller than the CDC value, the feed per tooth is too large, cutting mode turns to be brittle-regime. The maximal uncut chip thickness d_{max} is given as follows [163]:

$$d_{max} = R - \sqrt{R^2 + f^2 - 2f\sqrt{2Ra_p - a_p^2}} \qquad (4\text{-}2)$$

For 1 μm/rev feed per revolution f, the d_{max} can be calculated as around 20 nm. This value is much lower than the minimal value (approximately 50 nm) of the CDC in the plunge-cut tests. One of the reasons might be a shape of workpiece. Since the size of workpiece is very small (cylinder of 1 mm diameter and 1 − 2 mm length), the dynamic stiffness decreases compared to conventional substrate or wafer. Therefore, the cutting process can be much more unstable by the thrust force between tool and workpiece compared to face turning or plunge-cut. This also leads that a deflection in a radial direction easily occurs. In addition, the surface quality can be influenced by edge geometry i.e. size effect. It is assumed that the plowing could be conducted, however, the surface quality is enhanced in a low feed regime. Thus, the cutting edge is assumed to be extremely sharp e.g. less than 10 nm as shown by Sumiya [105]. Though it is difficult

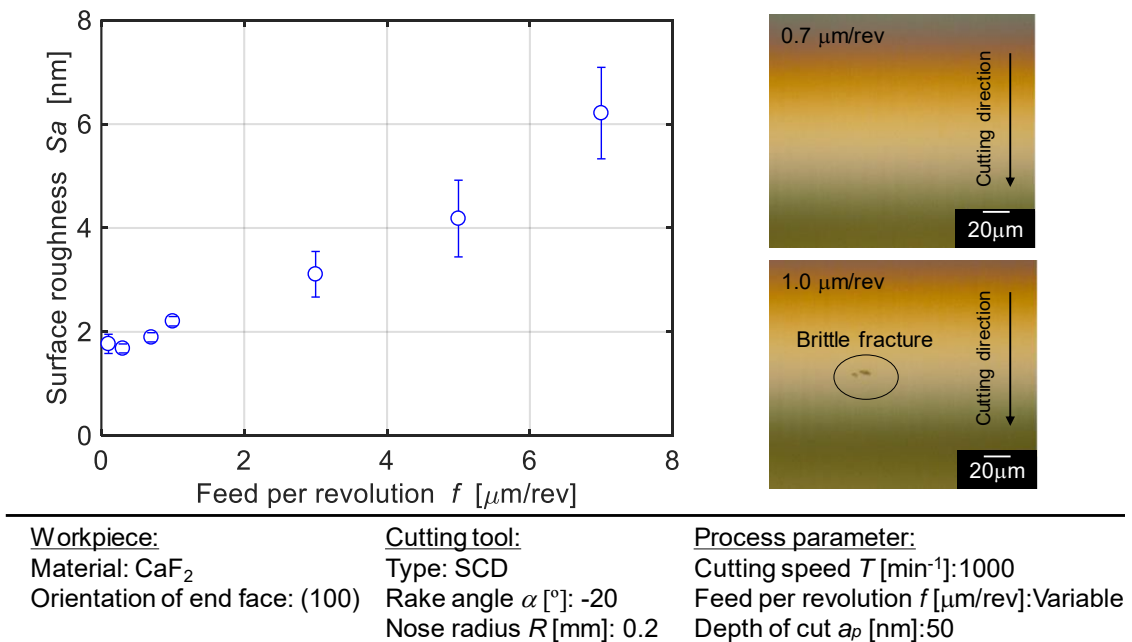| Workpiece:	Cutting tool:	Process parameter:
Material: CaF₂	Type: SCD	Cutting speed T [min⁻¹]:1000
Orientation of end face: (100)	Rake angle α [°]: -20	Feed per revolution f [μm/rev]:Variable
	Nose radius R [mm]: 0.2	Depth of cut a_p [nm]:50

Fig. 4-23 Variation of surface roughness S_a in accordance with feed per revolution f

to identify the causes for the mismatch of the results between the plunge-cut tests and UPCT tests ($0.1 \leq 0.7$ μm/rev), one could find some optimal cutting condition to achieve a crack-free surface.

Crystal anisotropy

As described in section 4.1, the machined surface strongly relates to cutting crystalline planes and directions. Similar tendency was seen in the case of UPCT. The S_a values and surface morphologies are characterized by three-fold symmetry when the end face is set as (111), as shown in Fig. 4-24 and Fig. 4-25. The plastic deformation parameter P and cleavage fracture parameter C could not be calculated in the case of the UPCT because the process force was not measured by a dynamometer due to the experimental setup. However, the anisotropic deformation behavior can be still discussed in a qualitative manner. For example, the surface morphologies at observation points (a) and (e) are smooth, whose crystalline plane and cutting directions correspond to (110) planes and 90 ° directions in the plunge-cut tests where the P parameter and CDC value
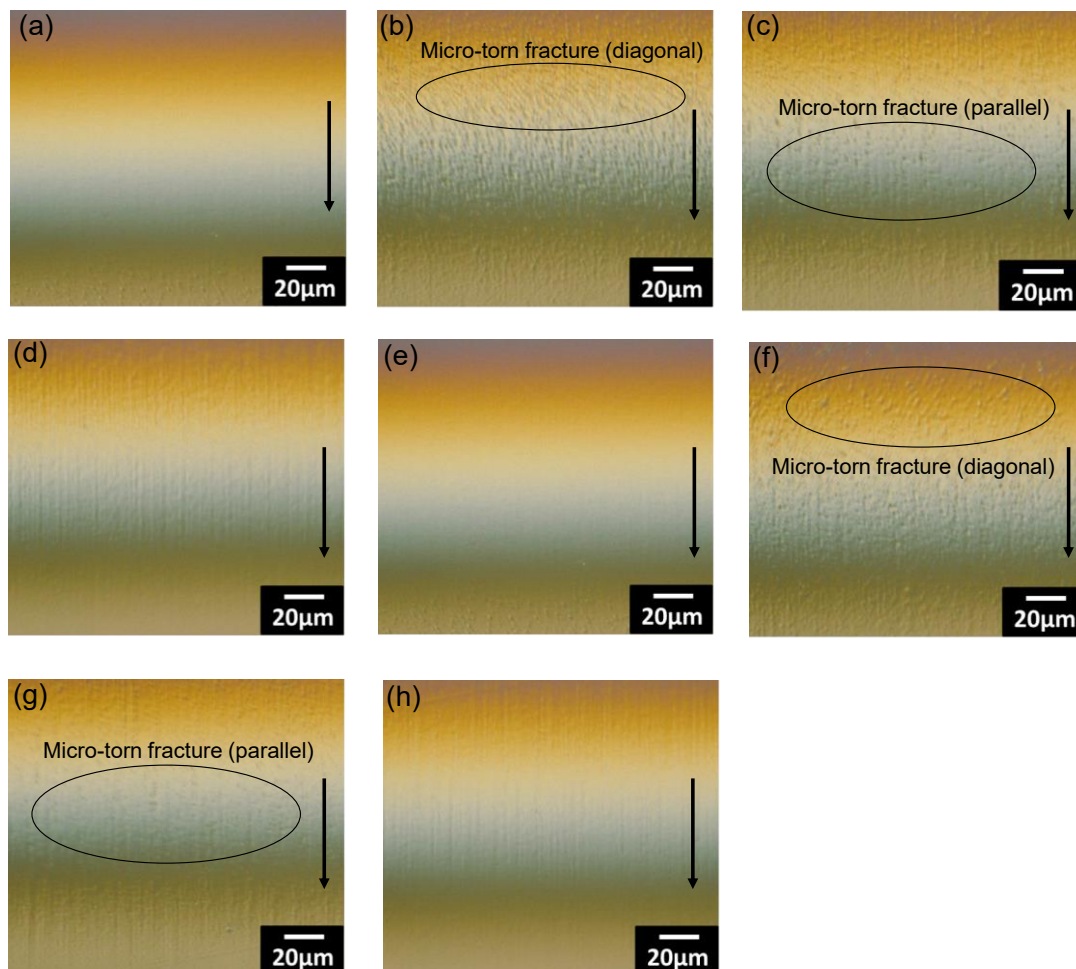
Fig. 4-24 Surface morphologies of the machined cylindrical surface with end face (111). (Each point corresponds to the observation points of Fig. 4-21 (c). A black arrow indicates a cutting direction.)

were high. When cutting at observation points (b) − (d) and (f) − (g), some cracks appear along some specific directions e.g. the microtorn fracture runs along the cleavage planes as shown in Fig. 4-24 and Fig. 4-26. The torn fracture is similar to the type I fracture that was observed in plunge-cut of (111) plane (Fig. 4-14 and Fig. 4-15). Considering the results of the plunge-cut tests, it is anticipated that the plastic deformation parameter P at these observation points is relatively lower than that at (a) or (e).

Strong dependency on the crystal anisotropy was seen in the case of end face (110) plane (see Fig. 4-27 and Fig. 4-28). The surface morphologies and CDC values exhibit two-fold symmetry i.e. the symmetric cycle appears at every 180 °. Analogous to the case of (111) end face, the qualitative discussion can be done. Although the cutting
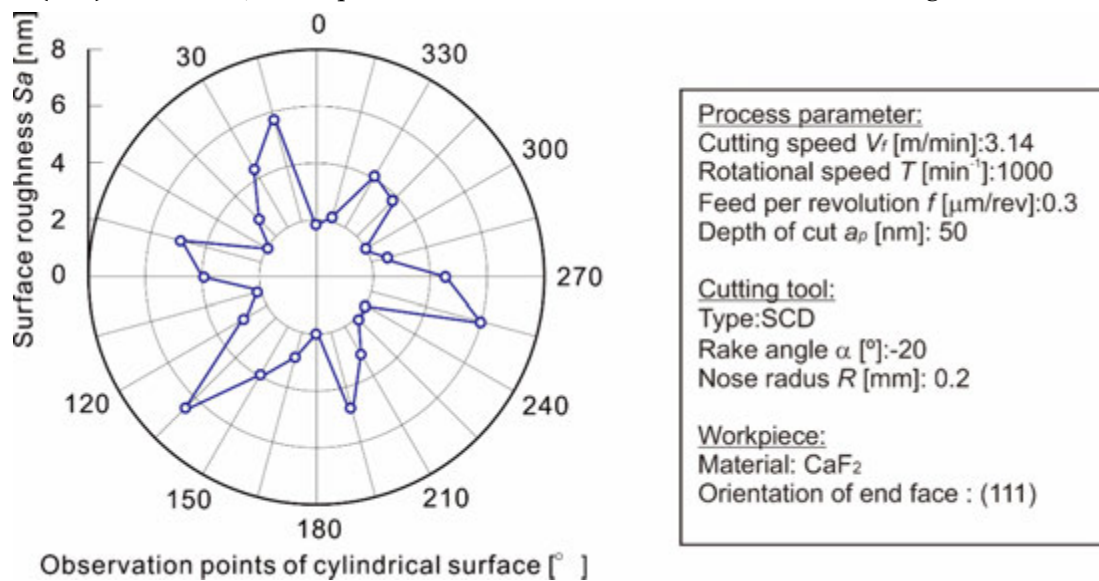
Fig. 4-25 Variation of surface roughness S_a in accordance with crystal anisotropy ((111) end face)
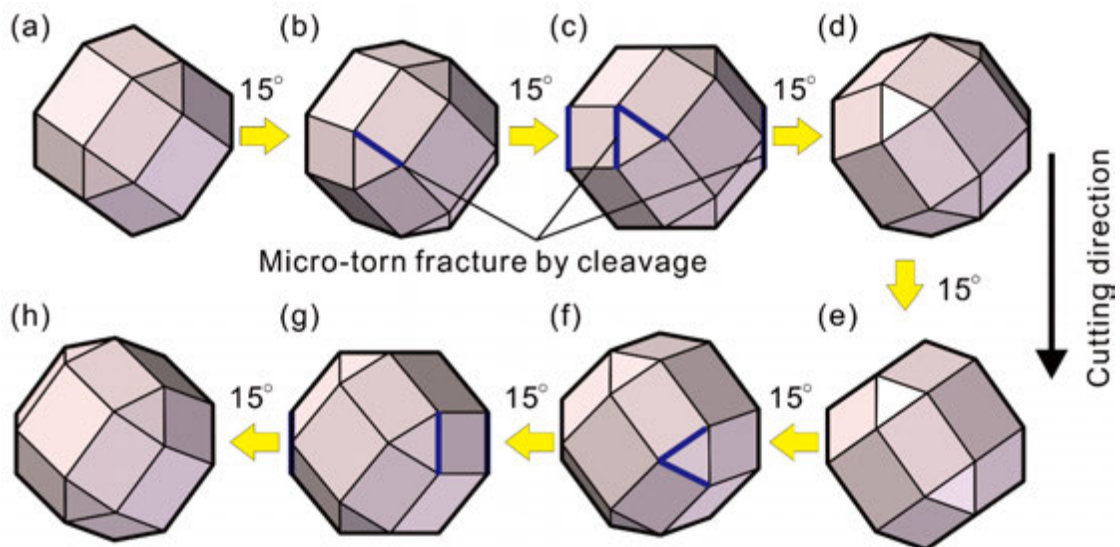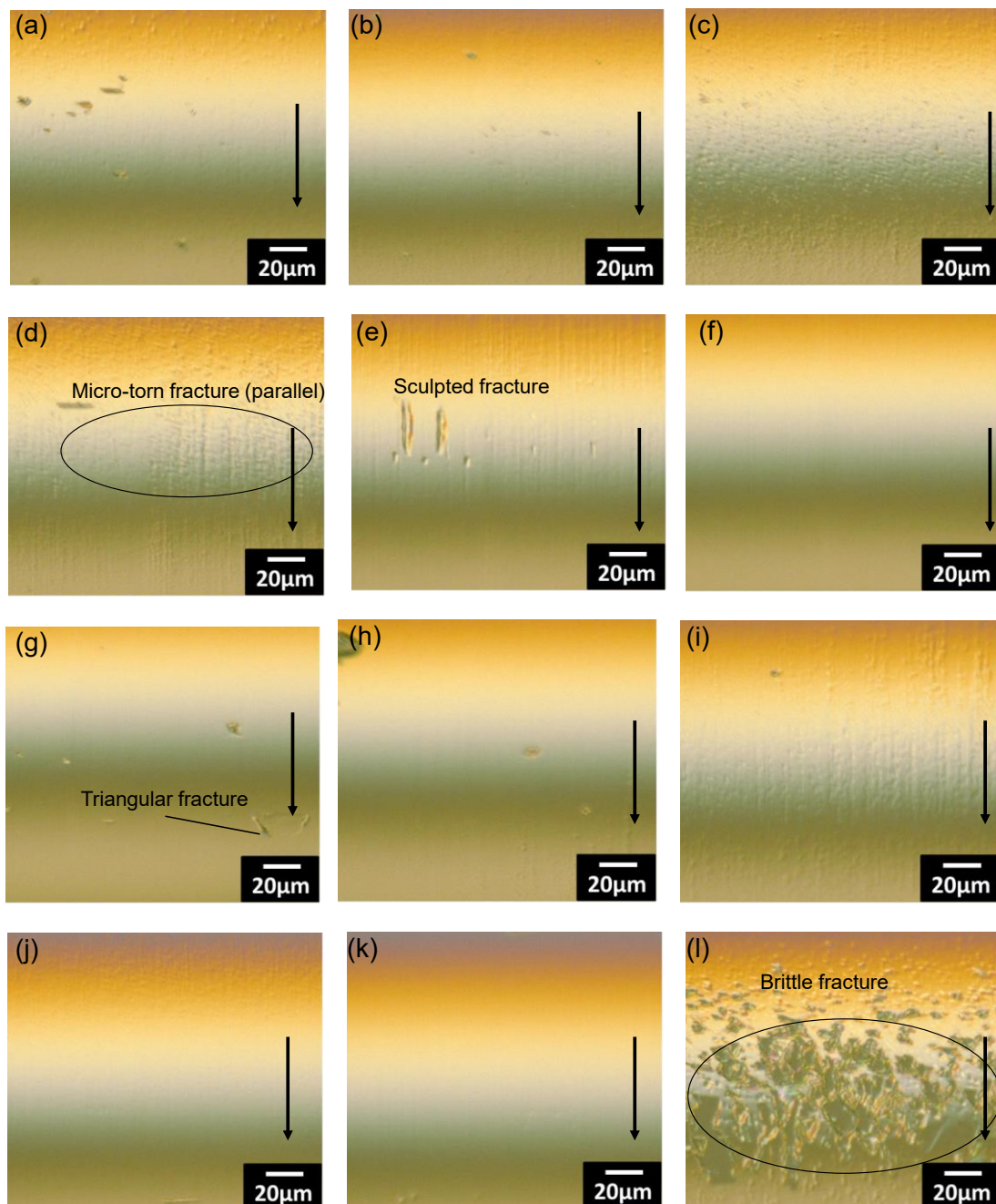

Fig. 4-26 Variation of geometrical relation of crystal model with end face (111) (Each point corresponds to the observation points of Fig. 4-21 (c))

crystalline plane is the same at observation points (a) and (f), the machined surface is rough at (a), whereas the smooth surface was obtained at (f). When referring the plunge-cut test on (111), the cutting direction at (a) corresponds to 270 ° directions where the CDC value and P parameter value were low. On the other hand, the CDC value and P parameter values are high in the direction of 90 ° i.e. at (e). The microtorn fracture which runs parallel to the cutting direction at observation point (d) and the sculpted fracture at observation point (e) were seen, both of which are assumed to be induced by {110} cleavages (see Fig. 4-29).

Fig. 4-27 Surface morphologies of the machined cylindrical surface with end face (110). (Each point corresponds to the observation points of Fig. 4-21 (b). A black arrow indicates a cutting direction.)

The pyramidal fracture was seen at observation point (g) which is well known fracture induced by {111} cleavage. The surface quality at observation points (h) − (k) is apt to be smooth. Considering the crystallographic diagrams at (i), (j), the cutting crystalline
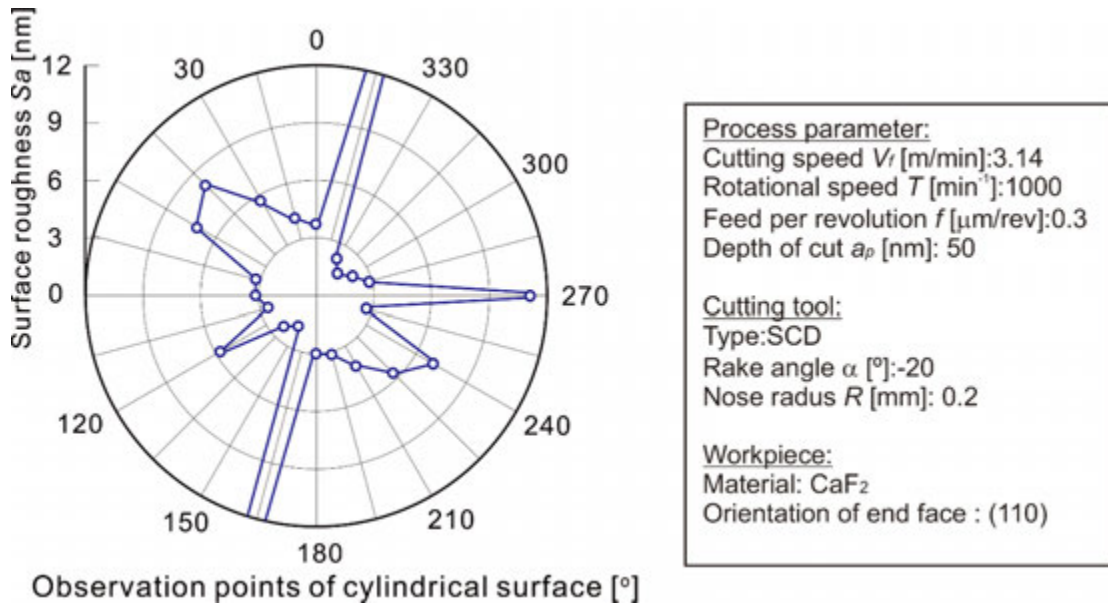

Fig. 4-28 Variation of surface roughness S_a in accordance with crystal anisotropy ((110) end face)
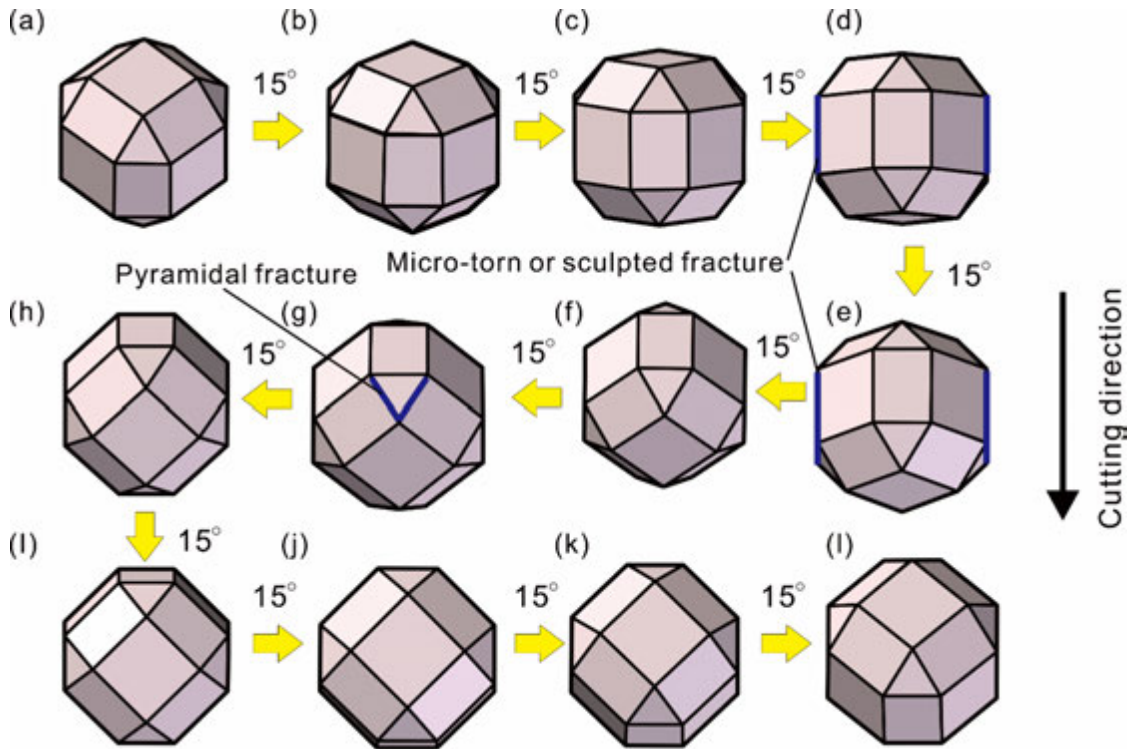

Fig. 4-29   Variation of geometrical relation of crystal model with end face (110) (Each point corresponds to the observation points of Fig. 4-21 (b))
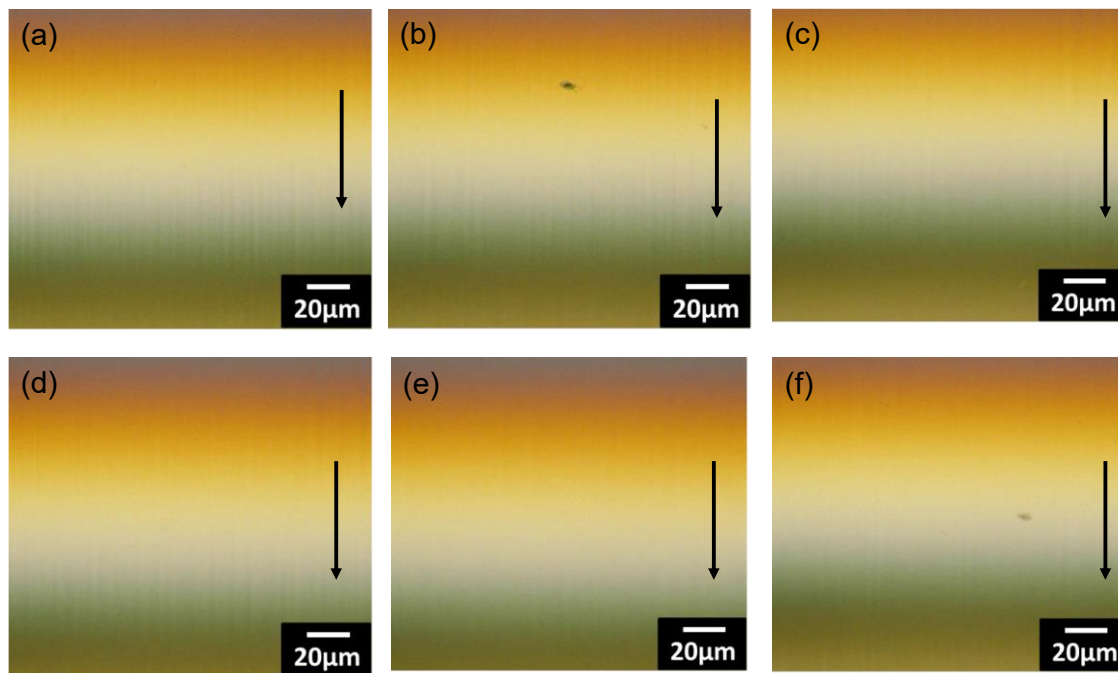
Fig. 4-30   Surface morphologies of the machined cylindrical surface with end face (100). (Each point corresponds to the observation points of Fig. 4-21 (a). A black arrow indicates a cutting direction.)
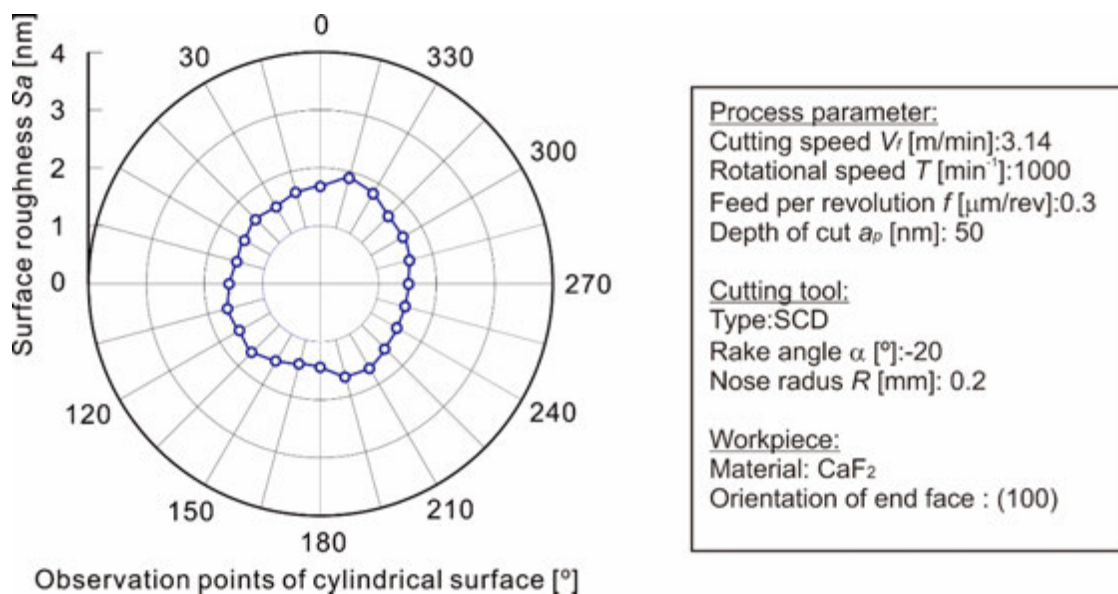

Fig. 4-31 Variation of surface roughness S_a in accordance with crystal anisotropy ((100) end face)

plane and cutting directions relatively correspond to (100) plane and [011] directions.

The CDC value and P value were high in the case of (100) plane and 0 °, 90 °, 180 °, and 270 ° cutting directions, thus, in the vicinity of the cutting (100) plane and [011] directions, the ductility is high, and the corresponding machined surface can be smoother. It should be mentioned that the surface morphology at (i) is slightly worse near the (100)

plane and [011] cutting direction. That can be a remaining crack originated from crack formation in rough cutting or some cleavage phenomena, however, the reason was unclear from the observation. A triangular crack was observed in the images of point (g). The triangular crack was well reported by other works [76, 86], and corresponds to the {111} cleavage families. It is evident that the brittle fracture dominates the machine surface at (l). Considering the previous results of plunge-cut and UPCT, P values can be extremely low at this point, and the brittle fracture which takes places in rough cutting process can remain even in the ductile-regime cutting.

On the contrary to the results of end faces (111) and (110), homogeneous surface was obtained at the entire observation points in the case of (100), although four-fold symmetry was expected, considering the crystal symmetry (Fig. 4-21(a)). At the entire cylindrical surface, the surface roughness S_a was below 1.7 nm, and few visible brittle fracture was observed (Fig. 4-30 and Fig. 4-31). The P value at (a) corresponds to the case of plunge-cut of (100) plane at 45 ° directions, and is low, however, the obtained surface is very smooth. The machined surface at (d) in Fig. 4-32 could be deteriorated, since the point corresponds to the results of plunge-cut tests of (110) plane at 150° directions where the CDC and P values were quite low (Fig. 4-9, Fig. 4-10, and Fig. 4-12). In the UPCT, a cutting model is different because feed force also acts, therefore, the applied force vector can be also different from plunge-cut process. It is assumed that the force vector can act on the directions which always activate the slip systems well or prohibit cleavage. Although the questions about the obtained surface quality still remain, it is concluded that the cylindrical surface with the end face of (100) plane is most suitable. It should be remarked that the surface quality sometimes changes even if the cutting condition is the same. One problem was found that a chatter-like vibration was
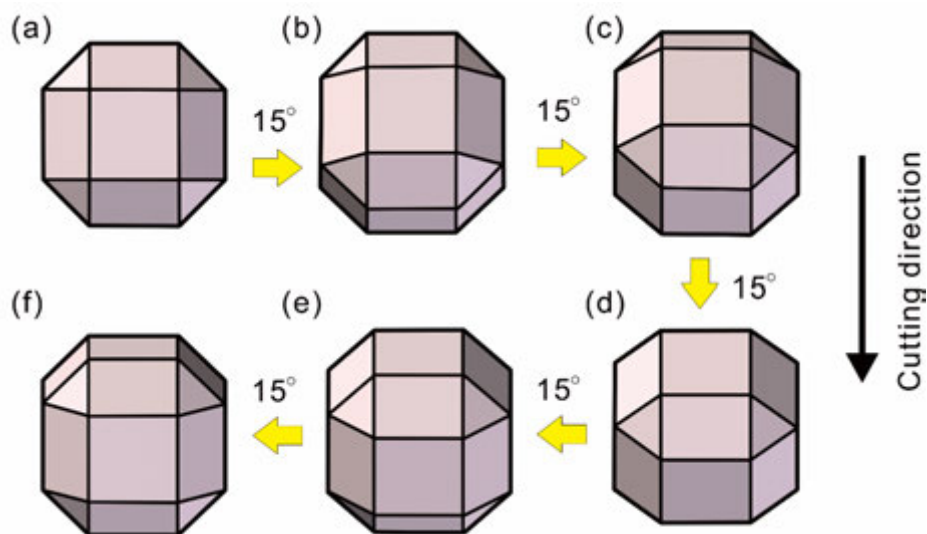

Fig. 4-32 Variation of geometrical relation of crystal model with end face (100). (Each point corresponds to the observation points of Fig. 4-21 (a))

observed as shown in Fig. 4-33. The chatter frequency was calculated by Eq.(4-3):

$$f_{chatter} = \frac{V_f}{60} / \frac{L_{chatter}}{n_{chatter}} \qquad (4\text{-}3)$$

From the equation, the chatter frequency $f_{chatter}$ is calculated as 4.85 kHz. Since the diameter of workpiece is quite small and the acting force can fluctuate due to the crystal anisotropy [77], the cutting process can be unstable. To suppress the instability, the thrust force should be reduced. The thrust force can be reduced using a smaller nose radius as reported by Nath [159]. In addition, the negative rake angle is favorable for ductile cutting, however, rather the negative rake causes the increase of thrust force [164]. Therefore, the tool geometry also has to be considered.
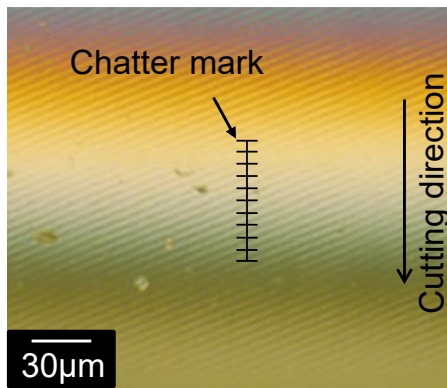

Fig. 4-33   Deterioration of the machined surface caused by chatter vibration [165] (Kakinuma Y, Azami S, Tanabe T. CIRP Ann-Manuf Techn 2015;64(1):117-20. Reprinted with permission from Elsevier B.V..).
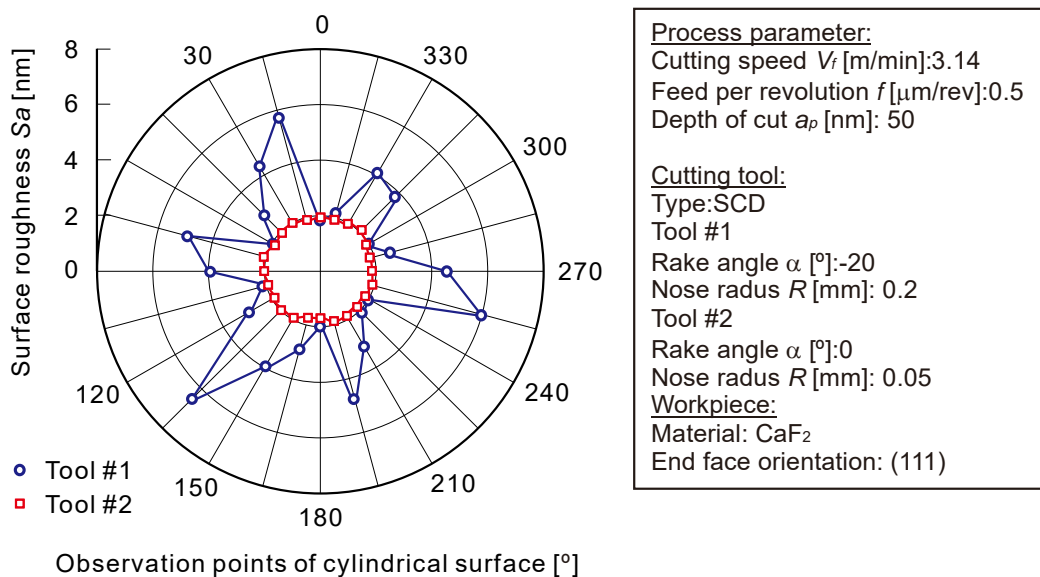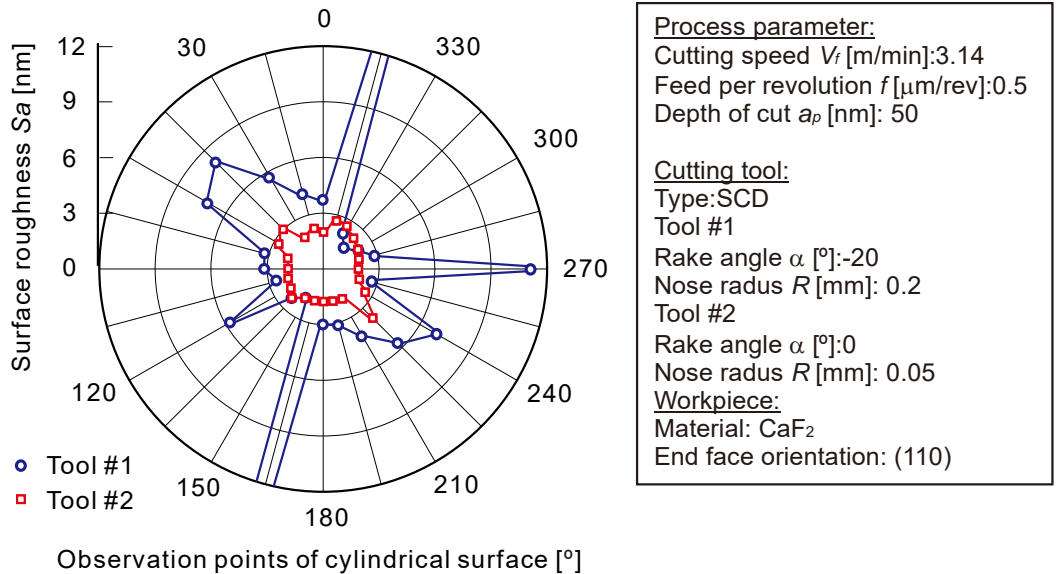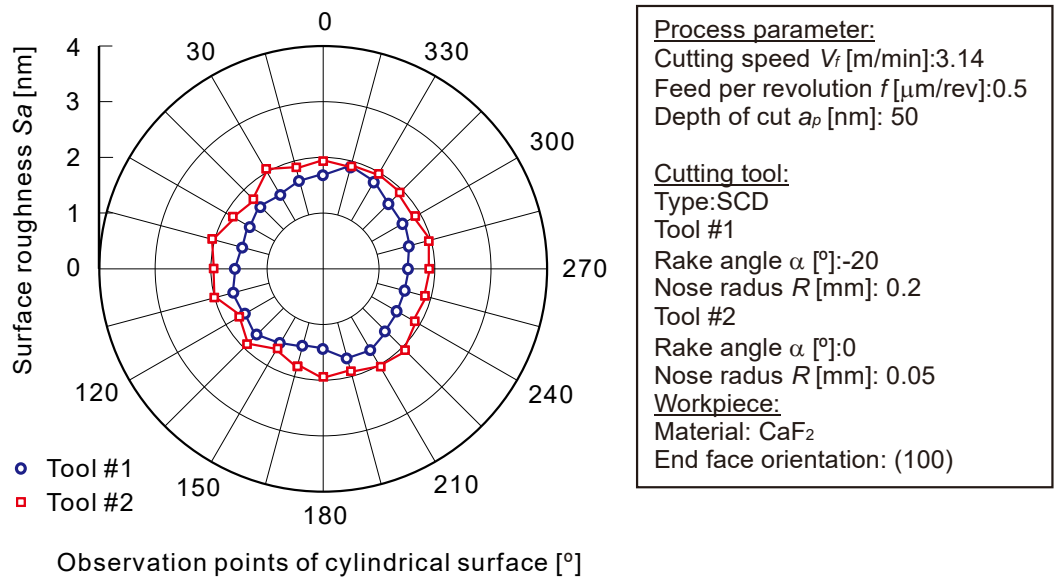

Fig. 4-34   Influence of tool geometry on surface roughness of CaF₂ cylinder with end face (111). [165] ((Kakinuma Y, Azami S, Tanabe T. CIRP Ann-Manuf Techn 2015;64(1):117-20. Reprinted with permission from Elsevier B.V..))

Fig. 4-35 Influence of tool geometry on surface roughness of CaF₂ cylinder with end face (110).[165](Kakinuma Y, Azami S, Tanabe T. CIRP Ann-Manuf Techn 2015;64(1):117-20. Reprinted with permission from Elsevier B.V..)

Fig. 4-36 Influence of tool geometry on surface roughness of CaF₂ cylinder with end face (100).[165](Kakinuma Y, Azami S, Tanabe T. CIRP Ann-Manuf Techn 2015;64(1):117-20. Reprinted with permission from Elsevier B.V..)

Tool geometry

To reduce the thrust force, a smaller nose radius tool (0.05 mm nose radius and 0 ° rake angle) is introduced (see the specification of tool #2 in Table 4-2). The Sa values were investigated on each CaF₂ with end faces (100), (110), and (111). For all crystalline planes, a homogenous surface was obtained, and fluctuated surface induced by chatter vibration was not seen (Fig. 4-34, Fig. 4-35, and Fig. 4-36). One of the reasons can be the rake angle i.e. the thrust force was reduced by the use of 0 ° rake angle tool.

69

Normally, the negative rake angle enhances the ductility of brittle materials because of the induced hydrostatic pressure formed by compressive stress region. Rather, the reduction of the compressive stress region can lead to reduce the thrust force which causes the instability of UPCT process. A nose radius could also contribute to the stabilization of the UPCT process. When changing the nose radius, the contact area between the tool and workpiece also changes. The contact length l can be calculated from the geometrical relationship shown in Fig. 4-37:

$$l = R\left(\pi - \cos^{-1}\left(\frac{f}{2R}\right) - \sin^{-1}\left(\frac{R - {a_p}/{\cos\alpha}}{R}\right)\right) \tag{4-4}$$

The tool contact lengths were calculated as 4.8 μm and 2.5 μm for tools #1 and #2, respectively. Although the difference is a micrometric scale, this can be crucial for the UPCT of the small workpiece. In UPCT, the material flow is related to the contact area of the tool (process force) because plastic flow area is assumed to be relatively small.

Overall, the surface quality strongly depends on the selection of an appropriate tool and crystal orientation. Although the surface quality was investigated, the SSD is also very essential for the optical devices. The process parameter and crystal anisotropy can affect the SSD formation. The subsurface quality will be investigated.
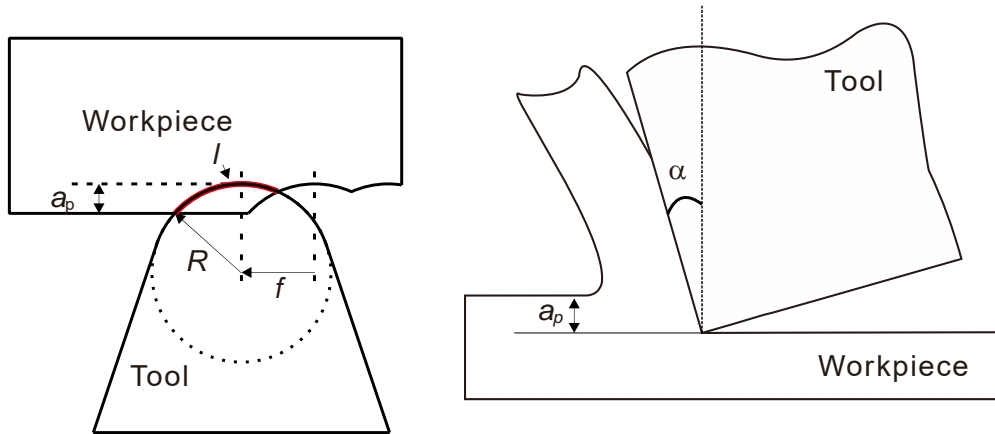

Fig. 4-37   Characterization of tool contact length in cylindrical turning

Table 4-4 Specification of the used tools in comparison of tool type

Specification	Tool #4	Tool #5
Nose radius R [mm]	0.2	0.2
Rake angle α [°]	0	0
Open angle [°]	90	90
Tool type	SCD	B-NPD
Orientation of rake face	(100)	–

Tool type

Since the cylindrical turning process is a continuous cutting (not intermittent), the surface integrity can be also influenced by frictional effect. SCD is much harder than CaF$_2$, thus, hardness of the tool type will not significantly affect the surface integrity, for example, PCD or NPD tools. However, in the case of ceramics, the friction coefficient at the interface can affect the surface quality. The ceramics cutting partially includes the friction between the flank face of the tool and finished surface (friction between insulators), hence, the friction coefficient of each materials cannot be ignored because a triboplasma can take place due to the stored electrons between the tool and workpiece [166]. Focusing on the electrical property of the tool, the B-NPD tool is used to investigate the influence of friction on surface integrity. The specification of the used tools is listed in Table 4-4. For the observation points, (100) plane was selected, which corresponds to point (a) in Fig. 4-21.

For both surfaces machined by SCD and B-NPD tools, there was no major difference regarding the surface morphologies and surface roughness S_a under wet and dry conditions (Fig. 4-38). It was assumed that the surface can be affected by triboplasma phenomena especially under dry condition such as in the case of BK7 glasses [110] or polymer [73]. Since the process force is assumed to be lower compared to other process such as sliding or turning of polymer, the machined surface was not affected by electrical phenomena.
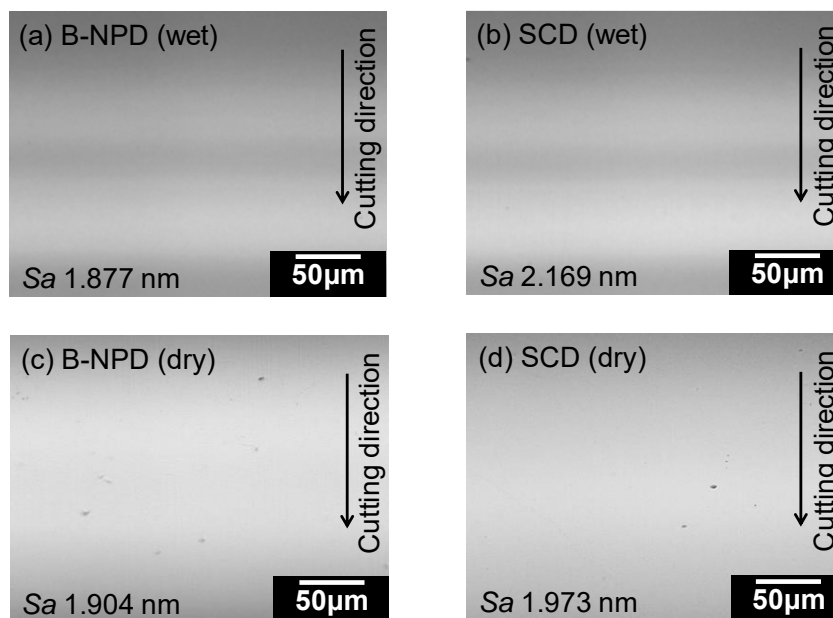
Workpiece:	Cutting tool:	Process parameter:
Material: CaF$_2$	Type: SCD, B-NPD	Cutting speed V_f [m/min]:3.14
Orientation of end face: (100)	Rake angle α [°]: 0	Feed per revolution f [μm/rev]: 0.5
Cutting plane: (010)	Nose radius R [mm]: 0.2	Depth of cut a_p [nm]:50

Fig. 4-38 Image of surface and corresponding surface roughness S_a machined by (a) B-NPD (b) SCD under wet condition and (c) B-NPD (d) SCD under dry condition

Overall, the surface quality strongly depends on the selection of the tool geometry and crystal orientation. Although the surface quality was investigated, the SSD is also very essential for the optical devices. The process parameter and crystal anisotropy can affect the SSD formation. In addition, the triboplasma phenomena induced by friction can also cause the subsurface quality because the friction coefficient is strongly related to the subsurface stress [167]. In the next section, the subsurface integrity will be also investigated in terms of the tool type.

4.2.3 Evaluation of subsurface damage

As described in section 2.2.3, the SSD has been widely studied in manufacturing, material science, and optics fields [91, 92]. The SSD can be induced by various mechanisms, and the subsurface crystalline structure is changed by crystal shear and rotation (Fig. 4-39 (a)) [168]. The valid measurement methods (e.g. XRD (X-Ray Diffraction), EBSD (Electron BackScatter Diffraction), Raman spectroscopy, TEM, releasing residual stress by etching) are selected depending on a material, size of specimen, or purpose. In this dissertation, TEM is chosen to elucidate the variation of crystalline lattice arrangement induced by ultra-precision cutting process. A field emission TEM (FE-TEM, TECNAI TM G2 F20 S-Twin) was used. Before the measurement, FIB was hired to slice the TEM specimen to around 50nm (Quanta 200 3 Di). The SSD of the cylindrical surface was viewed from the end face as shown in Fig. 4-39 (b). The obtained TEM images were rotated to adjust the cutting plane to the horizontal direction.
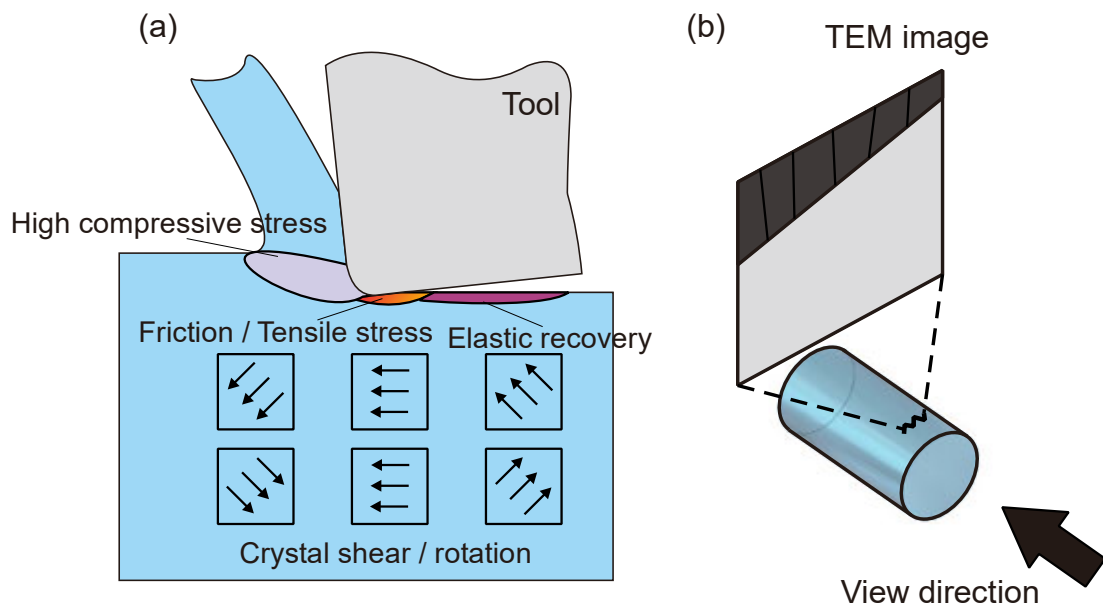

Fig. 4-39　Schematic illustration of the related mechanisms to SSD and its observation. (a) Plausible material flow under cutting process [65, 168]. (b) TEM observation of SSD on cylindrical surface.

Process parameter

Following the previous results, influence of process parameters (DOC and tool geometry) on SSD was investigated. For TEM observation, the cylindrical surface with end face (100) was selected. Firstly, the influence of tool geometry on SSD was investigated and compared (Fig. 4-40). The machined surface at an observation point (a) with (100) end face (see Fig. 4-21 (a)) was chosen for the investigation of influence of process parameters. To focus on the nose radius, the tools #2, #3, and #4 were used and compared. To evaluate the SSD under the same surface roughness, the feed per revolution f was determined as 0.1 μm/rev for tool #3 (0.01 mm nose radius). Although the S_a values are similar for each machined surface (approximately S_a 2 nm), the SSD depth tends to decrease in dependency with reduction of nose radius. As discussed in section 4.2.2, nose radius has a great influence on the surface integrity e.g. small nose radius contributes to obtain the smooth and homogeneous surface (Fig. 4-34). It indicates that the tool geometry affects the SSD more than surface roughness because the SSD changes with a few ten nanometric order. A decrease in the contact length between tool and workpiece is assumed to result in reduction of the process force, which influences surface integrity. In addition, plastic flow in severe stress zone is also affected by the tool contact length i.e. nose radius. The tool contact lengths are calculated as 4.8, 2.5, and 1.0 μm for tool #4, tool #2, and tool #3, respectively. Thus, the difference of the tool contact length also contributes to the reduction of the SSD.

Since the DOC determines the surface integrity, the influence of the DOC was also investigated. The tool #2 (0.05 mm nose radius) was used for the tests, and the DOC a_p was set as 20, 50, and 100 nm. It should be noted that smooth surfaces with approximately S_a 2 nm were obtained for each surfaces. It was assumed that the deeper the DOC is, the more the SSD depth increases (Fig. 4-41). The deeper DOC leads to the
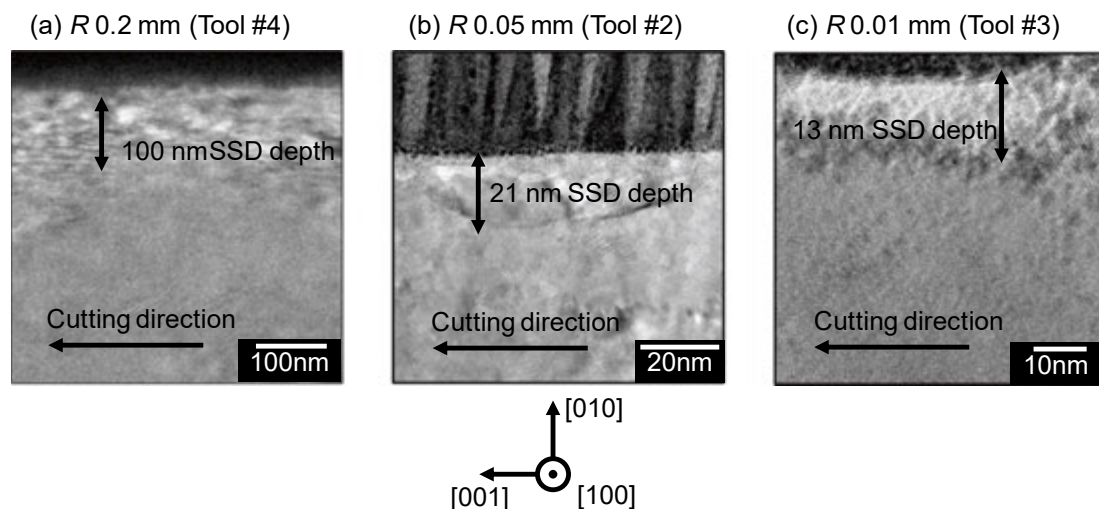

Fig. 4-40　TEM images of machined surface (010) plane machined with the tool of (a) R 0.2 mm (b) R 0.05 mm, and (c) R 0.01 mm.
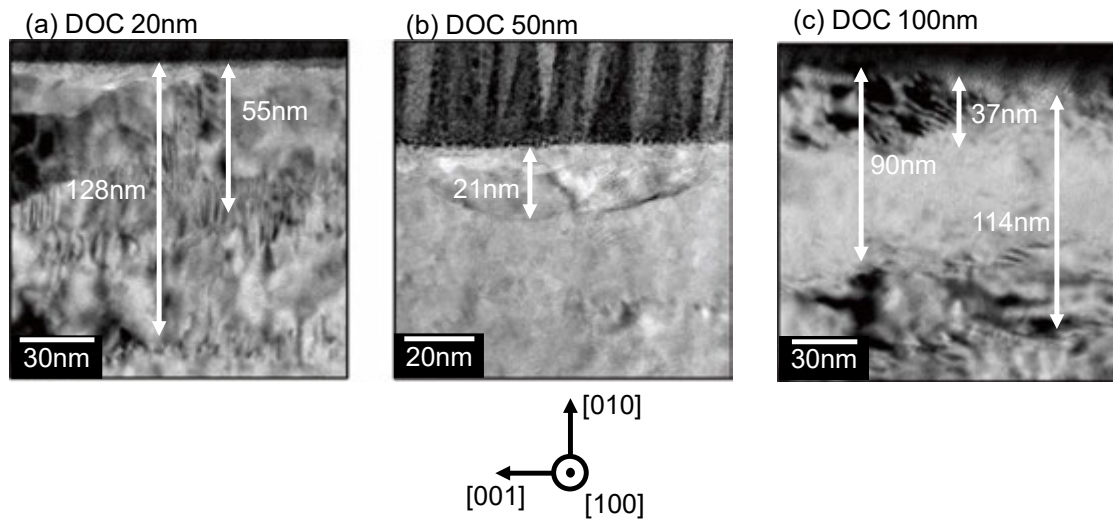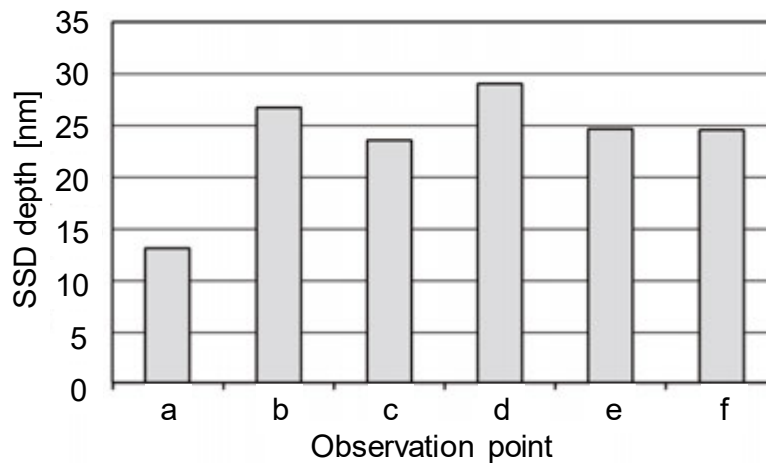
Fig. 4-41　TEM images of machined surface at the cutting direction of [001] with DOC of (a) 20 nm, (b) 50 nm, (c) 100 nm

Workpiece:	Cutting tool:	Process parameter:
Material: CaF$_2$	Rake angle α [°]: 0	Cutting speed V_f [m/min]:3.14
Orientation of end face: (100)	Nose radius R [mm]: 0.01	Feed per revolution f [μm/rev]: 0.1
Cutting direction: Variable		Depth of cut a_p [nm]:50

Fig. 4-42　Variation of SSD depth in dependency with observation points (crystal anisotropy)

increase of cutting volume and plastic deformation zone, therefore, the subsurface layer is more severely affected. Although one boundary line was observed in Fig. 4-41 (b), there are some boundary lines when the DOC is higher in Fig. 4-41 (c), which is assumed to be formed by a larger amount of dislocations compared to small DOC. However, when the DOC was set as 20 nm, the SSD depth was higher compared to the case of 50 nm DOC. The edge radius was estimated as less than 50 nm (Fig. 4-1). Hence, it is anticipated that plowing was performed because of the size effect and the higher compressive stress in front of the cutting tools caused the deeper SSD.
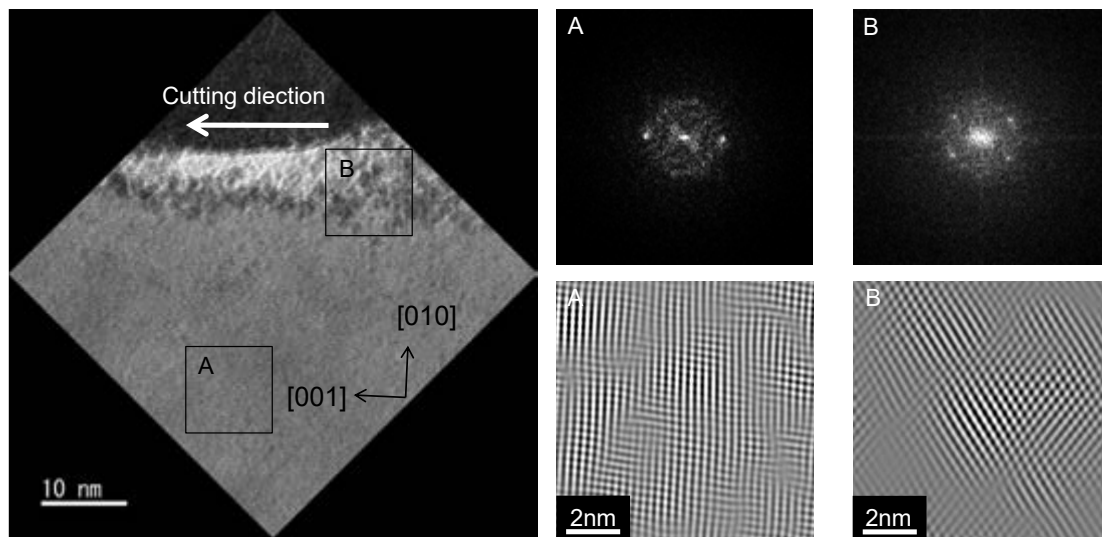
Fig. 4-43 TEM image at point (a) with end face (100). Region A (non-deformed region) and B (deformed region) are analyzed by FFT and IFFT.
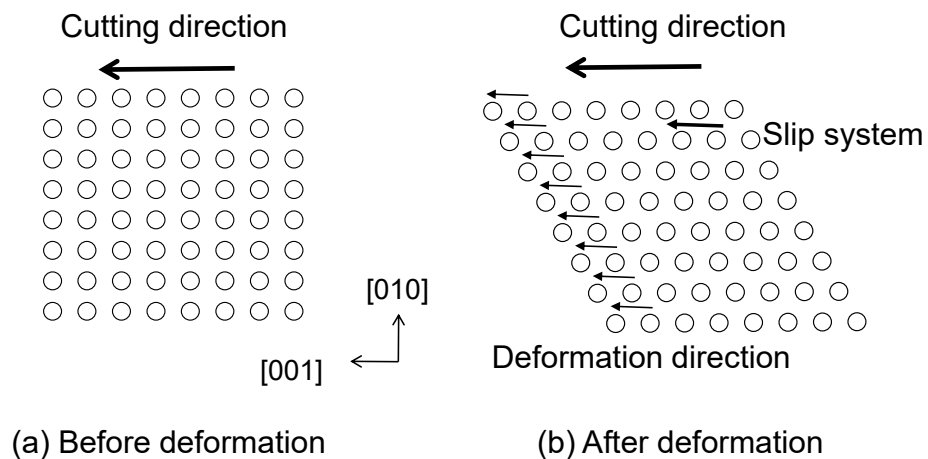

Fig. 4-44 Schematic illustration of the variation of crystalline structure in UPCT at point (a) with end face (100) (a) before deformation and (b) after deformation.

Even if the plowing occurs, the workpiece can be cut because the UPCT process is repeated (i.e. repetition of cutting and plowing), however, the residual compressive stress induced by plowing deteriorates the machinability, thus the SSD depth was higher. It is concluded that the DOC can affect the SSD, and the SSD depth was smallest when the DOC is 50 nm from the experiments.

Crystal anisotropy

Whereas the S_a values are almost the same, the subsurface quality changes according to the process parameter or tool geometry. The idea leads to the influence of crystal anisotropy. For the investigation of anisotropic deformation behavior of the SSD in UPCT, the workpiece with end face (100) was chosen because the surface roughness did not vary
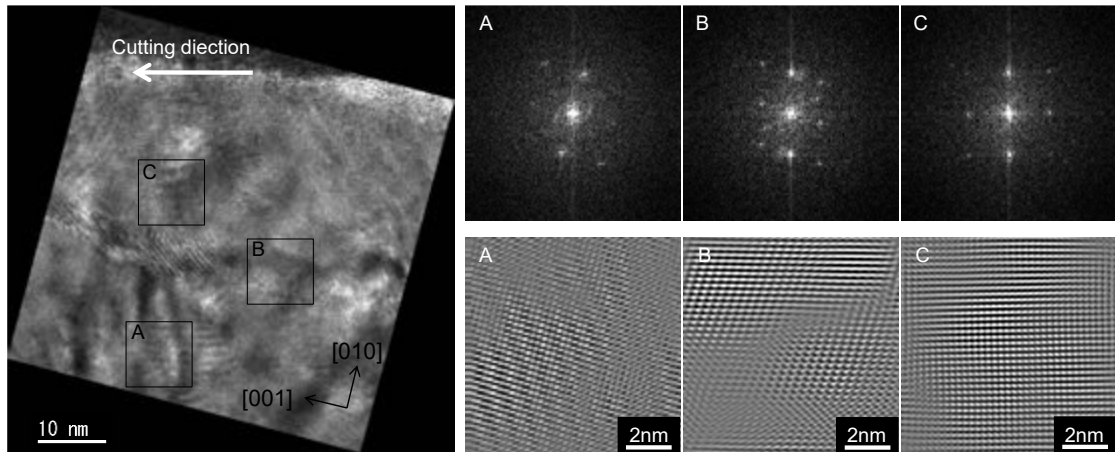
Fig. 4-45 TEM image at point (b) with end face (100). Region A (non-deformed region), B (boundary region), and C (rotational region) are analyzed by FFT and IFFT.

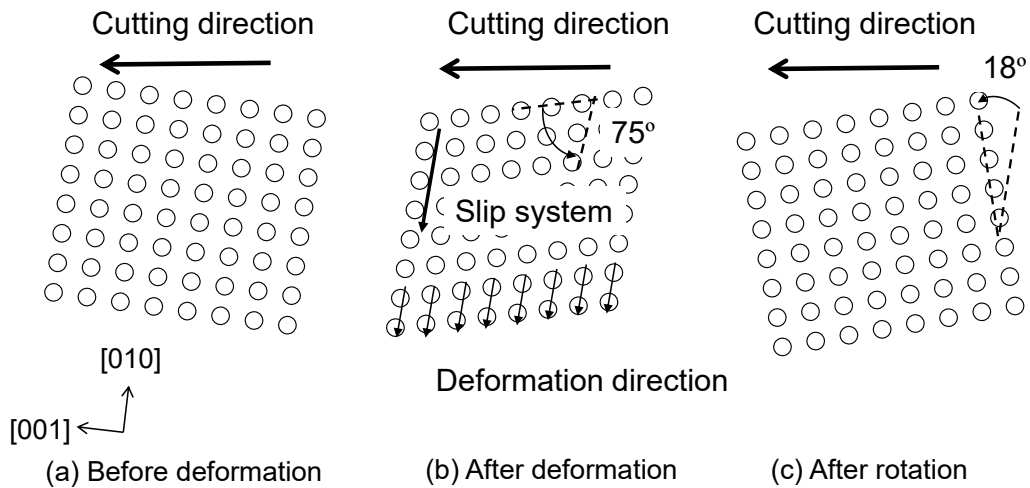(a) Before deformation   (b) After deformation   (c) After rotation

Fig. 4-46 Schematic illustration of the variation of crystalline structure in UPCT at point (b) with end face (100) (a) before deformation, (b) after deformation, and (c) after rotation.

depending on the tool geometry and it is easy to obtain the smooth surface from the experimental results. Considering the symmetry of crystalline structure, six observation points (a) to (f) were investigated (see the corresponding observation points in Fig. 4-21 (a)).

Variation of the SSD depth according to the observation points is shown in Fig. 4-42, and it is obvious that the SSD depth significantly differs. Especially, the SSD depth is the lowest at point (a). In order to analyze the crystalline lattice arrangement, FFT (Fast Fourier Transfer) and IFFT (Inverse Fast Fourier Transfer) analyses were employed to clearly show the crystalline structure in a real space. Since the raw TEM image includes both diffraction spots and appearance of specimen, it is difficult to clearly observe the crystalline lattice arrangement. Once the TEM image was processed by FFT, only diffraction spots were chosen to analyze the crystalline lattice information by IFFT
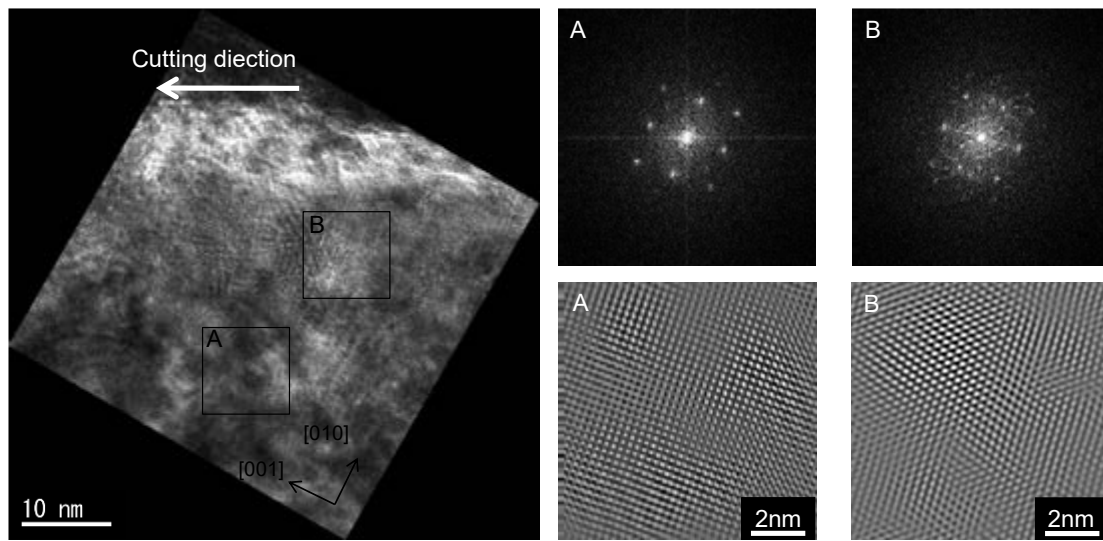
Fig. 4-47   TEM image at point (c) with end face (100). Region A (non-deformed region), B (deformed region) are analyzed by FFT and IFFT.
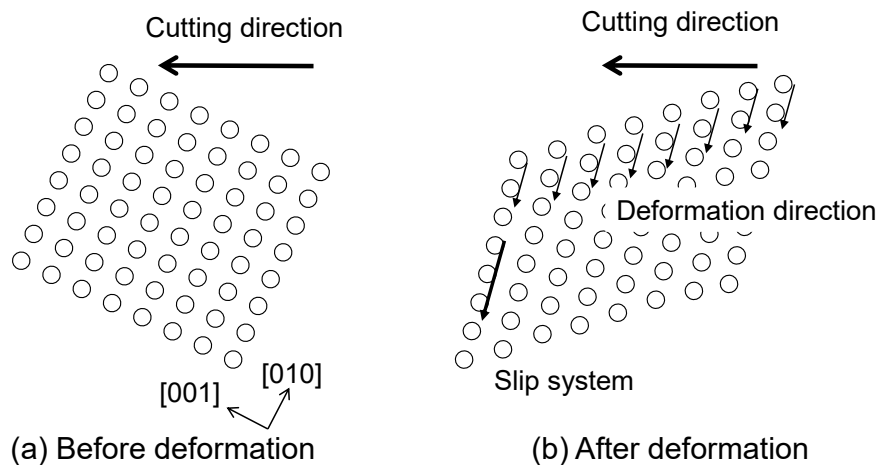

(a) Before deformation   (b) After deformation

Fig. 4-48   Schematic illustration of the variation of crystalline structure in UPCT at point (c) with end face (100) (a) before deformation and (b) after deformation.

processing. The TEM image of SSD at point (a) is shown in Fig. 4-43, closing up of non-deformed layer (Region A) and deformed layer (Region B) through FFT and IFFT analyses. Comparing the FFT and IFFT images, the crystalline lattice changes from a non-deformed layer (Fig. 4-43, Region A) to a deformed layer (Fig. 4-43, Region B). On one hand, it is observed that the crystalline lattice is arranged regularly with its original crystalline structure (the diffraction spots construct the cubic structure i.e. the view from (100) plane). On the other hand, although the crystalline lattice in Region B is also regularly arranged, its arrangement differs from the original crystalline structure. It indicates that the original non-deformed layer is deformed by slip induced by cutting process, which leads to the occurrence of deformed layer (Region B).
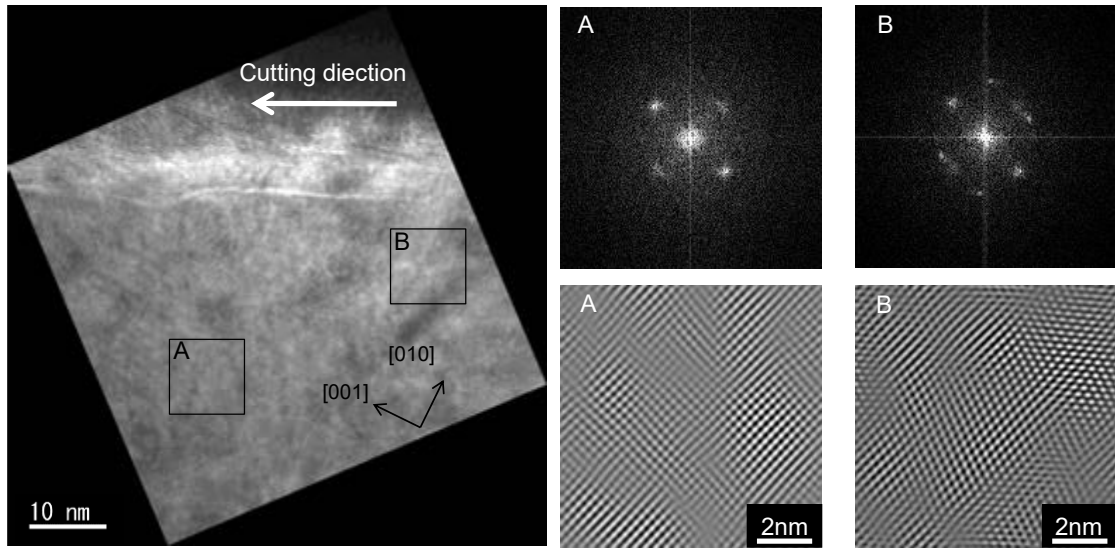
Fig. 4-49 TEM image at point (d). Region A (non-deformed region) and B (deformed region) are analyzed by FFT and IFFT.

(a) Before deformation   (b) After deformation
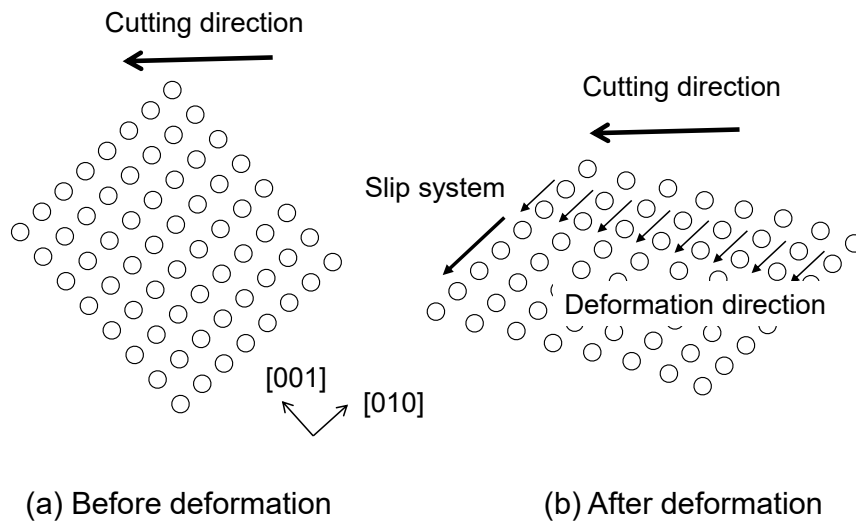
Fig. 4-50 Schematic illustration of the variation of crystalline structure in UPCT at point (d) with end face (100) (a) before deformation and (b) after deformation.

In Fig. 4-44, variation of the crystalline lattice arrangement is illustrated. Since the crystalline lattice arrangement changes from (a) before deformation to (b) after deformation states illustrated in Fig. 4-44, it is anticipated that slip takes place along the slip system $(010)[\bar{1}01]$ and $(010)[101]$, which the slip plane corresponds to the cutting plane. Since the slip direction viewed from (100) plane is identical to the cutting direction, the non-deformed layer is deformed along to the cutting plane.

Fig. 4-45 shows a TEM image of the SSD at point (b). Although the crystalline lattice arrangement changes along the slip direction at the boundary line (Region B), rather crystalline lattice rotates counterclockwise beneath the surface. Since the crystal rotation is induced by slip under tensile loading [144], the crystal shear in Region B can

78
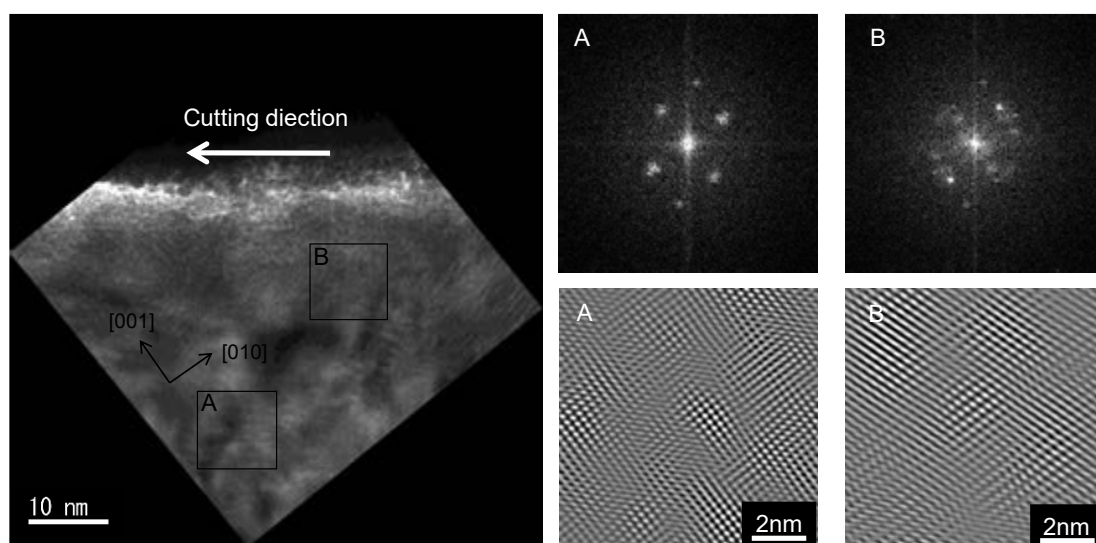
Fig. 4-51　TEM image at point (e). Region A (non-deformed region) and B (deformed region) are analyzed by FFT and IFFT.
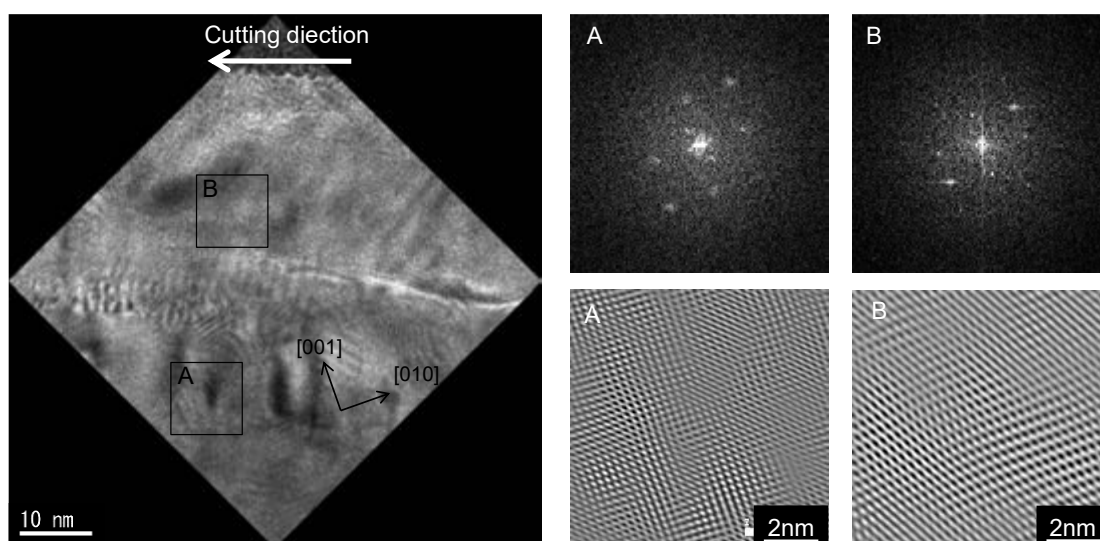
Fig. 4-52　TEM image at point (f). Region A (non-deformed region) and B (deformed region) are analyzed by FFT and IFFT.

be a trigger for the crystalline rotation as shown in Fig. 4-46.

Fig. 4-47 shows a TEM image of the SSD at point (c). The non-deformed layer (Region A) and deformed layers (Region B) are clearly identified from the image. The slip system (010)[1$\bar{1}$0] and (010)[$\bar{1}\bar{1}$0] contribute to the deformation as illustrated in Fig. 4-48. Similar tendency for the SSD formation was seen at point (d) as shown in Fig. 4-49 and Fig. 4-50. Since the same deformation mechanism was observed at point (e) and (f) i.e. the SSD induced by slips were seen along the slip direction, therefore, the detailed schematic illustration was omitted (Fig. 4-51 and Fig. 4-52).

Overall, the SSD depth changes depending on the observation points. In other words,

crystal anisotropy can influence on the SSD formation compared to surface roughness, and the SSD depth was shallow especially at point (a). This is because the cutting crystalline plane (010) is a slip plane, and the slip occurs parallel to the cutting direction. It is considered that the subsurface layer is pulled to the parallel direction by slip, and the SSD depth was shallow. Notably, the discussion in a depth direction in the TEM image is omitted because the FIB is destructive, therefore, it is impossible to see the same specimen from the different view. Additionally, from the front view of TEM image (viewing from the parallel direction to the cutting direction), activation of slip system is hard to identify because all of the slip system exist in a depth direction. For the cylindrical surface machined by tool #2 (0.05 mm nose radius), points (a), (d), and (e) were also observed. The SSD depth in dependency with nose radius are shown in Fig. 4-53. At every observation point the tool #3 reduces the SSD depth. As noted in section 4.2.2, the deviation of the contact area that is determined by tool geometry could contribute to the increments of SSD depth. It is concluded that although the surface roughness value does not vary depending on the tool geometry and crystal anisotropy (limited to the case of end face (100)), the SSD depth significantly changes.

Tool type

As shown in Fig. 4-54, the SSD depth also significantly depends on the tool type. Even though the surface roughness is uniform, the SSD depth changes with different atmosphere and tool type. For both cutting atmosphere, the B-NPD tool reduced the SSD depth compared to the SCD tools. It is clear that the lubrication also affects the SSD depth.

Since the undoped diamond tools are insulators, tribo-microplasma occurs and affects the sliding performance in both dry and oil-lubricated condition [166], and the induced
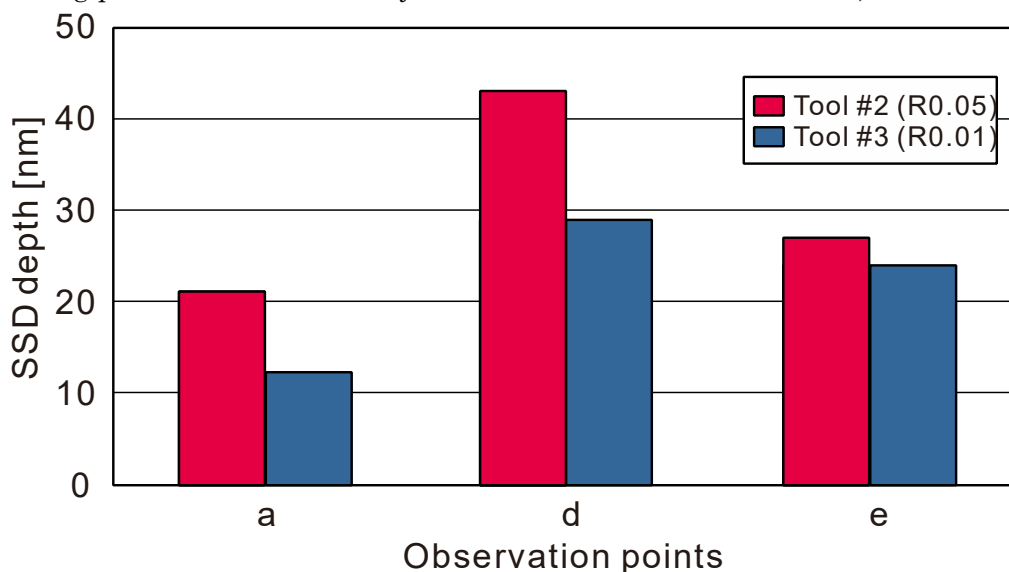

Fig. 4-53   Comparison of SSD depth depending on crystalline direction and nose radius.
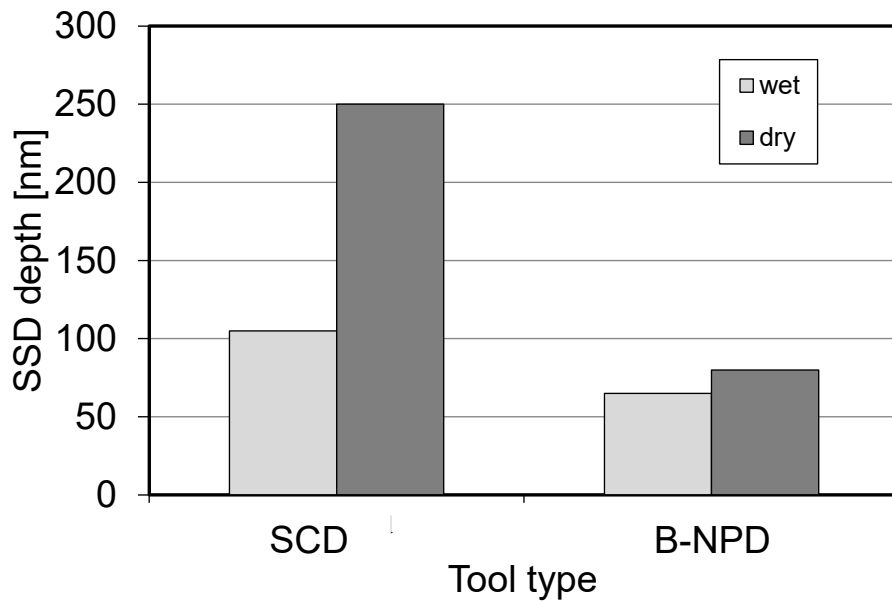
Fig. 4-54   Variation of SSD depth depending on tool type and cutting atmosphere

tribo-plasma affected the surface integrity [73, 110]. Not limited to the surface, the tribo-plasma can affect the subsurface quality as the friction coefficient at the interface between cutting tool and surface affects the subsurface stresses [167]. Owing to the boron doping, its frictional property is enhanced, and it is confirmed that the friction coefficient was lowered by boron-doping under both dry and wet conditions as shown by Sumiya [169]. The main reason is concluded as the formation of an oxide layer where solid lubrication effect is functioning on the diamond surface [110]. Considering the cutting model, the friction occurs on a rake face and a flank face, and thus, necessary cutting energy is assumed to be lower for the same amount of cutting. This is because the SSD depth decreased in the case of B-NPD.

4.3   Summary

In this chapter, the machinability of the CaF$_2$ was evaluated in plunge-cut tests and UPCT tests. Specifically, the anisotropic behavior of the machined surface and SSD formation were discussed. The contents are summarized as follows.

1. In the plunge-cut tests, nose radius of the cutting tools affected the CDC values whereas there was no major difference among other process parameters (rake face and cutting speed). The contact length in the gap of tools and surface which contributes to the plastic flow area is assumed to be dominant on the surface integrity.

2. The surface morphologies and CDC values are significantly dependent on the cutting crystalline planes and directions. The CDC values vary in the range of 80−400 nm. Those are characterized by two-, three-, four-fold symmetry on the basis of cubic

crystalline structures. For the discussion of variation of the CDC values, the plastic deformation parameter P which describes the slip mobility was used, and showed a good agreement with the corresponding CDC values. The crack morphologies were observed via FE-SEM, and the direction of brittle fracture coincide with the cleavage fracture parameter C that describes the possibility of cleavage. Overall, primary slip system {100}⟨011⟩, {111} and {110} cleavages are dominant on the anisotropic deformation behavior.

3. In the UPCT tests, similar tendency regarding the crystal anisotropy was found. Even though the axial DOC and uncut chip thickness was set as below CDC values, the surface integrity strongly depends on the corresponding cutting crystalline planes and directions. Although the discussion was qualitative, the obtained results agreed well with the plunge-cut tests. To suppress the thrust force, the smaller nose radius and 0 ° rake angle were used, and homogeneous surface were obtained regardless of the crystalline structure.

4. The subsurface integrity was investigated on the cylindrical surface via TEM observation. Even if the surface roughness is uniform, the SSD depth vary depending on process parameters, tool geometry, tool type or crystal anisotropy from 10 to 100 nm scale. For the process parameters, the lower process force is assumed to be required to decrease the SSD depth. The geometrical relation between slip systems and cutting planes caused the deviation of SSD depth.

5. Investigation of the cutting performance of sapphire

This chapter provides the influence of cutting parameters and crystal anisotropy on the machined surface of sapphire in plunge-cut tests. In section 5.1, the plunge-cut tests were conducted. The proposed parameters in chapter 3 were calculated to discuss the anisotropic fracture behavior in the plunge-cut tests. In order to scrutinize the anisotropic fracture mechanism, indentation tests and TEM observation were conducted.

5.1 Experimental setup

Since the plunge-cut tests were conducted in a same manner in the case of CaF_2, the detailed explanation of the experimental procedure is omitted (see section 4.1.1). The variation of process parameters is listed in Table 5-1. Considering manufacturing of the microcavity, similar values which were used in plunge-cut tests of CaF_2 were set to the cutting parameters.

5.2 Evaluation of surface quality

Process parameter

Although the CDC value slightly decreased in increments of cutting speed V_f in the range of $200 - 1000$ mm/min in [0001] direction on $(10\bar{1}0)$ plane (Fig. 5-1), there was no major difference. Thus, the results were similar to the CaF_2 case. The cutting speed defines the strain rate [141]. The higher the cutting speed, the bigger the induced stress in the material. More cutting power can be consumed in the same time window, which could lead to the slight reduction of CDC values. It should be noted that the extremely low scratch speed regime (less than 1 mm/min), the scratch speed affected the surface integrity [141]. In the case, higher scratch speeds lead to greater plastic deformation

Table 5-1 Process parameter of the plunge-cut tests of sapphire

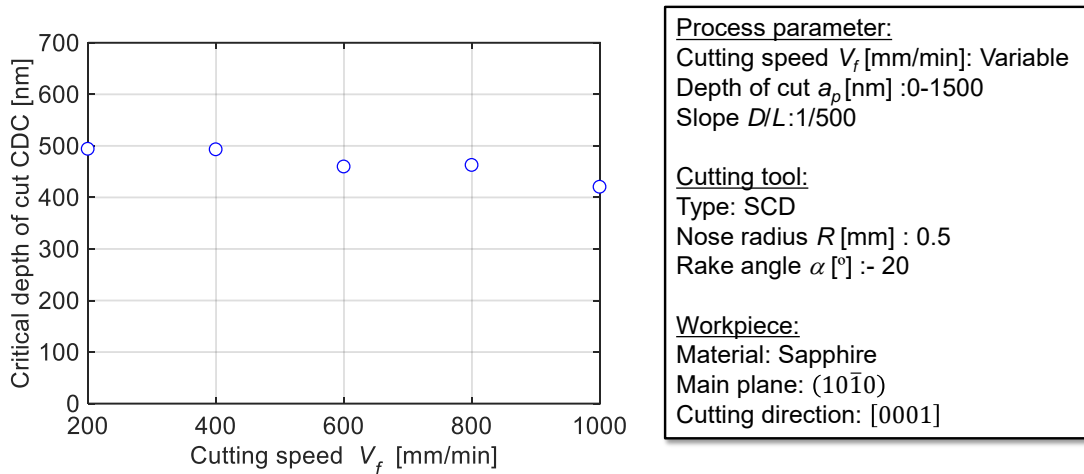| Parameter	Value
Cutting speed V_f [mm/min]	10, 20, 200, 400, 800, 1000
Depth of cut a_p [nm]	$0 - 1500$
Cutting slope D/L	1/500
Cutting direction δ [°]	$0 - 330$ (increments of 30)
Crystal orientation of cutting plane	(0001) and $(10\bar{1}0)$
Type of cutting tool	SCD, NPD, B-NPD
Nose radius R [mm]	0.5
Rake angle α [°]	0, -10, -20
Atmosphere	Dry

Process parameter:
Cutting speed V_f [mm/min]: Variable
Depth of cut a_p [nm] :0-1500
Slope D/L :1/500

Cutting tool:
Type: SCD
Nose radius R [mm] : 0.5
Rake angle α [º] :- 20

Workpiece:
Material: Sapphire
Main plane: $(10\bar{1}0)$
Cutting direction: [0001]

Fig. 5-1   Variation of CDC values in accordance with cutting speed

Process parameter:
Cutting speed V_f [mm/min]: 20
Depth of cut a_p [nm] :0-1500
Slope D/L :1/500

Cutting tool:
Type: B-NPD
Nose radius R [mm] : 0.5
Rake angle α [º] : Variable

Workpiece:
Material: Sapphire
Main plane: (0001)
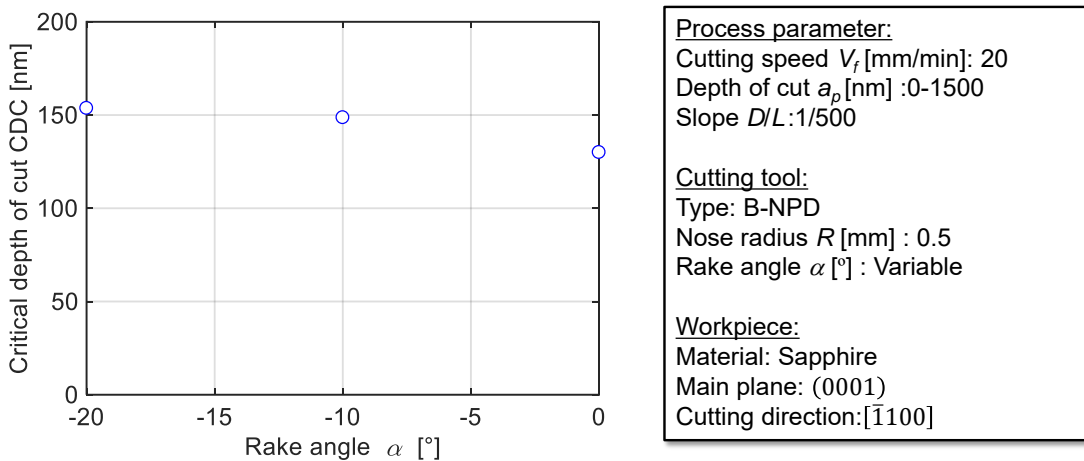Cutting direction:$[\bar{1}100]$

Fig. 5-2   Variation of CDC values in accordance with rake angle

portion, while avoiding chipping and brittle fracture. While conducting the high cutting speed more than 200 mm/min, the chipping frequently occurred on the cutting tool. To avoid the chipping, the low cutting speed (10 − 30 mm/min) was sometimes set in cutting process [170]. To prevent the tool breakage, in the following tests, lower cutting speed 20 mm/min was used.

The influence of rake angle with a B-NPD tool was examined. By applying a negative rake angle, the CDC value slightly increases (Fig. 5-2). As before discussed, since the hydrostatic compressive stress is formed in front of the tool, the crack propagation can be suppressed, and the CDC value increases [49]. However, similar to CaF_2 case, there was no major difference between rake angles, even though the larger nose radius (R 0.5 mm) was used, compared to the ones for CaF_2 (R 0.01, 0.05, and 0.2 mm). To investigate the validity of the obtained results, it is considered that the nose radius is necessary to be larger.

Crystal anisotropy

For the investigation of crystal anisotropy, the NPD tool was hired. The cutting speed and rake angle were set as 20 mm/min and 0 °, respectively. Other cutting condition is listed in Table 5-1.

The machined grooves and their corresponding CDC values are shown in Fig. 5-3. The CDC values change depending on the cutting direction, same as CaF$_2$. Interestingly, the surface morphology and CDC values were featured by a two-fold symmetry along a specific axis (indicated by a red-dotted line), although those were expected to exhibit the three- or six-fold symmetry based on its hexagonal crystalline structure or rhombohedral lattice system (see Fig. 5-7). In the tests, the NPD tool was partially fractured as shown in Fig. 5-9 during the tests. Therefore, the same tests were conducted using SCD tool. Though the CDC values were slightly different, the surface morphologies were featured by two-fold symmetry, therefore, the tendency was reasonably close.

Overall, the surface morphologies were classified into four categories (Fig. 5-5 and Fig. 5-7): Type I – a fracture formed by RC and PC (Fig. 5-5 (d)), Type II – a shallow fracture induced by RC and interchanging pattern of ductile and brittle surface. (Fig. 5-5 (c) and
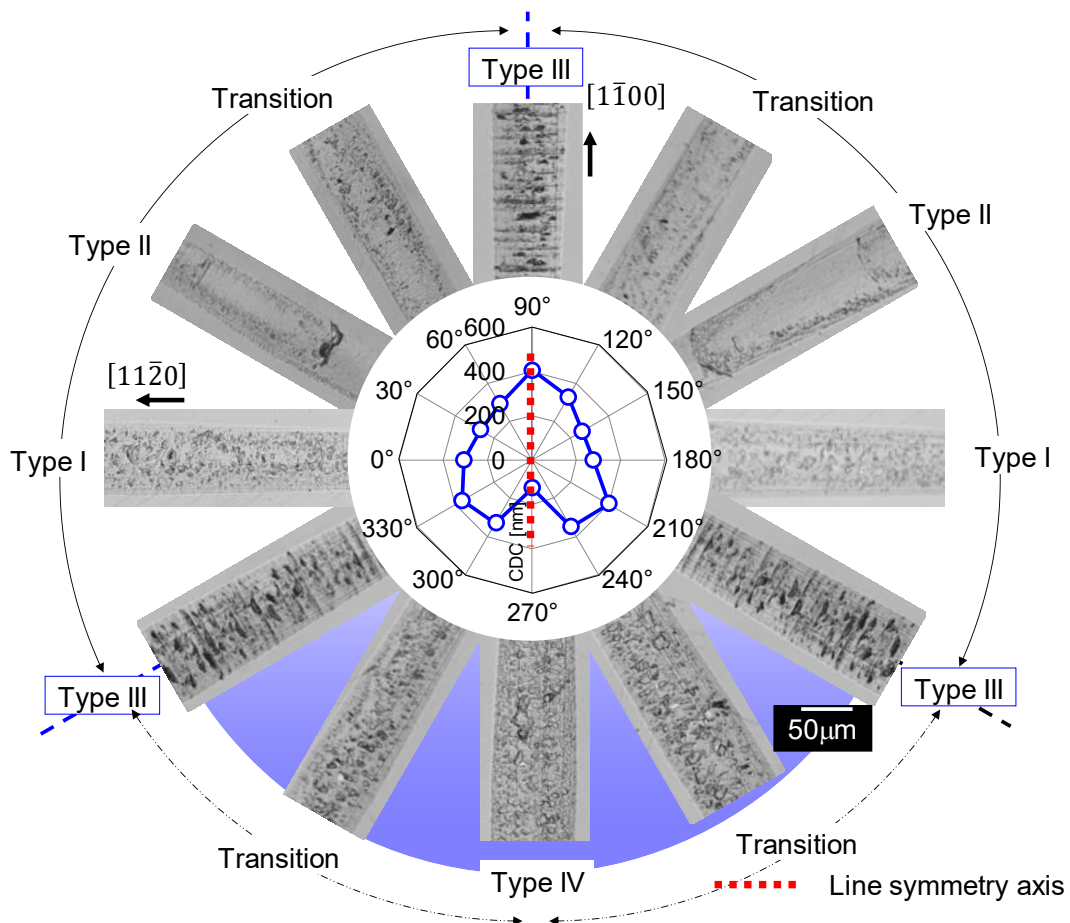

Fig. 5-3   Images of the machined grooves and variation of the CDC values machined by NPD tool.

Fig. 5-8), Type III – a lamellar fracture formed by PC (Fig. 5-5 (a) and (e)), and Type IV – pull-out fracture (Fig. 5-5 (f) and (g)). Notably, the Type II fracture was originally expected in the 270 ° direction due to the three-fold symmetry (rhombohedral family) or six-fold symmetry (hexagonal structure). In the direction of 60 ° and 300 °, lamellar fracture along $\{11\bar{2}0\}$ planes were observed. In the direction of 0 °, lamellar steps along $\{11\bar{2}0\}$ planes are also formed. The cleavage along this plane is not reported, however, some terrace which might relate to cleavage process is reported by in-situ TEM observation [97]. Therefore, the observed lamellar fracture in 60 ° and 300 ° directions can also originate from cleavage or other deformation system, such as the case of CaF_2 (some steps were formed in a specific direction which is not reported previously, as discussed in section 4.1.2). Otherwise, the lamellar step or fracture can be formed by plastic flow. To clarify the origin of formation mechanism, residual stress analysis by X-ray can be used, however, notably the analysis area is quite small, therefore, it was difficult to identify what actually occurred. Same as the case of CaF_2, the P and C parameters were calculated, estimating the inclination angle β as 45 ° from the measured process forces which is complemented in Appendix.
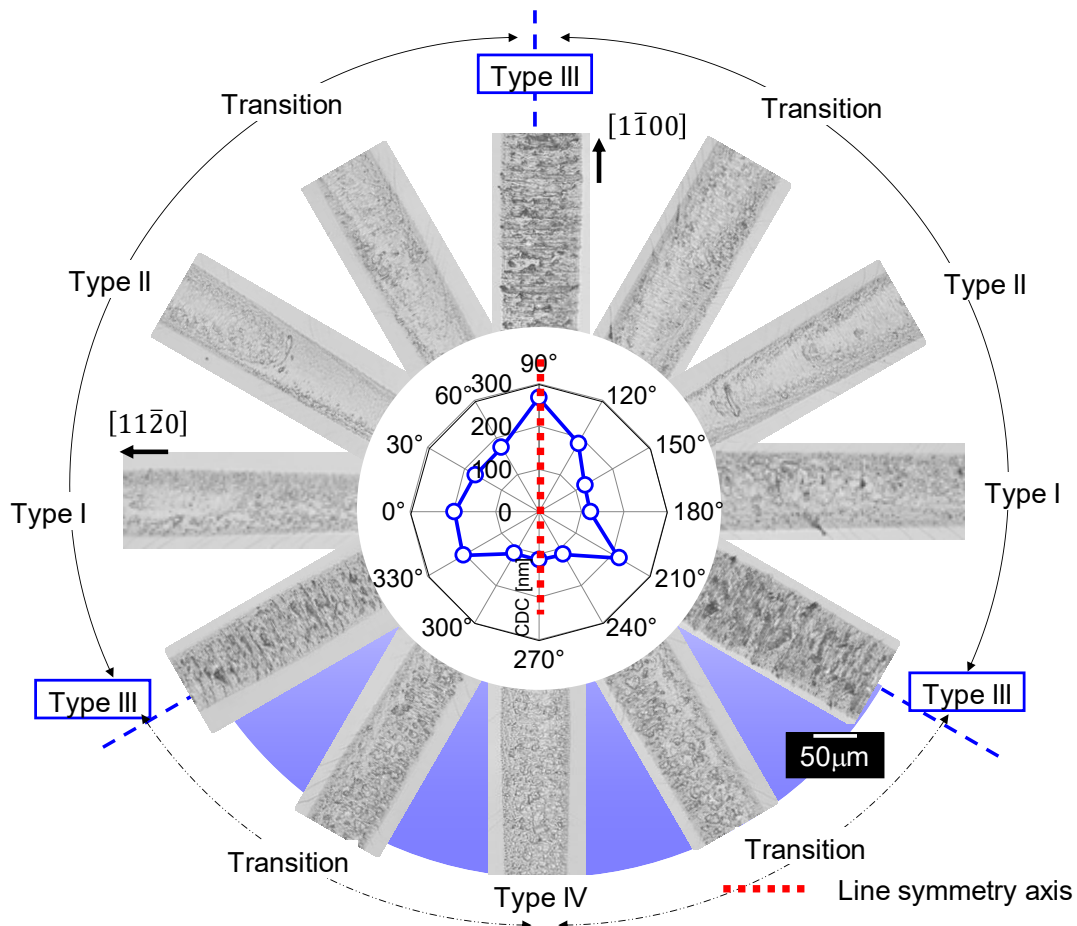
Fig. 5-4 Images of the machined grooves and variation of the CDC values machined by SCD tool.
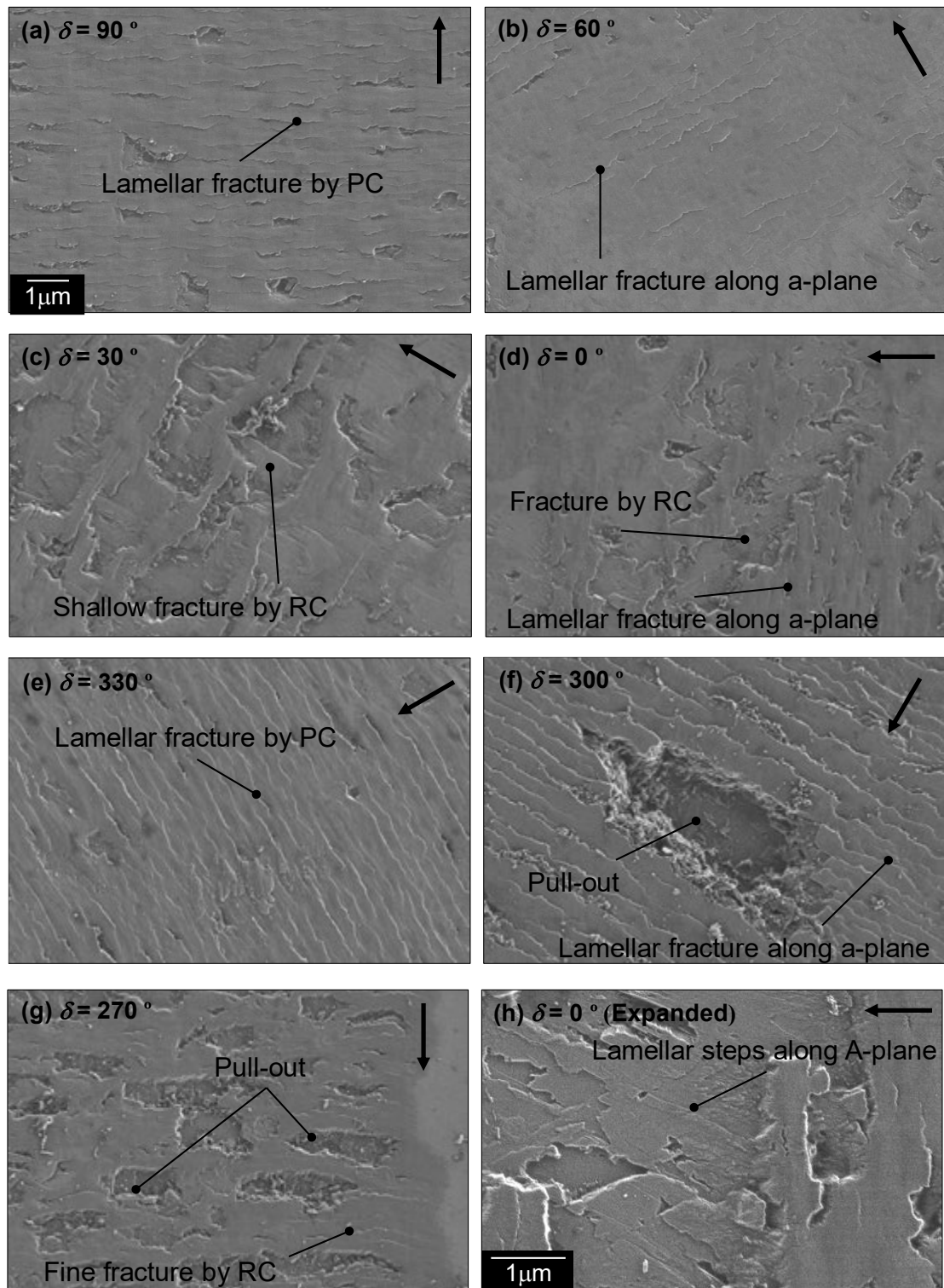
Fig. 5-5　Surface morphologies of the (0001) plane: (a), (e) Type III – a lamellar fracture formed by PC (c) Type II – a shallow fracture induced by RC and interchanging pattern of ductile and brittle surface, (d) Type I – a fracture formed by RC and PC, and (f),(g) Type IV – pull-out fracture. In transitional area, the lamellar fracture along $\{11\bar{2}0\}$ planes were formed.

Fig. 5-6 Variation of (a) Plastic deformation parameter P (b) Cleavage fracture parameter C of (0001) sapphire

Fig. 5-7   Schematic illustration of surface morphology of (0001) sapphire

The possibility of activation of each deformation system is indicated by P and C parameter values (Fig. 5-6). Conventionally, a slip system is a dominant deformation system for the ductility, however, rather the obtained results were sustained by $P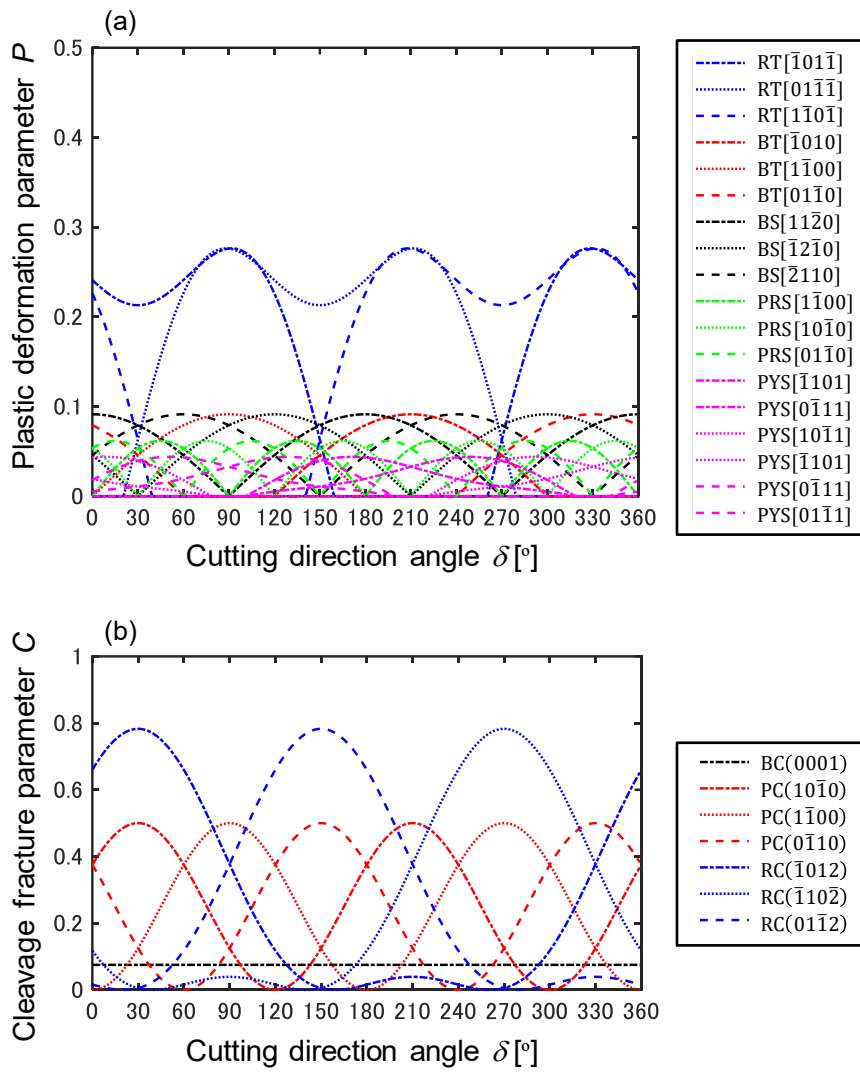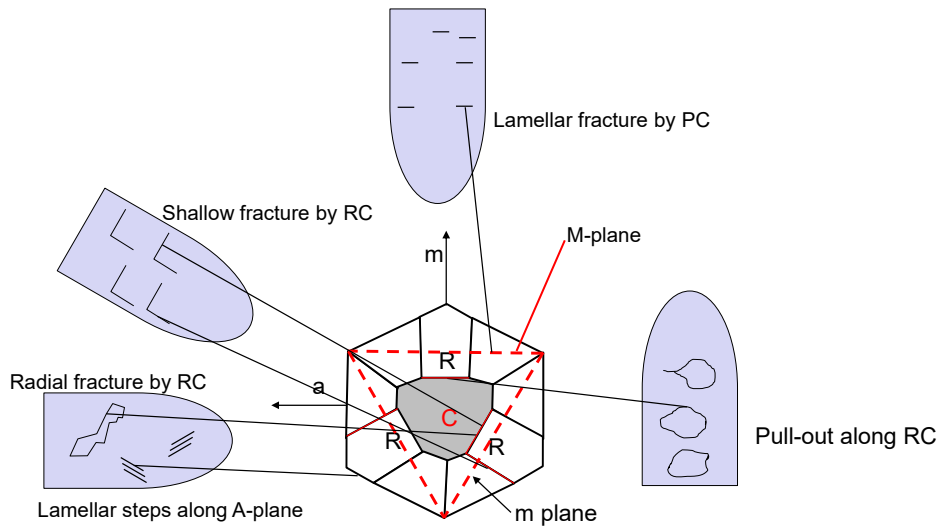$ parameter values of twinning. The maximum of CDC values agrees well with the P parameter values of rhombohedral twinning (RT) in the directions of 90 °, 210 °, and 330 °. The computation results are similar to the results of (111) plane CaF$_2$ (see section 4.1.4). Here, the C parameter values are minimum in the same directions, whereas C parameter values exhibit the maxima in the directions of 30, 150, and 270 °. In those directions, the CDC values were low, and the P parameters were the minima. On the contrary to CaF$_2$, the variation of CDC values was supported by both P and C parameter values. Compared to CaF$_2$ (158.3 kg/mm^2 Knoop hardness and 75 GPa Young's modulus [48]), sapphire is much harder (1500 to 2200 kg/mm^2 Knoop hardness and 345 GPa Young's modulus [57]). Thus, the results also show that one can use either or both of P and C parameters for the analysis of anisotropy according to the materials.

The unique surface morphology (Type II) was seen in the directions of 30 ° and 150 °, in form of interchanging patterns of smooth and rough surface i.e. ductile fracture and brittle fracture (Fig. 5-8). When more than two slip systems are activated, they promote slip dislocations simultaneously that share an intersection, and the dislocations pile up at this intersection plane. At the boundary, the stress grows locally so that cracks initiate[171]. For HCP crystals, the twinning is also considered to contribute the deformation process. Since the P parameter values are close each other for PYS, PRS,
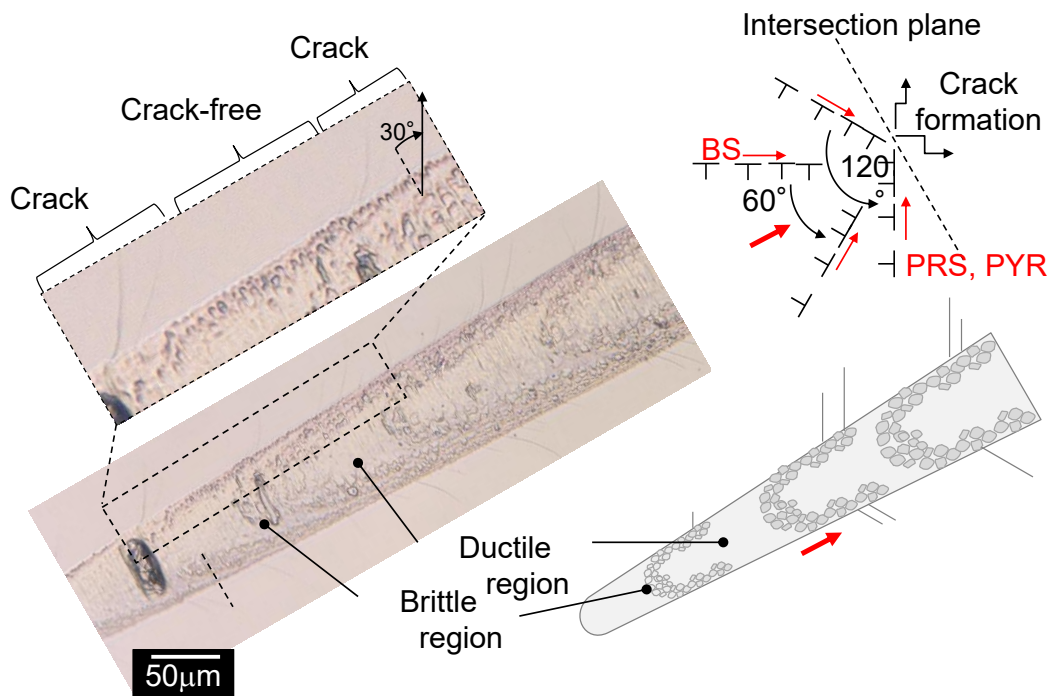

Fig. 5-8 Machined surface with interchanging pattern of ductile region and brittle region in cutting directions of 30 ° and 150 °.
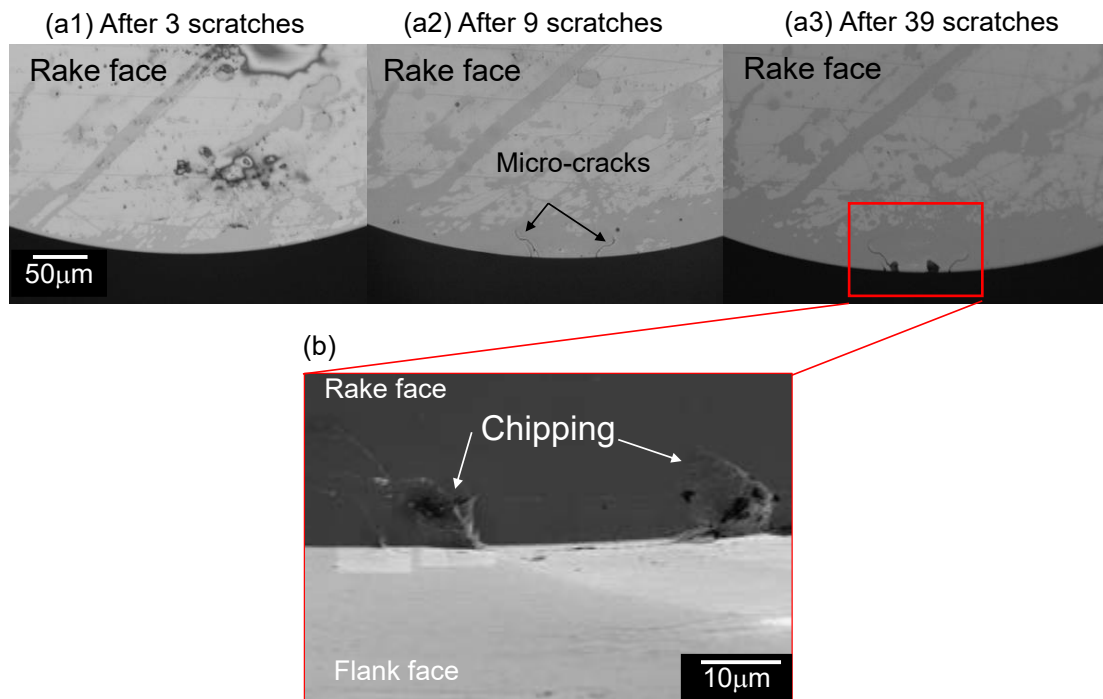
Fig. 5-9 Images of the tool used after (a1) 3 scratches, (a2) 9 scratches, and (a3) 39 scratches., and (b) chipping on the tool used after 39 scratches
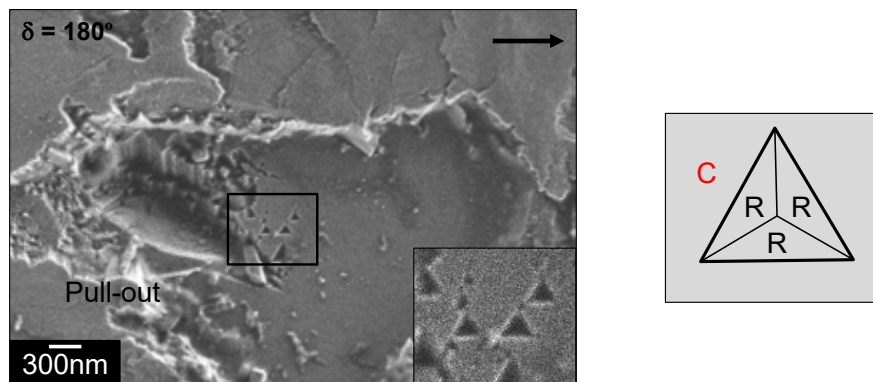
Fig. 5-10   The pyramidal shaped holes (similar to etch pits) on (0001) plane for the 180 ° direction. The holes are formed on a cleaved (0001) surface and under the machined surface.

BT, BS (the same values for PYS and BT), the twinning can be also initiator for the unique interchanging patters. Brittle fracture occurs on the machined surface due to the pile-up of BS, PRS, and PYS. After removing the brittle fracture, the plastic deformation can occur initiate by slip or twinning. The repetition of the pile-up and glide mechanisms was assumed to be a reason for interchanging patterns of the surface.

In some machined surface e.g. 180 ° direction, regularly aligned triangular pits existed where the machined surface was pulled off along RC as shown in Fig. 5-10. The pits are similar to etched pits on c-plane sapphire wafers [151, 172], the pyramidal face coincide with the rhombohedral planes that face towards each other with the interval of 120 ° and 57 ° inclined to c axis (Fig. 5-10). As the surface energy of rhombohedral plane is

lowest in sapphire, the pull-off process added an additional energy that induced the tensile stress on newly formed surface (the surface after pulled off), and the weakest atomic bonding planes were fractured. Since the cutting process was performed under dry condition, the surface, chemical etching effect is unlikely as the root of this phenomenon. Notably, the existence of pre-defects caused by crystal growth cannot be ignored.

The expected symmetry for anisotropic behavior was also indicated by the computation results of P and C parameter i.e. three-fold symmetry. Different directional movement (positive or negative) of activated deformations and interaction among themselves can be a trigger for the abnormal machined surface in 270 ° cutting direction. The error of crystalline direction in manufacturing sapphire substrate is less than 2 °, therefore, the misalignment of the crystal orientation is less likely.

During the tests, the NPD tool was slightly broken as shown in Fig. 5-9. The breakage part was partially involved in the ductile regime cutting in 240 ° to 330 ° cutting directions, therefore, the breakage was also anticipated to be a cause for the abnormal symmetry. Meanwhile, the same cutting tests with SCD tool was also conducted without any tool breakage, and the results showed the same tendency with the case of the NPD tool (compare Fig. 5-3 and Fig. 5-4). Thus, the tool breakage or even tool type was not the reason for the unexpected symmetry.

To elucidate the mechanism, additional tests were conducted, and the obtained results were comprehensively discussed in the next section.

5.3   Discussion

In this section, indentation tests were conducted to investigate the factor of the unexpected symmetry in terms of mechanical property. Additionally, TEM observation was conducted to the specific cutting directions to observe the material deformation behavior in subsurface region.

Table 5-2 Process parameter of the indentation tests of sapphire

Parameter	Value
Indentation Load [mN]	300, 500, 700, 900, 1100, 1300, 1500
Loading speed [mN/s]	35.0335
Dwell time [s]	5
Indenter type	Triangular pyramid indenter with 115° tip angle (Berkovich indenter)
Environment	Temperature 22°Celcius Relative humidity 50%
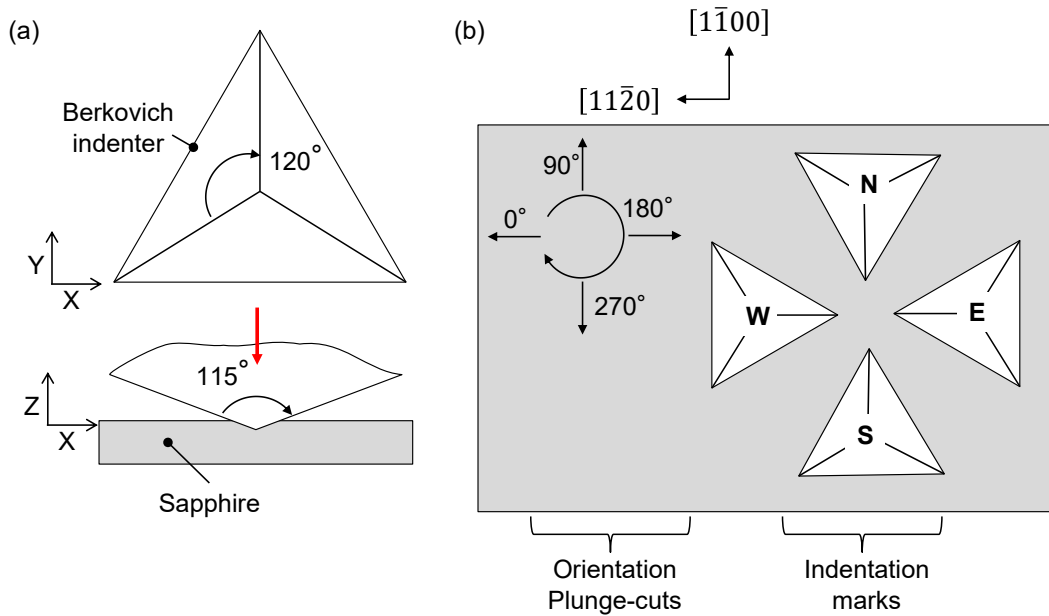
Fig. 5-11 Schematic illustration of (a) Berkovich-indentation process and (b) Indenter orientation in regards to the plunge-cut orientation
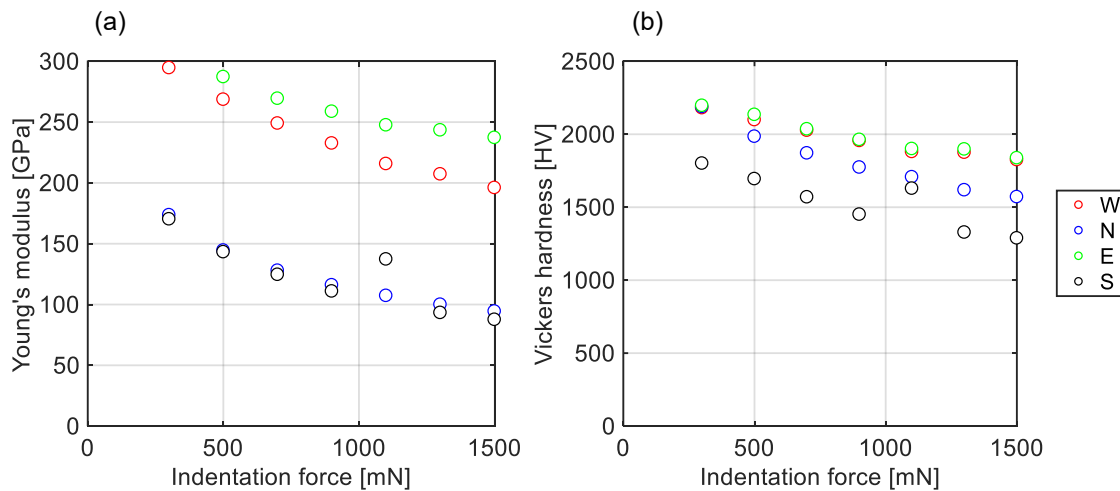
Fig. 5-12 Indenter orientation dependency on (a) Young's modulus and (b) Vickers hardness

Indentation test

Indentation tests were performed on the dynamic ultra-micro hardness tester (DUH-211S, SHIMAZU) and it was equipped with a triangular pyramidal indenter with 115 ° diamond tip (Berkovich indenter). The tests were performed at a room temperature and a relative humidity of 50 %. Sapphire substrate was fixed onto the stage of the machine by mechanical clamping system. Analogous to the plunge-cut, the indentation orientation is also important for investigation of the anisotropy. The material deformation mechanism could vary depending on the direction of the indenter facets, therefore, the technique was also used in a low strain regime [147]. By varying the

direction of the indenter, the influence of indenter orientation was investigated (denoted as E (east), N (north), W (west), S (south) as shown in Fig. 5-11). The indentation tests were conducted five times, and the mean values of Young's modulus and Vickers hardness were calculated. The indentation condition is listed in Table 5-2.

For Young's modulus and Vickers hardness, the values decrease according to the increase of indentation loading. Although the maximal indentation depth is over approximately 1 μm, the size effect can be a reason for the variation of those values. Overall, there is a deviation of Young's modulus between E and W orientation, whereas a deviation of Vickers hardness between N and S orientation. Considering the unexpected symmetry of the plunge-cut results, the mechanical properties were expected to show between N and S orientation since the indenter facets of N orientation push the material to 90 °, 210 °, and 330 ° directions whereas the ones of S orientation contribute to the deformation towards 30 °, 150 °, and 270 ° directions. The BDT mechanism was governed by both the ductility and brittleness, thus both mechanical properties were assumed to contribute to the abnormal symmetry. In other experiments, the similar results could be found [147], namely, in the indentation tests of (0001) sapphire with
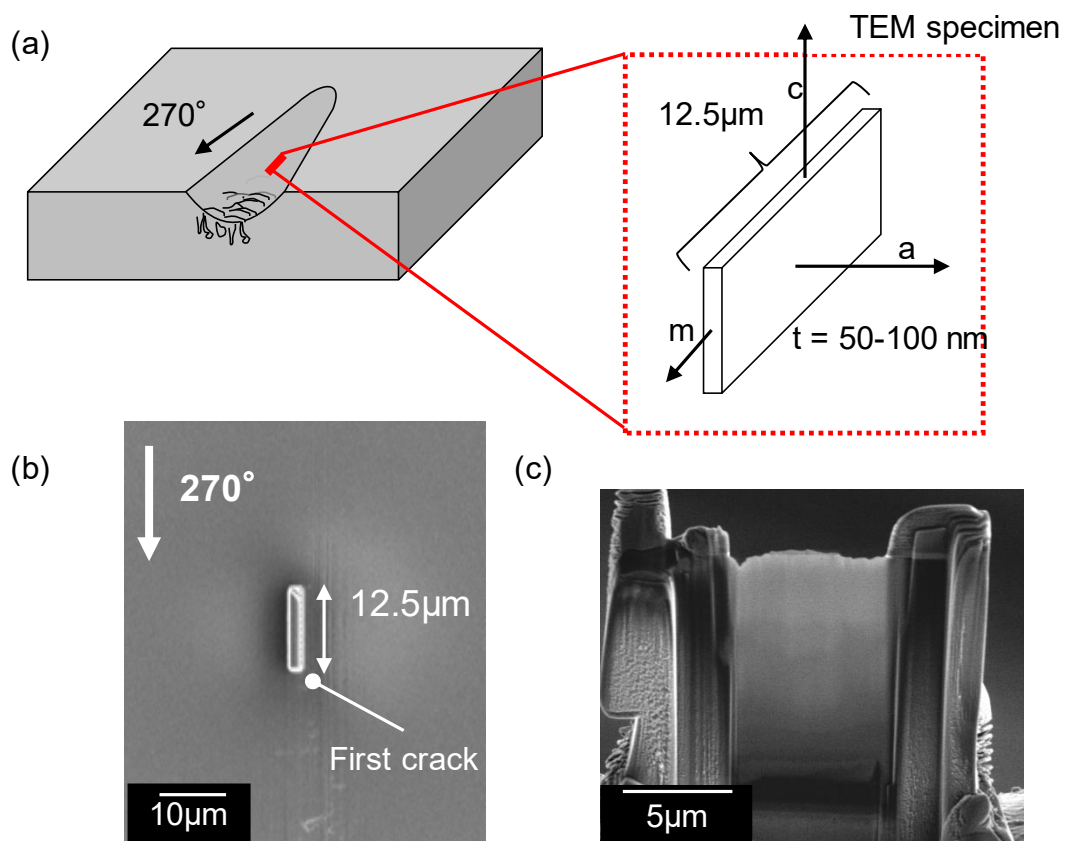
Fig. 5-13 Measurement procedure of TEM observation of plunge-cut grooves: (a) The SSD is viewed from a perpendicular direction to cutting direction (b) Pick-up point for TEM observation. The machined groove in front of a place where a first crack appears. (c) Extracted TEM-foil after the FIB-cut framed by support pillars.

Berkovich indenter, one could observe that a material piled up and brittle fracture propagated along one direction. Therefore, it can be said that the brittleness-related parameter such as hardness value that is related to crack initiation is more dominant on the abnormality of the obtained symmetry. Indeed, the computation results of C parameters coincided well with variation of the CDC values. For example, the higher CDC values agreed well with the lower C parameters. However, the discussion is still a primitive stage because a reason for disagreement of the hardness values is not clarified. For more in-depth investigation, the subsurface quality was analyzed via TEM to scrutinize the actual activated mechanism underneath the surface.

Subsurface structure

The subsurface structure was observed by TEM. The machined groove was sliced by FIB to obtain a thin specimen (Fig. 5-13 (a)), same as CaF_2 (thickness: $50 - 100$ nm). To mainly focus on observing the slip or twinning, the ductile-machined surface was chosen from SEM images (Fig. 5-13 (b)). The machined surfaces with NPD tool were used for TEM observation since the ductile surface was wider than the one machined by SCD tool.

For the 30 ° direction of the groove at approximately 100 nm where the type II surface morphology was seen, one defect line perpendicular to (0001) plane was seen as shown in Fig. 5-14. As shown in a close-up image of a part of the lines (Fig. 5-15), basal twin (BT) was formed in the subsurface region, although the P parameter of BT was relatively lower than other systems (Fig. 5-6). Notably, the boundary line of BT was not clearly observed from the TEM image. Therefore, the BT was identified from FFT images. The FFT spots in region II consists of the mixture of FFT spots in region I and III. One
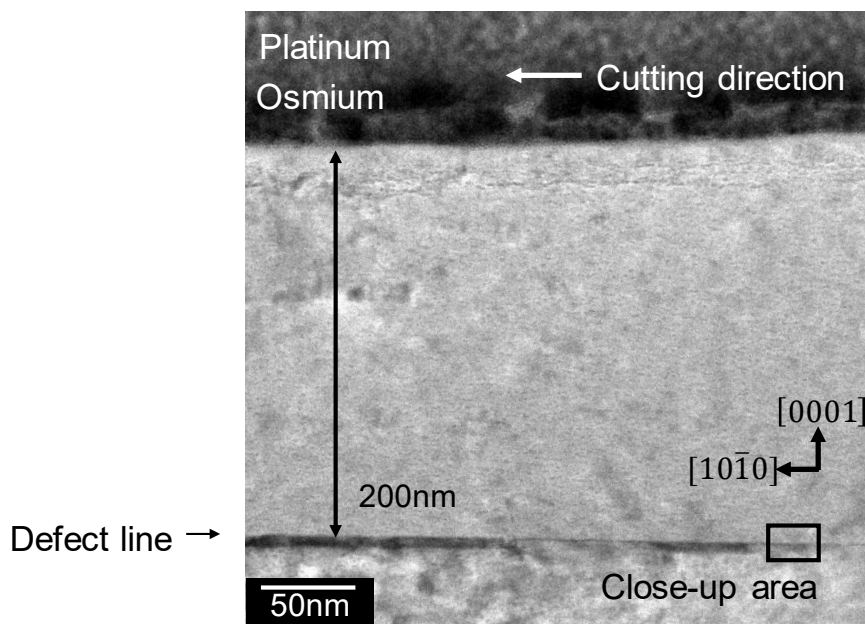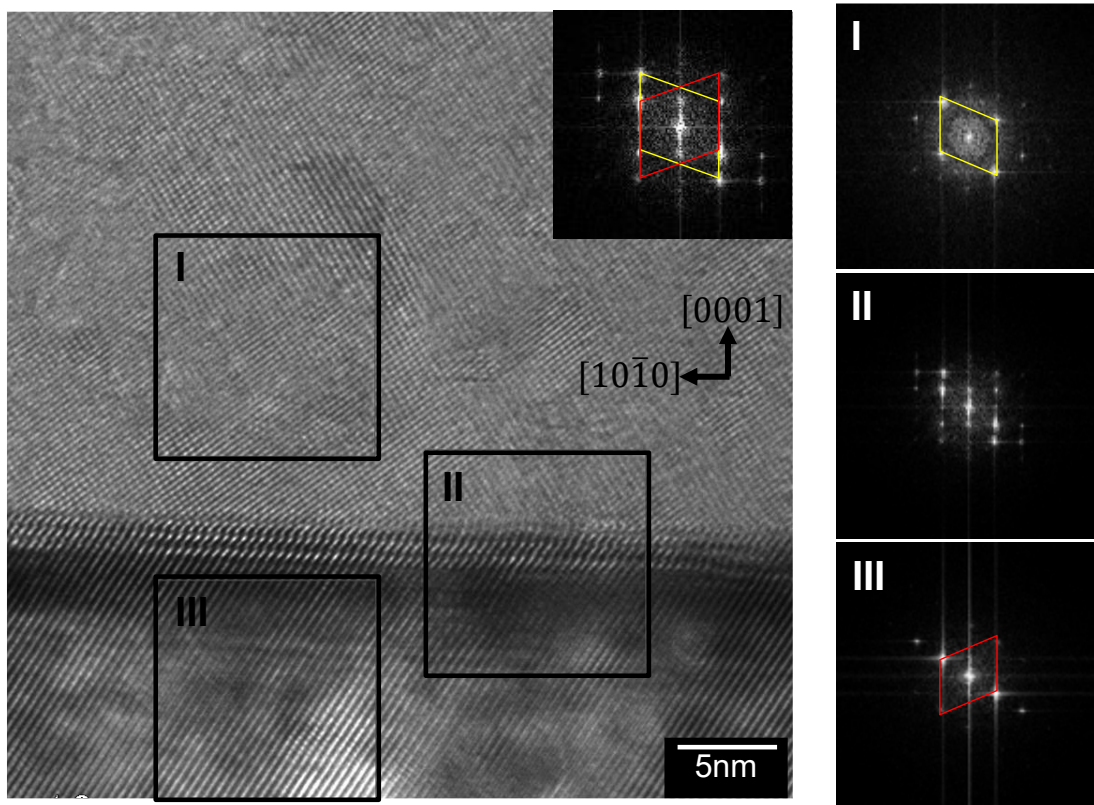

Fig. 5-14 TEM micrograph of subsurface at 30 ° cutting direction viewed from $[1\bar{2}10]$ direction.

Fig. 5-15 Close-up view of the defect line. FFT images of region I and III feature the mirror symmetry along (0001) plane, which can be sustained by the FFT image of region II

parallelogram is formed by four FFT spots in region I (indicated by yellow lines). For region III, one parallelogram is formed in the same procedure (indicated by red lines). By merging the parallelogram as shown in the inset of Fig. 5-15, the mirror symmetry relation appears each other, therefore, this is considered as twinning. The similar FFT images are shown, which feature the mirror symmetry along the (0001) plane that was seen in Zheng's work [173]. In previous TEM observation of abraded alumina surfaces the BT was found underneath the abraded (0001) sapphire that was ground at room temperature [96]. Therefore, the deformation is most likely BT. On the other hand, several twin bands were seen in the TEM image which shows the subsurface in 270 ° direction as shown in Fig. 5-16. Analogous to the subsurface in 30 ° direction, the defect lines are identical to the basal planes. The crystalline lattice arrangement in the expanded image of region A shows the mirror symmetry as before discussed i.e. BTs are formed (Fig. 5-17). There are also a few twin bands in region B as shown in Fig. 5-18. The multiple twin bands can be one of the plausible reasons for the unexpected symmetry. Although the slip and twinning contributes to the plastic deformation in HCP crystal, those deformation systems are sometimes barriers when intersecting each other [143] because the dislocations pile up at this intersection plane. Although only BT was found in the subsurface region, other deformation system e.g. RT, BS, PRS might also generate
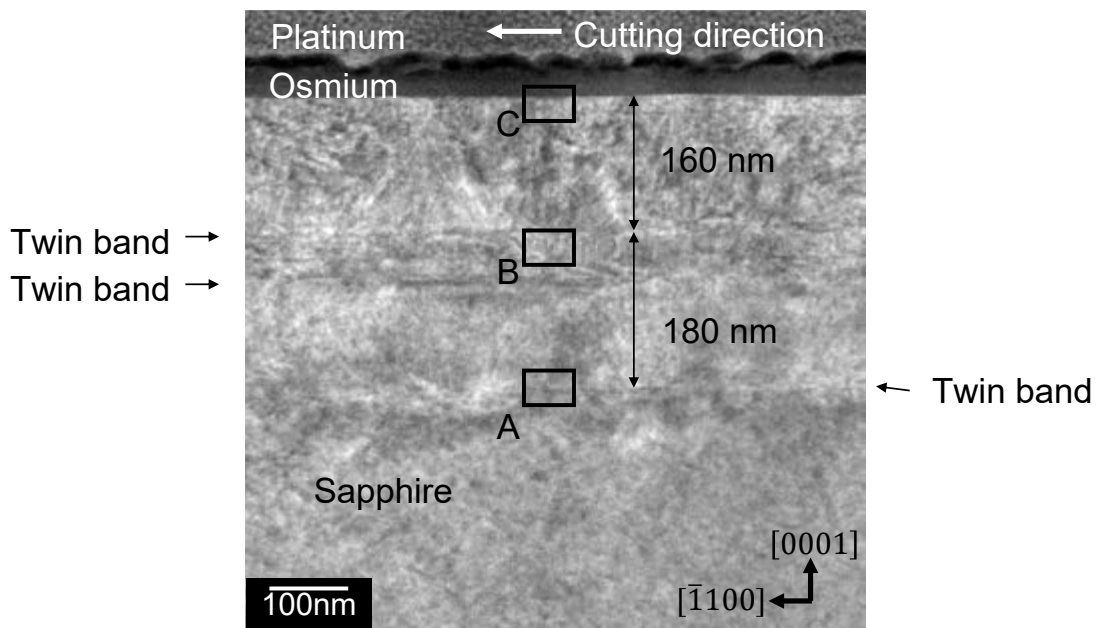
Fig. 5-16 TEM micrograph of SSD at 270° direction viewed from [11$\bar{2}$0] direction.
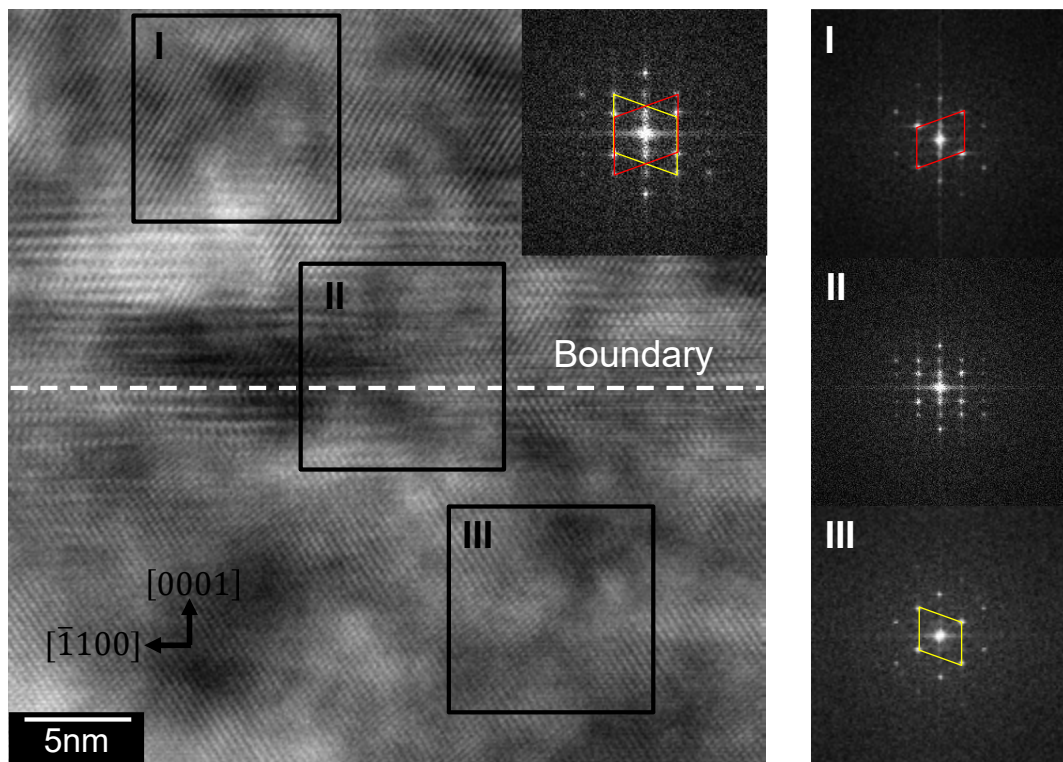
Fig. 5-17 Close-up view of region A. FFT images of region I and III feature the mirror symmetry along (0001) plane, which can be sustained by the FFT image of region II

since those P parameters were close each other (see Fig. 5-6), and the slip and twinning intersection occurred in a very initial stage in the cutting process compared to 30 ° directions. Here, it is concluded that the occurrence of the intersection of deformation
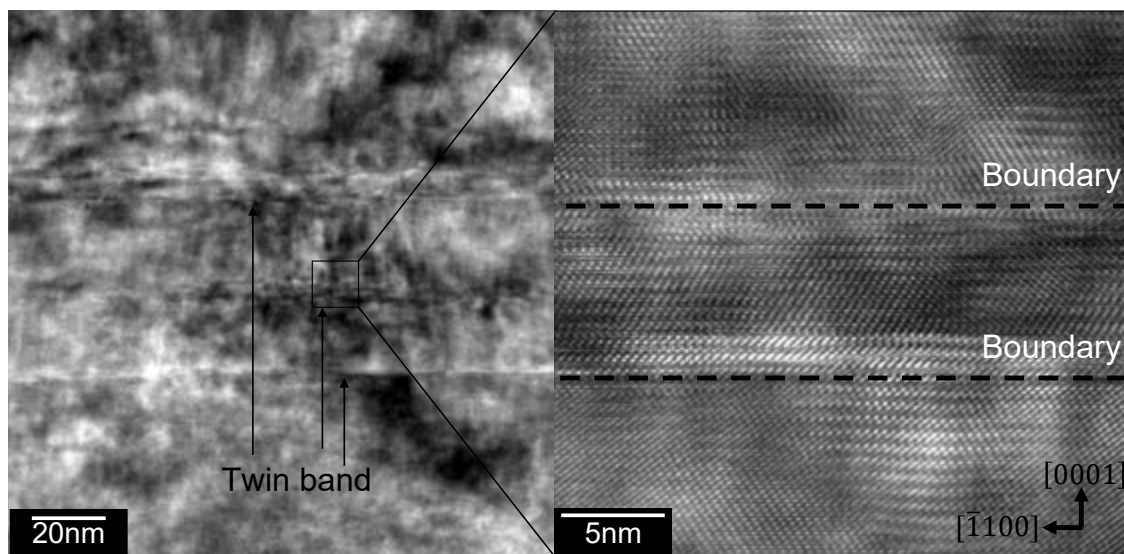
Fig. 5-18 Close-up view of region B. Several defect lines were observed in region B, and it is assumed that crystalline lattice arranges with mirror symmetry along (0001) plane boundary as shown in the close-up view.
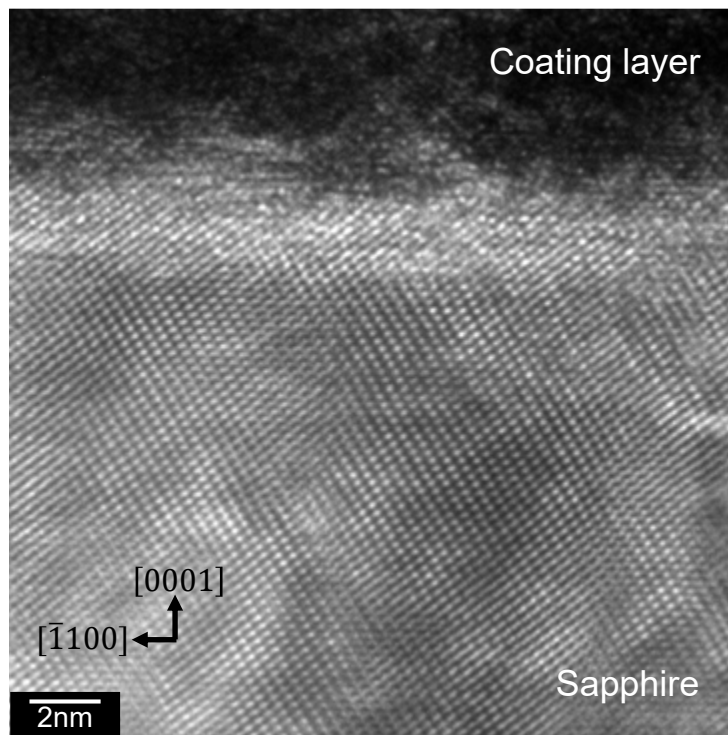
Fig. 5-19 Close-up view of region C. Compared to the CaF_2, the crystalline lattice regularly arranges, and no crystal shear or rotation was found.

systems can be a trigger for the unexpected symmetry. However, the origin of multiple twinning formation only for this direction is still unclear. The crystalline lattice is regularly arranged at the surface (Fig. 5-19). Normally, the crystalline lattice which is machined by cutting or grinding is severely damaged, and sometimes the phase

transforms to amorphous, for instance, in the case of silicon [79]. The surface shown in Fig. 5-19 was cut in ductile-regime, therefore, the surface should be uniform. If slip systems are dominant on the ductility, the crystalline lattice should be sheared or rotated as discussed in Chapter 4. Thus, this might be an evidence that the twinning which deforms with a certain amount of crystal body can be a trigger for generation of the plastic deformation in cutting of sapphire.

In this chapter, the machinability of sapphire was discussed from surface to subsurface region. Although the ductile surface can be achieved, the tool was easily chipped off due to the hardness of sapphire, hence, it can be said that it is difficult to manufacture the sapphire microcavity by only cutting. In the following chapter, only CaF_2 microcavity is fabricated.

5.4   Summary

In this chapter, the machinability of the sapphire was evaluated in plunge-cut tests. Specifically, the anisotropic behavior of the machined surface was discussed. The contents are summarized as follows.

1. In the plunge-cut tests, there was no major difference of the CDC values by variation of rake face and cutting speed. For plunge-cut tests, low cutting speed 20 mm/min was used in this dissertation to avoid the tool breakage.

2. On (0001) plane, CDC values changed in dependency with the cutting crystalline directions (100 nm − 300 nm in the case of SCD). The value and surface morphologies were characterized by two-fold symmetry while the three-fold or six-fold symmetry was expected on the basis of the hexagonal crystalline structure and rhombohedral lattice family. Variation of CDC values coincided well with the computed P and C parameters. Different from CaF_2, the CDC value was also characterized by C parameter which describes the possibility of cleavage generation. For example, the higher CDC values coincided with the higher P and lower C parameters.

3. The hardness values show the anisotropy depending on the indentation orientation (facets) in the indentation tests. The anisotropy can be related to the unexpected symmetry in the plunge-cut tests. The basal twins were observed in TEM observation. Whereas one twin band was observed in the 30 ° direction, multiple basal twin bands were formed in 270 ° direction which shows the unexpected surface morphology and CDC value. The intersection of the slip and twinning deformation systems is assumed to be a trigger for the unexpected BDT phenomena.

6. Manufacturing of WGM optical microcavity

This chapter provides the performance of the microcavity manufactured by cutting. Firstly, mono-material microcavity made of CaF$_2$ was manufactured. The influence of brittle fracture, cavity shape and subsurface quality on cavity performance was evaluated. Secondly, a trapezoidal microcavity was manufactured for the purpose of designing the cavity dispersion. Finally, a novel hybrid microcavity that consists of CaF$_2$ and brass was manufactured to suppress the thermal instability.

6.1 Mono-material optical microcavity

As reviewed in section 2.1, high Q microcavity can be attained by crystalline materials. Firstly, the CaF$_2$ microcavity that theoretically shows the highest Q in crystalline materials was manufactured, and its cavity performance was evaluated. As described in section 2.1.1, there are several factors that are related to the Q factor. In a fabrication process, the following properties have to be considered (Fig. 6-1).

1. Scattering loss
2. Absorption loss
3. Light distribution

The scattering loss from the surface can be determined by the surface quality e.g. surface roughness or existence of brittle fracture on the surface. The SSD formation can change the material property, in this case, the absorption coefficient. The light distribution that relates to the mode volume varies depending on the cavity shape. In this section, each influence on the cavity performance (brittle fracture, SSD, and cavity shape) was experimentally investigated.

Absorption loss
⇒Subsurface damage

Scattering loss
⇒Surface roughness

Light distribution
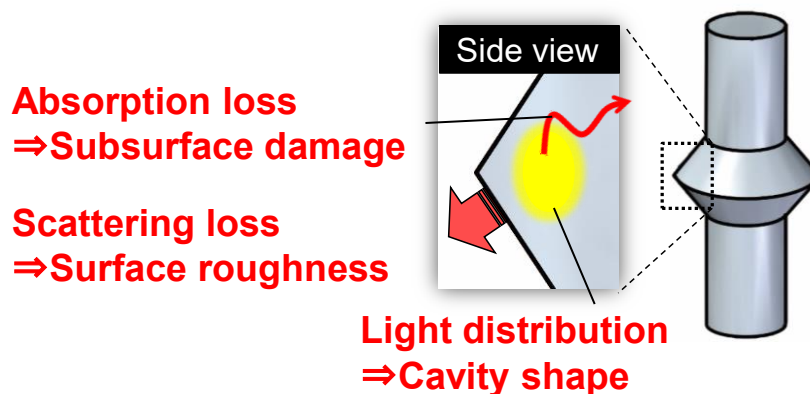**⇒Cavity shape**

Side view

Fig. 6-1 Schematic illustration of influential factors on cavity performance which can be induced in a fabrication process.

6.1.1   Manufacturing procedure

Microcavities were manufactured by UPCT on 4-axis aspheric machine tool. The detailed manufacturing procedure is described as follows (Fig. 6-2).

(1) The CaF$_2$ cylinder with 6 mm diameter was turned to decrease the diameter until approximately 500 μm through rough cutting, pre-finish cutting and finish cutting as described in section 4.2.1 (Fig. 6-2 (a) and (b)). The total DOC was set as 10 μm in pre-finish and finish cutting.

(2) The tool was fed at the inclined direction to rotational axis to form a triangular shape in a cross-sectional view (Fig. 6-2 (c), (d), and (e)).

(3) Final cavity shape was obtained with a specific aperture angle ψ. The angle can be attained by controlling the inclination rate of tool path to the rotational axis by NC.

The cutting condition listed in Table 6-1 was used for finishing and forming. The used tools were also listed in Table 4-2 and Table 4-4. The used cutting condition is based on the experimental results of the UPCT tests in chapter 4. After completing the cutting process, the workpiece was cleaned by ethanol or acetone.

For the measurement of high Q, the measurement method is also important. The measurement procedure is depicted in Fig. 6-3. A laser source TLD (TSL-510, SANTEC) was used as a laser source with 1 mW input power (100 kHz line width and 1 pm wavelength resolution). For the compensation of phase shifting, a PC was used. The tapered fiber with a diameter of 3 μm was used to couple the microcavity and waveguide. The procedure is described in details as follows:
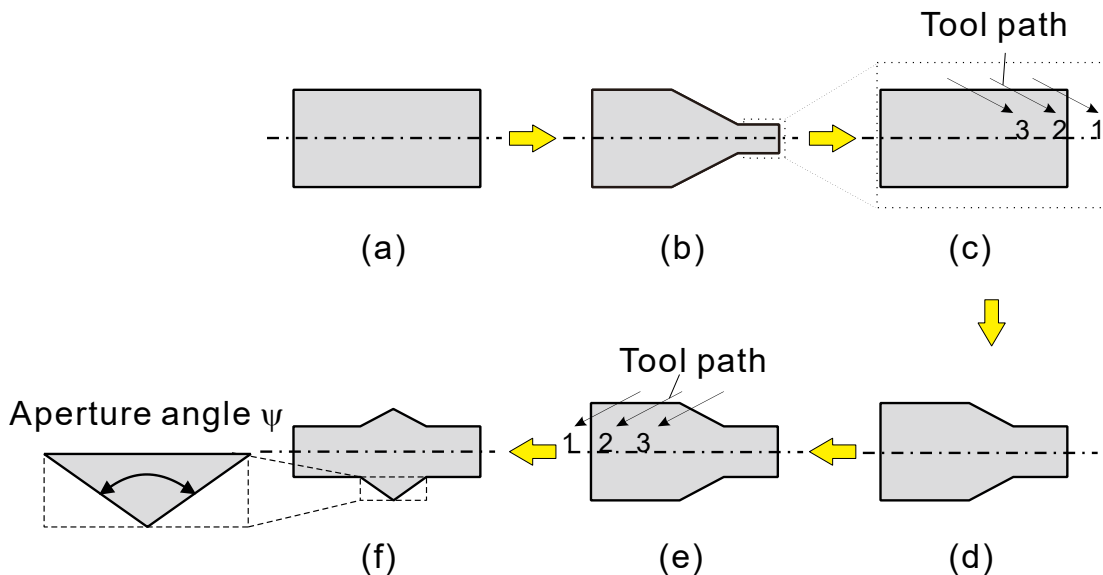

Fig. 6-2 Manufacturing procedure of mono-material microcavity. (a), (b) Initial CaF$_2$ cylinder with 6mm diameter is cut to decrease the diameter till less than approximately 500 μm. (c), (d), (e) By applying the diagonal tool path, the required cavity is obtained. (f) The final micro cavity geometry is determined by aperture angle ψ.

Table 6-1 Process parameter for manufacturing microcavity

Parameter	Value
Cutting speed V_f [m/min]	$0.94 - 1.57$
Rotational speed T [min⁻¹]	1000
Feed per revolution f [μm/rev]	$0.1 - 0.5$
Depth of cut a_p [nm]	50
Orientation of end face of workpiece	(100), (111)
Lubricant	Water-soluble oil (diluted by 1:100 ratio)

(1) PC and optical fiber were aligned to obtain a desired resonant mode.

(2) The input wavelength was constantly changed from the shorter wavelength to the longer one, and the transmittance intensity of each wavelength was scanned by PWM (Power Meter).

(3) The highest peak was chosen from all of the observed peaks that are induced by multiple resonances in the measurement.

The Q factor was calculated by Eq. (6-1).

$$Q = \lambda_r / \lambda_{FWHM} \qquad (6\text{-}1)$$

To interpolate the experimental data, Lorentz fitting method was used for the calculation of Q factor. Using Q factor, the trapping time τ_{phot} is given as follows:

$$\tau_{phot} = \frac{Q}{2\pi f_{res}} \qquad (6\text{-}2)$$

6.1.2　Results and discussion

Surface quality dependency on cavity performance

The microcavity with 168 ° aperture angle was manufactured with tool #1 (0.2 mm nose radius, $-20°$ rake angle) as shown in Fig. 6-4 (a) (here, named as type A). For a comparison, a microcavity whereon the brittle fracture exists was also manufactured as shown in Fig. 6-4 (b) (here named as type B). Although the same cutting condition was used, brittle fracture generated in the case of type B. The diameter of the type B cavity was approximately 300 μm, whereas the type A cavity shows 400 μm diameter. Since the UPCT of CaF_2 is unstable as shown in the occurrence of chatter vibration (see Fig. 4-33),
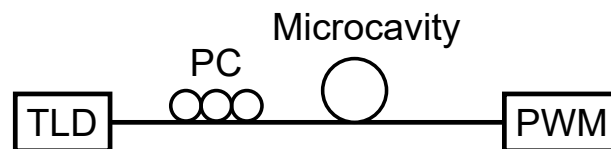
Fig. 6-3 Schematic illustration of measurement procedure of Q factor

slight difference e.g. the difference of diameter can cause the instability of the UPCT process. Otherwise, the misalignment of the tool position to the center of the workpiece in sub-nanometric scale is also a plausible reason.

The surface profile of the type A cavity was obtained by WLI (Fig. 6-5). It is clearly seen that a triangular shape was formed. Due to the obtained shape, the surface roughness could not be correctly measured. Nevertheless, the machined surface is fine (see Fig. 6-4 (a)), and no brittle fracture was seen at the whole cylindrical surface, therefore, the surface roughness S_a value can be estimated up to 6 nm or less, considering the previous results of UPCT in Chapter 4. Since the used wavelength for evaluation of cavity performance is around 1550 nm, the required surface roughness

Fig. 6-4 Comparison of crack influence on cavity performance. (a) Type A: microcavity whereon no crack was observed through optical microscopy. (b) Type B: microcavity with some brittle fracture. Both cavities show the same aperture angle i.e. cavity shape.
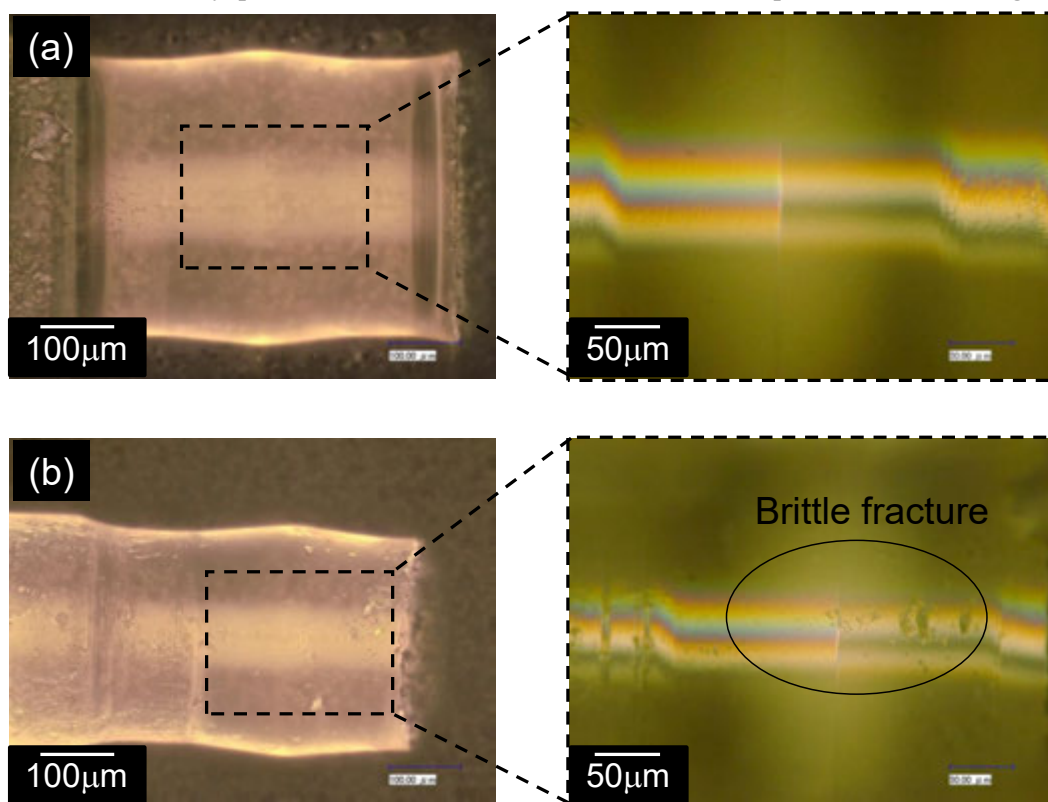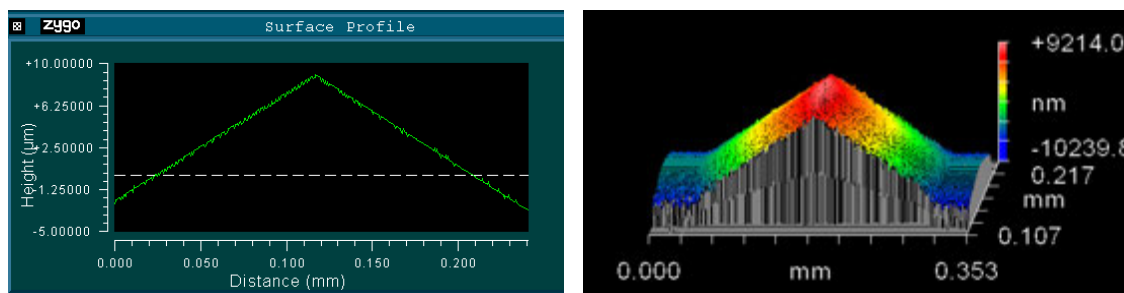

Fig. 6-5 3D profile of the microcavity surface obtained by WLI.

value can be, at least, less than 70 nm for preventing light scattering (the standard value was calculated from $\lambda_{res}/20$ [174]).

For both cavities, the cavity performance was evaluated. The type A cavity shows 1.4 $\times 10^5$ Q factor and 115 ps of trapping time, whereas the Q factor of 8.8×10^3 and 7 ps of trapping time was obtained in the case of type B cavity. Influence of brittle fracture on the cavity performance is apparent from the experimental results. In other words, if the Q value exceeds the 10^5 scale, it is less likely that brittle fracture affects the cavity performance in the following measurement. This result also indicates that even if a homogenous surface was obtained, existence of a few brittle fracture significantly deteriorate the cavity performance.

Shape dependency on cavity performance

Since the machine tool can be operated by NC programming, one can manufacture a microcavity with an arbitral feature, assuming that the cutting can be conducted in ductile-regime and the tool geometry is not considered. By changing the aperture angle of the cavity, influence of the cavity shape on cavity performance was evaluated.

Before manufacturing of the microcavities, it is necessary to know the tendency of shape dependency on the cavity performance. Electro-magnetic field analyses of the cavity were performed by a finite element method (COMSOL Multiphysics), assuming that the cavity diameter is 500 μm. The analysis results are shown in Fig. 6-6. The distribution of light changes accordingly, and the smaller the aperture angle is, the more inner the light tends to distribute. Especially, the red part shows the densest in the light
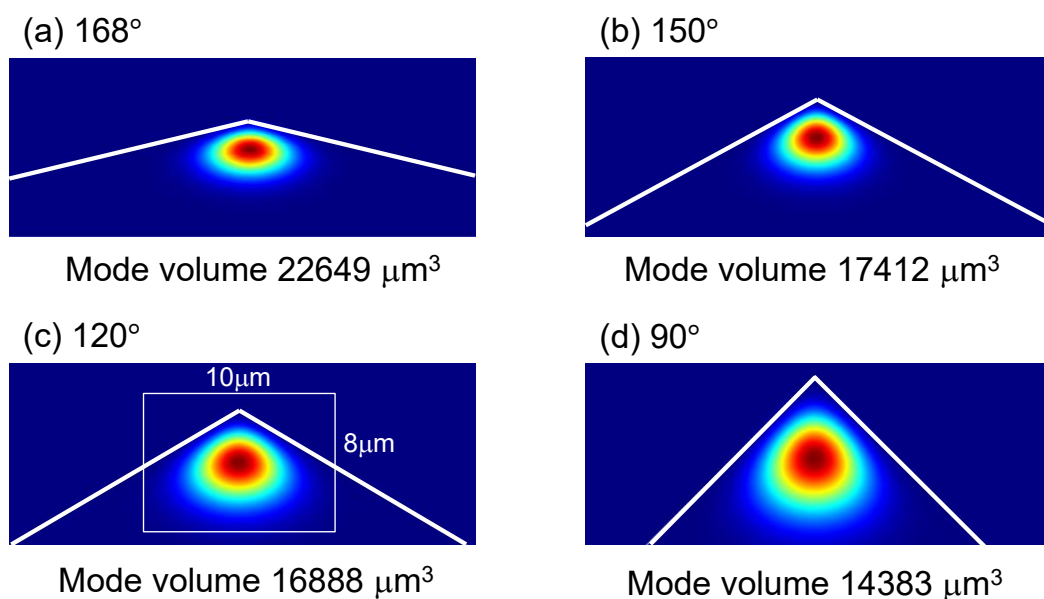
Fig. 6-6 Electromagnetic field analyses of the resonance in the cavity. The aperture angles are (a) 168 °, (b) 150 °, (c) 120 °, and (d) 90 °.

distribution, which is apt not to be affected by scattering loss from the surface according to the reduction of the aperture angle. Additionally, the mode volume was also calculated. The mode volume decreases when the aperture angle decreases, which means that the light-matter interaction can be stronger.

The manufactured microcavities are shown in Fig. 6-7, and each Q factor was measured (Table 6-2). The Q factor tends to increase according to the reduction of the aperture angle. However, there is little difference between 120 ° and 90 ° microcavities, and rather the cavity performance can be deteriorated in the case of 90 ° microcavity. Although the cutting tool was set perpendicular to the rotational axis and its nose is rounded, the surface quality can change as the tool position is not perpendicular to the microcavity surface. Additionally, the smaller the aperture angle is, the more unstable the cutting process is, due to the decreased dynamic stiffness. This could lead the slight instability of the cutting process, and deteriorate the surface integrity. In this research, the aperture angle of 120 ° is determined as an optimal value.
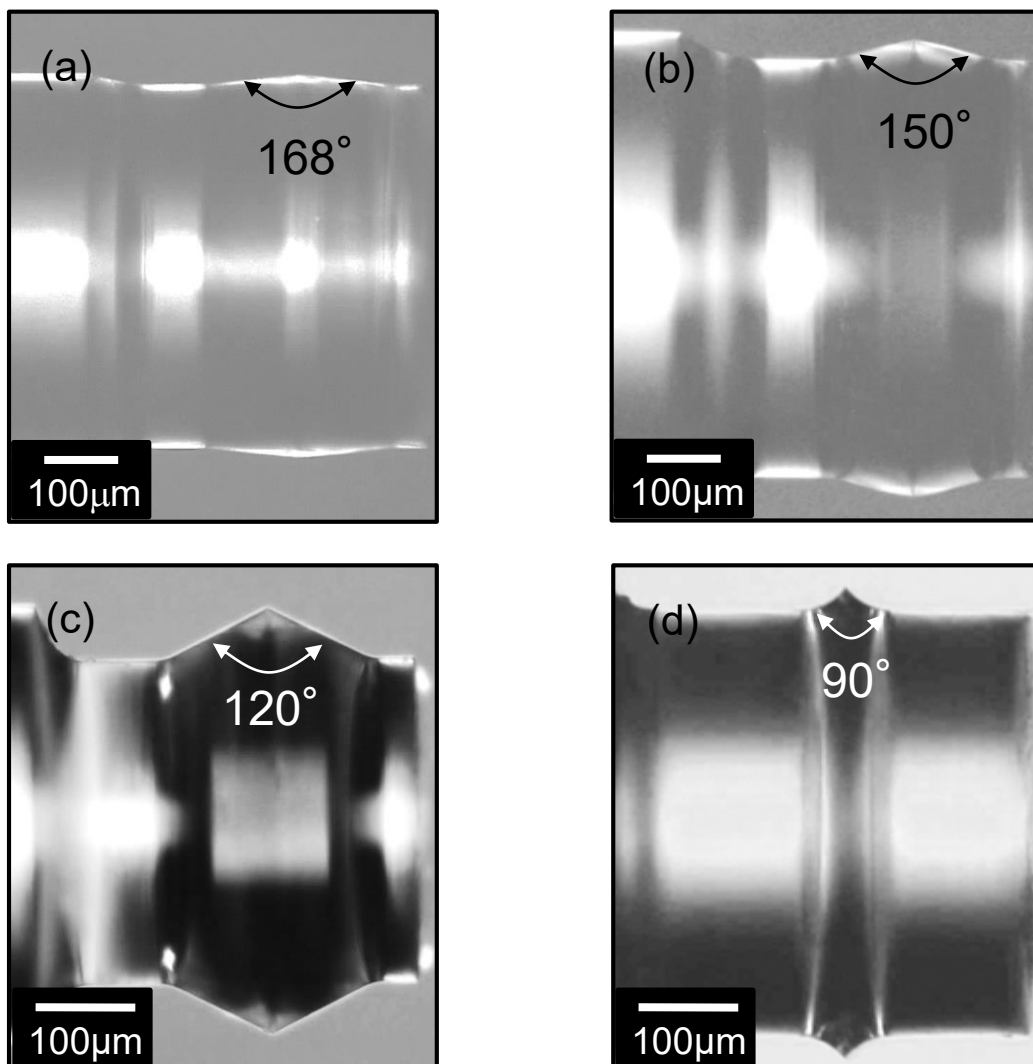
Fig. 6-7 Image of manufactured cavity with aperture angles (a) 168 °, (b) 150 °, (c) 120 °, and (d) 90 °.

Table 6-2 Variation of Q factor in dependency with the aperture angle of cavity

Aperture angle of microcavity [°]	Q factor
168	4.0×10^5
150	7.1×10^5
120	1.4×10^6
90	1.2×10^6

Subsurface quality dependency on cavity performance

As discussed in section 4.2.3, the SSD depth and its morphology are different depending on the tool geometry and tool type even if the surface roughness is almost same. Therefore, it is worth investigating the influence of SSD on the cavity performance. As shown in Fig. 6-8, the same shape microcavities (120 ° aperture angle) were manufactured using different tools (tools #2, #3, and #5 which are listed in Table 4-2.). Although the size of the resonance part is different, the part wherein the resonance occurs is limited in approximately 8 μm × 10 μm rectangle region as shown in Fig. 6-6 (c). Therefore, the difference of the resonance part among the microcavities is assumed not to affect the cavity performance. The over 10^5 Q factor was obtained for each microcavity; 6.6×10^5 of Q factor for the microcavity with tool #5 (0.2 mm nose radius and B-NPD), 1.4×10^6 of Q factor for the one with tool #2 (0.05 mm nose radius and SCD), 4.6×10^6 of Q factor for the one with tool #3 (0.01 mm nose radius and SCD). Thus, the tool #3 enhanced not only the SSD depth but also the cavity performance greatly. When using the CaF$_2$ with (100) end face orientation, the surface roughness values did not change depending on the tool type and crystal anisotropy.

Although the cutting direction and crystalline plane do not correspond to the UPCT tests (the diagonal tool path was hired in manufacturing of the cavity whereas the UPCT
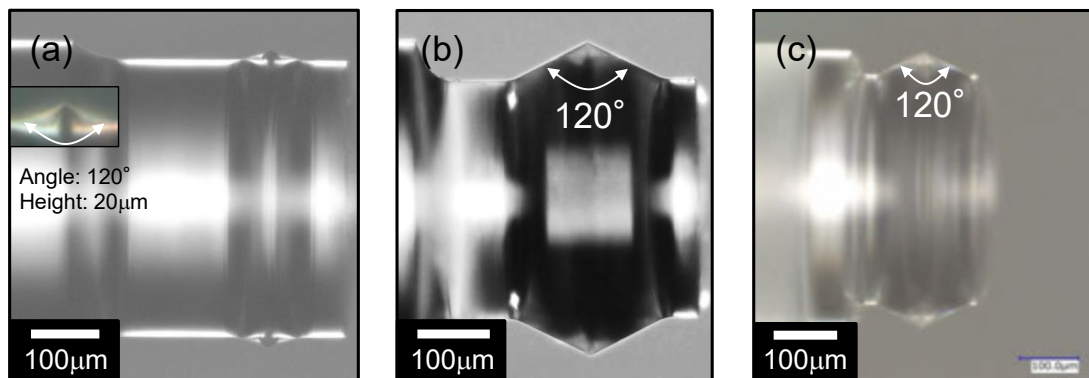
Fig. 6-8   Image of manufactured cavity. the shape of cavity shape which contributes to the resonance is the same, however, manufactured by using different SCD tools (a) Tool #5 (0.2 mm nose radius, B-NPD), (b) Tool #2 (0.05 mm nose radius, SCD), and (c) Tool #3 (0.01 mm nose radius, SCD). The detailed specification is listed in Table 4-2.

tests were conducted by feeding the tool parallel to the axial direction), it can be assumed that the surface roughness value does not differ. A resonance region in the microcavity does not change among the microcavities (see Fig. 6-6 (c)). The SSD depth varies in dependency with tool geometry (Fig. 4-40). The variation of SSD depth according to crystal anisotropy was also evaluated among tools #2 and #3, whose results show the difference of SSD depth in a nanometric size. Although the deviation of SSD depth is a few to ten nanometer scale, it is considered that the SSD depth affects the cavity performance. Notably, the difference of SSD between tool #5 and tool #2 was bigger than the one between tool #2 and #3, however, the Q factor did not greatly change. As aforementioned regarding the surface roughness, the criterion which is demanded for optical devices exists e.g. surface roughness S_a values has to be lower than the value of the used light wavelength $\lambda/20$ nm. Therefore, there might be also some critical value of SSD which significantly changes the optical performance.

Considering the surface roughness, the Q factor could be estimated as follows [21]:

$$Q \approx \frac{3\lambda_m^3 D}{8n\pi^2 B^2 R_q^2} \qquad (6\text{-}3)$$

Since the cavity size is demanded to be smaller, lower surface roughness values is demanded. To achieve the crack-free surface, the surface roughness S_a has to be lower of less than around 3 nm (see Fig. 4-34, Fig. 4-35, and Fig. 4-36). The existence of brittle fracture deteriorated the Q factor (Fig. 6-4). It can be said that partial deterioration of the surface roughness affected the Q factor from 10^5 order to 10^4. Considering the Q factor limited by absorption in the cavity, the Q factor could be also estimated [21]:

$$Q = \frac{2\pi n}{\alpha_{abs}\lambda_m} \qquad (6\text{-}4)$$

It is assumed that the variation of crystalline structure in subsurface layer causes the increase of absorption coefficient which relates to the resonance. Indeed, the reduction of the SSD enhanced the Q factor from 5.5×10^5 to 4.6×10^6. In terms of the surface integrity, the existence of the brittle fracture (surface roughness) was dominant on the cavity performance for the low Q factor regime (from 10^4 to 10^5), whereas the SSD was dominant for the high Q factor regime (more than 10^6).

In this study, the 4.6×10^6 was the highest Q factor. It should be noted that Grudinin obtained the CaF$_2$ microcavity with Q factor of up to 10^7 by only precision turning [21]. Since the influence of crack on the cavity performance was discussed, the crack existence is less likely. The SSD affected the cavity performance, therefore, the SSD formation can be a plausible reason for deterioration of Q factor. For enhancement of Q factor, polishing has been frequently used [21, 23-25]. Nevertheless, the polishing technique is demanded to avoid because the polishing changes the cavity shape manufactured by cutting. The microcavity shape is important not only for the high Q but the microcavity dispersion.

6.2 Dispersion-tailored microcavity

In previous section, the validity of the proposed cutting technique on manufacturing of microcavity was discussed. As aforementioned, the polishing technique is required to be avoided although the technique enables to enhance the surface integrity i.e. Q factor because the microcavity shape can change by polishing. In this section, a trapezoidal microcavity is manufactured which shows a possibility to realize an octave-spanning optical Kerr frequency comb.

6.2.1 Design of the dispersion-tailored microcavity

Dispersion in the cavity means variation of a refractive index of material in dependency with light frequency. Due to the dispersion an interval of resonant frequencies does not align with equally spaced intervals, which is called FSR (Free Spectral Range). The dispersion of a cavity is determined by combination of the geometrical and material dispersions. The FSR spacing changes when a dispersion exists in the cavity. The second-order dispersion β_2 is given as [175]:

$$\beta_2 = -\frac{1}{4\pi^2 R} \cdot \frac{\Delta(\Delta v_l)}{(\Delta v_l)^3} \tag{6-5}$$

$$\Delta v_l = \frac{v_{l+m} - v_{l-m}}{2m} \tag{6-6}$$

$$\Delta(\Delta v_l) = \frac{v_{l+m} - 2v_l + v_{l-m}}{m^2} \tag{6-7}$$

The β_2 was calculated according to the designed cavity shape (Fig. 6-9). Whereas the triangular microcavity and spherical microcavity feature positive values at around 1550 nm wavelength regime, the β_2 value for a trapezoidal microcavity was negative in the range of 1313 to 2771 nm wavelength. The negative value indicates that an anomalous dispersion can be obtained over one octave. Therefore, a trapezoidal microcavity shown in Fig. 6-9 (b) is more appropriate for anomalous dispersion.
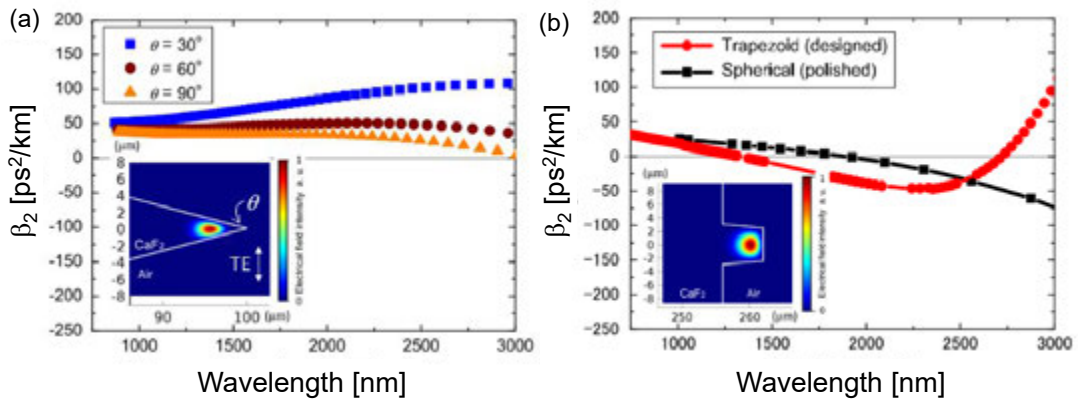
Fig. 6-9   Variation of the dispersion for (a) triangular, (b) trapezoidal and spherical shape [176].
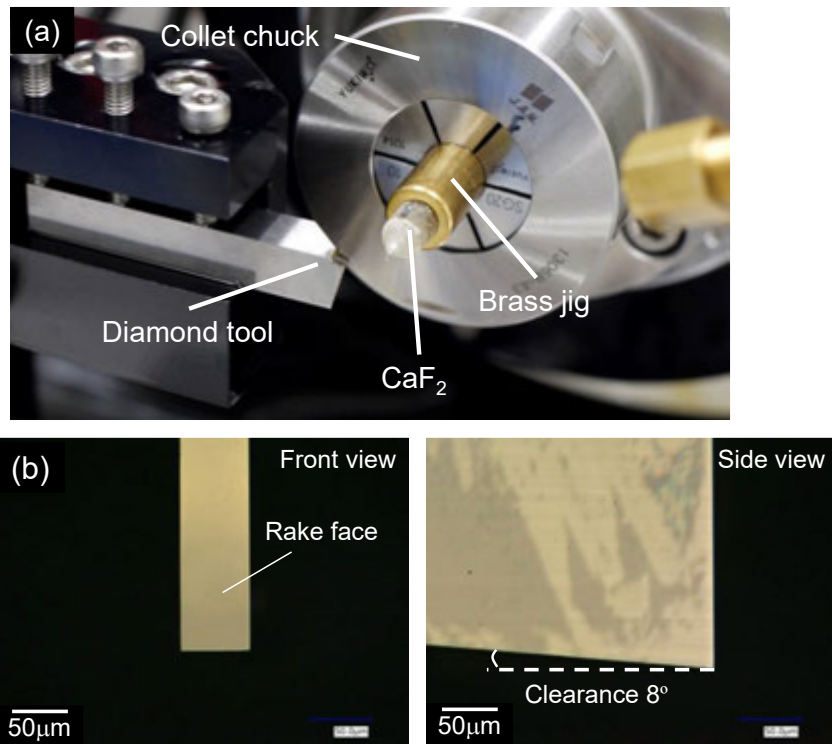
Fig. 6-10 Images of (a) experimental setup for manufacturing of the trapezoidal microcavity, and (b) used straight-nose SCD tool.
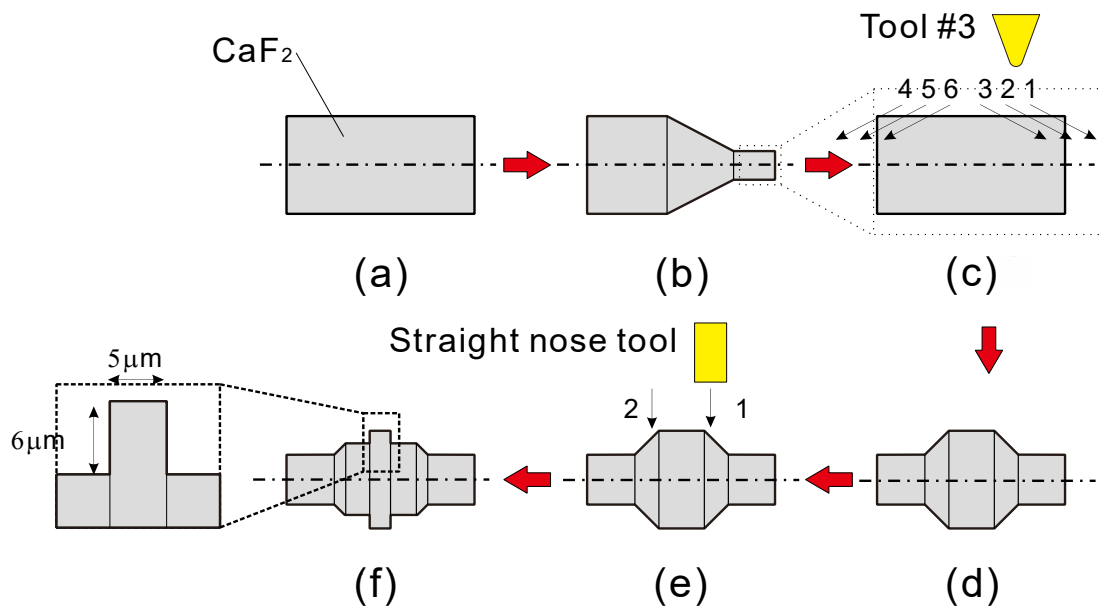
Fig. 6-11 Fabrication flow of trapezoidal microcavity. (a), (b) CaF$_2$ cylinder was firstly turned to form a conical shape. (c), (d) CaF$_2$ was cut with tool #3 by applying the diagonal tool path. (e) Bulged-shape cavity was cut by straight nose tool (f) Finally the trapezoidal cavity was obtained.

6.2.2   Manufacturing procedure

The manufacturing procedure of the trapezoidal cavity is shown in Fig. 6-11. Since it is more difficult to fabricate the shape compared to the triangular ones, 5-axis machine tool (FANUC, ROBONANO α-0iB) was used (Fig. 6-10 (a)). For finish cutting, the tool #3 (0.01 mm and 0 ° rake) was used. The straight-nose SCD tool was used for forming the trapezoidal part of the cavity as shown in Fig. 6-10 (b). The detailed procedure is described as follows (Fig. 6-11):

(1) Same as the case of triangular shape, the CaF_2 cylinder was firstly turned to form a conical shape (Fig. 6-11 (a) and (b)).

(2) The CaF_2 was cut with tool #3 (nose radius of 0.01 mm) by applying the diagonal tool path (Fig. 6-11 (c) and (d)).

(3) The bulged-shape microcavity was cut by straight nose tool as shown in Fig. 6-11 (e), and finally the trapezoidal cavity was obtained (Fig. 6-11 (f)).

6.2.3   Results and discussion

The manufactured trapezoidal microcavity is shown in Fig. 6-12. the trapezoidal shape was successfully formed without visible brittle fracture or scratches. The surface roughness on the resonance part was difficult to measure, therefore, the surface roughness at the same height as the resonance part (the red-pasted area in the WLI image (Fig. 6-12(b))) was measured, and the surface roughness S_a was approximately 3
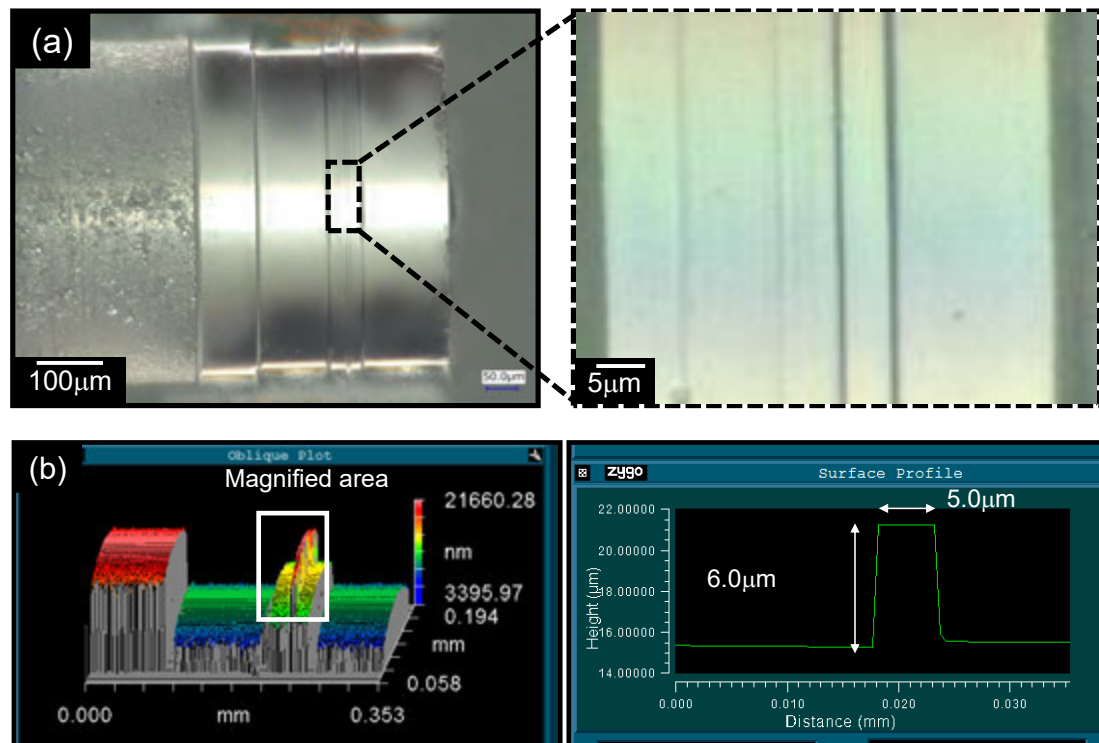
Fig. 6-12   Appearance of trapezoidal microcavity captured by (a) micrograph and (b) WLI.
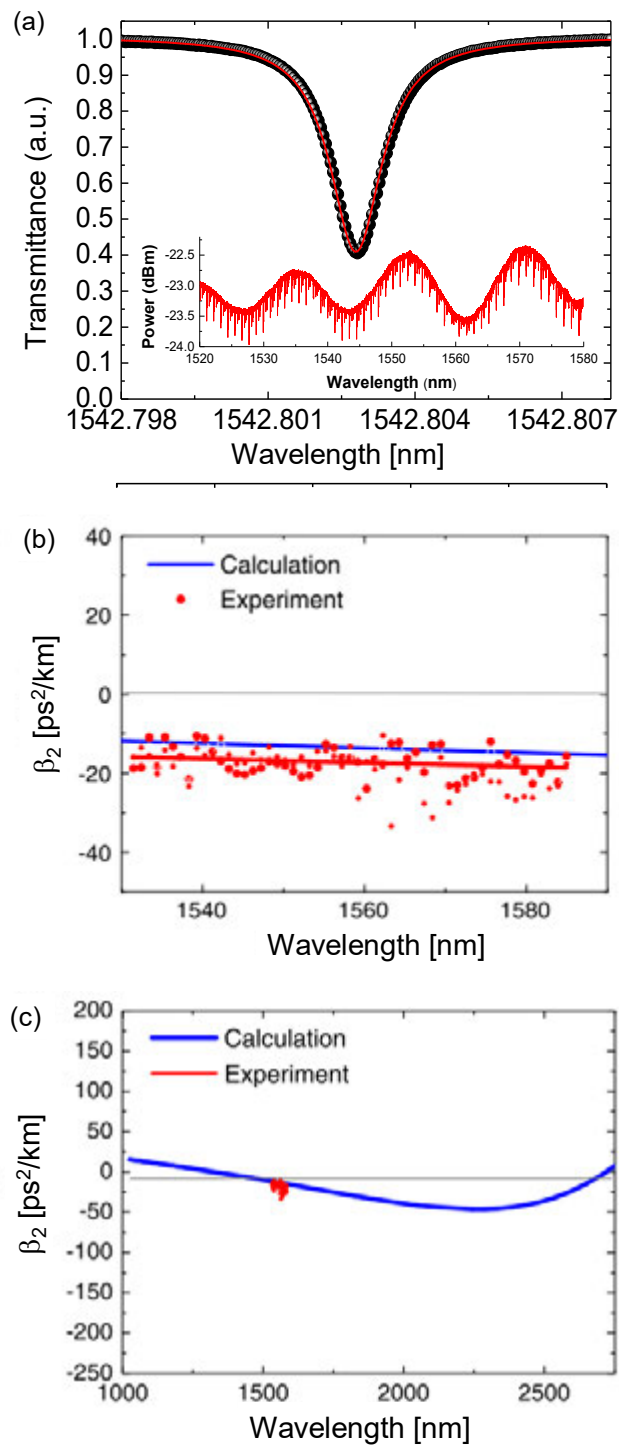
Fig. 6-13 Cavity performance of the trapezoid microcavity. (a) The transmittance spectra. The inset image shows the spectra in a wide range of wavelength. (b) Calculated and measured dispersion of the trapezoidal cavity. (c) The dispersion in the wide range [176].

nm. This is the same value of the polished surface in other work [18].

The Q factor of 1.2×10^6 was obtained, which corresponds to the cavity manufactured in section 6.1 and trapped light for 0.98 ns. Since the Q factor was higher than the microcavity with brittle fracture (Fig. 6-4 (b)), it is evident that there was no brittle

fracture on the resonance part (Fig. 6-12). Notably, the surface roughness on the side wall of the cavity could not be measured due to the difficulty of the measurement, however, the surface was assumed to be smooth, for the Q factor is over 10^6. The dispersion of the cavity was measured. Firstly, the wavelength from 1480 to 1640 nm was scanned at the input power of 10 μW to measure the resonance wavelengths. The transmittance spectra are partially shown in the inset of Fig. 6-13 (a). The dispersion was calculated by using Eq. (6-5) to Eq. (6-7), substituting m = 50. The experimental results coincide well with the calculated values (Fig. 6-13 (b)). Due to the limitation of measurement of wavelengths, the dispersion was not evaluated over the whole wavelength regime, however, the tendency of the experimental results can follow the calculated ones. Notably, the similar microcavity was designed in previous study [26], however, the negative dispersion bandwidth is broader than the previous one.

6.3   CaF$_2$-brass hybrid cavity

   Until previous section, only turning process was used to manufacture a CaF$_2$ microcavity. For stable generation of an optical Kerr frequency comb, it is necessary to diffuse heat induced by resonance. As mentioned in section 2.1.4, CaF$_2$ shows a negative thermos-optic coefficient, therefore, when the optical input power is high, the cavity performance becomes unstable due to the thermal issue. In this section, suppression of the TOM oscillation was attempted by manufacturing a microcavity with a hybrid structure.

6.3.1   Design of the hybrid cavity

   As explained in section 2.1.4, since the effective refractive index n_{eff} and cavity radius r change due to the input optical power, it is necessary to design a novel type cavity. Since the thermal conductivity of CaF$_2$ is quite low, the conventional structure has to be modified (Fig. 6-14 (a)). One solution is to combine a different material with CaF$_2$. The material has to be much more thermally conductive than CaF$_2$, and easy to be
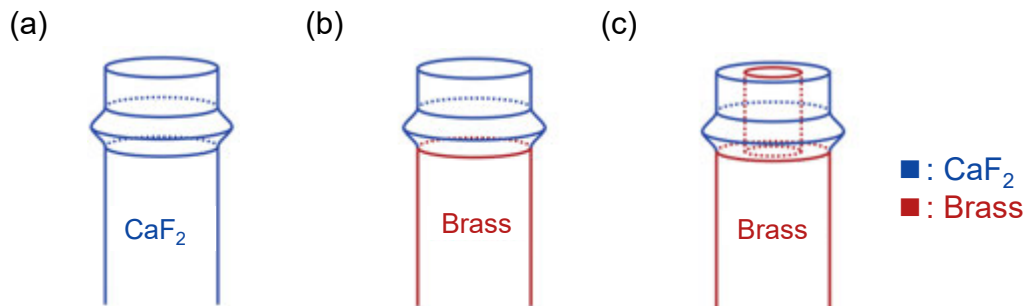
Fig. 6-14   Schematic illustration of the designed cavities (a) conventional structure (b) microcavity pedestaled on brass (denoted as junction type) (c) hybrid structure (denoted as embedded type)

Table 6-3 Temperature distribution simulation condition

Parameter	Value
Thermal conductivity [W/(m·K)]	9.7 (CaF_2), 401 (cooper)
Density [kg/m³]	3180 (CaF_2), 8960 (cooper)
Heat capacity [J/(kg·K)]	911.3 (CaF_2), 385 (cooper)
Cavity radius [µm]	247 (CaF_2)
Q value	1.0×10^7
Optical input power P_{in} [W]	1
Wavelength [nm]	1550
Refractive index	1.4261
Absorption coefficient [cm⁻¹]	2.0×10^{-5}
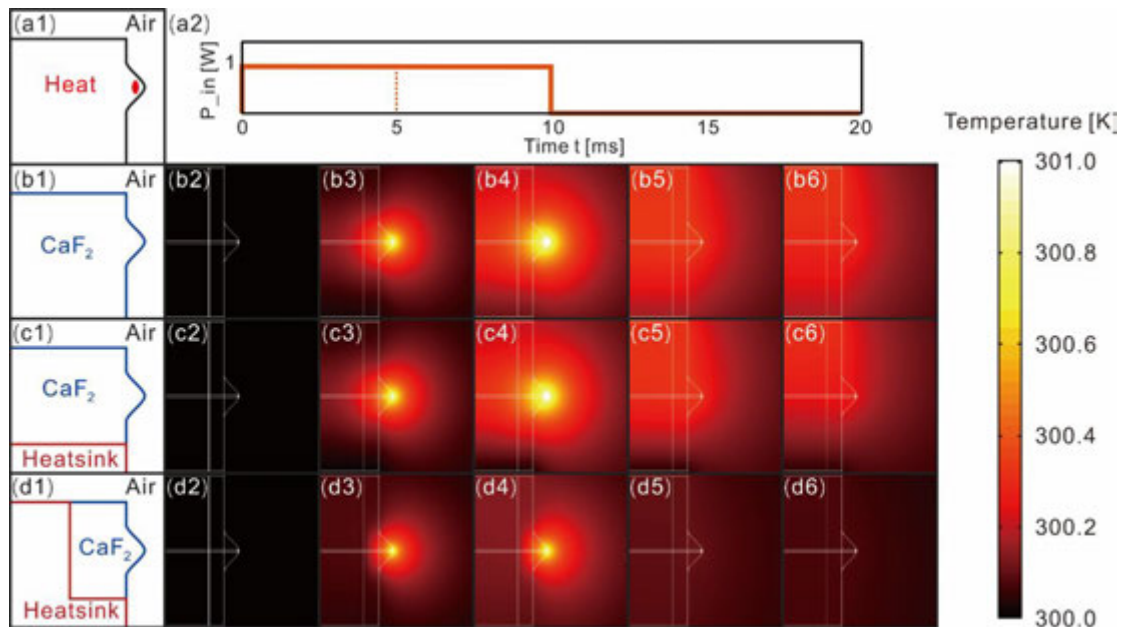
Fig. 6-15   FEM simulation of heat flow in the time domain: (a) Given optical input power. Cross section and thermal diffusion of the (b) conventional structure, (c) semi-hybrid structure, and (d) hybrid structure.

handled and machined. Then, the material can be a heatsink for the CaF_2 cavity, similar to Pavlov's approach [27] in the case of MgF_2. Two types of the cavity structure were proposed as shown in Fig. 6-14 (b) and (c). The junction type cavity is a semi-hybrid cavity whose CaF_2 microcavity part is placed on a brass material (Fig. 6-14 (b)). The hybrid cavity consists of CaF_2 microcavity with a through hole and brass with a stylate rod.

Before manufacturing of the hybrid cavity, validity of the designed cavity structure was confirmed by FEM simulation. The temperature distribution was simulated by the

same software (COMSOL, Multiphysics) which was used to simulate the distribution of electromagnetic field in section 6.1.2. The simulation conditions are listed in Table 6-3. Copper is a main element of the brass rod [177], therefore, the material properties of copper was employed (built in COMSOL database). The input heat source of 4.42 W/m was calculated from 1.0×10^7 Q factor, 1 W optical input power, and 2.0×10^{-5} cm^{-1} absorption coefficient. The initial input heat was given with an area that corresponds to the simulated electromagnetic field.

The heat distribution behavior varies depending on the cavity structure in the time domain as shown in Fig. 6-15. The simulation results of heat diffusion in each cavity structure in each time window (0, 5, 10, 15, and 20 ms) correspond to (bn), (cn), and (dn) (n = 2, 3, 4, 5, 6). Similar tendency was seen in the case of both conventional structure and semi-hybrid cavity (Fig. 6-15 (b) and (c)). The induced heat remains around the resonance region after stopping providing the input heat. On the contrary to those cases, the heat quickly diffuses from the resonance part in the case of hybrid cavity (Fig. 6-15).

Table 6-4 Experimental condition for drilling process

Parameter	Value
Rotational speed [min^{-1}]	10000
Cutting speed [m/min]	$0 - 12.6$
Hole depth [mm]	0.5
Crystal orientation of main plane	(100)
Lubrication	Water-soluble oil in 1:100 ratio
Cutting tool	Cemented carbide end-mill (0.4mm diameter)

■: CaF$_2$ ・ ■: Brass
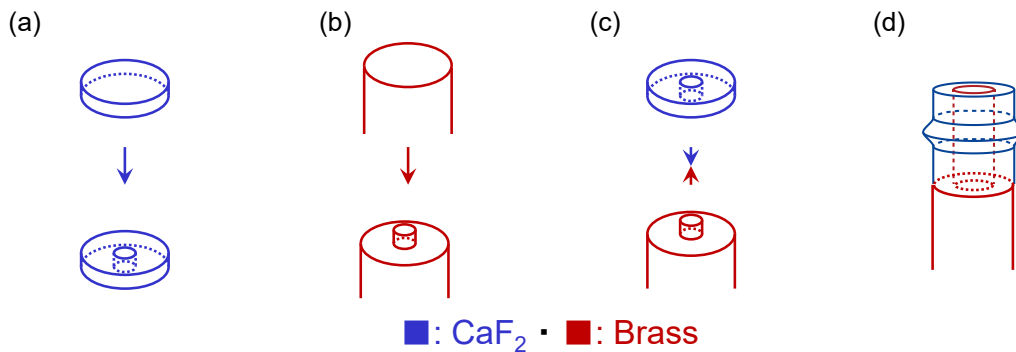
Fig. 6-16   Schematic illustration of manufacturing procedure of hybrid cavity. (a) A through hole was formed by a drilling process into CaF$_2$ wafer. (b) A stylate brass rod was manufactured by straight nose tool. (c) The CaF$_2$ wafer was mounted onto the stylate brass and fixed by wax. (d) The CaF$_2$ and brass jig were turned by UPCT simultaneously, and the final cavity shape and structure was formed.

The area wherein heat distributes is smaller than that of other structure (compare Fig. 6-15 (b5), (c5), (d5)). Therefore, it is evident that the hybrid structure made of the brass is functioning as a heatsink for quick heat diffusion. For the suppression of TOM oscillation, the CaF_2-brass hybrid microcavity was attempted to manufacture in this dissertation.

6.3.2 Manufacturing procedure

In addition to UPCT, additional fabrication process is necessary for manufacturing of hybrid structure microcavity. In order to make a through hole into the CaF_2, drilling process was used. The manufacturing procedure is depicted in Fig. 6-16 , and the detailed explanation is described as follows:

1. The CaF_2 workpiece (diameter of 6 mm, thickness of 0.5 mm) was prepared. In the CaF_2, a through hole of approximately 400 µm diameter was drilled using a cemented carbide tool under the condition listed in Table 6-4. One fed the cutting tool manually by NC operation with 100 nm steps (Fig. 6-16 (a)).
2. A stylate brass rod was manufactured from a brass cylinder with diameter of 6 mm under the cutting condition listed in Table 6-1 (Fig. 6-16 (b)). The straight-nose diamond tool (see Fig. 6-10 (b)) was used to form a stylate part with 370 µm diameter.
3. The CaF_2 workpiece was glued by wax onto the stylate brass into a through hole of CaF_2 (Fig. 6-16 (c)). Then, both materials were simultaneously turned under finish-cutting condition. Finally, the demanded hybrid structure shown in Fig. 6-16 (d) was manufactured.

6.3.3 Results and discussion

A through hole of 400 µm was formed without any large chipping around the hole (Fig. 6-17 (a)), and the brass stylate rod was manufactured (Fig. 6-17 (b)). The brass rod is embedded in the CaF_2 workpiece through a hole (Fig. 6-17 (c)). As the diameter of the hole in the CaF_2 and brass cylinder is not identical and fixture procedure of the CaF_2 and brass was conducted manually, the brass rod was not perfectly aligned at the cavity
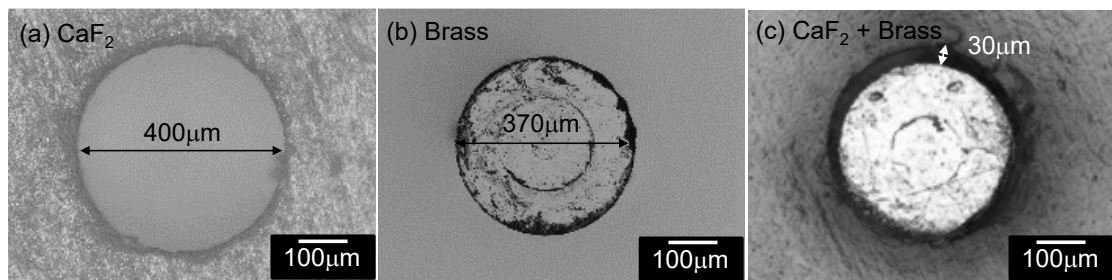
Fig. 6-17 Images of (a) the CaF_2 workpiece with a through hole of 400 µm diameter. (b) The brass with a stylate rod of 370 µm (c) the CaF_2 mounted onto brass through a stylate rod part.
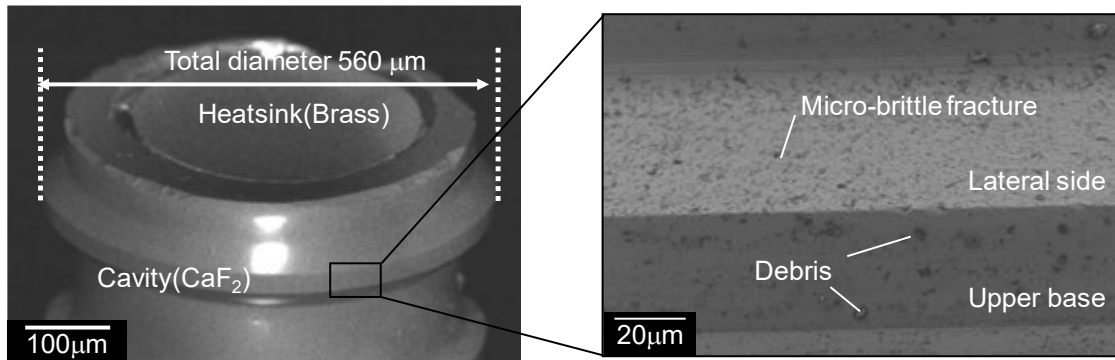
Fig. 6-19 SEM images of the manufactured hybrid cavity that consists of the CaF₂ and brass materials.
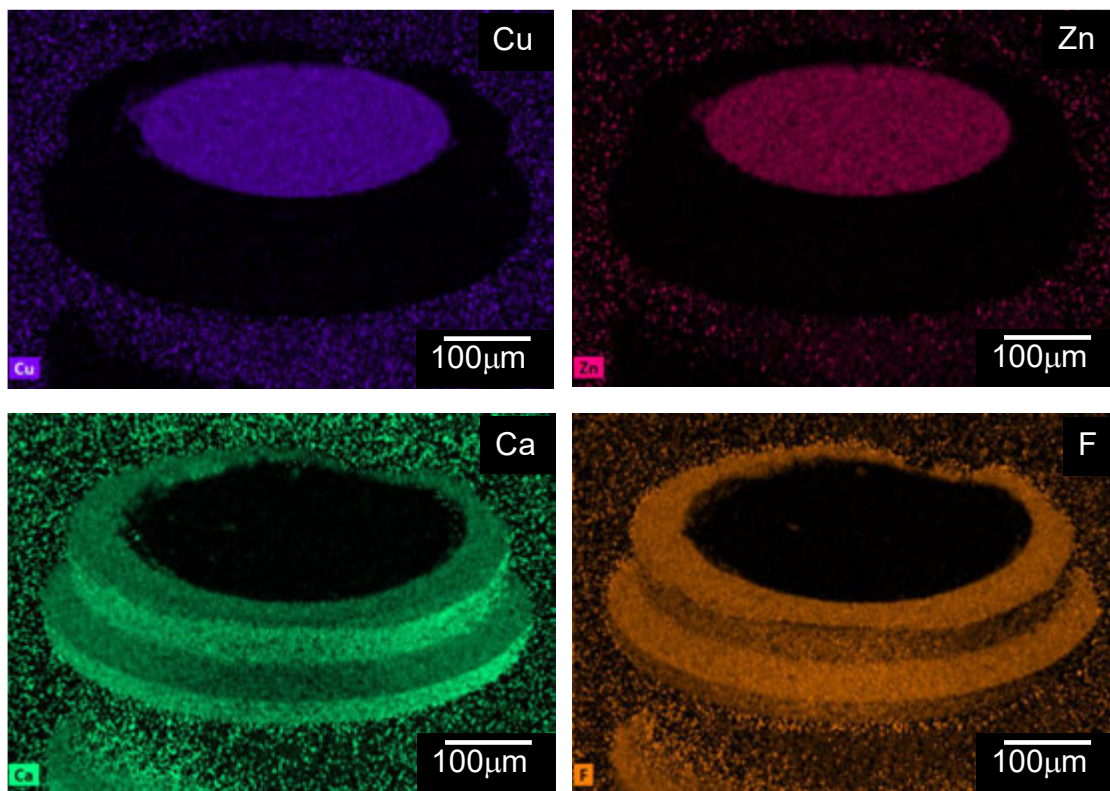
Fig. 6-18 EDX analyses of the hybrid cavity. The heatsink part consists of Cu and Zn while Ca and F correspond to the cavity part.

center. Therefore, the brass rod touches the inner hole at a certain area, and air or wax exists at the rest area. After fabrication, a hybrid cavity with 500 μm diameter was obtained as shown in Fig. 6-19. A trapezoidal–like shape was manufactured because the cutting process can be more unstable than when the triangular shape cavity made of mono-material was manufactured. Brittle fracture which causes the significant scattering loss from the cavity was not seen on the whole cylindrical surface, and the surface roughness S_a of approximately 2 nm was obtained. However, it should be mentioned that some debris on the upper base side of the microcavity and microbrittle

fracture on the surface along the lateral side of the cavity were confirmed, which can cause the deterioration of Q factor. Although the CaF_2 cylinder was partially supported from the inside (the brass rod), there is an air gap or wax between the inner surface of CaF_2 and cylindrical surface of brass. The total thickness of CaF_2 cavity is around 100 μm, therefore, the dynamic stiffness of the CaF_2 material can be much more decreased than that of the non-drilled CaF_2 material. It is obvious that copper (Cu) and zinc (Zn) are in the heatsink part, then, calcium (Ca) and fluorine (F) exist around the brass cylinder by EDX analyses. Thus, the result is an evidence that the brass rod is embedded inside the CaF_2 through a hole. It should be noted that aluminum (Al) was detected, which originates from the SEM stub. Carbon (C) is assumed to come from the adhered wax between the cavity and cylindrical brass. For comparison, the conventional structure cavity (mono-material) was also manufactured. To enhance the surface integrity, the surface was polished.

The Q value of the conventional structure cavity measures 1.0×10^7, whereas the Q value is 2.8×10^5 in the case of the hybrid cavity. Therefore, Q value was deteriorated to the order of 10^5. As discussed in section 6.1.2, Q value was deteriorated by the existence of brittle fracture to 10^3, 10^4 order. Although no brittle fracture is observed on the upper base of the hybrid cavity, the brittle fracture on the lateral side could deteriorate the Q factor. The cause for their existence might be the adhering debris that originates from the chip.
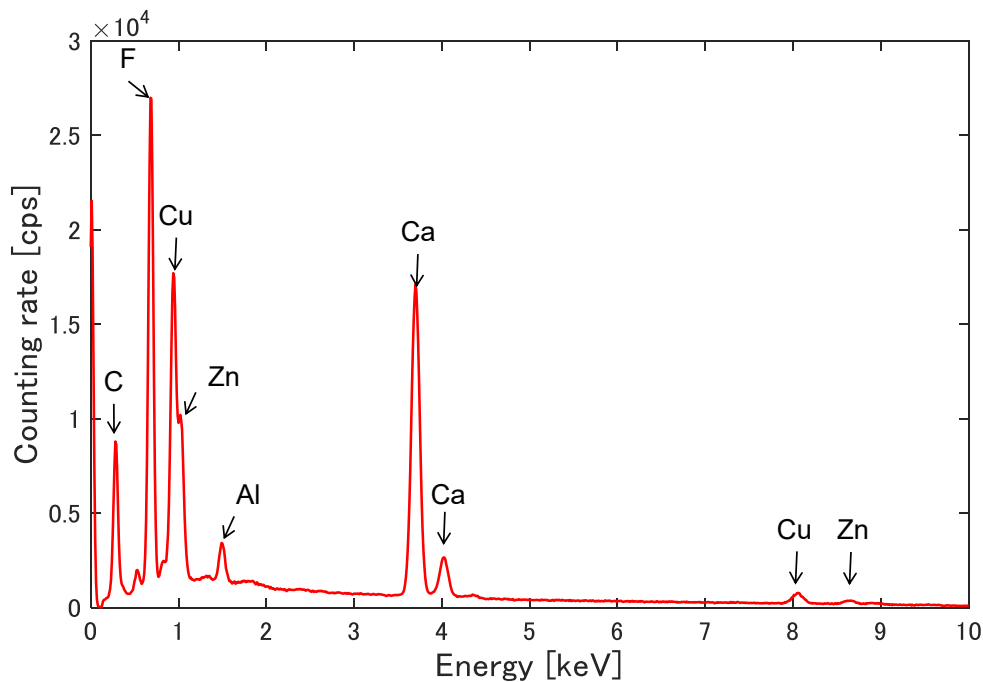
Fig. 6-20 The EDX spectrum of the whole cavity. Notably, aluminum (Al) of the SEM stub is detected. Carbon (C) originates from the element of wax.
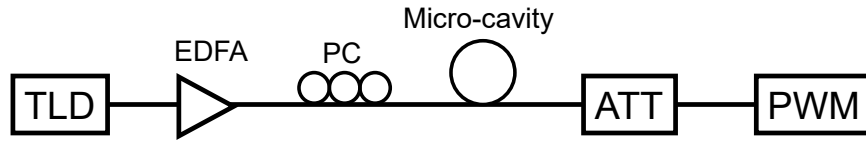
Fig. 6-21 Adapted measurement setup for TOM oscillation.
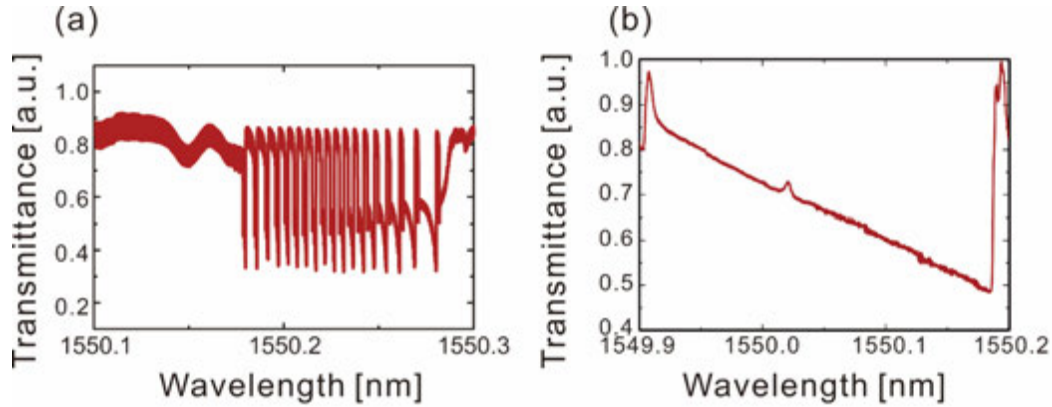
Fig. 6-22 Transmittance spectra for (a) conventional structure cavity and (b) hybrid cavity.

The aforementioned measurement setup (Fig. 6-3) was adapted to measure the TOM oscillation. Between TLD and PC, EDFA (Erbium Doped Fiber Amplifier) was inserted to amplify the input light. Further, ATT (Attenuator) was installed between microcavity and PWM to attenuate the light power (Fig. 6-21).

In the range of 1550.15 to 1550.30 nm wavelengths, several resonance peaks are observed in the case of the conventional structure cavity, whereas only one resonance peak appeared in the case of hybrid cavity (Fig. 6-22). As mentioned in section 2.1.4, the cavity performance (here, transmittance spectra) can be unstable by TOE oscillation that consists of the competition between TO and TE effects. The transmittance spectra of the conventional cavity form those jig-gag peaks due to the effects. The detailed mechanism is explained as follows (Fig. 6-23):

(1) The input wavelength λ_i continuously shifts from a shorter to a longer wavelength.

(2) When λ_i corresponds to the resonance wavelength λ_r, the light is confined in the cavity. In other words, resonance occurs.

(3) Due to the TO effects, the effective refractive index n_{eff} decreases, which leads that λ_r shifts to a shorter wavelength.

(4) Due to TE effects, the effective radius r_{eff} becomes larger because the cavity expands. Therefore, λ_r shifts to a longer wavelength.

(5) When λ_r corresponds to λ_i, the light is confined again. Thus, resonance occurs twice in one loop.
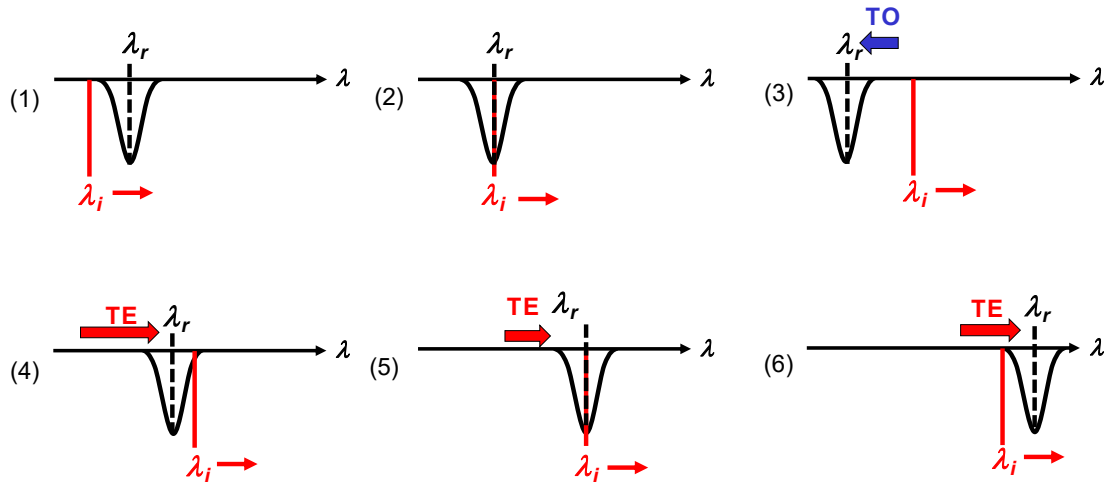
Fig. 6-23   Mechanism of unstable resonance caused by TOM oscillation. (1) λ_i shifts from a shorter to a longer wavelength side. (2) When λ_i corresponds to λ_r, resonance occurs. (3) Because of TO effects, λ_r shifts to a shorter wavelength. (4) Owing to cavity expansion induced by TE effects, λ_r shifts to a longer wavelength (5) When λ_r corresponds to λ_i, the light is trapped again (6) Due to TE effects, λ_r overtakes λ_i

(6) λ_r overtakes λ_i because r_{eff} becomes too large due to TE effects. After a certain time, the temperature in the cavity decreases and the TE effects become smaller. The value of λ_r moves towards that of λ_i, and the procedure returns to state (1).

When the value of λ_r cannot reach that of λ_i in state (6) the oscillation ends. Due to this loop, a lot of resonance peaks were seen in the range of quite short wavelength regime for the conventional cavity. However, only one resonance peak was observed for a longer time window, and the resonance spectra form triangular shapes induced by TE effects (repetition of states (4), (5), and (6)). The phenomenon can be seen for SiO_2 or MgF_2 [25], which is also the desired optical characteristic for CaF_2. In the hybrid cavity, the induced heat quickly dissipates through the heatsink. Therefore, the absolute time windows of TO and TE effects are shorter than those in the case of the conventional cavity. This leads the idea that TO effects, which take place in a shorter time window, are assumed to be suppressed, and the resonance occurred only once. It can be concluded that the thermal effects did not interfere the resonance, and the performance was stabilized.

6.4   Summary

In this chapter, the CaF_2 microcavities were manufactured by UPCT and the performance was evaluated. The contents are summarized as follows:

1.   The CaF_2 microcavity was manufactured by UPCT based on the experimental results which was described in chapter 4. Whereas the cavity with brittle fracture shows the

Q factor of approximately 10^4, the microcavity without any fracture shows a Q factor of over 10^5. The cavity shape also influenced on the cavity performance, and the Q factor was apt to increase in dependency with the reduction of the aperture angle. The subsurface quality could also affect the cavity performance, and the reduction of the SSD depth contributed to the enhancement of the Q factor by using different nose radius tools. Considering the above-mentioned influential factors on the cavity performance, as the highest Q value, 4.6×10^6 was obtained.

2. For the aim of anomalous dispersion, the trapezoidal microcavity was manufactured. 1.2×10^6 Q factor was obtained for the trapezoidal microcavity. The dispersion of manufactured trapezoidal cavity was experimentally measured, and showed a good agreement with the calculated values which are in the range of anomalous dispersion.

3. The CaF_2-brass hybrid microcavity was manufactured by combination of UPCT and drilling process, and the thermal instability on cavity performance was assumed to be stabilized by suppression of TO effect.

7.   Conclusions

In this dissertation, the surface and subsurface integrity of single crystalline calcium fluoride (CaF_2) and sapphire in ultra-precision cutting process were elucidated in the viewpoint of crystallography. On the basis of the obtained results, the whispering gallery mode (WGM) CaF_2 microcavity was manufactured using an ultra-precision cutting technique, and the cavity performance was related to the surface and subsurface integrity and cavity shape that were formed by ultra-precision cutting.

In Chapters 2, the current microcavities and their fabrication process were explained. Considering the form accuracy, surface quality, and material properties, the ultra-precision cutting was regarded as an appropriate fabrication process in this dissertation, and the state-of-the-art studies were explained. Challenges of the machinability of single crystalline CaF_2 and sapphire in cutting were described and necessity of WGM crystalline microcavity was presented.

In Chapter 3, the material fracture system that contributes to the ultra-precision cutting process of single crystalline materials were introduced; slip system, cleavage, and twinning. Firstly, the concept of slip, cleavage, and twinning was presented to explain how those mechanisms are related to the material deformation behavior. The influence of crystal anisotropy on the machined surface can be affected by those fracture systems. To analyze the ease of activation of the fracture systems, resolved stress models were explained. For slip system, Schmid factor was especially focused as a representative indicator for analyses of stress resolving. A similar factor was also presented in the case of cleavage. Those factors enabled to evaluate the influence of crystal anisotropy on the surface. For both CaF_2 and sapphire, several slip systems and cleavages exist, and the possibility of each activation is different from the system. Therefore, those factors were weighted by incorporation of critical resolved shear stress and surface energy, and those parameters were named as plastic deformation parameter P and cleavage fracture parameter C.

In Chapter 4, the plunge-cut tests were conducted to investigate the cutting performance of CaF_2. Nose radius of the tool was a main influential factor on the CDC value in plunge-cut tests. The surface morphologies and CDC values significantly changed in dependency with the cutting crystalline planes and directions, and those were characterized by a certain symmetry based on its cubic crystalline structure. For instance, when cutting (100) plane, the surface morphologies and CDC values were

characterized by four-fold symmetry. The P and C values were computed using the crystallographic information and experimentally obtained force vector to analyze the main deformation mechanism that affect the surface quality. Overall, the P value coincided well with the higher CDC values on each plane and vice versa. The observed brittle fracture was formed by the combination of {111} and {110} cleavages that agree with the high C parameter value. Primary slip system {100}⟨011⟩, {111} cleavage, and partially {110} cleavages were dominant on the surface integrity.

Next, the ultra-precision cylindrical turning (UPCT) tests were performed for the purpose of manufacturing of WGM microcavity. Tool geometry (nose radius and rake angle) greatly influenced on the surface integrity. The influence of crystal anisotropy on the machined surface was also found in the case of UPCT. The process force could not be measured due to the experimental setup, hence, the P and C parameter values were not calculated, nevertheless, the similar tendency with the plunge-cut tests was seen in UPCT tests. For instance, the machined surface without any fracture coincided with the cutting crystalline plane and direction where the P parameter value and CDC value were high in plunge-cut tests. Same as plunge-cut tests, the surface roughness and machined surface morphology were characterized by a certain symmetry. Whereas the surface roughness value and morphologies varied according to the observation points i.e. crystalline plane and direction in the case of end face orientation (111) and (110), the homogenous surface without brittle fracture was obtained at the whole cylindrical surface when the end face was set as (100). It is anticipated that the high P parameter was kept in the case of end face (100).

The subsurface damage (SSD) was also investigated via transmission electron microscopy (TEM) in UPCT tests. Even though the surface roughness was the same value in the nanometric level, the SSD depth and crystalline lattice structure were different depending on process parameter. Smaller nose radius and depth of cut reduced the SSD depth, therefore, the lowering of the thrust force that originated from the reduction of the tool contact length between tool and workpiece was assumed to be a main factor for SSD formation. The SSD depth also changed in dependency with the crystal anisotropy in the range of approximately $10 - 30$ nm, though the uniform surface was achieved at the entire cylindrical surface under the cutting condition which was optimized to minimize the SSD depth. TEM images revealed that the crystal shear and lattice rotation occurred in subsurface region, and the slip system was assumed to be a main factor on variation of SSD. When the cutting direction was identical to the slip planes which can be activated, the SSD depth was lower.

In Chapter 5, machinability of the sapphire was evaluated in plunge-cut tests. On (0001) plane, the surface morphology and CDC values were characterized by two-fold

symmetry while the three-fold or six-fold symmetry was expected based on its hexagonal crystalline structure or rhombohedral lattice family. Basically, variation of the surface morphology and CDC values coincided well with the computed P and C parameters, and high CDC values coincided with the high P parameter and low C parameters and vice versa.

The SSD was also investigated in cutting direction of $30°$ and $270°$ ($\langle 1\bar{1}00\rangle$ directions), both of which were expected to show the same surface morphology. Whereas only one basal twinning was observed in $30°$ cutting direction, several basal twins were observed in $270°$ cutting direction. Therefore, multiple basal twinning could cause the self-intersection, and rather the surface could be deteriorated.

Although it was found that the ductile-regime cutting could be conducted on sapphire substrate, the cutting tool was easily broken due to the high hardness of sapphire, thus, it was anticipated that manufacturing of the sapphire microcavity by cutting was difficult.

In Chapter 6, the CaF_2 microcavities were manufactured by UPCT and the performance was evaluated. The CaF_2 microcavity was successfully manufactured by UPCT based on the experimental results which were obtained in Chapter 4. The existence of brittle fracture, cavity shape and SSD quality significantly affected the cavity performance, and as the highest Q factor, 4.6×10^6 was obtained.

For the aim of anomalous dispersion, the trapezoidal microcavity was manufactured by UPCT. The dispersion of manufactured trapezoidal cavity was experimentally measured, and showed a good agreement with the calculated values which are in the range of anomalous dispersion.

The CaF_2-brass hybrid microcavity was manufactured by combination of UPCT and drilling process, and the thermal issue on cavity performance was assumed to be stabilized by suppression of TO effect.

To meet the high-level demands for the microcavity, the conventional fabrication process (etching or laser machining) are prohibited. For high Q, single crystalline materials such as CaF_2 or sapphire are the appropriate materials, and required to be formed of the spherical type to generate WGM resonance. Ultra-precision cutting is one of the promising fabrication methods, however, those materials are classified into difficult-to-cut materials. This dissertation provides the investigation of the cutting mechanisms of those materials based on the experimental results for aiming the manufacturing of WGM microcavities. A series of the experimental approach on crystalline materials in this dissertation is applicable to other crystalline materials e.g. MgF_2, silicon, BaF_2, $LiNbO_3$. Therefore, this dissertation can be a bridge between

machining process and manufacturing of the optical components with microfeatures. Although it is difficult to discuss the anisotropic machinability of single crystalline materials, the resolved stress model with incorporation of the energy-related parameters enabled to quantitatively analyze the anisotropic deformation behavior. The proposed approach can be also utilized for the machinability at an elevated temperature. The obtained Q factor of 4.6×10^6 is reasonably high in the category of the microcavity manufactured by only cutting process. In addition, the machining process made it possible to manufacture a trapezoidal microcavity which features an anomalous dispersion, or CaF_2-brass hybrid cavity which has a stability on a thermal issue. Thus, the cutting approach is valid for the microcavity with an advantage of flexibility on cavity shape. It should be remarked that the Q factor of the manufactured microcavity was relatively lower than other researchers works that hired the polishing process [18, 21, 23, 25, 28] (10^8 or 10^9). However, the polishing process deteriorates the form accuracy that is required for the cavity dispersion, therefore, another process has to be also considered. For instance, elastic emission machining [113, 114] is a candidate to remove only the SSD perfectly, maintaining the form accuracy.

Appendix

The appendix includes the utilized experimental equipment (specifications)

A) Specification of the used machine tools and measurement equipment

Firstly, specification of the used machine tools is listed.

Table A-1 Specification of 4-axis ultra-precision vertical machine tool (UVM-450C)

Maker / Type	TOSHIBA MACHINE / UVM-450C
Travel in each axis	X: 450 mm, Y: 450mm, Z: 200mm, A: −45° − 45°
Minimum / Maximum rotation speed [min-1]	10000 − 80000
XY stage [mm]	450×450
Resolution of position [nm]	X, Y, Z: 10
CNC System	FANUC Series 30i-MODEL A
Size of Machine tool [mm]	2100×2450×2150
Weight of Machine tool [kg]	5000

Table A-2 Specification of 4-axis ultra-precision aspherical machine tool (ULG-100E (HYC))

Maker / Type	TOSHIBA MACHINE / ULG-100E(HYC)
Travel in each axis	X:220mm, Y:20mm, Z:150mm, C: 360°
Work spindle speed [min-1]	0 − 1500
Resolution of position [nm]	X, Y, Z: 1
CNC System	FANUC Series 30i-MODEL A
Weight of Machine tool [kg]	2200

Table A-3 Specification of 5-axis ultra-precision vertical machine tool (Robonano α-0iB)

Maker / Type	FANUC / Robonano α-0iB
Travel in each axis	X:280mm, Y:40mm, Z:150mm, B, C: 360°
Work spindle speed [min-1]	0 – 250 (50,000 optionally)
Resolution of position [nm]	X, Y, Z: 1
CNC System	FANUC Series 30i-MODEL A
Weight of Machine tool [kg]	1700

Secondly, specification of the used measurement devices is listed.

Table A-4 Specification of 3-axis dynamometer

Maker / Type	Kistler / Type9256C1
Measurement force [N]	$-250 - 250$
Dynamic resolution of force [N]	0.002
Sensitivity [pC/N]	Fx:25, Fy:13, Fz:25
Weight of dynamometer [kg]	0.75

Table A-5 Specification of charge amplifier

Maker / Type	Kistler / Type5070A
Software	DynoWare 2.31
Measurement error [%]	Maximum ± 1
Weight [kg]	0.75

Table A-6 Specification of white light interferometer

Maker / Type	Zygo / New View TM6200
Vertical resolution [nm]	0.1
Measurement range [nm]	$0 - 15000$
Step height [%]	Accuracy ≤ 0.75
	Repeatability ≤ 0.5
RMS repeatability [nm]	≤ 0.1

Table A-7 Specification of FE-SEM

Maker / Type	Carl Zeiss Optics / Merlin Compact VP
Magnification	$12 - 2,000k \times$
Resolution [nm]	≤ 0.6
Accelaration voltage [V]	$20 - 30000$
Probe current [nA]	≤ 300
Modes	Secondary electron, Energy selective backscattering, STEM, EDS, EBSD

Table A-8 Specification of FE-TEM

Maker / Type	FEI / Technai TM G2 F20 S-Twin
Magnification	$12 - 1,030k \times$
Acceleration voltage [kV]	200
Resolution of point [nm]	0.18
Tilt of specimen [°]	± 20
Observation mode	Bright-field, Dark-field

Table A-9 Specification of a dynamic ultra-micro hardness tester

Maker / Type	SHIMADZU / DUH-211S model
Indenter type	Triangular pyramid indenter with tip angle of 115 °
Loading method	Electromagnetic coil
Test force range [mN]	Full scale of 0.1 to 1961
Test force accuracy	$\pm 19.6\,\mu N$ or $\pm 1\%$
Measureent method	Differential transformer
Measurement range [μm]	$0 - 10$
Measurement increment [μm]	0.0001

B) The detailed computation procedure of the plastic deformation parameter P and cleavage fracture parameter C

Transformation of Miller-Bravais indices and hexagonal system into Miller indices system and Cartesian system

The crystallographic information about sapphire is given in Miller-Bravais (4-index) indices, therefore, the indices are converted into Miller (3-index) indices by conversion matrices [153] (see Fig. B-1). The crystallographic plane $(h\ k\ i\ l)$. is transformed to the normal direction of the plane in three-axis hexagonal system $(H\ K\ L)$. Then, the third a-axis is not necessary to be written for the following relation holds.

$$i = -(h + l) \tag{B-1}$$

Whereas it is easy to calculate the vectors or distance in Cartesian coordinate systems e.g. CaF_2, the computation procedure in other crystal structure e.g. hexagonal or monoclinic structure are more complex. To calculate the distance between two points in an arbitrary coordinate system, a metric tensor g is introduced. The hexagonal lattice vectors are described by the real space metric tensor g for calculating the crystallographic direction [154].

$$g = \begin{pmatrix} a^2 & -\dfrac{a^2}{2} & 0 & 0 \\ -\dfrac{a^2}{2} & a^2 & 0 & 0 \\ 0 & 0 & 0 & c^2 \end{pmatrix} \tag{B-2}$$

To compute the corresponding basis vectors (orthogonal vector) for a plane within the reciprocal space, the metric tensor g^* is given as follows:

$$g^* = \begin{pmatrix} \dfrac{4}{3a^2} & \dfrac{2}{3a^2} & 0 & 0 \\ \dfrac{2}{3a^2} & \dfrac{4}{3a^2} & 0 & 0 \\ 0 & 0 & 0 & \dfrac{1}{c^2} \end{pmatrix} \tag{B-3}$$

The equal Miller-indices for a hexagonal direction $[u\ v\ t\ w]$ are rewritten as $[U\ V\ W]$ by the transformation matrix D, which originates from the angular relationships between the auxiliary axis and orthogonal axis:

$$D = \begin{pmatrix} 2 & 1 & 0 & 0 \\ 1 & 2 & 0 & 0 \\ 0 & 0 & 0 & 1 \end{pmatrix} \tag{B-4}$$

The vectors of the crystallographic directions are written in the hexagonal coordinate system, wherein the axis of the first two coordinates are non-perpendicular to each other but 120 ° contorted. Therefore, the calculated vectors in the of $(a_1\ a_2\ a_3)^T$ are transformed by a translation matrix in the Cartesian coordinate system $(x\ y\ z)^T$:

$$D = \begin{pmatrix} a & -a\sin\dfrac{\pi}{6} & 0 \\ 0 & a\cos\dfrac{\pi}{6} & 0 \\ 0 & 0 & c \end{pmatrix} \begin{pmatrix} a_1 \\ a_2 \\ a_3 \end{pmatrix} \qquad (B\text{-}5)$$

From there on, the crystallographic plane normal and direction are handled as normal vectors expressed in the Cartesian coordinate system (Fig. B-2).

Initialization and force direction

For the calculation the crystal system has to be orientated. With the pre-known the main orientation plane of the substrate and the side face orientation of the substrate, the vectors of the resultant force $\boldsymbol{F_r}$ depending on the specific force inclination angle β and the force direction on the main plane can be computed using the Rodrigues-rotation calculation specification. The Rodrigues calculation formula describes a three-dimensional rotation for a given axis and rotation angle. Rodrigues' rotation formula is an efficient computing method of a rotation by an angle θ about a fixed axis given by the unit vector $\boldsymbol{\omega} = (\omega_1 \ \ \omega_2 \ \ \omega_3)$.

In an orthogonal cutting model, the resultant process force $\boldsymbol{F_r}$ is expressed by synthesis of cutting force vector $\boldsymbol{F_c}$ and thrust force vector $\boldsymbol{F_t}$ (Fig. B-3). As shown in

$$(h\ k\ i\ l)_{hex} \xrightarrow{g^*} [H\ K\ L]_{hex}$$
$$[u\ v\ t\ w]_{he\overline{x}} \xrightarrow{D} [U\ V\ W]_{hex}$$
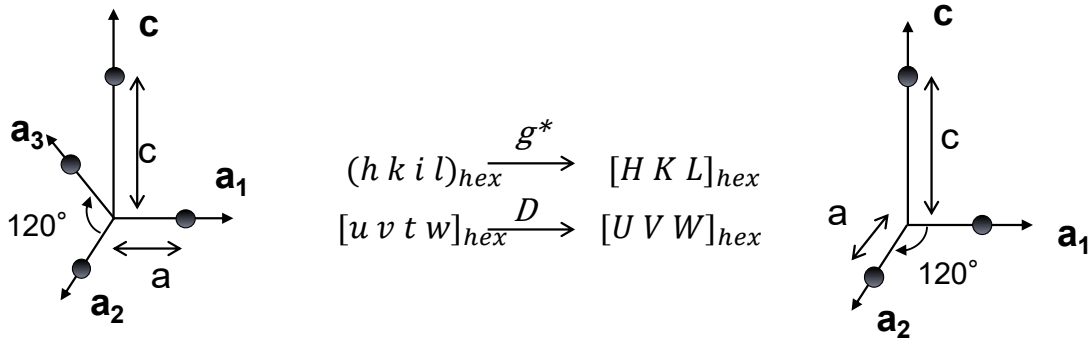
Fig. B-1 Transformation of Miller-Bravais indices into Miller-indices

$$\vec{sd} = \begin{pmatrix} U \\ V \\ W \end{pmatrix}_{cart} = A \begin{pmatrix} U \\ V \\ W \end{pmatrix}_{hex}$$

$$\vec{sp} = \begin{pmatrix} H \\ K \\ L \end{pmatrix}_{cart} = A \begin{pmatrix} H \\ K \\ L \end{pmatrix}_{hex}$$

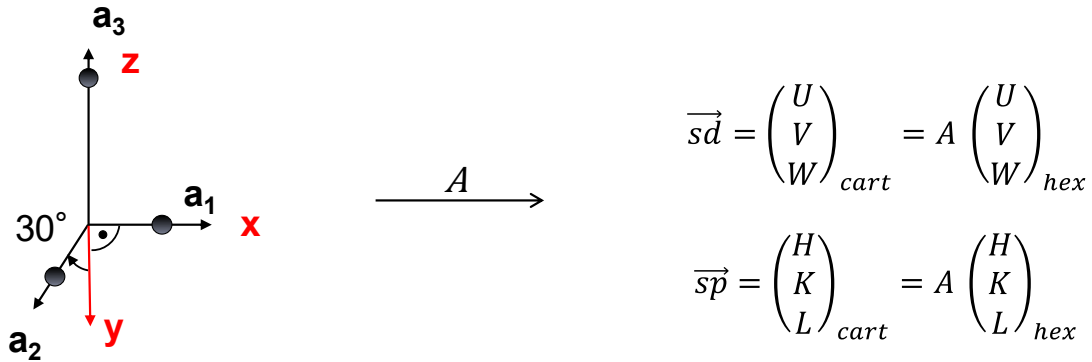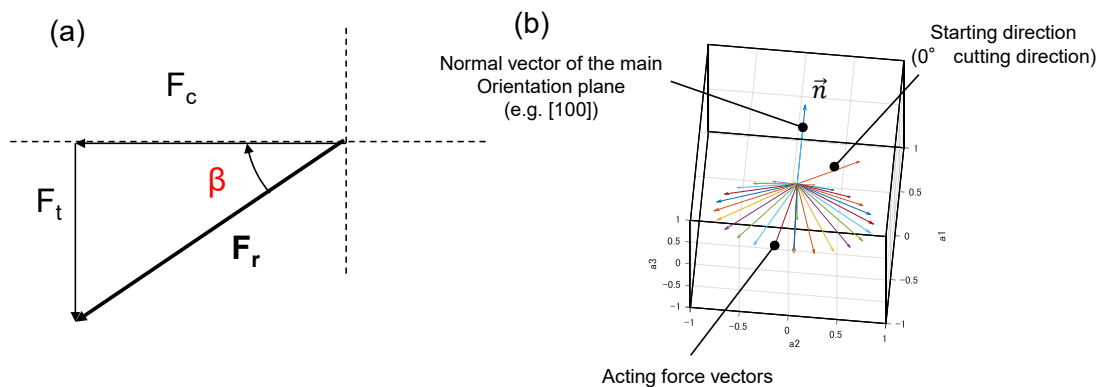Fig. B-2 Transformation of the Miller-indices into the notation of the Cartesian coordinate system

Fig. B-3 Schematic illustration of the calculation (a) Relation of force vectors in orthogonal cutting model (b) presentation of force vectors with the 15° step of cutting direction δ ((100) cutting crystalline plane of CaF₂)

Fig. B-4 and Fig. B-5, the inclined angle β can be calculated from the measured process force in the plunge-cut tests. The process force can vary depending on the time (DOC) and cutting crystalline plane and directions, however the variation range of the inclined angle β was limited. The variation was stabilized in the range of 20 ° to 30 ° for CaF₂, and 40 ° to 60 ° for sapphire, therefore, the values of 25 ° for CaF₂ and 50 ° for sapphire were used, respectively. At first, a vector on the main orientation plane is inclined about the angle β by adding the angular component while transforming the orientation vectors, which were transformed into Cartesian coordinates by the algorithm shown in the section before, in spherical coordinates. The inclined vector (the resultant force vector) is, then, rotated by the Rodrigues' rotation formula around the normal vector of the main orientation plane with the angular step with δ. To align the starting vector of the Rodrigues' rotation with the actual orientation face vector, the angle between the projected starting vector on the main plane and the orientation face vector is calculated and then added as an angular deviation. Furthermore, due to the fact that the Rodrigues' rotation is based on the right-handed coordinate system, the rotation is computed anti-clockwise, whereas the actual experimental order is set to be a clock wise rotation. After calculating all force vectors, the order is adapted to match a clockwise rotation.
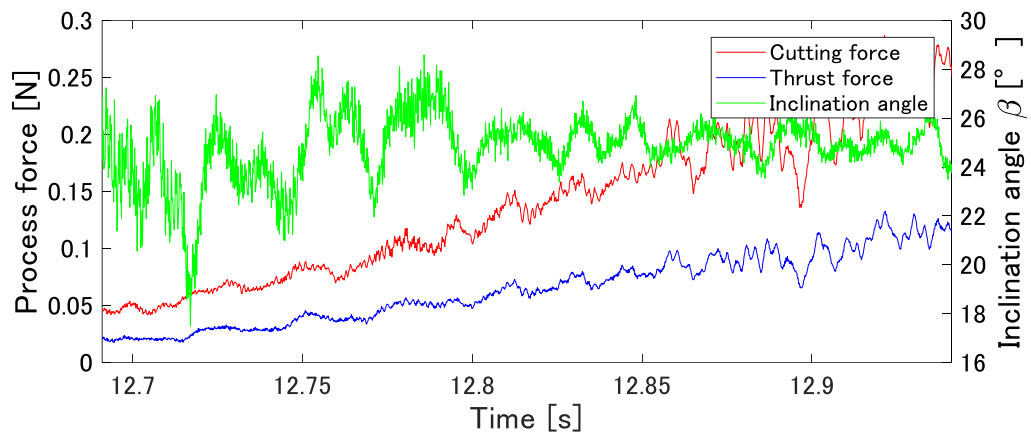
Fig. B-4 Measured force curve in the plunge-cut tests of CaF₂ ((100) plane and 120 ° cutting direction)
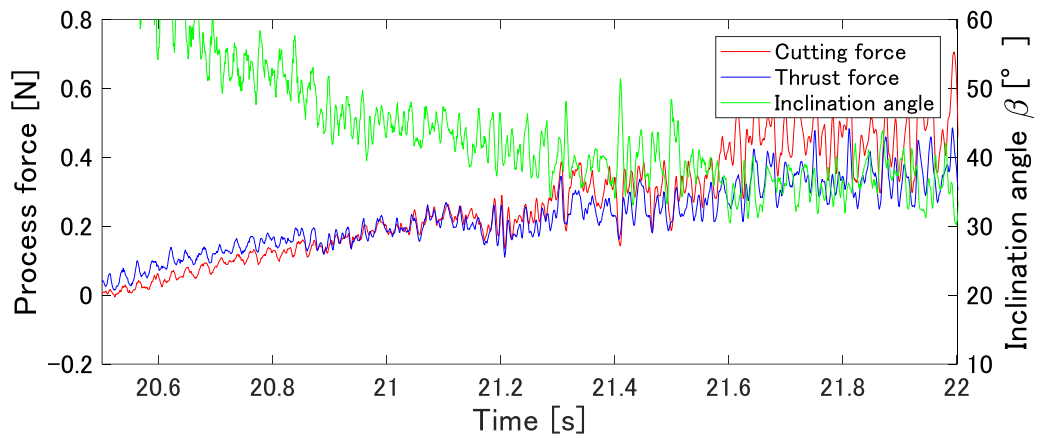

Fig. B-5   Measured force curve in the plunge-cut tests of sapphire ((0001) plane and 0 ° direction)

References

[1] Blake PN, Scattergood RO. Ductile-Regime Machining of Germanium and Silicon. J Am Ceram Soc 1990;73(4):949-57.

[2] Vahala KJ. Optical microcavities. Nature 2003;424(6950):839-46.

[3] Jimbo T. Optics Electronics. Tokyo: Ohmusha, 2009 (In Japanese).

[4] Naiman A, Desiatov B, Stern L, Mazurski N, Shappir J, Levy U. Ultrahigh-Q silicon resonators in a planarized local oxidation of silicon platform. Opt Lett 2015;40(9):1892-5.

[5] Kippenberg TJ, Spillane SM, Vahala KJ. Demonstration of ultra-high-Q small mode volume toroid microcavities on a chip. Appl Phys Lett 2004;85(25):6113-5.

[6] Holonyak N, Bevacqua SF. Coherent (Visible) Light Emission from Ga(As1-Xpx) Junctions. Appl Phys Lett 1962;1(4):82-3.

[7] Rempe G, Thompson RJ, Kimble HJ, Lalezari R. Measurement of Ultralow Losses in an Optical Interferometer. Opt Lett 1992;17(5):363-5.

[8] Hood CJ, Lynn TW, Doherty AC, Parkins AS, Kimble HJ. The atom-cavity microscope: Single atoms bound in orbit by single photons. Science 2000;287(5457):1447-53.

[9] Gerard JM, Barrier D, Marzin JY, Kuszelewicz R, Manin L, Costard E, et al. Quantum boxes as active probes for photonic microstructures: The pillar microcavity case. Appl Phys Lett 1996;69(4):449-51.

[10] Gerard JM, Sermage B, Gayral B, Legrand B, Costard E, Thierry-Mieg V. Enhanced spontaneous emission by quantum boxes in a monolithic optical microcavity. Phys Rev Lett 1998;81(5):1110-3.

[11] Tanabe T, Notomi M, Kuramochi E, Shinya A, Taniyama H. Trapping and delaying photons for one nanosecond in an ultrasmall high-Q photonic-crystal nanocavity. Nat Photonics 2007;1(1):49-52.

[12] Ooka Y, Tetsumoto T, Fushimi A, Yoshiki W, Tanabe T. CMOS compatible high-Q photonic crystal nanocavity fabricated with photolithography on silicon photonic platform. Sci Rep-Uk 2015;5.

[13] Oraevsky AN. Whispering-gallery waves. Quantum Electron+ 2002;32(5):377-400.

[14] Kandas I, Zhang BG, Daengngam C, Ashry I, Jao CY, Peng B, et al. High quality factor silica microspheres functionalized with self-assembled nanomaterials. Opt Express 2013;21(18):20601-10.

[15] Michihata M, Hayashi T, Adachi A, Takaya Y. Measurement of probe-stylus sphere diameter for micro-CMM based on spectral fingerprint of whispering gallery modes. CIRP Ann-Manuf Techn 2014;63(1):469-72.

[16] Armani DK, Kippenberg TJ, Spillane SM, Vahala KJ. Ultra-high-Q toroid microcavity on a chip. Nature 2003;421(6926):925-8.

[17] Kato T, Yoshiki W, Suzuki R, Tanabe T. Octagonal silica toroidal microcavity for

controlled optical coupling. Appl Phys Lett 2012;101(12).

[18] Savchenkov AA, Ilchenko VS, Matsko AB, Maleki L. Kilohertz optical resonances in dielectric crystal cavities. Phys Rev A 2004;70(5):051804(R).

[19] Ilchenko VS, Savchenkov AA, Matsko AB, Maleki L. Nonlinear optics and crystalline whispering gallery mode cavities. Phys Rev Lett 2004;92(4).

[20] Seidel H, Csepregi L, Heuberger A, Baumgartel H. Anisotropic Etching of Crystalline Silicon in Alkaline-Solutions .1. Orientation Dependence and Behavior of Passivation Layers. J Electrochem Soc 1990;137(11):3612-26.

[21] Grudinin IS, Matsko AB, Savchenkov AA, Strekalov D, Ilchenko VS, Maleki L. Ultra high Q crystalline microcavities. Opt Commun 2006;265(1):33-8.

[22] Fang FZ, Zhang XD, Weckenmann A, Zhang GX, Evans C. Manufacturing and measurement of freeform optics. CIRP Ann-Manuf Techn 2013;62(2):823-46.

[23] Grudinin IS, Yu N, Maleki L. Generation of optical frequency combs with a CaF_2 resonator. Opt Lett 2009;34(7):878-80.

[24] Hofer J, Schliesser A, Kippenberg TJ. Cavity optomechanics with ultrahigh-Q crystalline microresonators. Phys Rev A 2010;82(3):031804(R).

[25] Wang CY, Herr T, Del'Haye P, Schliesser A, Hofer J, Holzwarth R, et al. Mid-infrared optical frequency combs at 2.5 μm based on crystalline microresonators. Nat Commun 2013;4:1345.

[26] Grudinin IS, Yu N. Dispersion engineering of crystalline resonators via microstructuring. Optica 2015;2(3):221.

[27] Pavlov NG, Lihachev G, Koptyaev S, Lucas E, Karpov M, Kondratiev NM, et al. Soliton dual frequency combs in crystalline microresonators. Opt Lett 2017;42(3):514-7.

[28] Ilchenko VS, Savchenkov AA, Matsko AB, Maleki L. Generation of Kerr frequency combs in a sapphire whispering gallery mode microresonator. Opt Eng 2014;53(12):122607.

[29] Kudo H, Ogawa Y, Kato T, Yokoo A, Tanabe T. Fabrication of whispering gallery mode cavity using crystal growth. Appl Phys Lett 2013;102(21):211105.

[30] Michael Pollinger AR. All-optical signal processing at ultra-low powers in bottle microresonators using the Kerr effect. Opt Express 2010;18(17):17764-75.

[31] Spillane SM, Kippenberg TJ, Vahala KJ. Ultralow-threshold Raman laser using a spherical dielectric microcavity. Nature 2002;415(6872):621-3.

[32] Chen R, Tran TTD, Ng KW, Ko WS, Chuang LC, Sedgwick FG, et al. Nanolasers grown on silicon. Nat Photonics 2011;5(3):170-5.

[33] Vollmer F, Arnold S. Whispering-gallery-mode biosensing: label-free detection down to single molecules. Nat Methods 2008;5(7):591-6.

[34] Udem T, Holzwarth R, Hansch TW. Optical frequency metrology. Nature 2002;416(6877):233-7.

[35] Lee M, Fauchet PM. Two-dimensional silicon photonic crystal based biosensing platform

for protein detection. Opt Express 2007;15(8):4530-5.

[36] Yang AHJ, Moore SD, Schmidt BS, Klug M, Lipson M, Erickson D. Optical manipulation of nanoparticles and biomolecules in sub-wavelength slot waveguides. Nature 2009;457(7225):71-5.

[37] Rindorf L, Jensen JB, Dufva M, Pedersen LH, Hoiby PE, Bang O. Photonic crystal fiber long-period gratings for biochemical sensing. Opt Express 2006;14(18):8224-31.

[38] Matsko BA. Practical Applications of Microresonators in Optics and Photonics. USA: CRC Press, 2009.

[39] Sasada H. Current Status and Prospect of Optical Frequency Comb Technology. Optics 2012;41(9):460-6 (in Japanese).

[40] Diddams SA, Jones DJ, Ye J, Cundiff ST, Hall JL, Ranka JK, et al. Direct link between microwave and optical frequencies with a 300 THz femtosecond laser comb. Phys Rev Lett 2000;84(22):5102-5.

[41] Holzwarth R, Udem T, Hansch TW, Knight JC, Wadsworth WJ, Russell PSJ. Optical frequency synthesizer for precision spectroscopy. Phys Rev Lett 2000;85(11):2264-7.

[42] Miyake S. Anomalous Dispersion of X-Rays, in Terms of the Classical Theory of Vibration. Nihon Kessho Gakkaishi 1977;19(2):47-50.

[43] Del'Haye P, Arcizet O, Schliesser A, Holzwarth R, Kippenberg TJ. Full stabilization of a microresonator-based optical frequency comb. Phys Rev Lett 2008;101(5).

[44] Riesen N, Afshar VS, Francois A, Monro TM. Material candidates for optical frequency comb generation in microspheres. Opt Express 2015;23(11):14784-95.

[45] Lin GP, Chembo YK. On the dispersion management of fluorite whispering-gallery mode resonators for Kerr optical frequency comb generation in the telecom and mid-infrared range. Opt Express 2015;23(2):1594-604.

[46] He LN, Xiao YF, Zhu JG, Ozdemir SK, Lan Y. Oscillatory thermal dynamics in high-Q PDMS-coated silica toroidal microresonators. Opt Express 2009;17(12):9571-81.

[47] Technical Document of OKEN Co. Ltd.

[48] Yan J, Tamaki J, Syoji K, Kuriyagawa T. Single-point diamond turning of CaF_2 for nanometric surface. Int J Adv Manuf Tech 2004;24(9-10):640-6.

[49] Chen X, Xu J, Fang H, Tian R. Influence of cutting parameters on the ductile-brittle transition of single-crystal calcium fluoride during ultra-precision cutting. Int J Adv Manuf Tech 2017;89:219-25.

[50] Bezuidenhout DF. Handbook of Optical Constants of Solids. London: Academic Press, 1997.

[51] Janicki MJ, Drzymala J, Kowalczuk PB. Structure and Surface Energy of Both Fluorite Halves after Cleaving Along Selected Crystallographic Planes. Physicochem Probl Mi 2016;52(1):451-8.

[52] Yoshizawa T. Handbook of Optical Metrology: Principles and Applications. Boca Raton:

CRC Press, 2009.

[53] Schick M, Dabringhaus H, Wandelt K. Macrosteps on CaF_2(111). J Phys Condens Matter 2004;16(6):33-7.

[54] Liberman V, Bloomstein TM, Rothschild M, Sedlacek JHC, Uttaro RS, Bates AK, et al. Materials issues for optical components and photomasks in 157 nm lithography. J Vac Sci Technol B: Microelectron Nanometer Struct 1999;17(6):3273.

[55] Reichling M, Wilson RM, Bennewitz R, Williams RT, Gogoll S, Stenzel E, et al. Surface colloid evolution during low-energy electron irradiation of CaF_2(111). Surf Sci 1996;366(3):531-44.

[56] Chen L, Hu LC, Xiao C, Qi YQ, Yu BJ, Qian LM. Effect of crystallographic orientation on mechanical removal of CaF2. Wear 2017;376:409-16.

[57] Dobrovinskaya ER, Lytvynov LA, Pishchik V. Sapphire: Material, Manufacturing, Applications. New York: Springer Science+Business Media, 2009.

[58] Haney EJ, Subhash G. Damage Mechanisms Perspective on Superior Ballistic Performance of Spinel over Sapphire. Exp Mech 2013;53(1):31-46.

[59] Wang YG, Zhang LC. A Review on the CMP of SiC and Sapphire Wafers. Adv Mater Res-Switz 2010;126-128:429-34.

[60] Li ZC, Pei ZJ, Funkenbusch PD. Machining processes for sapphire wafers: a literature review. P I Mech Eng B-J Eng 2011;225(B7):975-89.

[61] Namba Y, Tsuwa T. Ultra-Fine Finishing of Sapphire Single Crystal. CIRP Ann-Manuf Techn 1977;25(1):325-9.

[62] Kondo E. Principle of micro and nano fabrication for machine and material. Tokyo: Kyoritsushuppan, 2005 (In Japanese).

[63] Taniguchi N. Current Status in, and Future Trends of, Ultraprecision Machining and Ultrafine Materials Processing. CIRP Ann-Manuf Techn 1983;32(2):573-82.

[64] Corbett J, McKeown PA, Peggs GN, Whatmore R. Nanotechnology: International developments and emerging products. CIRP Ann-Manuf Techn 2000;49(2):523-45.

[65] Goel S, Luo XC, Agrawal A, Reuben RL. Diamond machining of silicon: A review of advances in molecular dynamics simulation. Int J Mach Tool Manu 2015;88:131-64.

[66] Masuzawa T, Tonshoff HK. Three-dimensional micromachining by machine tools. CIRP Ann-Manuf Techn 1997;46(2):621-8.

[67] Masuzawa T. State of the art of micromachining. CIRP Ann-Manuf Techn 2000;49(2):473-88.

[68] Dornfeld D, Min S, Takeuchi Y. Recent advances in mechanical micromachining. CIRP Ann-Manuf Techn 2006;55(2):745-68.

[69] Brinksmeier E, Mutlugünes Y, Klocke F, Aurich JC, Shore P, Ohmori H. Ultra-precision grinding. CIRP Ann-Manuf Techn 2010;59(2):652-71.

[70] Fang FZ, Zhang XD, Gao W, Guo YB, Byrne G, Hansen HN. Nanomanufacturing—

Perspective and applications. CIRP Ann-Manuf Techn 2017;66(2):683-705.

[71] Inasaki I. Machining system. Tokyo: Yokendo, 2009 (in Japanese).

[72] Aramcharoen A, Mativenga PT. Size effect and tool geometry in micromilling of tool steel. Precis Eng 2009;33(4):402-7.

[73] Gubbels GPH. Diamond turning of glassy polymers [Ph.D thesis]: Technische Universiteit Eind-hoven, 2006.

[74] Bifano GT, Dow TA, Scattergood RO. Ductile-regime grinding of brittle materials: Experimental results and the development of a model. 32nd Annual Technical Symposium, International Society for Optics and Photonics 1989:108-15.

[75] Fang FZ, Chen LJ. Ultra-precision cutting for ZKN7 glass. CIRP Ann-Manuf Techn 2000:17-20.

[76] Yan J, Syoji K, Tamaki J. Crystallographic effects in micro/nanomachining of single-crystal calcium fluoride. J Vac Sci Technol B: Microelectron Nanometer Struct 2004;22(1):46-51.

[77] Nakasuji T, Kodera S, Hara S, Matsunaga H, Ikawa N, Shimada S. Diamond Turning of Brittle Materials for Optical Components. CIRP Ann-Manuf Techn 1990;39(1):89-92.

[78] Yan J, Syoji K, T. K. Ductile-Brittle Transition at Large Negative Tool Rake Angles. Japan Journal of Precision Engineering 2000;66(1):1130-4.

[79] Yan J, Asami T, Harada H, Kuriyagawa T. Crystallographic effect on subsurface damage formation in silicon microcutting. CIRP Ann-Manuf Techn 2012;61(1):131-4.

[80] Yan J, Syoji K, Kuriyagawa T, Suzuki H. Ductile regime turning at large tool feed. J Mater Process Tech 2002;121(2-3):363-72.

[81] Yan J, Asami T, Harada H, Kuriyagawa T. Fundamental investigation of subsurface damage in single crystalline silicon caused by diamond machining. Precis Eng 2009;33(4):378-86.

[82] Bifano TG, Dow TA, Scattergood RO. Ductile-Regime Grinding - a New Technology for Machining Brittle Materials. J Eng Ind-T Asme 1991;113(2):184-9.

[83] Ngoi BKA, Sreejith PS. Ductile regime finish machining - A review. Int J Adv Manuf Tech 2000;16(8):547-50.

[84] Min S, Dornfeld D, Inasaki I, Ohmori H, Lee D, Deichmueller M, et al. Variation in Machinability of Single Crystal Materials in Micromachining. CIRP Ann-Manuf Techn 2006;55(1):103-6.

[85] Shibata T, Fujii S, Makino E, Ikeda M. Ductile-regime turning mechanism of single-crystal silicon. Precis Eng 1996;18(2-3):129-93.

[86] Wang H, Riemer O, Rickens K, Brinksmeier E. On the mechanism of asymmetric ductile–brittle transition in microcutting of (111) CaF_2 single crystals. Scr Mater 2016;114:21-6.

[87] Marsh ER, John BP, Couey JA, Wang J, Grejda RD, Vallance RR. Predicting surface figure in diamond turned calcium fluoride using in-process force measurement. J Vac Sci

Technol B 2005;23(1):84-9.

[88] Huo D, Choong ZJ, Shi Y, Hedley J, Zhao Y. Diamond micro-milling of lithium niobate for sensing applications. J Micromech Microeng 2016;26(9):095005.

[89] Shizuka HO, K.; Nunobiki, M.; Li, W.; Inaoka, T.; Utsumi, Y.; Saiki, T. Ductile mode cutting of lithium niobate. Journal of the Japan Society for Abrasive Technology 2012;56(2):118-23 (in Japanese).

[90] Matsumura T, Endo Y, Ozawa H. Micro Cutting of Sapphire. Emerging Technology in Precision Engineering Xiv 2012;523-524:99-104.

[91] Jawahir IS, Brinksmeier E, M'Saoubi R, Aspinwall DK, Outeiro JC, Meyer D, et al. Surface integrity in material removal processes: Recent advances. CIRP Ann-Manuf Techn 2011;60(2):603-26.

[92] Lucca DA, Brinksmeier E, Goch G. Progress in assessing surface and subsurface integrity. CIRP Ann-Manuf Techn 1998;47(2):669-93.

[93] Ohnishi N, Yoshida S, Namba Y. High resolution transmission electron microscopy study of calcium fluoride single crystal(III) surfaces processed by ultraprecision machining. Materials Transactions 2006;47(2):267-70.

[94] Namba Y, Ohnishi N, Yoshida S, Harada K, Yoshida K, Matsuo T. Ultra-Precision Float Polishing of Calcium Fluoride Single Crystals for Deep Ultra Violet Applications. CIRP Ann-Manuf Techn 2004;53(1):459-62.

[95] Sumiya H, Yamaguchi K, Ogata S. Deformation microstructure of high-quality synthetic diamond crystal subjected to Knoop indentation. Appl Phys Lett 2006;88(16):161904.

[96] Inkson BJ. Dislocations and twinning activated by the abrasion of Al_2O_3. Acta Mater 2000;48(8):1883-95.

[97] Sasaki T, Shibata N, Matsunaga K, Yamamoto T, Ikuhara Y. Direct observation of the cleavage plane of sapphire by in-situ indentation TEM. Journal of the Ceramic Society of Japan 2012;120(1407):473-7.

[98] Ono T, Matsumura T. Influence of tool inclination on brittle fracture in glass cutting with ball end mills. J Mater Process Tech 2008;202(1-3):61-9.

[99] Yan J, Asami T, Kuriyagawa T. Nondestructive measurement of machining-induced amorphous layers in single-crystal silicon by laser micro-Raman spectroscopy. Precis Eng 2008;32(3):186-95.

[100] Wermelinger T, Borgia C, Solenthaler C, Spolenak R. 3-D Raman spectroscopy measurements of the symmetry of residual stress fields in plastically deformed sapphire crystals. Acta Mater 2007;55(14):4657-65.

[101] Wermelinger T, Mornaghini FCF, Hinderling C, Spolenak R. Correlation between the defect structure and the residual stress distribution in ZnO visualized by TEM and Raman microscopy. Mater Lett 2010;64(1):28-30.

[102] Gu W, Yao Z, Li H. Investigation of grinding modes in horizontal surface grinding of

optical glass BK7. J Mater Process Tech 2011;211(10):1629-36.

[103] Namba Y, Yoshida T, Yoshida S, Yoshida K. Surfaces of calcium fluoride single crystals ground with an ultra-precision surface grinder. CIRP Ann-Manuf Techn 2005;54(1):503-6.

[104] Zhang W, Zhu JQ. Subsurface damage of Nd-doped phosphate glasses in optical fabrication. Optik 2008;119(15):738-41.

[105] Sumiya H, Harano K, Murakami H. Application of Nano-Polycrystalline Diamond o Cutting Tools. SEI TECHNICAL REVIEW 2012;75:18-23.

[106] Sumiya H. Novel Development of High-Pressure Synthetic Diamonds"Ultra-hard Nano-polycrystalline Diamonds". SEI TECHNICAL REVIEW 2012;74:15-23.

[107] Irifune T, Kurio A, Sakamoto S, Inoue T, Sumiya H. Materials - Ultrahard polycrystalline diamond from graphite. Nature 2003;421(6923):599-600.

[108] Li XP, Cai MB, Neo WCL, Seah KHW. Effect of crystalline orientation of a diamond tool on the machined surface in ductile mode cutting of silicon. P I Mech Eng B-J Eng 2008;222(12):1597-603.

[109] Nakayama K, Nevshupa RA. Characteristics and Pattern of Plasma Generated at Sliding Contact. J Tribol 2003;125(4):780.

[110] Sumiya H, Ikeda K, Arimoto K, Harano K. High wear-resistance characteristic of boron-doped nano-polycrystalline diamond on optical glass. Diam Relat Mater 2016;70:7-11.

[111] Harano K, Ikeda K, Arimoto K, Sumiya H. Cutting performances of B-doped binder-less nano polycrystalline-diamond. Proceedings of 2016 JSPE Autumn Meeting 2016:695-6 (in Japanese).

[112] Sekiguchi R, Mizumoto Y, Yoshikawa S, Kakinuma Y, Fukuta M, Tanaka K. High-efficiency ductile-mode grinding of optical glass lens by controlling tool feed rate and workpiece velocity. Journal of the Japan Society for Abrasive Technology 2016;60(5):254-60 (in Japanese).

[113] Yamauchi K, Hirose K, Goto H, Sugiyama K, Inagaki K, Yamamura K, et al. First-principles simulations of removal process in EEM (Elastic Emission Machining). Comp Mater Sci 1999;14(1-4):232-5.

[114] Mori Y, Yamauchi K, Endo K. Elastic Emission Machining. Precis Eng 1987;9(3):123-8.

[115] Takei Y, Kume T, Motoyama H, Hiraguri K, Hashizume H, Mimura H. Development of a numerically controlled elastic emission machining system for fabricating mandrels of ellipsoidal focusing mirrors used in soft x-ray microscopy. Advances in X-Ray/Euv Optics and Components Viii 2013;8848.

[116] Motzer C, Reichling M. High resolution study of etch figures on CaF$_2$ (111). J Appl Phys 2009;105(6):064309.

[117] Chryssolouris G, Ling FF. Laser Machining: Theory and Practice. New York: Springer New York, 1991.

[118] Allen DM, Redondo R, Dany M. Fabrication methods for the manufacture of sapphire

microparts. Microsystem Technologies 2012;18(11):1835-41.

[119] Jamali AA, Witzigmann B, Morarescu R, Baumert T, Trager F, Hubenthal F. Local near field assisted ablation of fused silica. Appl Phys a-Mater 2013;110(4):743-9.

[120] Kizaki T, Ogasahara T, Sugita N, Mitsuishi M. Ultraviolet-laser-assisted precision cutting of yttria-stabilized tetragonal zirconia polycrystal. J Mater Process Tech 2014;214(2):267-75.

[121] Kudo H, Suzuki R, Tanabe T. Whispering gallery modes in hexagonal microcavities. Phys Rev A 2013;88(2).

[122] Kudo H, Suzuki R, Tanabe T. Whispering gallery modes in hexagonal microcavities by crystal growth. Phys Rev A 2013;88(2).

[123] Byrne G, Dornfeld D, Denkena B. Advancing cutting technology. CIRP Ann-Manuf Techn 2003;52(2):483-507.

[124] Yan JW, Zhao HW, Kuriyagawa T. Effects of tool edge radius on ductile machining of silicon: an investigation by FEM. Semicond Sci Tech 2009;24(7):075018.

[125] Goel S, Luo XC, Reuben RL. Molecular dynamics simulation model for the quantitative assessment of tool wear during single point diamond turning of cubic silicon carbide. Comp Mater Sci 2012;51(1):402-8.

[126] Goel S, Luo X, Reuben RL, Rashid WB. Atomistic aspects of ductile responses of cubic silicon carbide during nanometric cutting. Nanoscale research letters 2011;6:589.

[127] Furukawa Y, Moronuki N. Effect of Material Properties on Ultra Precise Cutting Processes. CIRP Ann-Manuf Techn 1988;37(1):113-6.

[128] Phillips WL. Deformation and Fracture Processes in Calcium Fluoride Single Crystals. J Am Ceram Soc 1961;44(10):499-506.

[129] Munoz A, Dominguezrodriguez A, Castaing J. Slip Systems and Plastic Anisotropy in $CaF2$. J Mater Sci 1994;29(23):6207-11.

[130] Engelhardt JB, Dabringhaus H, Wandelt K. Atomic force microscopy study of the CaF_2(111) surface: from cleavage via island to evaporation topographies. Surf Sci 2000;448(2-3):187-200.

[131] Puchin VE, Puchina AV, Huisinga M, Reichling M. Theoretical modelling of steps on the CaF_2(111) surface. J Phys Condens Matter 2001;13(10):2081-94.

[132] Wu Z, Zhou F, Chen K, Wang Q, Zhou Z, Yan J, et al. Microstructure, mechanical and tribological properties of CrSiC coatings sliding against SiC and Al_2O_3 balls in water. Appl Surf Sci 2016;368:129-39.

[133] Funkenbusch PD, Zhou YY, Takahashi T, Golini D. Grinding of single crystal sapphire: workpiece roughness correlations. Wear 1998;218(1):1-7.

[134] Zhou YY, Atwood M, Golini D, Smith M, Funkenbusch PD. Wear and self-sharpening of vitrified bond diamond wheels during sapphire grinding. Wear 1998;219(1):42-5.

[135] Liang Z, Wang X, Wu Y, Xie L, Jiao L, Zhao W. Experimental study on brittle–ductile

transition in elliptical ultrasonic assisted grinding (EUAG) of monocrystal sapphire using single diamond abrasive grain. Int J Mach Tool Manuf 2013;71:41-51.

[136] Liang Z, Wang X, Wu Y, Xie L, Liu Z, Zhao W. An investigation on wear mechanism of resin-bonded diamond wheel in Elliptical Ultrasonic Assisted Grinding (EUAG) of monocrystal sapphire. J Mater Process Tech 2012;212(4):868-76.

[137] Zhang YN, Lin B, Li ZC. An overview of recent advances in chemical mechanical polishing (CMP) of sapphire substrates. Ecs Transactions 2013;52(1):495-500.

[138] Aida H, Doi T, Takeda H, Katakura H, Kim SW, Koyama K, et al. Ultraprecision CMP for sapphire, GaN, and SiC for advanced optoelectronics materials. Curr Appl Phys 2012;12:S41-S6.

[139] Zhu HL, Tessaroto LA, Sabia R, Greenhut VA, Smith M, Niesz DE. Chemical mechanical polishing (CMP) anisotropy in sapphire. Appl Surf Sci 2004;236(1-4):120-30.

[140] Wang JJJ, Liao YY. Critical depth of cut and specific cutting energy of a microscribing process for hard and brittle materials. J Eng Mater-T Asme 2008;130(1).

[141] Feng PF, Zhang CL, Wu ZJ, Zhang JF. Effect of Scratch Velocity on Deformation Features of C-plane Sapphire during Nanoscratching. Strojniski Vestnik-Journal of Mechanical Engineering 2013;59(6):367-74.

[142] Tymiak NI, Gerberich WW. Initial stages of contact-induced plasticity in sapphire. I. Surface traces of slip and twinning. Philosophical Magazine 2007;87(33):5143-68.

[143] Pelleg J. Mechanical Properties of Materials. Springer Science+Business Media 2013.

[144] Mittemeijer EJ. Fundamentals of Materials Science: The Microstructure-Property Relationship Using Metals as Model Systems. Berlin: Springer-Verlag, 2010.

[145] Nakai Y, Kubo S. Fracture mechanics. Tokyo: Asakurashoten, 2014 (in Japanese).

[146] Nowak R, Sekino T, Maruno S, Niihara K. Deformation of sapphire induced by a spherical indentation on the (10-10) plane. Appl Phys Lett 1996;68(8):1063-5.

[147] Nowak R, Sakai M. The anisotropy of surface deformation of sapphire: Continuous indentation of triangular indenter. Acta Metall Mater 1994;42(8):2879-91.

[148] Clayton JD. A continuum description of nonlinear elasticity, slip and twinning, with application to sapphire. Proceedings of the Royal Society A: Mathematical, Physical and Engineering Sciences 2009;465(2101):307-34.

[149] Lagerlof KPD, Heuer AH, Castaing J, Riviere JP, Mitchell TE. Slip and Twinning in Sapphire (Alpha-Al2o3). J Am Ceram Soc 1994;77(2):385-97.

[150] François D, Pineau A, Zaoui A. Mechanical Behaviour of Materials Volume II Fracture Mechanics and Damage. Dordrecht: Springer Science+Business Media, 2013.

[151] Wiederhorn S. Fracture of sapphire. J Am Ceram Soc 1969;52(9):485-91.

[152] Frank F. On Miller–Bravais indices and four-dimensional vectors. Acta Crystallographica 1965;18(5):862-6.

[153] Hammond C. The basics of crystallography and diffraction. New York: Oxford

University Press Oxford, 2009.

[154] Graef DM, McHenry EM. Structure of materials: an introduction to crystallography, diffraction and symmetry. 2nd ed. Cambridge: Cambridge University Press, 2012.

[155] Wang SF, An CH, Zhang FH, Wang J, Lei XY, Zhang JF. An experimental and theoretical investigation on the brittle ductile transition and cutting force anisotropy in cutting KDP crystal. Int J Mach Tool Manu 2016;106:98-108.

[156] Brinksmeier E, Preuss W, Riemer O, Rentsch R. Cutting forces, tool wear and surface finish in high speed diamond machining. Precis Eng 2017;49:293-304.

[157] Wang B, Liu ZQ, Su GS, Song QH, Ai X. Investigations of critical cutting speed and ductile-to-brittle transition mechanism for workpiece material in ultra-high speed machining. Int J Mech Sci 2015;104:44-59.

[158] Chen WY. Cutting forces and surface finish when machining medium hardness steel using CBN tools. Int J Mach Tool Manu 2000;40(3):455-66.

[159] Nath C, Rahman M, Neo KS. A study on the effect of tool nose radius in ultrasonic elliptical vibration cutting of tungsten carbide. J Mater Process Tech 2009;209(17):5830-6.

[160] Arif M, Rahman M, San WY. Analytical model to determine the critical feed per edge for ductile-brittle transition in milling process of brittle materials. Int J Mach Tool Manu 2011;51(3):170-81.

[161] Kountanya R, Al-Zkeri I, Altan T. Effect of tool edge geometry and cutting conditions on experimental and simulated chip morphology in orthogonal hard turning of 100Cr$_6$ steel. J Mater Process Tech 2009;209(11):5068-76.

[162] Blackley WS, Scattergood RO. Ductile-Regime Machining Model for Diamond Turning of Brittle Materials. Precis Eng 1991;13(2):95-103.

[163] Liu K, Zuo DW, Li XP, Rahman M. Nanometric ductile cutting characteristics of silicon wafer using single crystal diamond tools. J Vac Sci Technol B 2009;27(3):1361-6.

[164] Matsubara T, Yamamoto H, Mizumoto H. Study on regenerative chatter vibration with dynmic cutting force. Japan Journal of Precision Engineering 1984;50(7):11-5 (in Japanese).

[165] Kakinuma Y, Azami S, Tanabe T. Evaluation of subsurface damage caused by ultra-precision turning in fabrication of CaF2 optical micro resonator. CIRP Ann-Manuf Techn 2015;64(1):117-20.

[166] Nakayama K. The plasma generated and photons emitted in an oil-lubricated sliding contact. Journal of Physics D: Applied Physics 2007;40(4):1103-7.

[167] Elsharkawy AA. Effect of friction on subsurface stresses in sliding line contact of multilayered elastic solids. Int J Solids Struct 1999;36(26):3903-15.

[168] Panin V, Kolubaev A, Tarasov S, Popov V. Subsurface layer formation during sliding friction. Wear 2001;249(10-11):860-7.

[169] Sumiya H, Harano K, Ikeda K, Arimoto K. Material properties of boron-doped nano-polycrystalline diamonds. Proceedings of 2016 JSPE Spring Meeting 2016:693-4 (in

Japanese).

[170] Kasuga H, Nemoto A, Mizutani M, Itoh N, Ohmori H. Effective part of diamond cutting edge for ductile regime of sapphire (3nd report) Relationships between cutting force and groove depth in nano-cutting area. Proceedings of 2016 JSPE Autumn Meeting 2016:343-4.

[171] Chou YT, Whitmore RW. Single and Double Pile-up of Dislocations in Mgo Crystals. J Appl Phys 1961;32(10):1920-6.

[172] Aota N, Aida H, Kimura Y, Kawamata Y, Uneda M. Fabrication Mechanism for Patterned Sapphire Substrates by Wet Etching. Ecs Journal of Solid State Science and Technology 2014;3(5):N69-N74.

[173] Zheng Y, Lin CH, Shen P, Chen SY. The basal twin of α-Cr_2O_3 nanocondensates: occurrence and first-principles calculations. Crystengcomm 2013;15(32):6374-80.

[174] Schroder S, Duparre A, Coriand L, Tunnermann A, Penalver DH, Harvey JE. Modeling of light scattering in different regimes of surface roughness. Opt Express 2011;19(10):9820-35.

[175] Del'Haye P, Arcizet O, Gorodetsky ML, Holzwarth R, Kippenberg TJ. Frequency comb assisted diode laser spectroscopy for measurement of microcavity dispersion. Nat Photonics 2009;3(9):529-33.

[176] Nakagawa Y, Mizumoto Y, Kato T, Kobatake T, Itobe H, Kakinuma Y, et al. Dispersion tailoring of a crystalline whispering gallery mode microcavity for a wide-spanning optical Kerr frequency comb. J Opt Soc Am B 2016;33(9):1913-20.

[177] Webster P. The Brasses properties & applications: Copper Development Association, 2005.

Acknowledgement

This dissertation is a summary of my research as a member of laboratory for manufacturing engineering in Keio University. I could manage to complete the PhD study with the endless guidance and support of many individuals. Firstly, I would like to express my deepest gratitude to my supervisor, Associate Professor Dr. Yasuhiro Kakinuma. He warmly accepted me as a member of the laboratory since when I was a Bachelor student. His enthusiastic instruction was always an important step for advancement of my research. He also gave me a plenty of opportunities which are mandatory for researchers such as attending conferences, journal writing, making a proposal for new projects, engaging in collaborative research in both academia and industry. I would also like to express my immense gratitude to Professor Emeritus Dr. Tojiro Aoyama, who encouraged me to work in Leibnitz University Hannover when I was a Master student. The experience which I had in Germany as a researcher was a trigger for me to study in the course of PhD program.

I would like to show my sincere gratitude to Professor Dr. Hideki Aoyama, Professor Dr. Jiwang Yan, and Associate Professor Dr. Takasumi Tanabe who provided me with beneficial comments and suggestions in writing this dissertation.

I would extend my sincere thanks to Associate Professor Dr. Sangkee Min in University of Wisconsin Madison who gave me an opportunity to work on sapphire machining. Owing to his plentiful knowledge and experience of ultra-precision machining, the discussion with him was always fruitful. I would also like to extend my appreciations to the technical staff in central service facilities for research, particularly, Dr. Tomoaki Mitani, Dr. Jechol Lee, Dr. Kayoko Kawano, and Sachiko Kamiyama. Their advanced technique and guidance opened a novel avenue in the ultra-precision cutting field.

I am greatly thankful to Dr. Katsutoshi Tanaka and Dr. Masahiko Fukuta from Toshiba Machine Ltd., for providing an excellent ultra-precision machine tool. Their advice for the experimental procedure was essential and critical to the results. I would like to thank Dr. Hitoshi Sumiya and Katsuko Harano from Sumitomo Electric Industry Ltd., for providing valuable NPD and B-NPD tools. The tools and discussion with the subsurface formation advanced my research.

I appreciate my former and current students; Shunya Azami, Hiroi Kangawa, Philipp Alexander Maas, and Hikaru Amano in Kakinuma laboratory, Hiroshi Kudo, Yosuke Nakagawa, Hiroki Itobe, and Mika Fuchida in Tanabe laboratory. I would also like to thank Dr. Ryo Koike and Dr. Yuki Yamada for giving me profitable comments relating to my research and supporting me to prepare for this dissertation. I am grateful for Michie

Ishiwata and Kana Igarashi for their continuous contributions to keep research environments and mental supports.

Finally, my special appreciation goes to my beloved parents for their endless supports.

<div align="right">

January, 2017

Yuta Mizumoto

</div>